PROBING THE FUSION OF NEUTRON-RICH NUCLEI WITH MODERN RADIOACTIVE BEAM FACILITIES

Jessica Elizabeth Vadas

Submitted to the faculty of the University Graduate School in partial fulfillment of the requirements for the degree Doctor of Philosophy in the Department of Chemistry,
Indiana University
December 2018

Accepted by the Graduate Faculty, Indiana University, in partial fulfillment of the requirements for the degree of Doctor of Philosophy.

Doctoral Committee:

Romualdo T. de Souza, Ph.D., Chair

Caroline C. Jarrold, Ph.D.

Peter J. Ortoleva, Ph.D.

Charles J. Horowitz, Ph.D.

December 2018

Acknowledgements

There are many people who have played a pivotal role in helping me get to where I am today. I have been encouraged my whole life to continue pursuing academics by all of the wonderful people from whom I have had the privilege to learn. In particular, I would like to thank Mr. Steve Schuh, Dr. Michael Lerner, Dr. Corinne Deibel, and Dr. Lori Watson for being wonderful mentors and friends throughout my academic career.

I want to thank Dr. Romualdo de Souza for accepting me into his research group and helping me to hone my research skills. Since the time I met him at the Nuclear Chemistry Summer School, he has challenged me every step of the way to exceed expectations. Although it has been difficult at times to face such challenges, I am ultimately a better scientist because of it.

Dr. Sylvie Hudan deserves special recognition for taking me under her wing and teaching me many skills I will use throughout my career. Without her help, my time in graduate school would have been much more difficult. She has been a great mentor, making sure I learned how she approached problems so that I would be able to do the same thing myself in the future. I am thankful for her friendship through all these years.

I have cherished my time with all of the students in the IU Nuclear Chemistry who have come and gone. In particular, I am grateful for the comraderie and friendship I found in Dr. Blake Wiggins and Dr. Tracy Steinbach, who have been with me since the beginning. I fully believe the support we have given each other, both intellectually and emotionally, has helped us to stick it out and get through graduate school together.

I want to especially thank Dr. Varinderjit Singh for being down in the trenches with me every step of the way throughout all of the experiments that will be discussed in this dissertation. These experiments would not have been anywhere near as successful without Dr. Singh's support. I am also grateful for the friendships I found in the students who joined the group later, in particular Jacob Huston, James Johnstone, and Carley Folluo. Even our summer students Ally Pauly and Rebecca Su, who had only been in the group for two months, left an impression on me, and I am grateful to them for helping me through one of the most difficult summers of my graduate career.

For helping to make these experiments possible, I would like to thank the members of the IU Chemistry Department's Mechanical Instrument Services and Electronics Instrument Services. Even though we have pushed them hard to help us build our detectors and mechanical equipment, they have always come through for us. I also want to thank Gerard Visser for his help in developing the amplifier for the RIPD detector.

The success of these experiments is due largely to the wonderful support we have received at the various beam facilities. At Florida State University, I want to thank Dr. Ingo Wiedenhöver, Dr. Lagy Baby, Dr. Vandana Tripathy, and Dr. Sean Kuvin for providing us with high quality beams and on-site support throughout our experiments. At Michigan State University, I would also like to thank the ReA3 technical staff, with special thanks to Dr. Antonio Villari, Dr. Alain LaPierre, and Sam Nash, for helping us make the first fusion measurement performed at ReA3 successful. I also extend my gratitude to Massimo Loriggiola at Legnaro National Laboratory for providing us with the ^{28}Si target foils.

I could not have made it through graduate school without the help of my family and closest friends. My parents have always been and continue to be my biggest supporters. My chosen family, Jain Waldrip and P.j. Smith, have always been there to catch me when I fall and help me through anything, no matter how difficult. I am so grateful for their love and support. My partner, Alex Luibrand, has been absolutely amazing, supporting me when the stress of graduate school would get the best of me while also pushing me hard to succeed. Thank you, Alex, for being so patient with me while I finished earning my degree; I love you. I also want to thank many of my other friends for their support as well. Though we do not see each other very often, I know we will always be there for each other. Thank you all, for helping me achieve the biggest milestone of my life.

Jessica Elizabeth Vadas

PROBING THE FUSION OF NEUTRON-RICH NUCLEI WITH MODERN RADIOACTIVE BEAM FACILITIES

Fusion in neutron-rich environments is presently a topic of considerable interest. For example, the optical emission spectrum from the neutron star merger GRB170817A clearly establishes this neutron-rich environment as an important nucleosynthetic site. Fusion of neutron-rich light nuclei in the outer crust of an accreting neutron star has also been proposed as responsible for triggering X-ray super-bursts. The underlying hypothesis in this proposition is that the fusion of neutron-rich nuclei is enhanced as compared to stable nuclei. A good approach to understand how fusion proceeds in neutron-rich nuclei is to measure the fusion excitation function for an isotopic chain of nuclei. Modern radioactive beam facilities provide the opportunity to systematically address this question. An experimental program has been established to measure the fusion excitation function for light and mid-mass neutron-rich nuclei using low-intensity radioactive beams. The technique was initially demonstrated by measuring the fusion excitation functions for ^{18}O and ^{19}O nuclei incident on a ^{12}C target. The beam of ^{19}O ions was produced by the ^{18}O(d,p) reaction with an intensity of 2-4 $\times$ 10^4 p/s at Florida State University. Evaporation residues resulting from the de-excitation of the fusion product were distinguished by measuring their energy and time-of-flight. To explore mid-mass neutron-rich nuclei much further from stability, the fusion excitation functions for ^{39,47}K + ^{28}Si were measured using the ReA3 reaccelerator facility at the National Superconducting Cyclotron Laboratory at Michigan State University. Incident ions were identified on a particle-by-particle

basis by ΔE-TOF just upstream of the target. Fusion products were directly measured and identified by the E-TOF technique with an efficiency of ∼70%. The measured fusion excitation functions for both the light and mid-mass systems have been compared to various theoretical models to elucidate how structure and dynamics impact the fusion of neutron-rich nuclei.

Romualdo T. de Souza, Ph.D., Chair

Caroline C. Jarrold, Ph.D.

Peter J. Ortoleva, Ph.D.

Charles J. Horowitz, Ph.D.

Contents

List of Figures

List of Tables

Chapter 1

Neutron stars, NS mergers, and r-process nucleosynthesis

1.1 Introduction to nucleosynthesis

Understanding the origin of the elements, including where and how they were formed, is a topic of considerable interest that is being actively explored today. Approximately 90 elements are found on Earth, and can undergo an enormous range of geological, chemical, and biological processes while retaining the identity of the nucleus. Nuclear reactions, such as cosmic ray bombardment and radioactive decay, can alter the identity of a nucleus. Within the 90 elements found naturally on Earth, there are 272 stable isotopes and 55 radioactive isotopes [1]; thus, the vast majority of elements on Earth were present when the Earth was formed. The origin of the elements is therefore extraterrestrial.

The universe is composed of a large variety of massive objects distributed in an enormous volume, where the properties of most celestial environments are very different than that of Earth. The interior of stars like our sun, for example, are very dense ($\sim 2\times10^5$ kg/m^3) and very hot ($\sim 1.6\times10^7$ K). In these extreme environments, the temperature and density are high enough to ionize elements with high enough thermal velocities to induce nuclear reactions. Observations of stellar systems can thus provide insight into the process of nucleosynthesis, such as the relative abundances of the elements present in a star.

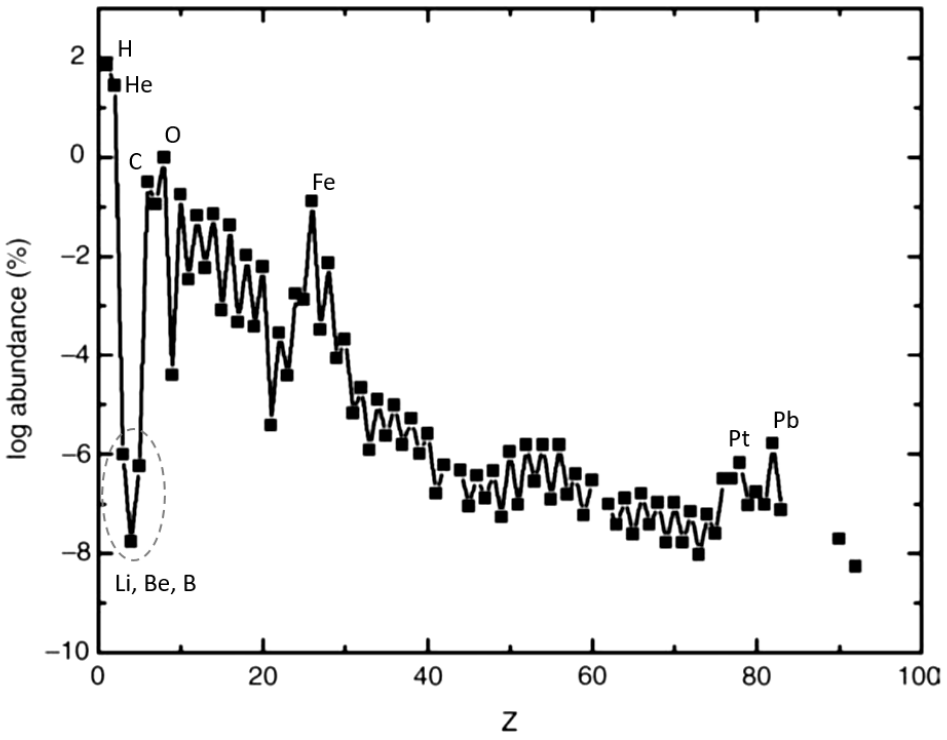

FIGURE 1.1: Abundances of the elements as a percentage by mass of the solar system [2].

Figure 1.1 shows the relative abundances of the elements in our sun [2]. The lightest two elements hydrogen and helium comprise approximately 99% of the mass, and the abundance has a logarithmic decline with increasing atomic number. Exceptions to this trend include a large dip at lithium, beryllium, and boron, a peak around iron (Z = 26), and a peak near some of the heaviest elements between platinum (Z = 78) and lead (Z = 82). There is also a strong odd-even effect, where the even-Z elements are more abundant than the odd-Z elements, which could be attributed to the fact that even-Z nuclei are more stable than odd-z nuclei due to pairing. Atomic abundances observed from stars combined with nuclear properties measured in the lab on Earth can be used together to test theories of nucleosynthesis.

The Chart of Nuclides [3] is shown in Figure 1.2, where each known nucleus is organized by neutron number on the abscissa and proton number on the ordinate. Most

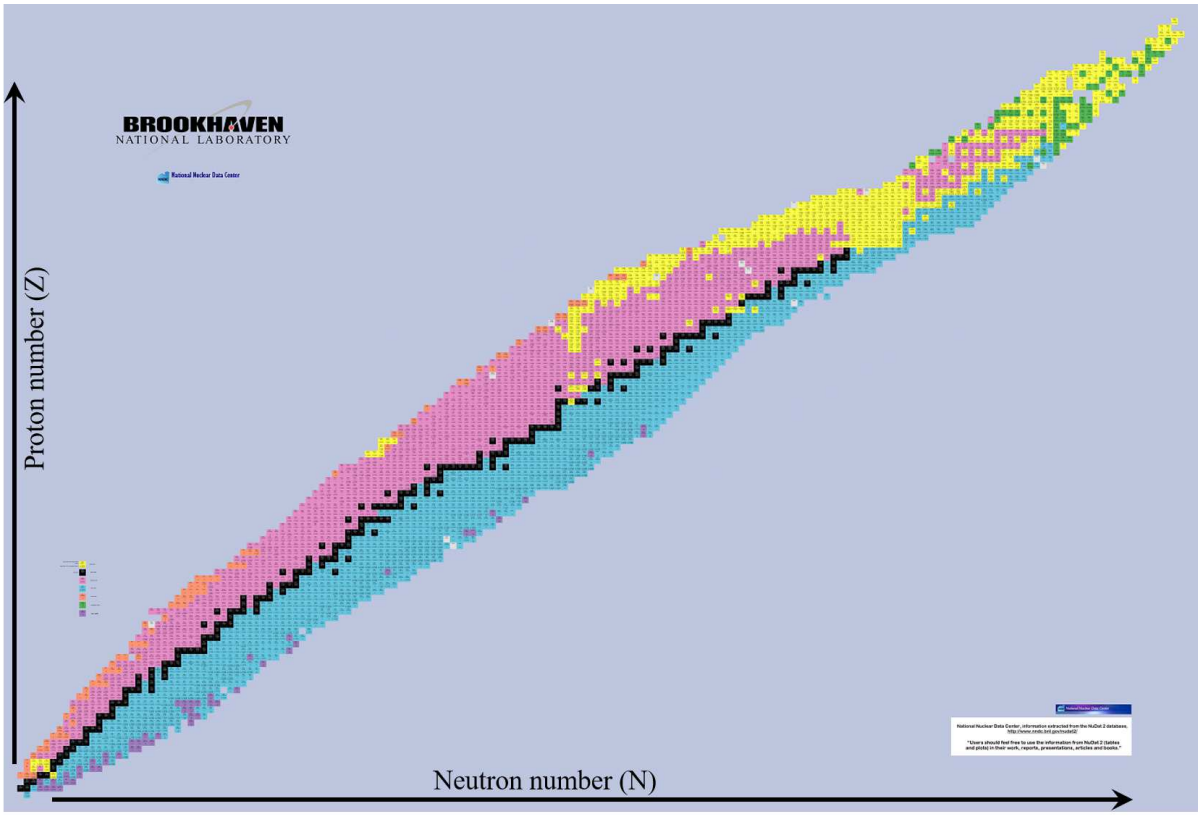

FIGURE 1.2: The Chart of Nuclides [3], which organizes nuclides by proton number vs. neutron number. The colors represent different decay modes. Stable nuclei are shown in black, and nuclei that undergo β^- decay are shown in blue, β^+ decay and electron capture in pink, α decay in yellow, spontaneous fission in green, proton emission in orange, and neutron emission in purple.

neutron and proton number combinations do not exist, as indicated by the unfilled space in the diagram. The nuclei that do exist fall along a line of $N/Z = 1$ for $Z \leq 20$, and for $Z \geq 90$ the trend increases to $N/Z \approx 1.4$. The color of each nucleus indicates the type of decay it will undergo. Stable nuclei, shown in black, make up only a small fraction of the known nuclei. Nuclei shown in blue are neutron-rich, and will undergo β^- decay in order to move towards stability. On the other side of the line of stability are the proton-rich nuclei, shown in pink. These nuclei will undergo β^+ decay or electron capture in order to move towards stability. The nuclei shown in orange on the left-most side of the chart are also proton-rich, but their outermost protons are so loosely bound that they will undergo proton emission. Similarly, the nuclei shown in purple on the right-most side of

the chart are so neutron-rich that they will undergo neutron emission. The remaining nuclei, mainly at higher masses, will undergo α-decay (shown in yellow) or spontaneous fission (shown in green) to move back down towards stability.

1.1.1 Big Bang and stellar nucleosynthesis

Based on abundance patterns and other astrophysical observations, it has been determined that there are a few different processes by which the known nuclei are formed. The lightest elements, namely hydrogen, helium, and trace amounts of lithium, were initially created during the Big Bang [4, 5]. Immediately following the Big Bang, matter existed as a quark-gluon plasma. As the universe expanded, the temperature and pressure decreased, and the quarks and gluons condensed into nucleons and mesons within 10^{-6} s. The temperature eventually dropped after $\sim$10 s to a point where nucleosynthesis could begin; neutrons and protons reacted to form deuterons, and soon after ^{3}He, ^{4}He, and ^{7}Li were being produced. This process lasted for about three minutes after the Big Bang, after which the temperature dropped too much for nuclear reactions to keep occurring.

Approximately 10^{6} years after the Big Bang, as the universe continued to expand, local inhomogeneities in the matter distribution of the universe gave rise to gas clouds that coalesced under the influence of gravity to form galaxies. Within these galaxies, clouds of hydrogen and helium collapsed under gravity to form stars. As the hydrogen and helium condenses under gravity within a star, the temperature of the star rises as the local density increases. For a star with a mass greater than 0.08 $M_{\odot}$, the temperature attained is high enough to ignite nuclear fusion reactions between the protons in the core of the star, where the density and temperature are the highest. The fusion reactions release energy that helps counterbalance the force of gravity. The star condenses to a point where the fusion reactions are happening at a rate high enough to sustain hydrostatic equilibrium against the force of gravity. This is the hydrogen burning phase of the star. After the

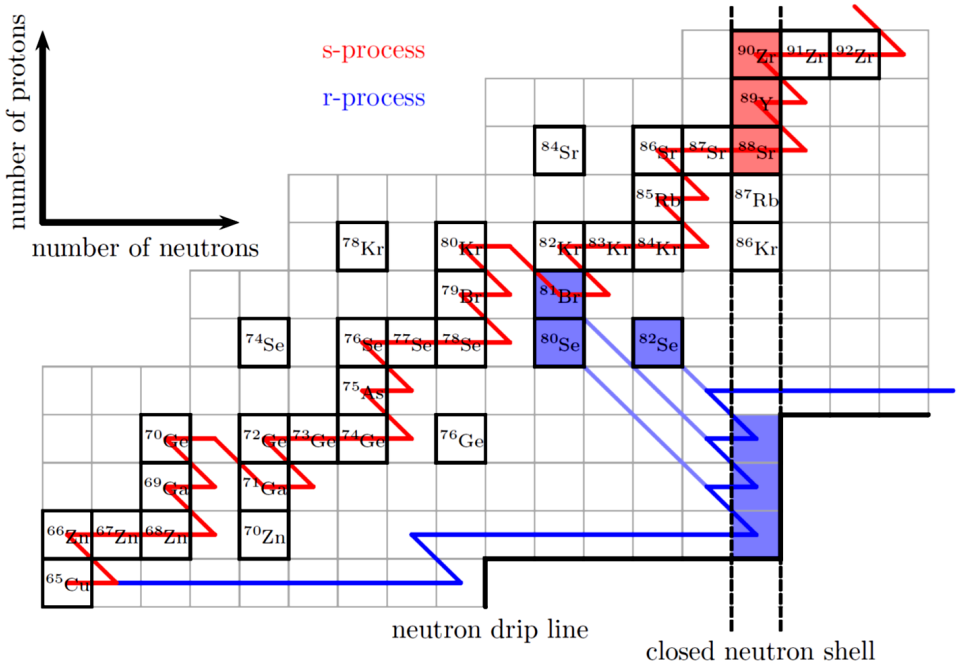

FIGURE 1.3: A section of the Chart of Nuclides showing the s-process path in red and the r-process path in blue [6]. The s-process proceeds along the valley of stability and the r-process along the neutron drip line.

hydrogen fuel is exhausted, the core of the star is enriched in helium, the product of the hydrogen burning phase. Without the fusion reactions providing a counterbalancing force to gravity, the star collapses. When the core of the star reaches $\sim 10^8$ K, helium burning commences, producing ^{12}C and ^{16}O. The life cycle of the star will continue with ^{12}C/^{16}O burning, then ^{28}Si burning, up until ^{56}Fe is created. Since this particular nucleus has the highest binding energy per nucleon, fusion reactions involving this nucleus will be endoergic instead of exoergic, and will not proceed. Without the nuclear energy release, hydrostatic equilibrium cannot be achieved, and the star collapses. The nuclei thus produced in the core of a star include stable nuclei up to A $\sim$60 [2].

1.1.2 s-process

Heavier elements are created by different capture processes for both proton- and neutron-rich isotopes. Since fusion reactions such as those described in the prior phase of stellar nucleosynthesis are energetically inhibited from producing elements with A $\gtrsim$ 60, alternate synthesis scenarios must exist. Neutron capture reactions, followed by β^- decay, are largely responsible for the production of heavy elements. As might be expected, the reaction rate for producing heavy nuclei through neutron capture is critically dependent on the neutron density of the environment. Neutron capture processes are categorized into two groups based on the reaction rate: the slow neutron capture process (s-process) and the rapid neutron capture process (r-process). The distinction between these two categories lies in the neutron capture timescale relative to the timescale for β^- decay. As a nucleus becomes more neutron-rich, it becomes unstable, and will decay back to stability. The lifetime on which β^- decay occurs ranges from milliseconds to days [3], so neutron capture reactions with timescales on the order of 10^2-10^5 years are understandably considered slow. The interior of a red giant star provides one such environment with a low neutron flux [1]. Due to the slow neutron capture rate, this process is designated the s-process. The nuclei produced in the s-process are mainly at or near stability. Figure 1.3 depicts the s-process path as a red line on a section of the Chart of Nuclides. The s-process is responsible for stable or near-stable nuclei between 23 $\leq$ A $\leq$ 46 as well as 63 $\leq$ A $\leq$ 209, and terminates at ^{209}Bi [1, 2].

1.1.3 r-process

Environments in which a large neutron flux exists can synthesize elements via the rapid neutron capture process. This process allows nucleosynthesis to occur when the β^- decay lifetime is short. Due to the neutron capture occuring on a much shorter timescale

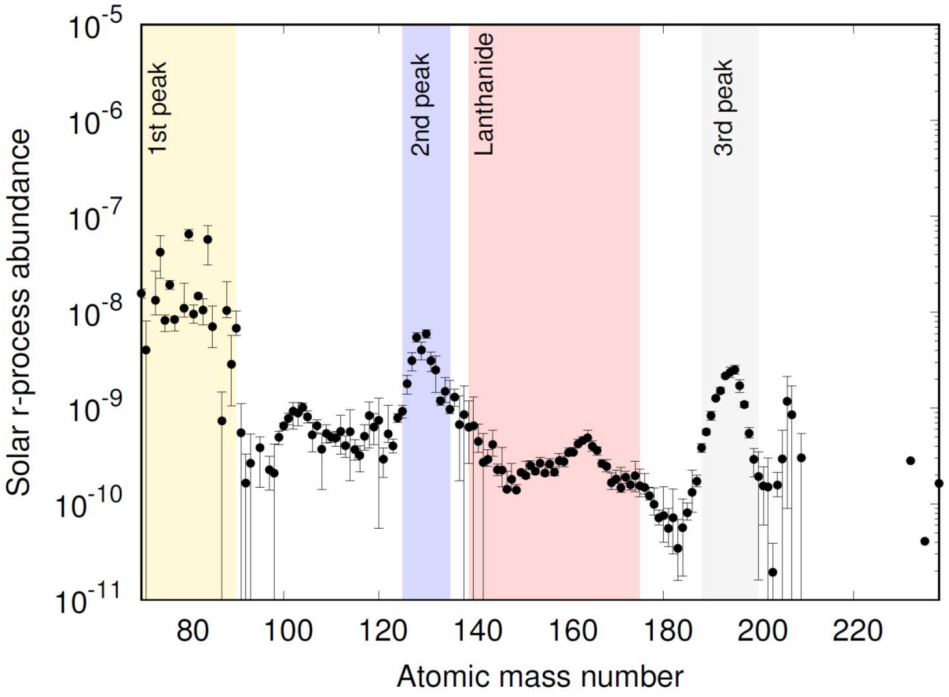

FIGURE 1.4: Solar abundance pattern of r-process elements [12]. The three main peaks are represented by yellow, blue, and grey bands, and the lanthanides are designated by the red band.

than β^- decay, extremely neutron-rich nuclei can be formed. Nucleosynthesis via the r-process requires large neutron densities ($\sim 10^{28}$ neutrons/m^3) [7, 8]. Figure 1.3 shows the neutron capture paths for the r-process in blue. Multiple successive neutron capture reactions occur before the nucleus decays, pushing nucleosynthesis towards the neutron drip line - the point at which an additional neutron is no longer bound to a nucleus. The standard environment associated with such large neutron densities is in a supernova explosion [9]. Recently, neutron star mergers have been suggested as a site for the r-process [10]. At which site and with what frequency the r-process occurs is still a topic of debate [11].

For a long time core-collapse supernovae (CCSN) have been considered the favored production site for the r-process [9]. Early models and simulations have indicated that a CCSN would have the right conditions for the r-process to take place [13, 14]. There

are four important features to consider in the abundance pattern of r-process material. These regions are represented as shaded bands in the r-process abundance pattern shown in Figure 1.4. The three major peaks and the band of lanthanides provide signature benchmarks against which theoretical models of r-process nucleosynthesis can be tested. The most recent investigations of r-process nucleosynthesis in neutrino-driven winds from a CCSN are able to produce a "weak" version of the r-process, producing elements up to A $\sim$130 [15, 16]. In order to reproduce the lanthanides and 3rd peak, the mass of the resulting neutron star following the supernovae would have to exceed 2 $M_{\odot}$, which is unrealistic based on the observed mass distribution of neutron stars [16].Simulations of a rare type of CCSN that is driven magnetorotationally have been able to produce the full r-process [17]. However, because of the conditions required for this type of supernova only a very small fraction ($\lesssim$0.1%) of CCSN would result in a magnetorotational supernova [17].

1.2 Neutron star mergers

Two neutron stars that exist in a binary system will radiate gravitational waves, which will shrink the orbit and eventually cause the two neutron stars to merge [19, 20]. During the merging of two neutron stars, a small fraction of their mass (0.1% - 1%) can be ejected through a few different processes [21]. As the two neutron stars approach, the neutron stars can become tidally deformed and distrupted due to the influence of each other's gravity, flinging out material in the form of spiral arms. A simulation of a neutron star merger is shown in Figure 1.5 at different time intervals in the simulation. In the top three frames, the two neutron stars can be seen becoming deformed as they approach and then touch. The dynamical ejecta is seen in the spiral arms evident in the bottom three frames. Material can also be ejected from the collision interface of the merging neutron

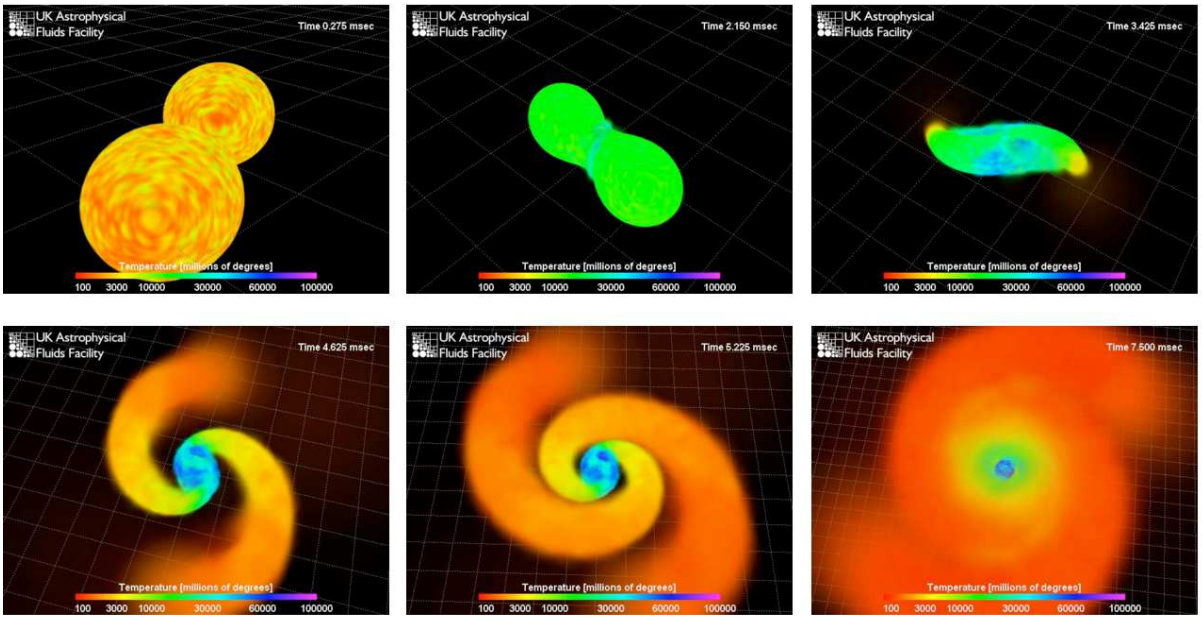

FIGURE 1.5: Simulation of two neutron stars merging, shown at different times in the simulation [18].

stars. The dynamical ejecta from neutron star mergers is very neutron-rich, and is thus an ideal site for r-process nucleosynthesis [22].

Integral to the understanding of r-process nucleosynthesis in neutron star mergers are the questions of how often mergers occur, how much mass is ejected per event, and how the relative abundances are distributed [23]. The Laser Interferometer Gravitational Wave Observatory (LIGO) was developed to measure gravitational waves radiated from mergers between black holes, neutron stars, or a black hole with a neutron star [24].

LIGO is a laser interferometer consisting of two orthogonal 4 km long vacuum chambers, representing the second largest vacuum chamber in the world [25]. It is the most sensitive instrument in the world, and is able to detect changes in the distances between its mirrors on the order of 10^{-20} m [25]. There are two installations, one in Hanford, WA and one in Livingston, LA, which operate in unison in order to cancel out local vibrational

noise. A smaller interferometer located in Italy, known as the Virgo interferometer, operates in coincidence with the LIGO installations and can provide additional information about merger events [26].

Observations of neutron star mergers can provide constraints on model calculations, such as the rate at which mergers occur [27]. In addition to the gravitational waves radiated by the system, it has been inferred that a binary neutron star merger gives rise to a short duration gamma ray burst (sGRB) [28, 29], providing an electromagnetic signature of the merger event. If the merger is indeed responsible for producing r-process material, the very neutron-rich nuclei produced will eventually decay back to stability and release energy, powering a transient in the optical or infrared band called a kilonova [30, 31].

The coincident detection of a gravitational wave and sGRB provides a unique signature of a neutron star merger event. Such a coincidence was detected for the very first time on August 17, 2017 [33]. The gravitational wave, designated GW170817, was detected with the LIGO and Virgo detectors [34]. A time-frequency representation of the data from all three detectors is shown in Figure 1.6 [32]. The signal is clearly visible for the Hanford and Livingston detectors but absent in the Virgo data since the Virgo detector was out-of-plane with respect to the merger event [32]. The long duration of the merger signal is indicative of the merging of two low-mass objects, such as two neutron stars [32]. In addition, an sGRB designated GRB170817A was detected by the Fermi Gamma-ray Burst Monitor 1.7 seconds after the initial gravitational waves were detected by LIGO [35]. This coincident detection confirms that binary neutron star mergers are the progenitors of at least some sGRB [34]. The combination of data from the LIGO and Virgo detectors also allowed a sky position localization to an area of 28 deg^2 [34]. This triggered a campaign of electromagnetic follow-up observations, which led to the

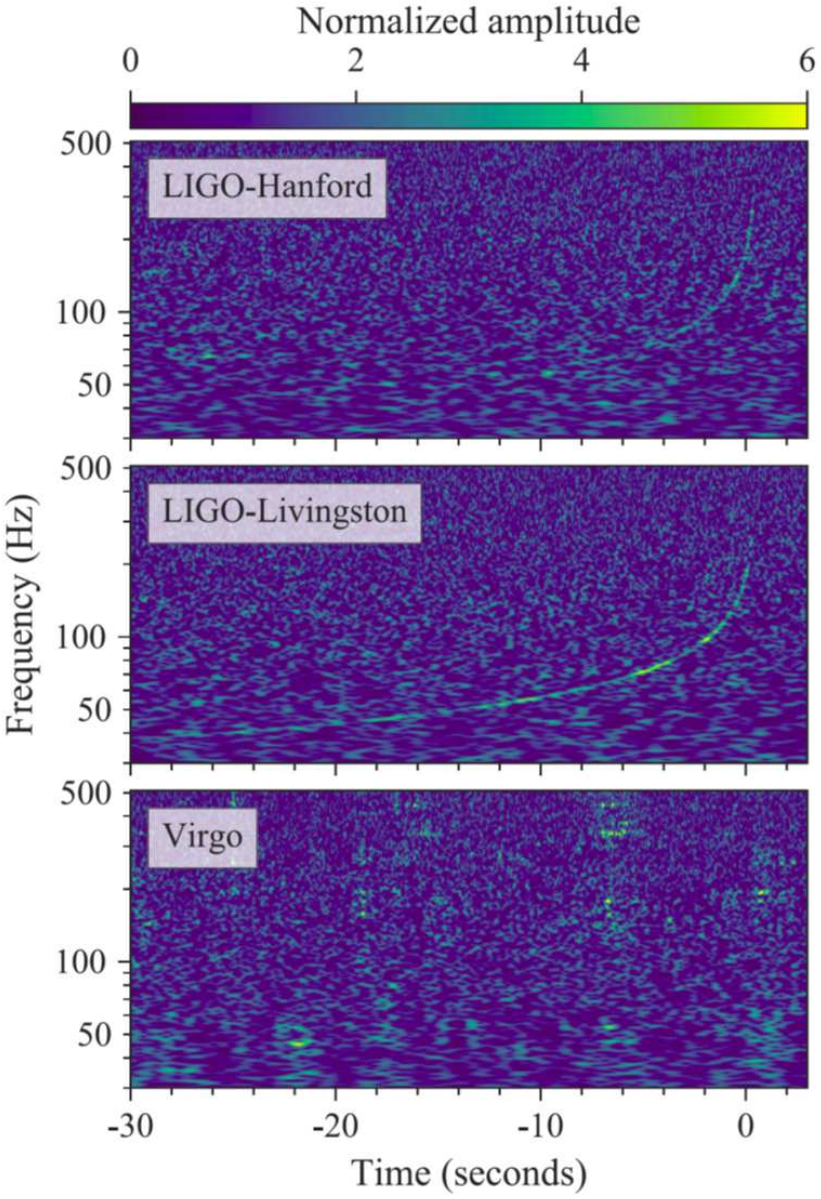

FIGURE 1.6: Time-frequency representations of data containing the gravitational-wave event GW170817 [32]. The top panel is from the Hanford LIGO detector, the middle panel from the Livingston LIGO detector, and the bottom panel from the Virgo detector. The time is shown relative to August 17, 2017 12:41:04 UTC.

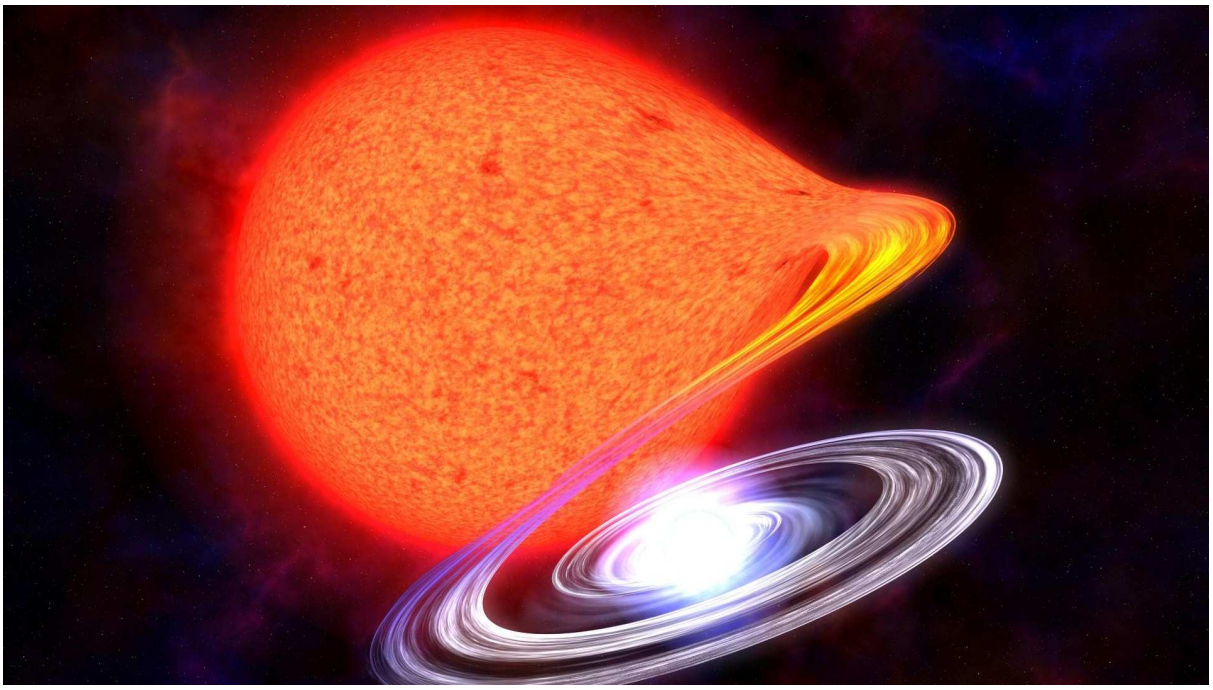

FIGURE 1.7: Artist's rendering of an accreting neutron star.

identification of NGC 4993 as the host galaxy of GRB170817A [36]. The delayed optical emission spectrum that followed indicated the presence of heavy elements in the neutron star ejecta [37]. This result clearly established binary neutron star mergers as an important, potentially primary, site for heavy element nucleosynthesis [38]. Ejecta resulting from the tidal disruption of the neutron stars as they merge reflects both their initial composition as well as reactions that occur during the merger. Understanding the composition of the neutron stars is thus an important question in understanding heavy element nucleosynthesis.

1.3 Accreting neutron stars

Some insight into the composition of some neutron stars prior to merging may be realized by considering the case of accreting neutron stars [39]. Neutron stars, the stellar remnants of supernova explosions, provide exotic astrophysical environments under

extreme conditions [40]. The typical radius of a neutron star is ∼10 km, and its mass is on the order of 1-2 $M_\odot$ [41]. It is composed mostly of neutrons, and has a density of $\sim 7\times10^{14}$ g/cm^3, which is 2-3 times larger than the density of an atomic nucleus. Neutron stars can exist in binary systems with other luminous stars and accrete material from the companion star. This material, which is composed of mostly hydrogen, will accumulate in an accretion disk orbiting the neutron star. An artist's rendering of a neutron star accreting material from its companion star is depicted in Figure 1.7. The hydrogen will eventually fall onto the surface of the neutron star and fuse into helium. When enough helium has accumulated, it will ignite unstable burning of all the material and produces an x-ray burst. The x-ray burst typically lasts ∼10 seconds to a few minutes and releases $\sim10^{38}$ ergs of energy [42]. For comparison, the total output of the Sun per second is $\sim3.8\times10^{33}$ ergs [43]. Material will begin to accrete again and this cycle will repeat regularly, so these types of neutron star systems are also known as pulsars.

As well as producing regular repeating X-ray bursts some neutron star binary systems can also produce irregular x-ray superbursts. Superbursts can last from 2 to 12 hours and release $\sim10^{42}$ ergs of energy. The origin of these energetic x-ray superbursts are thought to involve the ignition of ^{12}C + ^{12}C. However, due to the higher Coulomb barrier, carbon burning requires a temperature of at least 5×10^8 K. Current models put the surface temperature of the neutron star at $\sim3\times10^6$ K, which is too low for fusion of ^{12}C to readily occur. The heavy elements in the outer crust of an accreting neutron star are produced by fusion reactions [44, 45]. Some of the resulting heavy nuclei become neutron-rich through electron capture reactions [46]. It has been proposed that fusion of neutron-rich nuclei occurring in the outer crust may be enhanced relative to their β-stable counterparts providing an important heat source that triggers the x-ray superburst [47].

1.4 Fusion of neutron-rich nuclei

As a nucleus becomes increasingly neutron-rich, the extent of the neutron density distribution increases. Consequently, even if the density distributions were frozen through the fusion process the fusion cross-section would increase in response to the larger geometric cross-section. However, the fusion process is not static but dynamic. The decreased average binding energy of the outermost neutrons with increasing neutron number and the existence of low-energy collective modes act to make neutron-rich nuclei more polarizable. This increased polarizability, which can be viewed as the prelude to neutron transfer, increases the likelihood for fusion to occur. Thus, both static and dynamic factors impact the fusion cross-section. By examining the fusion cross-section with increasing neutron number for an isotopic chain and observing an increase beyond the geometric expectation, one might extract the increased role of dynamics.

To determine how fusion evolves for increasingly neutron-rich nuclei in an isotopic chain, it is advantageous to measure fusion at near-barrier energies. It is in this near and sub-barrier regime that one is most sensitive to the shape of the barrier which reflects both structure and dynamics. A new generation of radioactive beam facilities [48–50] with the capability of high-quality re-accelerated beams provide, for the first time, the opportunity to systematically address this question. These facilities together with facilities on the horizon [51] present an unprecedented opportunity to examine fusion of neutron-rich nuclei approaching the neutron drip line.

Chapter 2

Fusion Models

2.1 The fusion barrier

When nuclei collide in a nuclear reaction, the interaction between them consists of two parts: the long-range repulsive Coulomb interaction and the short-range attractive nuclear strong interaction. The combination of these two forces results in an interaction potential between the two nuclei that depends on their separation distance, r. An illustration of this potential is depicted in Figure 2.1. The heightened region of the potential where the Coulomb force meets the nuclear force is known as the Coulomb barrier. In a classical picture, the barrier represents the minimum energy the two nuclei must have in order to get close enough to fuse. If the nuclei do not have enough energy, there is a probability they can quantum mechanically tunnel through the barrier in order to fuse. This illustration is a simplistic one-dimensional static representation of two inert spherical nuclei in a head-on collision. In reality, the shape of the barrier is dependent on the size, shape, and structure of the nuclei, as well as collision dynamics and angular momentum of the system if the projectile collides with the target nucleus off-axis (non-zero impact parameter). If the two nuclei are deformed, the shape of the barrier would also depend on the relative orientation of the two nuclei as they collide. Thus, it is appropriate to consider the potential experienced by the two nuclei as consisting of a distribution of

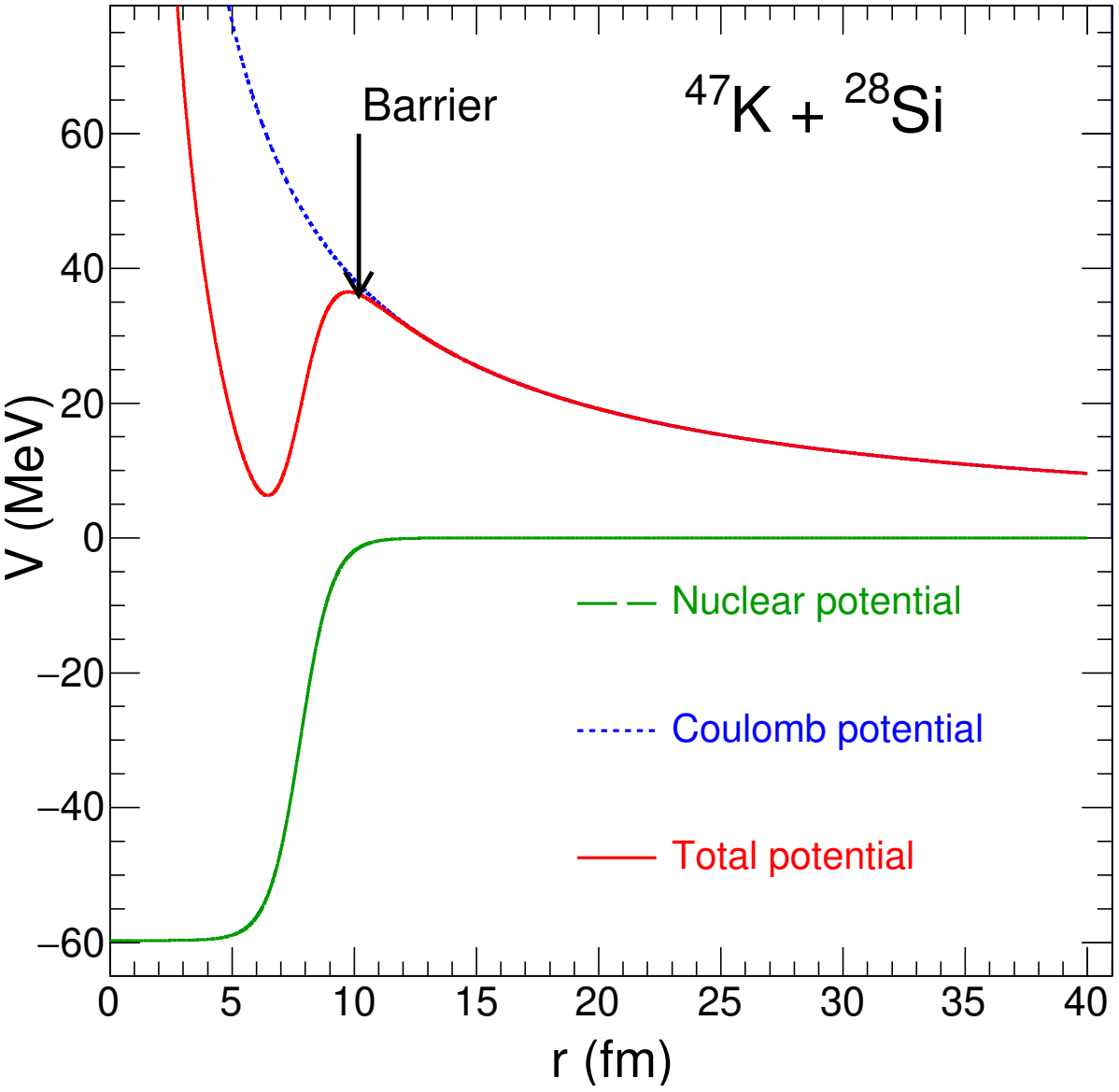

FIGURE 2.1: Illustration of the Coulomb barrier for the system ^{47}K + ^{28}Si. The Coulomb and nuclear parts of the potential are shown as the dotted and dashed lines respectively, and the total potential is shown as the solid red line.

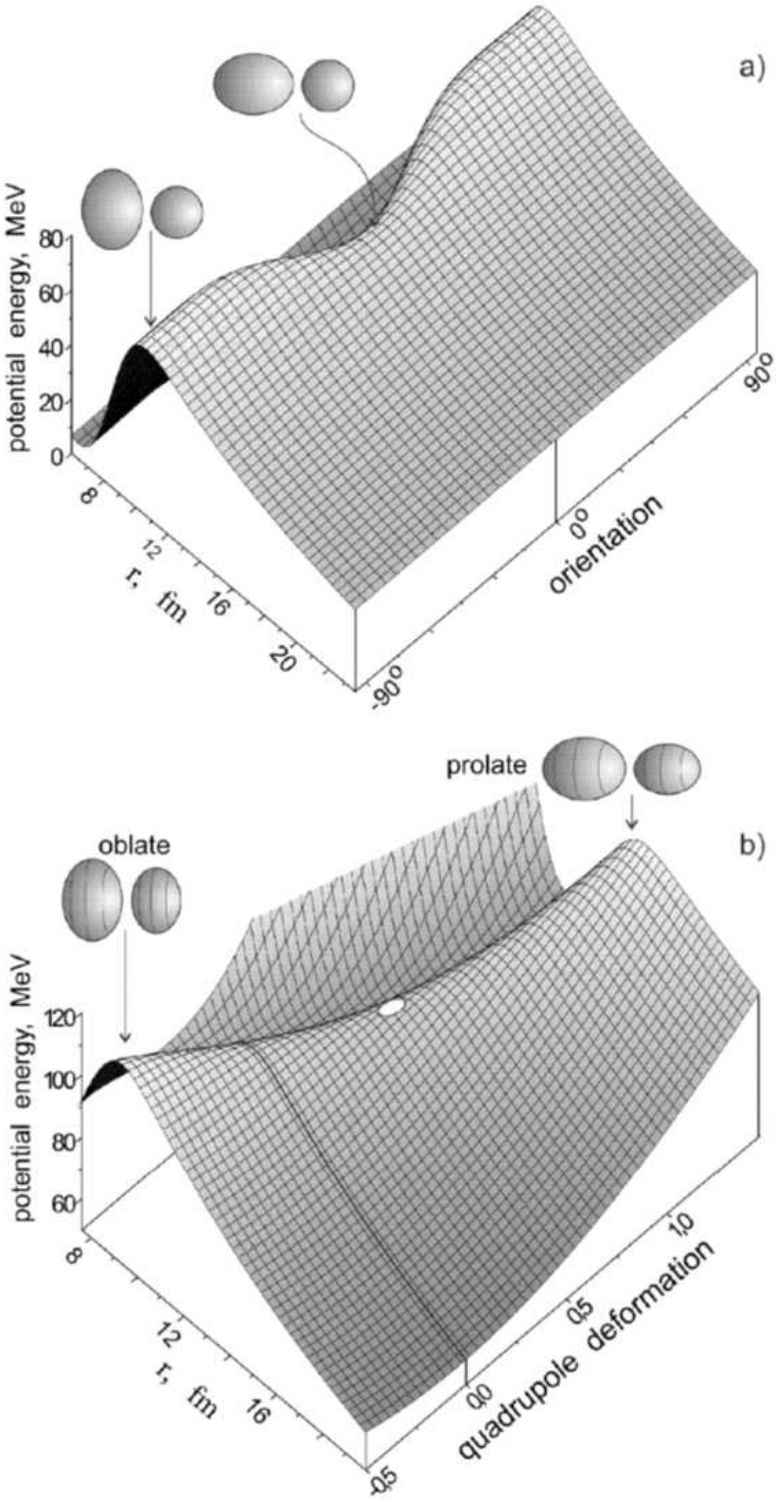

FIGURE 2.2: (a) Potential energy between a spherical nucleus and a prolate nucleus as a function of their separation as well as their mutual orientation. (b) Potential energy surface of two nuclei depending on their quadrupole deformations. The white oval marks the saddle point, or minimum of the fusion barrier.

barriers as opposed to a single static barrier [52]. Figure 2.2a depicts how the barrier changes based on the orientation of a deformed prolate nucleus. When the prolate nucleus approaches head-on along its major axis, the barrier is lower than if it approached side-on perpendicular to its major axis. If the nucleus is treated as having a point charge, then the Coulomb potential between the two nuclei does not change, but the nuclear part of the potential extends out to larger r for the head-on collision and lowers the fusion barrier. Figure 2.2b shows the barrier dependence on the degree to which a nucleus is deformed [53]. In addition to the initial static deformation of the nuclei, coupling to collective modes in the nuclei can also change the shape of the barrier. Understanding the dynamics of the fusion process thus requires an accurate knowledge of the potential as it relates to the size, shape, structure, and time evolution of the system.

2.2 One-dimensional barrier penetration model

The fusion cross-section can be calculated using a number of models with different assumptions and complexity. The simplest of these models, known as the one dimensional barrier penetration model (1D-BPM), has the following assumptions [54]:

1. Both the projectile and target nuclei are spheres with well-defined surfaces and radii given by $R = r_0(A^{1/3})$ where A is the mass number of the nucleus in question.

2. The potential of the system is comprised of an attractive nuclear potential, a repulsive Coulomb potential, and a centrifugal potential that depends on the angular momentum of the system.

3. The shapes of the nuclei remain static as they approach and the potential is constant in time.

The potential of the system is given by

$$V(r) = V_N(r) + V_C(r) + V_l(r) \tag{2.1}$$

where V_N(r) is the nuclear part of the potential, V_C(r) is the Coulomb part of the potential, and V_l(r) is the centripetal part of the potential for the lth partial wave. These different potentials are taken with the following forms:

$$V_N = \frac{-V_0}{1 + exp[(r - R_0)/a]} \tag{2.2}$$

$$V_C(r) = \frac{Z_1 Z_2 e^2}{r} \tag{2.3}$$

$$V_l(r) = \frac{\hbar^2}{2\mu} \frac{l(l+1)}{r^2} \tag{2.4}$$

For the Woods-Saxon form of V_N, V_0 is the depth of the potential well, R_0 is the combined nuclear radius of the two nuclei, and a is the diffuseness parameter, which describes the "fuzziness" of the tail of the distribution. The Coulomb term is expressed as the electrostatic interaction between two point charges, with atomic numbers Z_1 and Z_2 separated by a distance r. The centrifugal term includes the angular mometum, l, and the reduced mass of the system, μ.

In a classical picture, the interaction region of the target nucleus can be thought of as concentric rings with radii equal to integer values of the reduced de Broglie wavelength of the two nuclei, $\lambda\!\!\!^{-}$ [55]. Impact parameters for the lth partial wave fall between $l\lambda\!\!\!^{-}$ and $(l+1)\lambda\!\!\!^{-}$. The cross-sectional area for a given l-wave is therefore

$$\sigma_l = (2l + 1)\pi\lambda\!\!\!^{-2}. \tag{2.5}$$

As a consequence of quantum mechanics, the transmission probability of the incoming wave, T_l must be taken into account. The semi-classical expression for the partial cross-section then becomes

$$\sigma_l = (2l+1)\pi\lambda\!\!\!^{-2} T_l. \tag{2.6}$$

The total fusion cross-section is therefore the sum of the cross-sections for each partial wave, given by the expression [56, 57]:

$$\sigma_{fus}(E) = \pi\lambda\!\!\!^{-2} \sum_{l=0}^{\infty} (2l+1) T_l(E). \tag{2.7}$$

For simplicity, the shape of the barrier can be approximated as an inverted parabola with a height V_B and a width $\hbar\omega$, and the corresponding transmission coefficient is given by the Hill-Wheeler formula [58]:

$$T_l(E) = \frac{1}{1 + exp[\frac{2\pi}{\hbar\omega}(V - E)]} \tag{2.8}$$

The potential parameters are typically calculated using an Akyuz-Winther formalism [59] but they can also be chosen in order to match experimental cross sections measured far above the barrier [60–62] where the cross-section is basically geometric. Since this model does not include any dynamics which would lower the barrier of the system as the energy of the system decreases, the 1D-BPM calculations typically underpredict the experimental cross-sections at sub-barrier energies [63].

2.3 Sao Paulo model with a relativistic mean field approach

There is another approach to calculating the fusion cross-sections between two inert spherical nuclei that describes the global behavior of the fusion process in a parameter free way [64]. The Sao Paulo model for calculating fusion cross-sections is based on the effects of the Pauli nonlocality and utilizes a double folding potential [65, 66]. Within the nonlocal model, the nuclear interaction potential $V_N(R,E)$ is related to the folding potential V_F through

$$V_N(R,E) = V_F(R)e^{-4v^2/c^2}, \tag{2.9}$$

where c is the speed of light, and v is the local relative velocity between the two nuclei,

$$v^2(R,E) = \frac{2}{\mu}[E - V_C(R) - V_N(R,E)]. \tag{2.10}$$

Here, μ is the reduced mass of the two nuclei, and $V_C(R)$ is the Coulomb potential between them. The folding potential V_F can be obtained either by using the nucleon density distributions of each nucleus with an appropriate form of the nucleon-nucleon interaction, or by using the matter density distributions of the nuclei with a zero-range approach for $v(\overrightarrow{r})$. With the zero-range approach, the folding potential takes the following form:

$$V_F(R) = \int \rho_1(r_1)\rho_2(r_2)v(\overrightarrow{R} - \overrightarrow{r_1} + \overrightarrow{r_2})d\overrightarrow{r_1}d\overrightarrow{r_2}. \tag{2.11}$$

The nucleon density distributions were calculated with a relativistic mean field (RMF) approach [67]. RMF theory is a phenomenological theory with three basic assumptions: nucleons are treated as point-like particles, the theory is fully Lorentz invariant, and it obeys strict causality. The nucleus is treated as a quantum mechanical many body problem of fermions interacting by a two-body interaction. This interaction has its origin in the exchange of mesons between the two nucleons, which involves a relativistic Lagrangian describing point-like nucleons interacting through the exchange of different types of mesons. The parameters of this Lagrangian, such as the number of mesons, their masses and coupling constants, are phenomenological quantities that are determined in such a way as to reproduce experimental data of many nucleon systems. By using this approach, the ground state properties of a nucleus can be determined, including the ground state binding energy, charge radius, and nucleon density distributions.

The nucleon density distributions calculated from RMF theory can be used in the Sao Paulo folding potenial. The resulting nuclear potential is shown as the dashed curve in Figure 2.3. For comparison, a Woods-Saxon potential with Akyuz-Winther parameters is represented by the solid red line. The Sao Paulo potential is much deeper and more diffuse than the Woods-Saxon potential. The area enclosed by the dashed box is shown in a zoomed-in view in the inset of the figure to highlight where the two potentials start to deviate at $\sim$8 fm. The corresponding Coulomb barriers are shown in Figure 2.4. As expected, the nuclear potential well is much deeper for the Sao Paulo potential as compared to the Woods-Saxon potential. A zoomed-in view of the Coulomb barrier is shown in the inset, where the two barriers are approximately the same above 8 fm but then deviate at closer distances. This has implications for calculating sub-barrier fusion cross-sections, where the Sao Paulo barrier is narrower than the Woods-Saxon barrier. As with the 1D-BPM, the Sao Paulo method also calculates the fusion cross-section with Equations 2.7 and 2.8, describing the penetration of a static parabolic barrier.

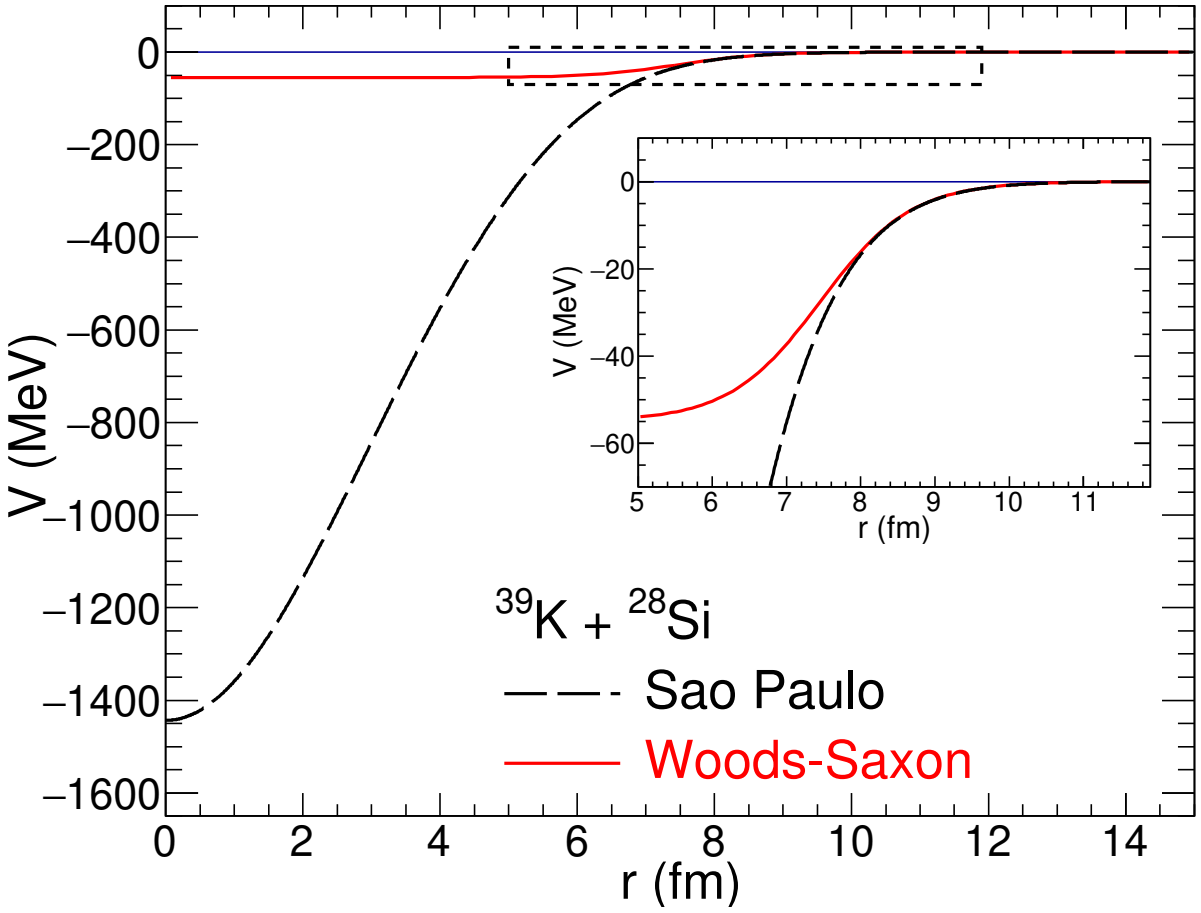

FIGURE 2.3: Nuclear potential as calculated with the Sao Paulo method (dashed black line) and the Woods-Saxon form (solid red line). A zoomed-in view of the area enclosed by the dashed box is shown in the inset.

2.4 Coupled channels approach

The simple barrier penetration models of fusion are adequate for describing the fusion of stable light nuclei such as ^{14}N + ^{12}C, but consistently underpredict the fusion cross-sections for heavier and more exotic systems like ^{16}O + ^{154}Sm [68]. The assumption in these models is that fusion occurs in the elastic channel only, so the only dynamical variable is the distance between the two nuclei. For heavier and more exotic nuclei, non elastic channels must be taken into account, including inelastic excitations and particle transfer.

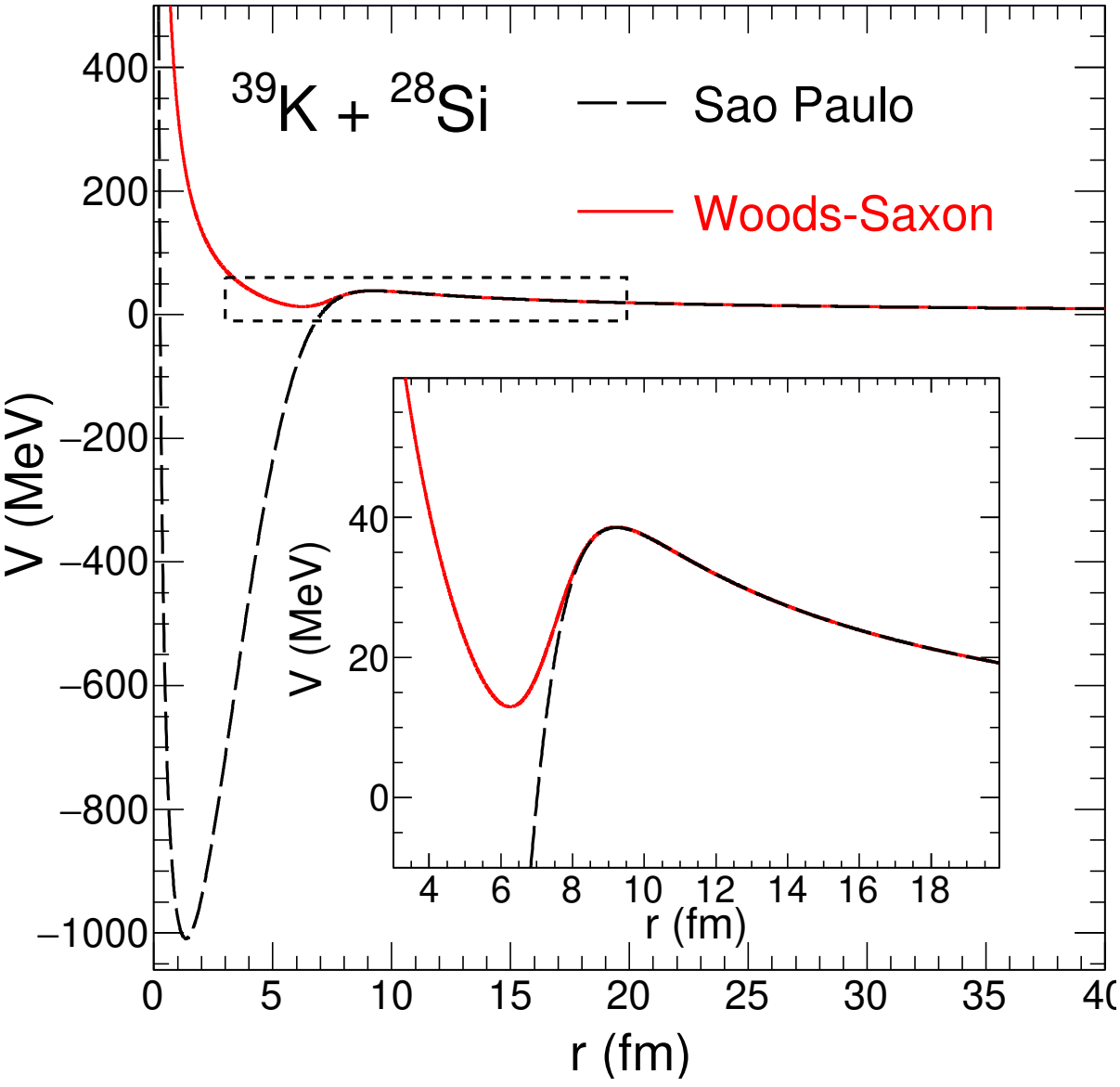

FIGURE 2.4: Coulomb barrier using the Sao Paulo nuclear potential (dashed black line) and the Woods-Saxon nuclear potential (solid red line). A zoomed-in view of the area enclosed by the dashed box is shown in the inset.

As the two nuclei approach each other, they can transition from their ground states to excited states and transfer nucleons between themselves before forming a compound nucleus [69]. These considerations are important for the fusion of heavy systems where the number of low-lying collective modes are large, as well as the fusion of radioactive isotopes where the Q-value for nucleon transfer between the projectile and target makes such a process more energetically favorable. A framework for considering the couplings of the relative motion between the colliding nuclei to nuclear intrinsic degrees of freedom such as low-lying collective excitations and nucleon transfer processes has been developed, known as the coupled-channels method [69].

There are three major assumptions made in the coupled-channels approach. First, only low-lying collective modes are considered, so non-collective excitations and giant resonances are ignored. Second, the coupling strength and energy levels for each state are considered to be the same as an isolated nucleus, and unaltered during the fusion process. Third, multiple excitations to higher collective states are approximated as a rigid rotor for deformed nuclei and as a harmonic oscillator for vibrational nuclei.

Though coupled-channel calculations are in good agreement with experimentally measured cross-sections for some reactions, there are cases where these coupled-channel calculations fail to fully characterize the measured cross-sections. Figure 2.5 depicts two examples of a measured deep sub-barrier fusion hindrance relative to coupled-channel calculations, which could potentially be due to an energy-dependent variation in the coupling strengths used in the calculation [73] or a different interaction potential than that used in the calculation [76]. Multiple excitations to higher collective states have also been shown to play a role, as seen in Figure 2.6 for two systems. The no coupling limit depicts essentially the result of a single barrier penetration problem, and the addition of levels used in the coupled-channel calculations sequentially works to increase the sub-barrier cross-sections to better agree with the data. The inclusion of higher lying states

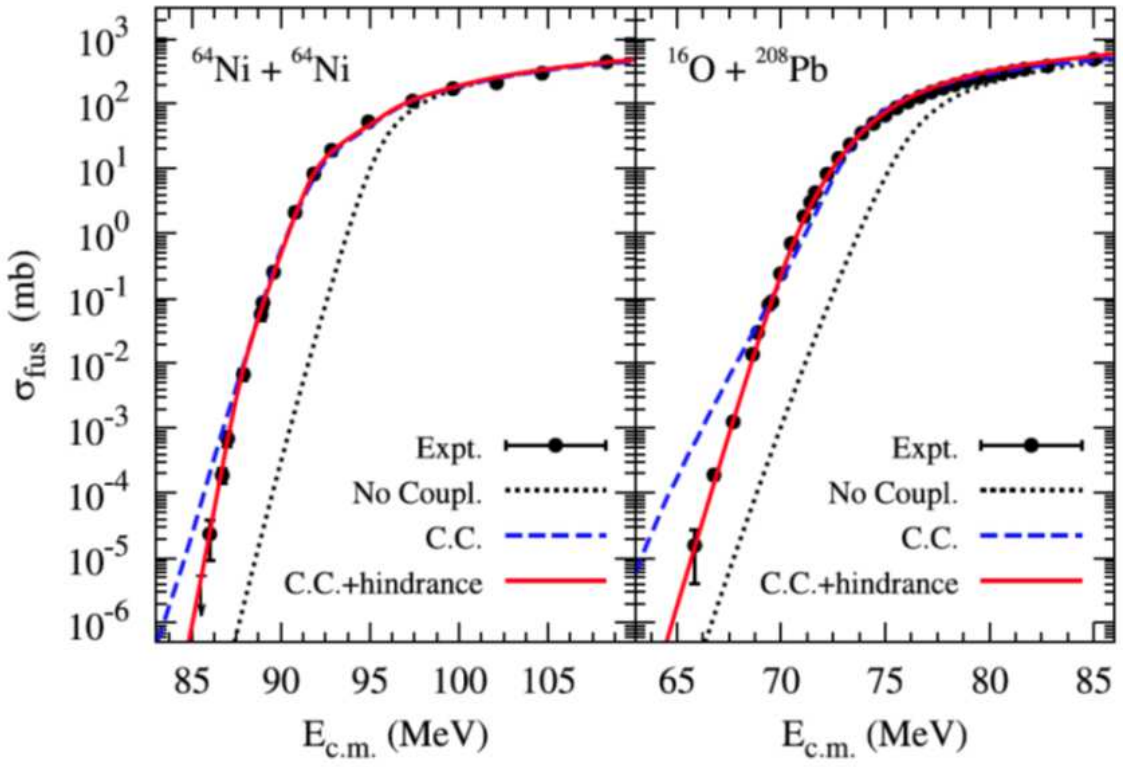

FIGURE 2.5: Fusion excitation functions for ^{64}Ni + ^{64}Ni and ^{16}O + ^{208}Pb [68]. The solid black circles correspond to experimental data taken from Reference [70] for ^{64}Ni + ^{64}Ni and Reference [71] for ^{16}O + ^{208}Pb. The dotted black lines correspond to the no coupling limit, which is identical to the single barrier penetration model. The dashed blue line is the result of standard coupled-channel calculations, and the solid red line corresponds to a correction to the coupled-channel calculation and is described in Reference [72].

relies on harmonic oscillator and rigid rotor approximations, so the calculations will be less valid for nuclei without a pure harmonic oscillator spectrum or a pure rigid body rotational band. Unstable nuclei whose spectroscopic properties are more difficult to measure will not have a well known level diagram established, therefore making accurate coupled-channel calculations more difficult.

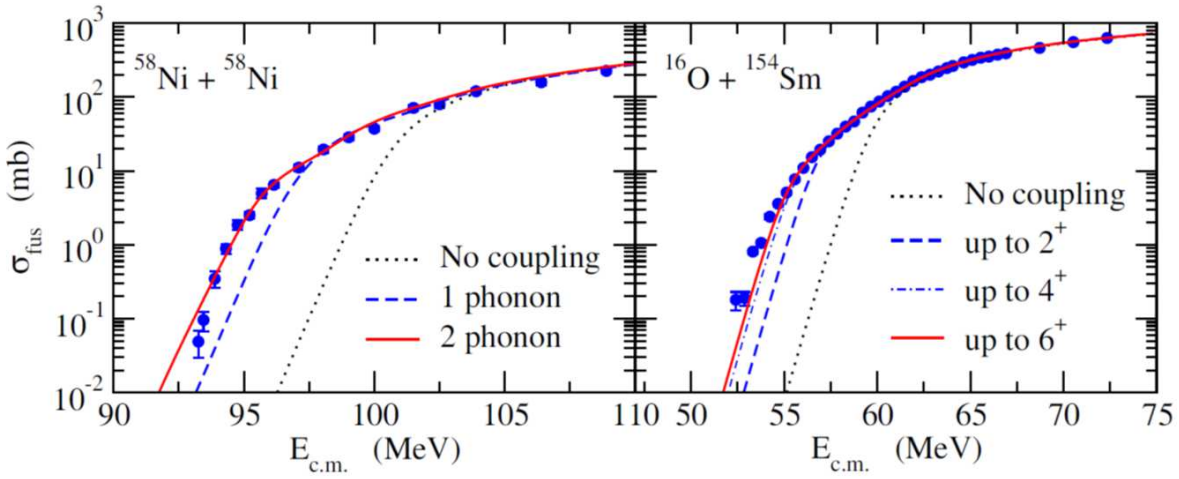

FIGURE 2.6: Fusion excitation functions for ^{58}Ni + ^{58}Ni and ^{16}O + ^{154}Sm [73]. The solid blue circles correspond to experimental data taken from Reference [74] for ^{58}Ni + ^{58}Ni and Reference [75] for ^{16}O + ^{154}Sm. The dotted black lines correspond to the no coupling limit, which is identical to the single barrier penetration model. For ^{58}Ni + ^{58}Ni, the dashed blue line and solid red line correspond to coupled-channel calculations which include 1- and 2-phonon excitations, respectively. For the ^{16}O induced reaction, the dashed blue line, dot-dash blue line, and the solid red line correspond to coupled-channel calculations which include rotational levels up to the 2^+ state, 4^+ state, and 6^+ state respectively.

2.5 Density-constrained time-dependent Hartree-Fock

A different approach to describe heavy-ion reactions is the time-dependent Hartree-Fock (TDHF) method. TDHF theory provides a useful foundation for a fully microscopic many-body theory of large amplitude collective motion based on a time-dependent nuclear energy-density functional [77]. It is therefore well suited to describe deep inelastic and fusion reactions [78–80]. TDHF theory, unlike coupled-channel calculations, does not have to specify individual channels because they are all included at the mean field level, both surface excitations and nucleon transfer [81]. The main advantage of the TDHF approach is that the dynamic response calculation is constructed on a static Hartree-Fock calculation, allowing the static and dynamic calculations to be performed using the same Hamiltonian description [82]. Until recent years it was not feasible to perform

these calculations on a three-dimensional Cartesian grid without symmetry restrictions [78, 79]. Though semiclassical TDHF theory exhibits good agreement with experiment for the lightest systems, it is only possible to calculate fusion cross-sections above the barrier [78].

A further refinement of the TDHF theory is one that employs a density constraint to provide a microscopic description of the formation of shape resonances in light systems [84]. This density-constrained TDHF (DC-TDHF) theory has been utilized to calculate fusion cross-sections both above and below the barrier. The only input for the DC-TDHF method is the Skyrme effective nucleon-nucleon interaction and there are no adjustible parameters [79, 80]. While it cannot describe the barrier penetration of the full many-body system, it can be used to extract the interaction potential between the colliding nuclei as well as a coordinate-dependent mass. These potentials and masses can then be applied to calculate the fusion cross-section in a one-dimensional barrier penetration model. The interaction potentials incorporate entrance channel effects such as neck formation, particle exchange, internal excitations, and deformation effects [79, 83]. Figure 2.7 depicts such effects in the fusion of ^{16}O + ^{24}O [83]. The nuclear density contours of the projectile and target are plotted in the x-z plane during the TDHF time-evolution of the system at four different separation distances. The top panel corresponds to the distance of the peak of the corresponding potential barrier. As the nuclei get closer they have a substantial overlap and develop a neck, a feature that is notably missing from other approaches which utilize the frozen-density approximation. The TDHF method allows the response of the reacting nuclei to change self-consistently as the nuclei start to overlap.

Results of DC-TDHF calculations for ^{16,18,19,20}O + ^{12}C are shown in Figure 2.8 [80, 85]. These calculations use the Skyrme SLy4 interaction for the nucleons [86, 87] including all of the time-odd terms in the mean field Hamiltonian. The calculations are

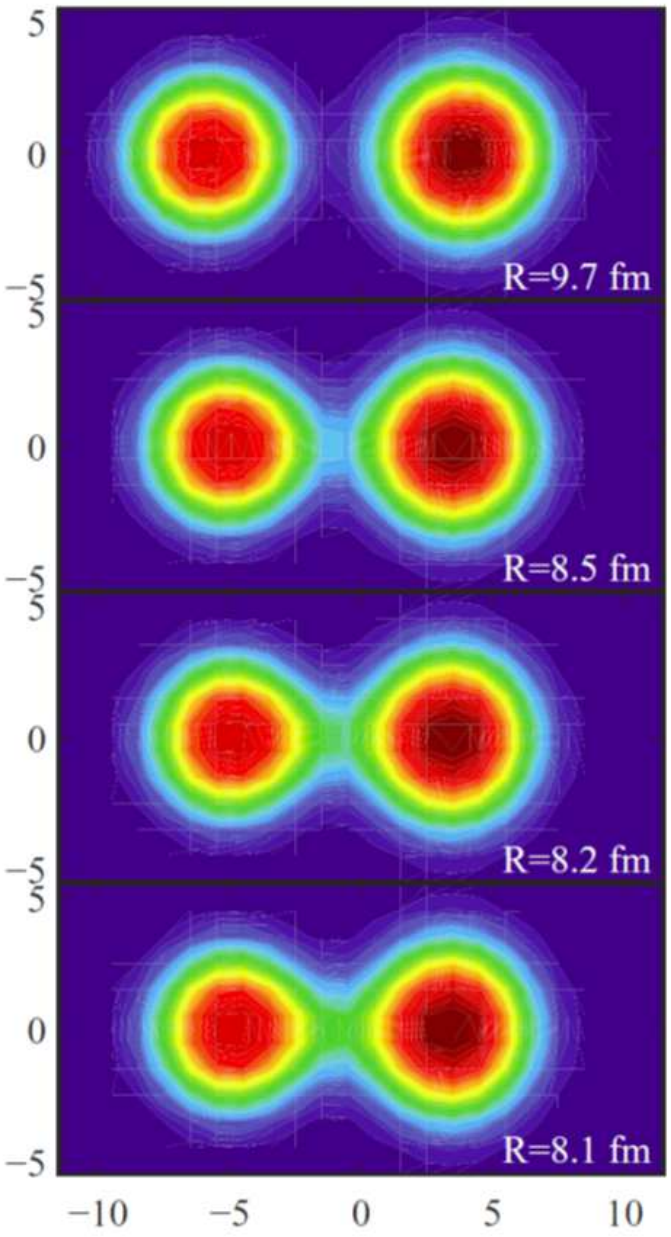

FIGURE 2.7: Snapshot of the nuclear density contours in the x-z plane for ^{16}O + ^{24}O at different separation distances [83]. The top panel corresponds to the distance of the peak of the potential barrier, and the subsequent panels show the nuclear density for closer distances.

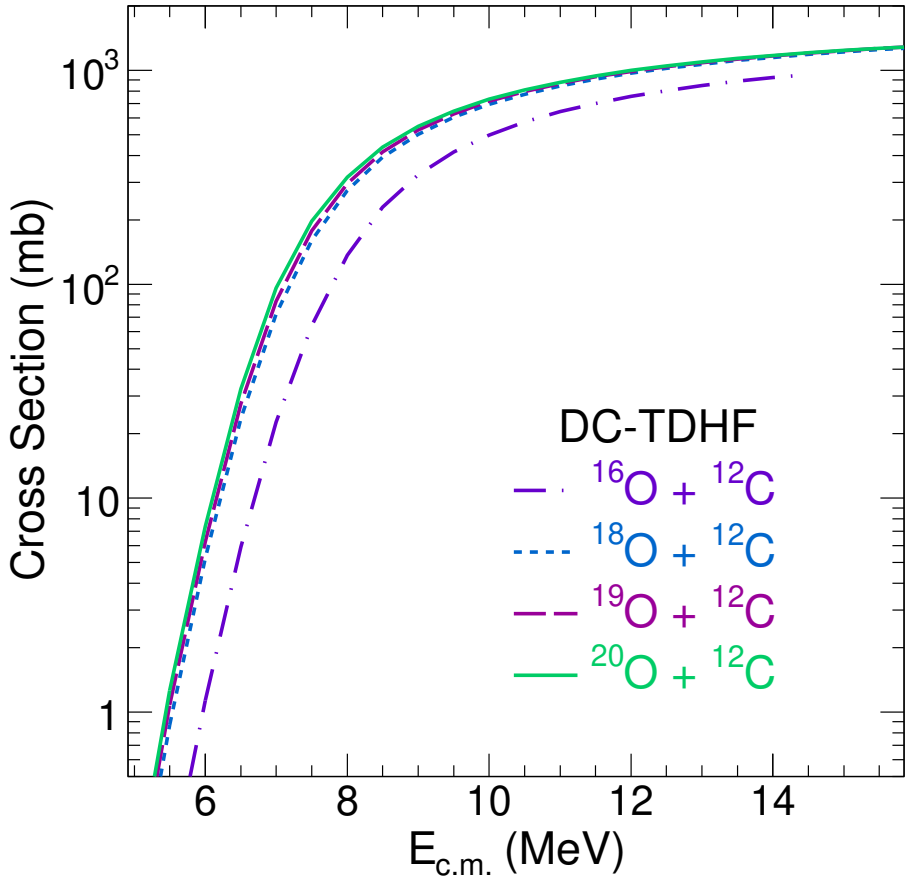

FIGURE 2.8: Fusion excitation functions for ^{16,18,19,20}O + ^{12}C from DC-TDHF calculations [80, 85].

carried out on a three-dimensional Cartesian lattice that spans 40 fm along the collision axis and 24-30 fm in the other directions [80]. In the DC-TDHF approach, the TDHF time evolution proceeds uninhibitedly. At certain times or, equivalently, at certain internuclear distances, the instantaneous TDHF density is used to perform a static Hartree-Fock energy minimization while constraining the proton and neutron densities to be equal to the instantaneous TDHF densities. This means that the single-particle wavefunctions are allowed to rearrange themselves in such a way that the total energy is minimized, subject to the DC-TDHF constraint [79, 80]. The fusion cross-sections are calculated using the one-dimensional barrier penetration model from Equation 2.7, but the transmission coefficient $T_l(E)$ is calculated by integrating the Schrödinger equation for the ion-ion interaction potential with a coordinate-dependent mass [80, 88].

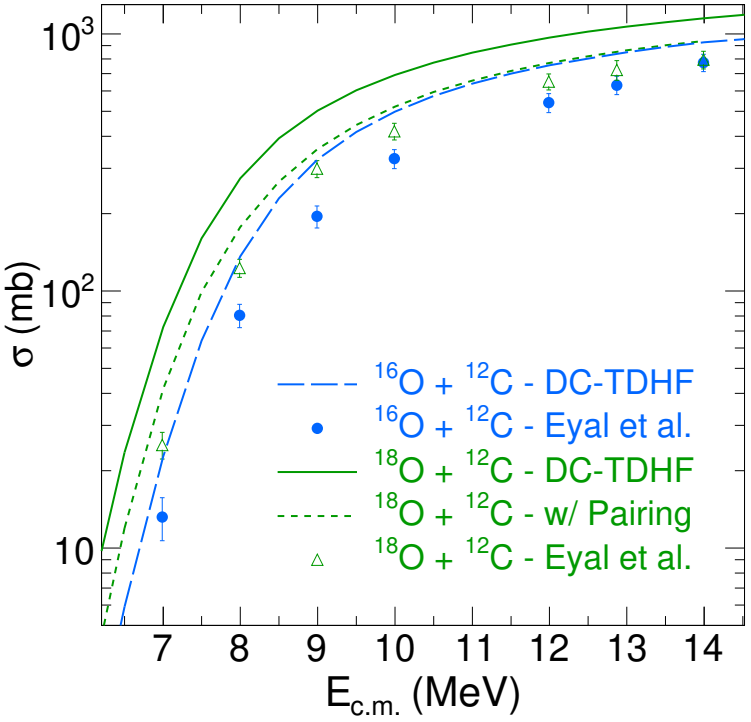

FIGURE 2.9: Fusion excitation functions for ^{16,18}O + ^{12}C. Experimentally measured cross-sections for ^{16}O + ^{12}C are represented by the solid blue circles, and those for ^{18}O + ^{12}C are shown as the open green triangles [89]. The dashed blue line corresponds to DC-TDHF calculations for ^{16}O + ^{12}C [85]. The green lines correspond to DC-TDHF calculations for ^{18}O + ^{12}, where the dotted line includes nucleon pairing [90] and the solid line does not include pairing [80].

Figure 2.8 shows that the DC-TDHF calculations of the fusion cross-sections for ^{18,19,20}O + ^{12}C are enhanced relative to ^{16}O + ^{12}C. However, there is very little difference between the heavier three systems. An expanded view of the calculations for ^{16,18}O + ^{12}C in the near-barrier region is shown in Figure 2.9 along with experimentally measured cross-sections [89]. The experimental measurements are depicted as solid blue circles for ^{16}O + ^{12}C and open green triangles for ^{18}O + ^{12}C. The DC-TDHF calculation for ^{16}O + 12C is represented by the dashed blue line [85], and the calculations for ^{18}O + ^{12}C are shown as the green lines, where the dotted green line includes nucleon pairing [90] and the solid green line does not. Without pairing, there is a significant enhancement in ^{18}O + ^{12}C as compared to ^{16}O + ^{12}C, and the calculation for ^{18}O + ^{12}C vastly overpredicts the measured cross-sections. However, the inclusion of nucleon pairing significantly decreases

the calculated cross-sections. Clearly accounting for pairing correctly has a dramatic influence on the predicted cross-section. After accounting for pairing, there is very little difference between ^{18}O + ^{12}C and ^{16}O + ^{12}C at higher energies, where the ^{18}O system gradually increases above ^{16}O at sub-barrier energies. For both of these systems, the DC-TDHF calculations overpredict the experimental data, which can be attributed to various breakup channels present for these systems, which are not accounted for in the DC-TDHF calculations [80].

Fusion is a complex process which provides insight into the interaction potential between two nuclei as well as the dynamics which occur as the two nuclei approach and begin to overlap.The complexity of the fusion process increases as the nuclei increase in mass number, A, as the role of collective dynamics increases. For nuclei away from β-stability, complexity also increases as the neutron number, N, increases and the role of neutron transfer becomes more important for the weakly bound valence neutrons. The development of radioactive beam facilities provides the opportunity to investigate how fusion proceeds in this regime, emphasizing the importance of understanding the fusion of neutron-rich nuclei.

Chapter 3

Experimental Approach

When an atomic nucleus is accelerated and enters a medium, it interacts with the atoms that compose the medium. Since the particle is charged, and electron orbitals are 5 orders of magnitude larger than atomic nuclei, most interactions will be electromagnetic interactions with the electrons in the medium. When the projectile nucleus approaches a target nucleus, they can interact in a number of ways. The specific way in which the two nuclei interact depends on the projectile's energy and the impact parameter of the collision. The impact parameter describes the perpendicular distance between the

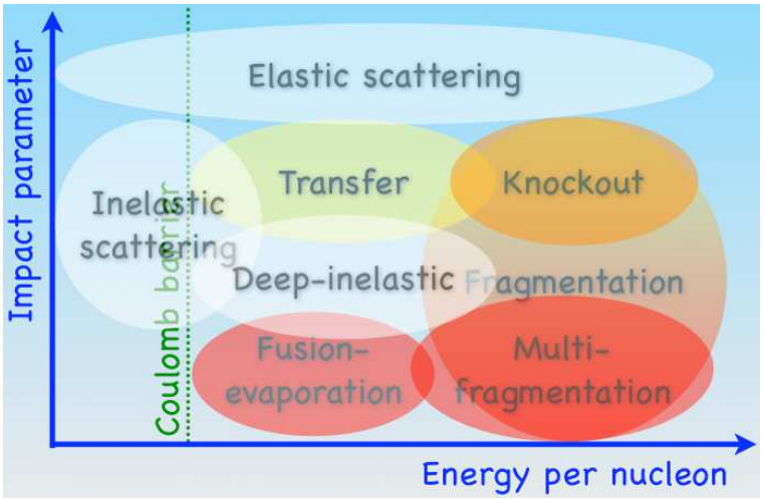

FIGURE 3.1: Classification of nuclear reactions based on impact parameter and energy [91].

trajectory of the projectile and the center of the target nucleus. Figure 3.1 summarizes these different types of interactions.

When the impact parameter is larger than the range of the nuclear force, the two nuclei can only interact electrostatically via the Coulomb force. Consequently, for impact parameters larger than the sum of the radii of the projectile and target nucleus, the projectile will be elastically deflected by the Coulomb field of the target nucleus.

For a smaller impact parameter at energies comparable to the Coulomb barrier, the projectile nucleus can inelastically scatter. At higher energies, for the same impact parameter, other reaction types referred to as transfer or knockout reactions occur. In these reactions one or a few nucleons are either transferred between the projectile and target nuclei or ejected from one of the two nuclei as a direct result of the collision. For even more central collisions at low energy, reactions referred to as deep-inelastic collisions occur. These collisions involve transfer of many nucleons between projectile and target nuclei in a stochastic dissipative process. Following the rapid exchange of many nucleons and dissipation of hundreds of MeV in less than a rotational period, the system separated into projectile-like and target-like nuclei. Complete amalgamation and equilibration of projectile and target nuclei has not occured.

In the case of the most central collisions, namely head-on collision of the two nuclei, fusion of the two nuclei into a single nucleus occurs. The resulting mononucleus is referred to as a compound nucleus. The compound nucleus is typically excited and will de-excite by emission of γ rays and light particles such as protons, neutrons, and α particles. The emission of the light particles follows a statistical process identical to evaporation in macroscopic liquids and hence are designated evaporated particles. The residual heavy nucleus is known as an evaporation residue.

In order to determine the probability for fusion, or the fusion cross-section, one must measure the fraction of incident beam particles that result in fusion. The cross-section σ is determined by bombarding a thin foil of target material with a beam. By measuring the intensity of the beam together with the number of fusion reactions that occur, the fusion cross-section can be ascertained from the relation:

$$\sigma_{fus} = \frac{N}{It} \tag{3.1}$$

where N is the number of fusion events, I is the number of beam particles, and t is the target thickness. It is therefore necessary to be able to identify a fusion event when it occurs. This chapter will describe different techniques to achieve this identification, including a novel technique well-suited for measuring the fusion cross-sections of radioactive neutron-rich nuclei.

3.1 Established techniques

3.1.1 Gamma ray measurement

When the compound nucleus de-excites, it emits γ rays. The energies of these γ rays are specific to the level transitions in the nucleus, which are characteristic for each nucleus. Thus, one can determine if a fusion event occured by measuring the γ rays emitted following bombardment of the target. A nuclear level diagram for the residues following fusion of ^{7}Li + ^{12}C is shown in Figure 3.2 [92]. A characteristic γ ray is emitted from an evaporation residue in an excited state. The integral of the measured gamma rays for a particular nucleus therefore corresponds to the population of excited nuclei for that exit channel. In order to extract the cross-section for that channel, a branching factor must be applied, which is simply the fraction of nuclei in that exit channel which

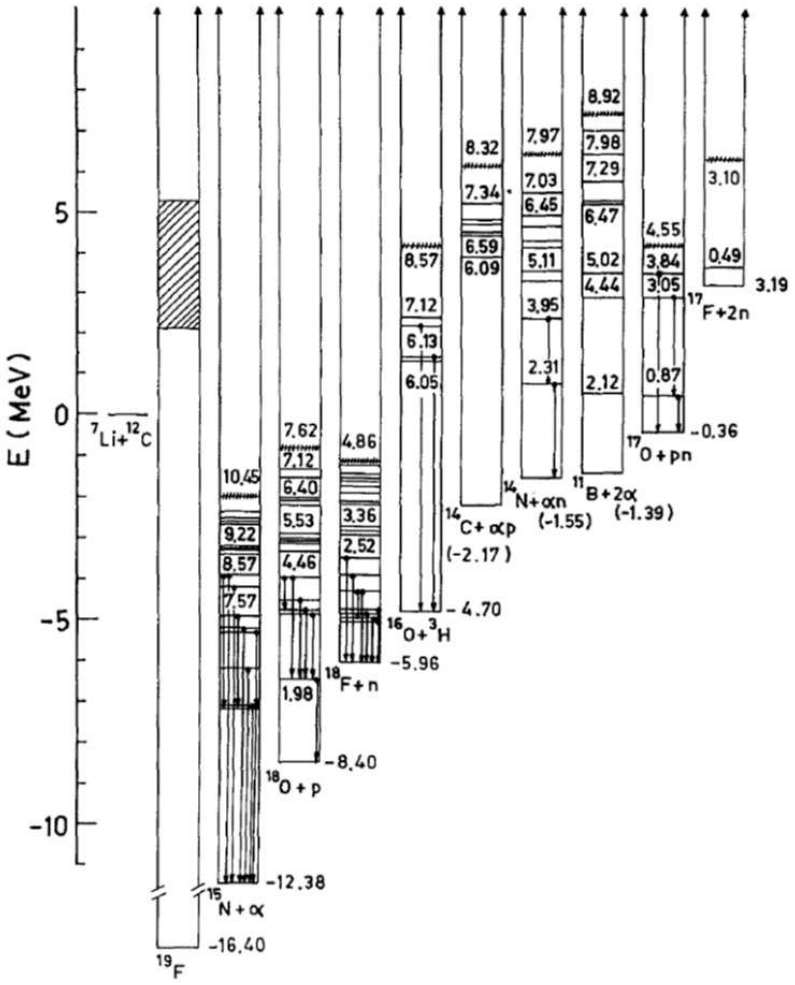

FIGURE 3.2: Energy level diagram for the reaction ^{7}Li + ^{12}C [92]. The level transitions depicted by the vertical arrows between levels are the γ ray energies measured in the experiment.

populate the measured excited states. In order to determine the branching factor, one needs the relative populations of the different bound states and their branching ratios, which can be calculated using Hauser-Feshbach statistical model calculations [92]. The total fusion cross-section is then obtained by summing the individual exit channel cross-sections. This method can be used when the levels of the residual nuclei are well known, but it still relies on the use of statistical model calculations. In some cases, the inability of the statistical model to accurately describe experimental data has been demonstrated [93].

3.1.2 ΔE-E method

Another method is to directly measure the fusion products. If the projectile is incident on a stationary target, the momentum of the projectile will result in the compound nucleus having a forward momentum in the laboratory frame. The evaporated particle are isotropically emitted in the center-of-mass frame and impart only a modest momentum change to the evaporation residue, so the residue also possesses a forward momentum in the laboratory frame. Since the evaporation residue is the result of fusion between the projectile and target nuclei, it will have a higher Z than either the projectile or target nucleus independently. The evaporation residue can be distinguished from elastically scattered projectile nuclei on the basis of its atomic number Z. When an ion with atomic number Z, mass number A, and kinetic energy E traverses a medium, it loses energy at a rate

$$\frac{\Delta E}{\Delta x} = \frac{Z^2 A}{E}. \tag{3.2}$$

Particle discrimination can therefore be achieved by using a detector telescope which consists of a thin entrance detector and a thick backing detector. The particles will travel through the entrance detector and deposit a certain amount of energy ΔE and pass through to the backing detector, where they will deposit the remaining energy $E_{residual}$. By plotting $E_{residual}$ vs. ΔE, particles with different Z can be distinguished. The evaporation residues can be distinguished from the elastically scattered beam and the fusion cross-section can be determined.

A limitation of this approach however is that it requires that the evaporation residues possess sufficient kinetic energy to be able to emerge from the target foil and traverse the dE detector. With this approach typically small area surface barrier silicon

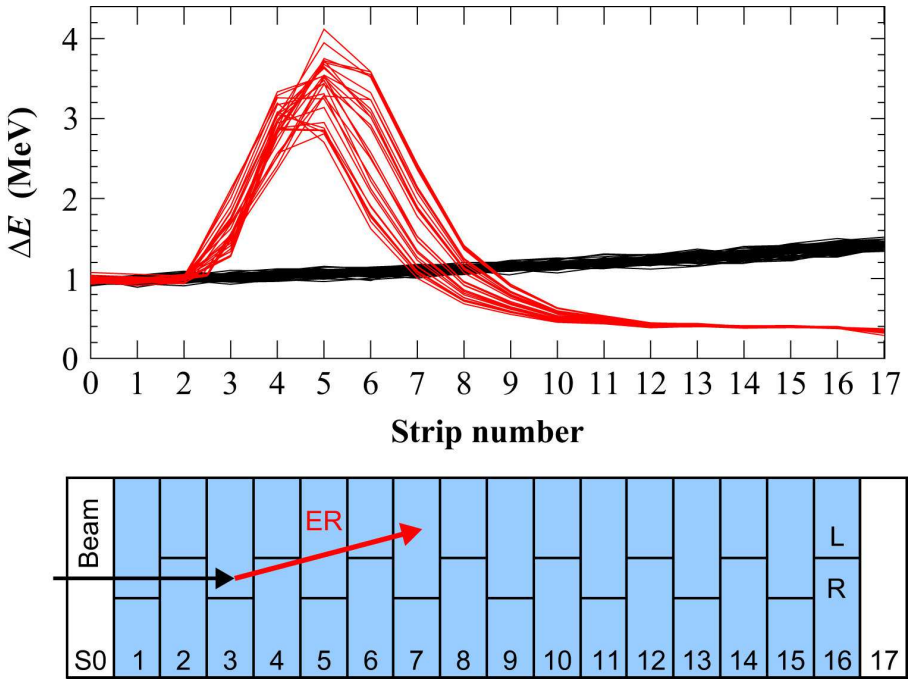

FIGURE 3.3: Top: Experimental traces measured with the MUSIC detector [94]. The black lines correspond to beam particles passing through the detector. The red lines correspond to evaporation residues produced following fusion of the projectile with the detector gas in strip 3.

detectors have been used and the measured angular distribution of evaporation residues integrated to yield the fusion cross-section. Use of large area detectors presents the problem of the uniformity of the ΔE detector. Variations of 5-10% which are typical make the use of large area silicon detectors unfeasible. While this approach with small surface barrier detectors is suitable for fusion studies at higher incident energies, in the case of the near-barrier fusion measurements, particularly radioactive beam studies which necessitate somewhat thicker targets, this approach is unfeasible.

3.1.3 MUSIC detector

Identification of the evaporation residues based on their atomic number can also be accomplished in an active target system, where the target of the reaction also serves as the detector. This allows for ΔE-E measurements with very low energy reactions,

since there is no energy threshold for the evaporation residues to enter the detector. One such detector design is a MUlti Sampling Ionization Chamber (MUSIC) [94], which is an ionization chamber with multiple anodes where the detector gas also serves as the reaction target. A schematic diagram of a MUSIC detector is shown in Figure 3.3. As in the case of the ΔE-E method, particle identification is achieved by taking advantage of the difference in energy loss through the gas volume. In the top panel of Figure 3.3, signals from evaporation residues following fusion are shown to be inherently different from the signals related to the beam passing through the detector gas. Because of the anode segmentation, the initial location of the fusion reaction can be determined, which can be used to calculate the energy of the reaction. This is advantageous for measuring the cross-section at multiple projectile energies without tuning the beam to different energies.

This approach however suffers from two drawbacks. Since the detector gas serves as the target, and only a limited number of gases are suitable as a detector gas, this dual use of the gas represents a limitation on the choice of target. In addition, since the detector used is a transverse ionization chamber, it is limited to a maximum beam rate of $\sim 10^4$ particles/s [94]. This rate limitation is particularly problematic as the beam passes through the detector ionizing the gas. It restricts this approach to measurement of the fusion cross-section at above barrier energies for low intensity radioactive beams.

3.2 E-TOF approach

The evaporation residues can also be identified based on their mass by taking advantage of the kinematics of the reaction. When the compound nucleus de-excites, the emission of evaporated particles imparts transverse momentum on the evaporation residue, deflecting it from the beam axis. Detectors can be placed downstream of the target around

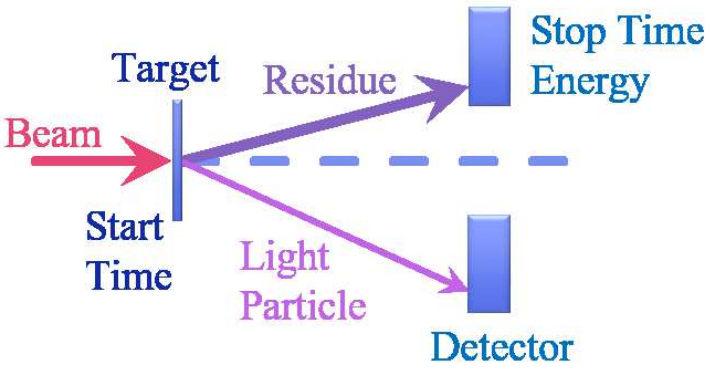

FIGURE 3.4: Illustration of the ETOF technique. The beam impinges on the target, producing a start time for the residue. The residue is deflected from the beam axis, impinging on a detector which measures its energy and stop time.

the beam to directly measure the ERs, allowing the unreacted beam to pass through without impinging on the detectors. A schematic diagram of this is illustrated in Figure 3.4. The beam also has a probability of elastically scattering into the detectors, so the ERs must be discriminated from the scattered beam. This is accomplished by measuring the energy and time-of-flight of the reaction products. Use of the time-of-flight means that the evaporation residues do not have to traverse a ΔE detector as in the ΔE-E approach. The velocity of a particle is proportional to its energy divided by its mass, so two particles with the same energy and different masses will travel across the same distance at different times. Thus, by plotting the measured particle's energy versus time-of-flight, the heavier evaporation residues can be distinguished from the beam particles.

3.2.1 Detectors

A schematic of a typical experimental setup is shown in Figure 3.5. The beam first passes through two microchannel plate (MCP) timing detectors, here labeled MCP_{US} for the upstream microchannel plate detector and MCP_{TGT} for the downstream microchannel plate detector. The secondary emission foil of MCP_{TGT} serves as the target of the

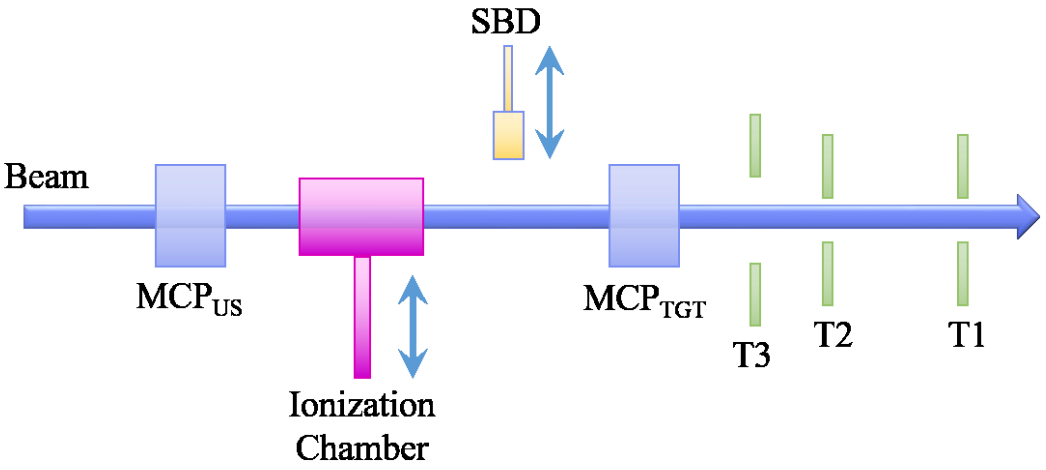

FIGURE 3.5: Schematic of the setup for a typical E-TOF experiment.

experiment. The time-of-flight of the beam is measured between the two MCP detectors in order to count the number of beam particles incident on the target and reject reaction products resulting from reactions with the MCP$_{US}$ secondary emission foil. For radioactive beams, an ionization chamber is placed between the MCP detectors to provide particle identification of the beam. A silicon surface barrier detector (SBD) is periodically inserted into the beam to measure the energy of the beam just before the target. The MCP$_{TGT}$ also provides the start time for the reaction products' time-of-flight measurement. Downstream of the MCP$_{TGT}$ are segmented annular silicon detectors, labeled T1, T2, and T3. The energy of the reaction products are measured in these silicon detectors, as well as the stop time for the time-of-flight measurement. Details about these detectors are provided in the following sections.

3.2.1.1 E×B MCP detectors

A microchannel plate is an array of 10^4 to 10^7 parallel channels made from lead glass material [96]. The channels are typically oriented at an angle of 5-15° relative to the face of the plate [97], with a diameter of 10-100 μm per channel. An illustration of an MCP

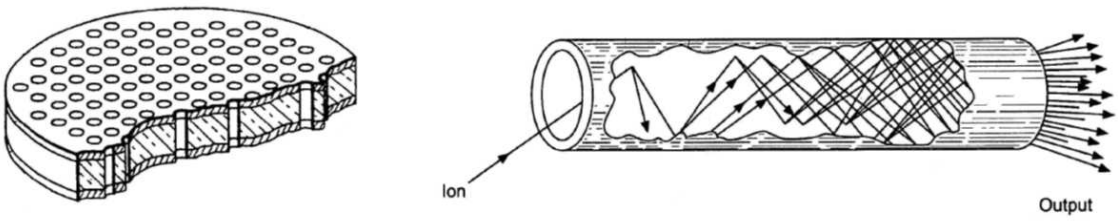

FIGURE 3.6: Left: Artist illustration of a microchannel plate. Right: Conceptual illustration of the electron multiplication along a single channel [95].

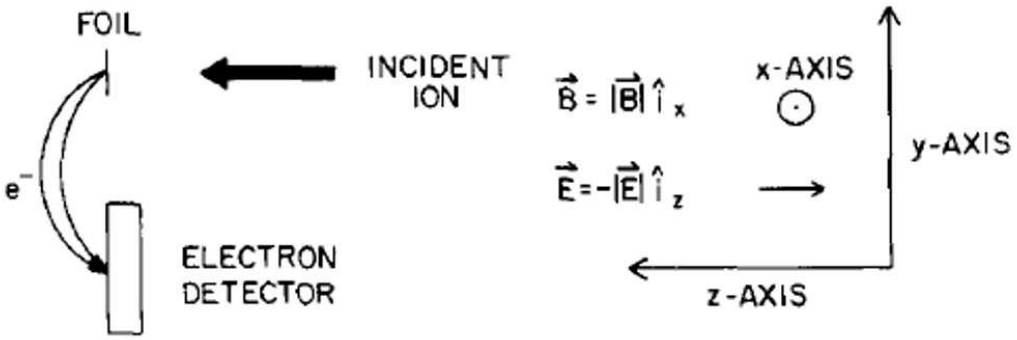

FIGURE 3.7: Conceptual drawing of the operation of an E×B MCP detector [98]. Ions are incident along the positive z direction. The magnetic field is in the positive x direction, and the electric field is in the negative z direction.

is shown on the left of Figure 3.6, and a single channel is shown on the right. The MCP is an electron multiplier, that can provide a timing resolution of ∼100 ps [96]. When a voltage is applied across the microchannel plate, a charged particle incident on the front of the MCP will liberate electrons that cascade down the channel exponentially, creating an electron avalanche that exits the MCP as a measureable signal. A single MCP has a gain of $\sim 10^4$, but multiple plates can be stacked together to achieve gains of 10^7-10^8.

The MCP detectors used in this setup utilize an E×B design, where crossed electric and magnetic fields transport electrons from a secondary emission foil to the MCP [98]. This design minimizes the amount of material traversed by the beam. A schematic of the concept is illustrated in Figure 3.7. As the beam passes through the secondary emission foil, it liberates electrons. These electrons are then accelerated forward by an applied

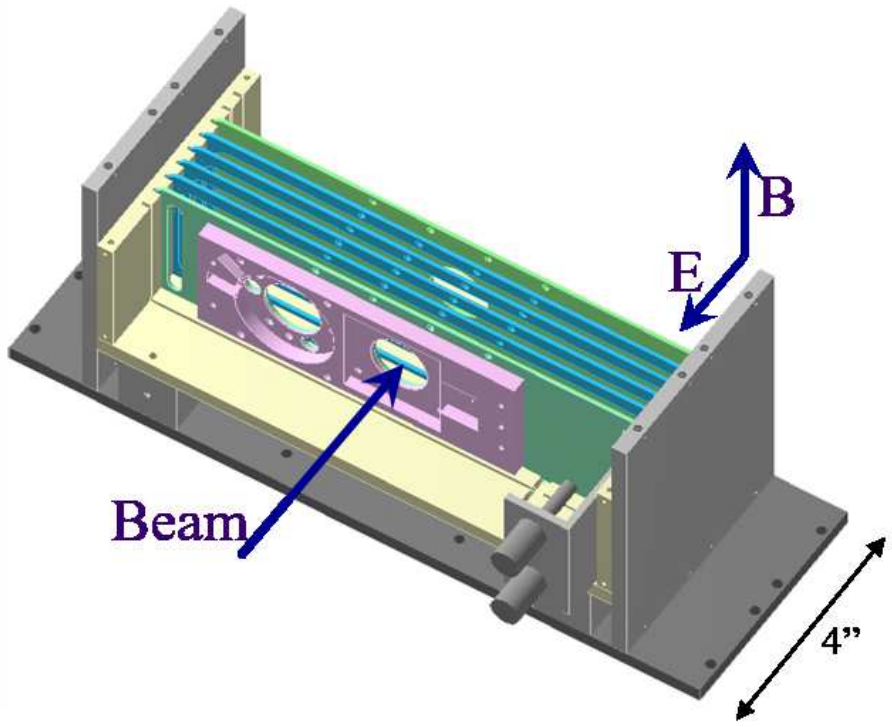

FIGURE 3.8: CAD drawing of an E×B detector, shown in a cutaway view.

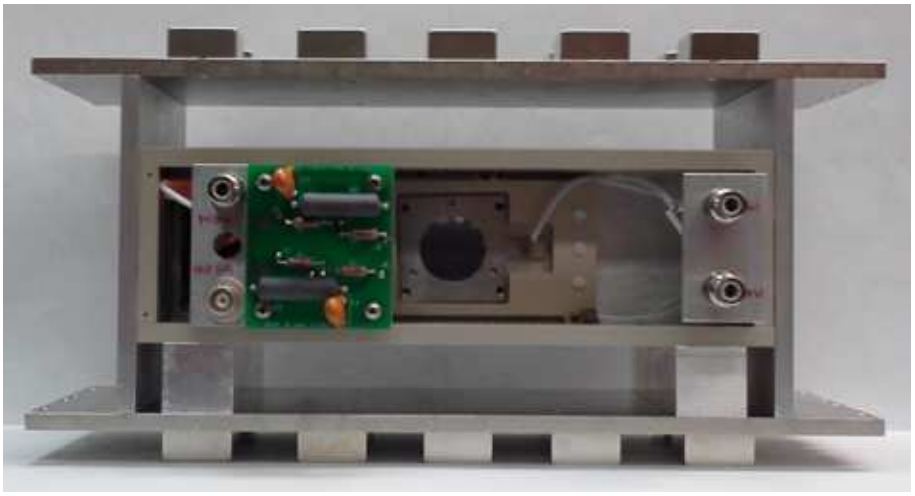

FIGURE 3.9: Photograph of an E×B detector.

electric field, and then bent 180° by a static magnetic field onto the face of the MCP stack. The electric field is created by applying a voltage to a series of ring plates situated downstream of the target foil. A resistor network is used to step the voltage between ring plates, providing a linear field along the detector length. The magnetic field is created by an array of neodymium permanent magnets situated above and below the detector. A CAD representation of the detector is depicted in Figure 3.8 presented in a cutaway view, and a photo of the detector is shown in Figure 3.9. The timing resolution between two MCP detectors has been measured to be 730 ps [99], corresponding to an individual timing resolution of ∼520 ps for a single detector.

3.2.1.2 Silicon detectors

Silicon semiconductor detectors are commonly used for high resolution energy [100] and time measurements [101]. Silicon detectors utilize the depletion region at the junction of n and p-type material. The depletion region is the active region of a solid state detector. When ionizing radiation is incident on the depletion region, electron-hole pairs can be created. The electrons will migrate to the n-type side of the detector while the holes migrate to the p-type side. This creates a signal proportional to the energy that the incident radiation deposited into the detector [2].

Silicon detectors have been developed over the past couple of decades that utilize ion-implantation, where dopants are implanted into the silicon by bombarding a semiconductor crystal with a beam of impurity ions. This ion-implantation technique has also been combined with oxide passivation, which reduces surface leakage current and thus noise [100, 101]. Improvements to silicon wafer processing have allowed these types of detectors to be made out of up to 8 inch wafers. Not only are these detectors able to be made much larger, but they also have the capability of being highly segmented to provide position sensitivity [2, 100, 102].

3.2.1.2.1 S2 design

In the early stages of developing this E-TOF experimental technique [103], the silicon detectors used for measuring evaporation residues were of the S2 design created by Micron Semiconductor [102]. This design has an inner active diameter of 22 mm and an outer active diameter of 76 mm, with a nominal thickness of ∼300 μm. The detector is divided into 16 pie-shaped segments on the ohmic side, and 48 concentric rings on the junction side. The high segmentation of this detector resulted in an artifact in the E-TOF spectrum due to charge trapping in the interstrip regions of the detector [104]. When an ionizing particle enters the Si detectors, it produces electrons and holes that are accelerated by an applied electric field to the ohmic (pie) and junction (ring) sides of the detector respectively. When charge trapping occurs, the total charge read out by the ohmic side is not equal to the total charge read out by the junction side. The magnitude of this effect correlates with the degree of segmentation of the detector, possibly due to the silicon-oxide interstrips. Since the evaporation residues measured in these experiments are low energy, they do not penetrate the detector very far, stopping close to the highly segmented surface where the charge trapping effect could be exacerbated. To minimize this effect, a new detector design with less segmentation was commissioned for use in subsequent experiments.

3.2.1.2.2 S5 design

The detectors used for the experiments discussed in this work are of the S5 design from Micron Semiconductor. This detector is similar to the S2 design, but with reduced segmentation. An illustration of the S5 design is shown in Figure 3.10. The ohmic side still has 16 pie-shaped segments, but the junction side has 6 concentric rings instead of 48. The inner- and outer-most rings are 1.667 mm wide while the middle rings are 5 mm wide.

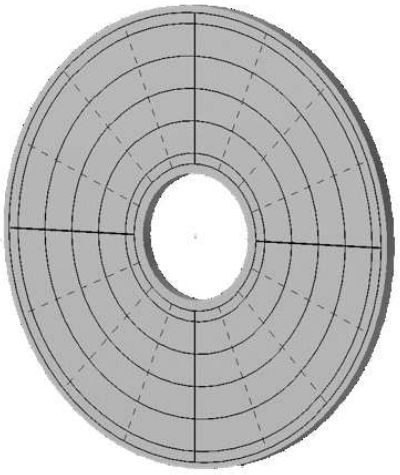

FIGURE 3.10: Illustration of the S5 detector design. The solid lines show the 6 rings divided into quadrants for a total of 24 ring segments. The dashed lines indicate the 16 pie-shaped segments on the opposite side of the detector.

Particles measured near the edge of a detector are likely to have abhorrent timing signals due to edge effects from nonuniformity in the applied electric field, which can create artifacts in the ETOF spectrum. To generate the cleanest spectra, data associated with these inner-most ring segments can be rejected. Therefore, these edge rings are designed to be narrower to minimize the amount of data rejected. To minimize the capacitance of each segment, the rings are further divided into four quadrants. The S5 design also utilizes a new manufacturing technique to realize a dead-layer entrance window thickness of just 0.1-0.2 μm of inactive material, compared to 0.7 μm in the S2 design. This is especially beneficial for the detection of low-energy evaporation residues, which have a range of only 4-10 μm in silicon. The width of the interstrips has also been decreased from 100 μm to 50 μm. The reduction in segmentation in the new design has decreased the charge trapping problem from impacting 20-30% of the data to just 2% of the data [104].

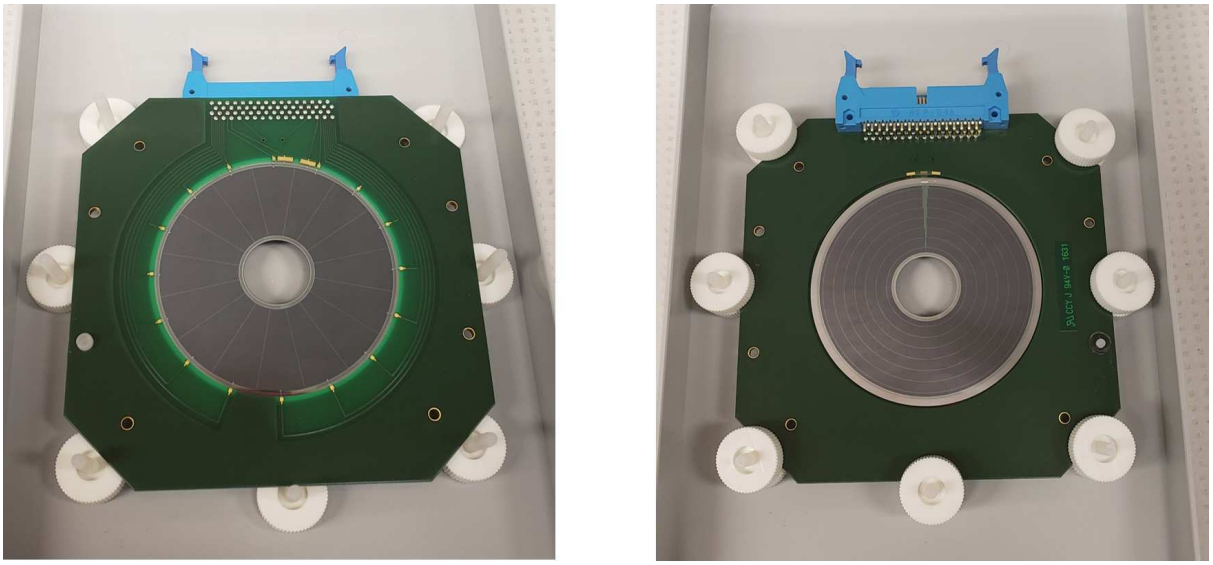

FIGURE 3.11: Photo of the S9 detector. Left: Ohmic side of the detector. Right: Junction side of the detector.

3.2.1.2.3 S9 design

Following the completion of the experiments discussed in this work, a new detector design has been commissioned to address some of the challenges faced with the S5 design. The segmentation of the rings into quadrants was found to produce artifacts in the pie segments at the boundaries of the quadrants. Details about these artifacts are discussed in Chapters 5 and 6. In the new S9 design, the rings are no longer segmented into quadrants, and the number of rings has been increased to 8. The inner- and outer-most rings are still narrower than the middle rings, measuring 1.128 mm compared to 3.485 mm for the middle rings. There are still 16 pie-shaped segments on the ohmic side, but they have been rotated by 11.25° in order to fit the traces of the ring segments onto a single pie segment instead of split across two. A photograph of the detector is shown in Figure 3.11. This detector will be utilized in upcoming radioactive beam experiments, which are expected to be executed in the next couple years.

3.2.1.3 Ionization chambers

A particular challenge faced when performing experiments with radioactive beams is the presence of contaminants in the beam. Since many radioactive beams are produced via nuclear reactions in-flight, there is a possibility for other reaction products besides the ion of interest to be delivered to the experimental setup. Therefore, it is necessary to have a way of identifying the beam on a particle-by-particle basis. This can be accomplished with the use of a gas ionization chamber. Since the energy loss of an ion traversing a medium is proportional to Z^2, a particle's identity can be determined by measuring its ΔE in an ionization chamber, and its time-of-flight between two MCP timing detectors. Two different ionization chambers have been developed for the experiments discussed in later chapters, and their properties are summarized in the sections below.

3.2.1.3.1 Compact Ionization Detector (CID)

Radioactive beams are produced using nuclear reactions, hence the cross-section to produce the ion of interest is an important quantity. The energy of the beam has to be sufficiently high in order to produce the ions of interest at an appreciable rate. Thus the energy necessary to produce the radioactive beam is poorly matched with the near-barrier fusion experiments of interest. For the experiments discussed in the following chapters, it was necessary to degrade the beam energy before impinging on the target. This was accomplished using the Compact Ionization Detector (CID), which is a muti-segmented transverse ionization chamber. It has an active path length of 3.45" [103] and also provides particle identification. Carbon tetrafluoride is used as the detector gas due to its high electron drift velocity [105]. By varying the gas pressure in CID, the beam energy could be decreased to an appropriate range. For the experiment discussed

in Chapter 5, CID was used to reduce the beam energy from 3 MeV/A to 1-2 MeV/A just prior to the target.

3.2.1.3.2 Rare Ion Purity Detector (RIPD)

Experiments at Michigan State University's ReA3 facility provide reacceleration of the radioactive beam to the desired energy, eliminating the need for degrading the beam just prior to the target. Consequently, it was only necessary to provide identification of the beam with a detector upstream of the target. To address this need, the Rare Ion Purity Detector (RIPD) was developed. The goal of this detector was to minimize the drift distance of the electrons, thus increasing the operating rate. By utilizing an axial field design with a 2 cm total active path length, the electron collection time has reduced from 1 μs to 100 ns and the rate of operation extended to $\sim 3 \times 10^5$ particles/s [106]. More details about this detector will be discussed in Chapter 6.

3.2.2 Analysis

The analysis of the data is done using ROOT v5.34/36, which is a C++ based data analysis framework for big data processing, statistical analysis, visualization, and storage [107]. A flow chart of the analysis process is shown in Figure 3.12. After the raw data is collected, it is imported into ROOT. Since all of the measured data is recorded in terms of electronic channel numbers, the detectors need to be calibrated to real quantities. The first step is to calibrate the SBD, since it measures the energy of the beam directly. Calibration is done using a combination of α sources and the different beam energies, which are calculated from the accelerator parameters. If the experiment utilizes an ionization chamber for particle identification, as is the case for radioactive beams, then the ionization chamber needs to be calibrated next. This is done by measuring the energy of the

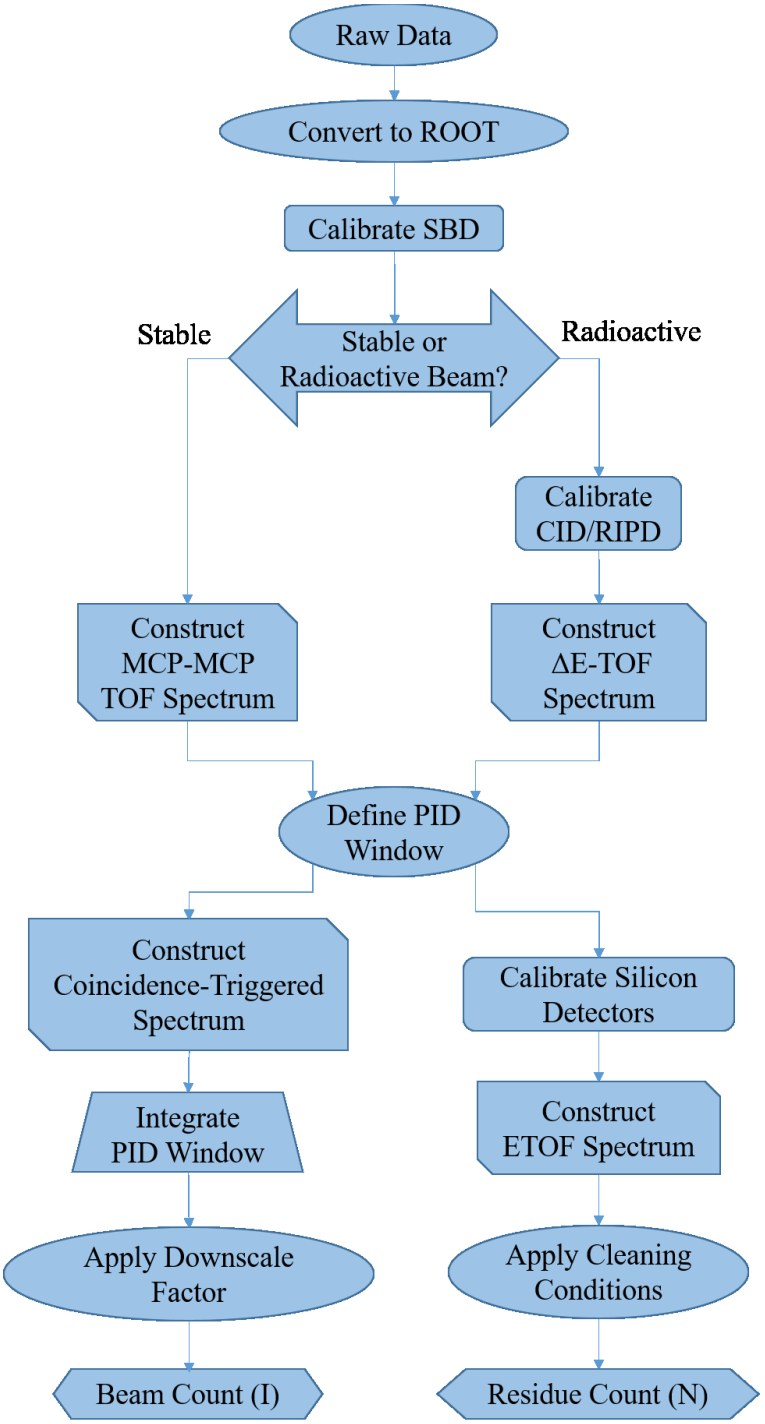

FIGURE 3.12: Flow chart illustrating the general data analysis process.

beam in the SBD with and without the ionization chamber in the beam path to determine the energy loss in the ionization chamber. Once calibrated, the measured ΔE is plot as a function of time-of-flight between the MCP detectors, and a gate is drawn around the particle of interest in the ΔE-TOF spectrum. For stable beams without an ionization chamber, the time-of-flight between the two MCPs is reconstructed, and a narrow window for an appropriate time-of-flight is applied. Once particle identification has been established, each segment of the annular silicon detectors is calibrated independently in energy and time using the elastic peak of the beam. An ETOF is then constructed with the energy in the silicon detector versus the time-of-flight between the MCP_{TGT} and the silicon detector. Conditions required to populate the ETOF spectrum are imposed on the data in order to reduce background in the spectrum. These conditions are discussed in detail in Chapters 5 and 6. With a clean ETOF spectrum, the number of evaporation residues is determined by integrating the region of the ETOF spectrum populated by the residues. The detection efficiency is then determined accounting for the cleaning conditions required and the geometry of the setup. To determine the number of beam particles incident on the target, a coincidence between the two MCP detectors is included in the trigger. This coincidence is downscaled to a rate of $\sim$100 Hz in order to not overwhelm the data acquisition system. Gating the time-of-flight between the two MCP detectors on this coincidence trigger provides a downscaled count of the number of beam particles on target independent of the other detectors in the setup. The integral of this downscaled coincidence time-of-flight measurement within the particle identification window gives the downscaled beam count, and multiplying by the downscale factor provides the actual number of beam particles on target. The target thickness is determined by measuring the energy loss incurred by α particles from a radioactive source and using energy loss calculations. With the number of evaporation residues, number of beam particles on target, target thickness, and detection efficiency, the cross-section is calculated.

Chapter 4

^{18}O + ^{12}C: High Precision Stable Reference

4.1 Experimental details

Before measuring the fusion cross-sections involving neutron-rich radioactive beams, the capabilities of this measurement technique were first demonstrated in 2014 with a stable reference system: ^{18}O + ^{12}C. In addition, this measurement provided a high quality reference for systematic comparisons with more neutron-rich oxygen isotopes. To conduct the experiment, a beam of ^{18}O ions was accelerated to energies between E_{lab} = 16.25 MeV and E_{lab} = 36 MeV using the FN tandem at Florida State University's John D. Fox accelerator center. The beam was pulsed at a frequency of 12.125 MHz. As the beam energy is critical to the accurate measurement of the fusion excitation function, the accuracy of the accelerator energy calibration was checked using known proton resonance energies and determined to be within 7 keV. After optimizing the beam optics, the beam intensity was decreased to an intensity of 1.5-4$\times10^5$ p/s by inserting a pinhole apeture plate just upstream of the last bending magnet. Use of a low-intensity beam ($<10^6$ ions/s) was necessitated by the technique employed and faciltated comparison with future experiments using low-intensity radioactive beams [99].

After passing through a microchannel plate (MCP) detector approximately 1 m upstream of the target (US MCP), the beam was incident on a 93 μg/cm^2-thick ^{12}C

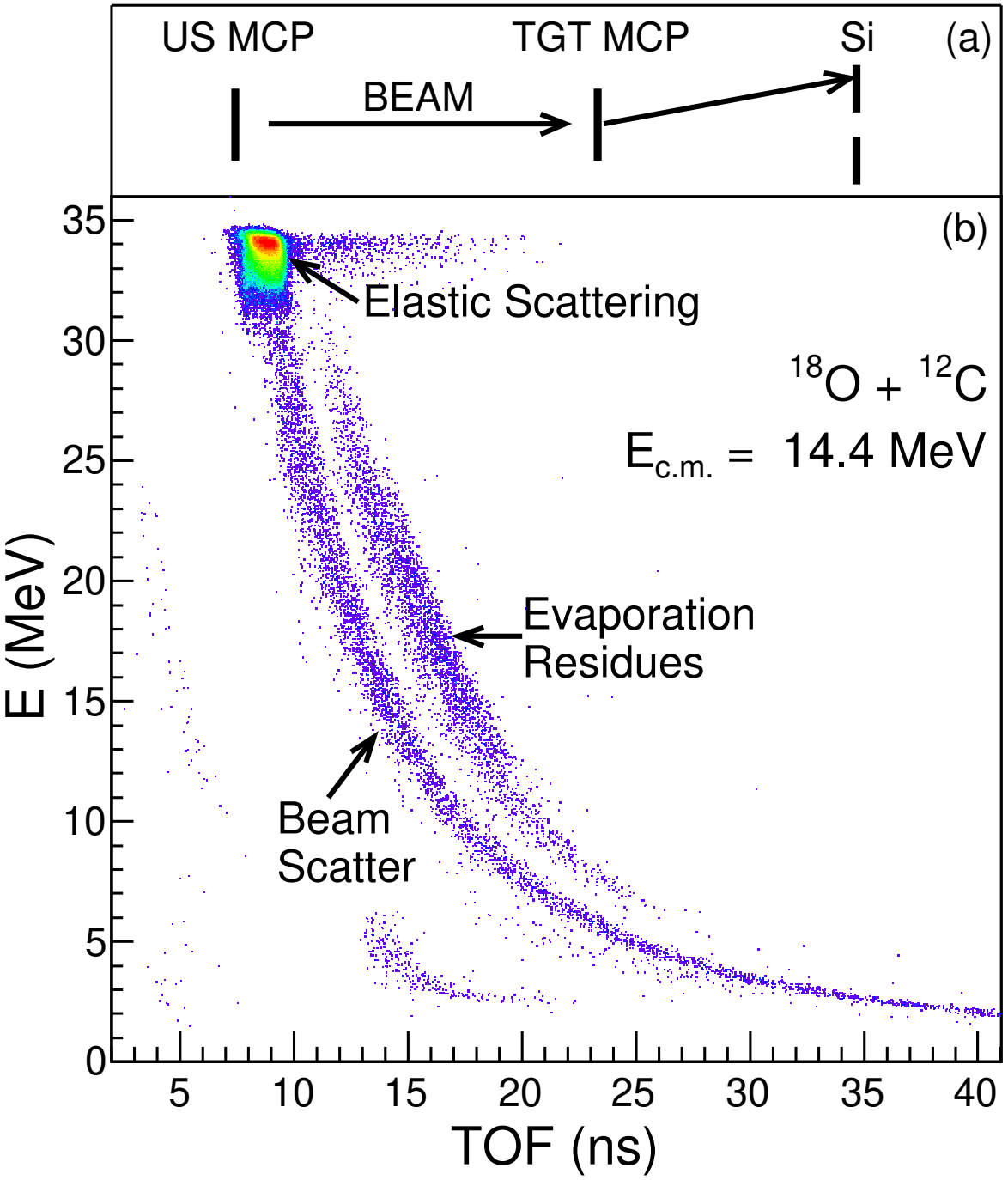

FIGURE 4.1: Top panel: Schematic illustration of the experimental setup. Bottom panel: Energy versus time-of-flight spectrum for ^{18}O ions incident on ^{12}C target nuclei at $E_{c.m.}$=14.4 MeV. Color is used to represent yield (logarithmic scale) in the two dimensional spectrum.

foil which served as the target (TGT MCP) as depicted in Figure 4.1a. The ^{12}C target foil also served as a secondary emission foil for a microchannel plate detector [99] thus providing a timing signal for a time-of-flight (TOF) measurement. Measurement of the TOF between the two MCPs allowed rejection of beam particles scattered or degraded prior to the target.

Reaction products were detected in the angular range $4.3^\circ \leq \theta_{\text{lab}} \leq 11.0^\circ$ using a segmented, annular silicon detector which provided both an energy and fast timing signal [101]. Due to the kinematics of the reaction, the angular range subtended by this detector resulted in a high geometric efficiency (50-59%) for detection of fusion residues. Reaction products were distinguished on the basis of their energy and time-of-flight (ETOF) [99]. A typical ETOF spectrum measured is depicted in Figure 4.1b where the energy corresponds to the energy deposited in the silicon detector while the time-of-flight is the time difference between the target MCP and the silicon detector.

The most prominent feature in Figure 4.1b is the peak at E $\approx$ 34 MeV that corresponds to elastically scattered particles. Originating from this peak is a locus of points with lower energies and longer TOF values. Points in this locus are scattered beam particles. Visible at larger TOF and clearly separated from the beam scatter line is an island of reaction products. This island is populated by evaporation residues that result from fusion of the projectile and target nuclei to form a compound nucleus which subsequently de-excites. Protons and alpha particles which are emitted during this de-excitation cascade of the compound nucleus manifest themselves in the spectrum with a characteristic energy time-of-flight relationship. Alpha particles are observed with energies between 10 MeV and 25 MeV and TOF values of approximately 5 ns. Protons are observed at deposited energies of E $<$ 6 MeV, consistent with the Si detector thickness, and TOF values of approximately 15 ns. The larger TOF values observed for protons as compared to the alpha particles is due to the slower risetime exhibited by protons and the leading

edge discrimination employed. Also visible in the spectrum is a tail on the elastic peak which is constant in energy and extends to larger TOF values. This tail occurs with low probability (0.4%) as compared to the elastic peak.

4.2 Determination of the excitation function

The measured evaporation residue cross-section was ascertained by using the measured number of beam particles incident on the target, the measured number of evaporation residues, and the known target thickness. The total number of beam particles incident on the target was determined by counting the coincidences between the MCP at the target position and the upstream MCP. The number of residues detected was established by selecting the appropriate region of the ETOF spectrum and summing the number of evaporation residues contained within it. The limits of the region of integration were established by calculating the TOF for different mass residues and using the beam scatter line as a reference. After accounting for the finite time resolution, an interval in mass number, $22 \leq A \leq 30$ was used for measurements at $E_{c.m.} > 7.5$ MeV and $24 \leq A \leq 30$ for $E_{c.m.} \leq 7.5$ MeV.

In order to determine the total fusion cross-section it is necessary to know the geometric efficiency of the experimental setup. The efficiency was determined by using a statistical model, EVAPOR [110], which simulates the decay of a compound nucleus using a Hauser-Feshbach approach. By calculating the fraction of the evaporation residues that lie within the detector acceptance, the geometric efficiency of the experimental setup is obtained. The bombarding energy dependent efficiency lies between 50% and 59%. Using the efficiency together with the measured evaporation residue cross-section, the total fusion cross-section is extracted. Since the MCP efficiency affects both the counting of the total number of beam particles and the number of evaporation residues, it does not impact the measured total fusion cross-section.

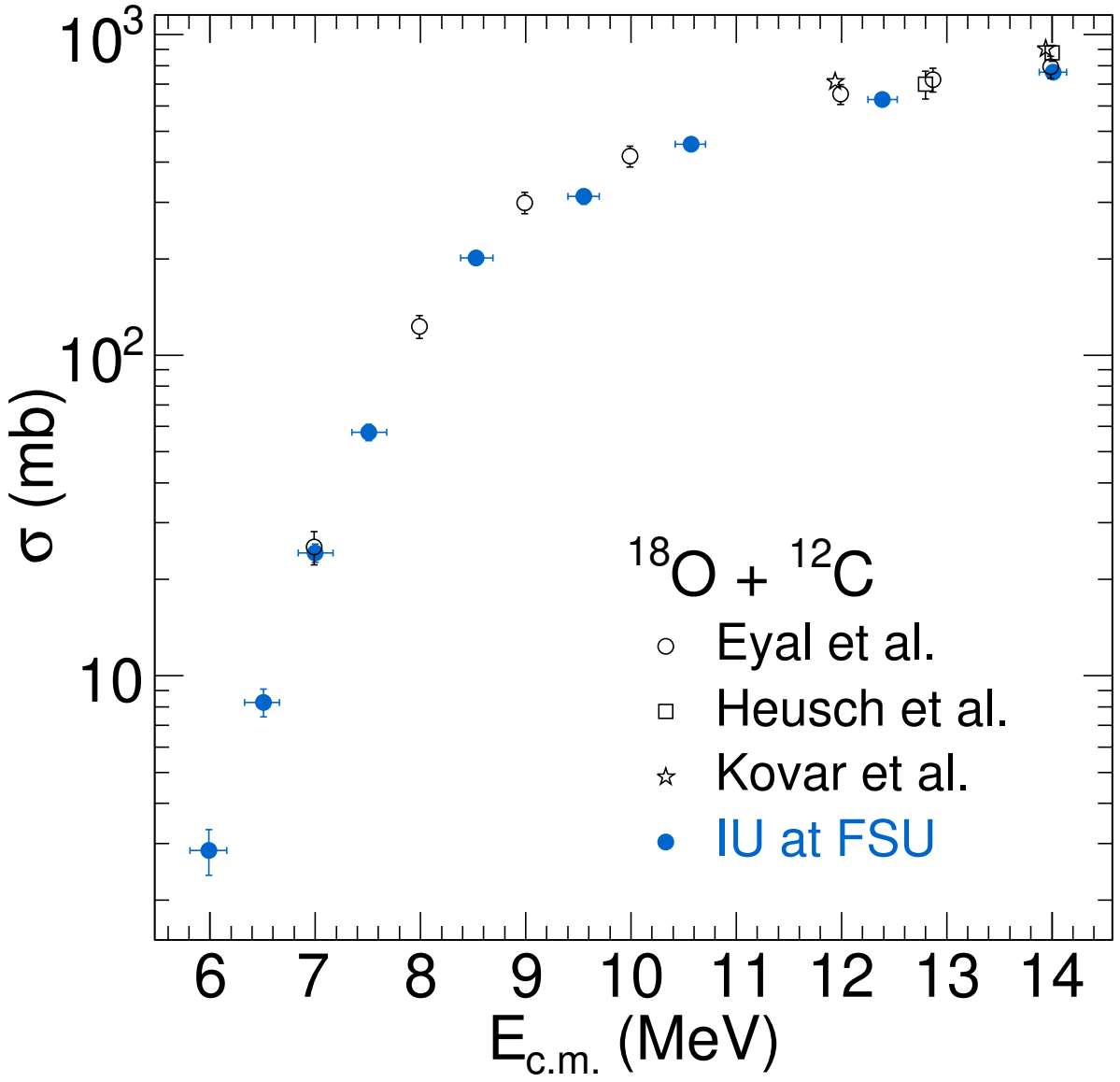

FIGURE 4.2: The fusion excitation function for ^{18}O + ^{12}C is shown at energies near and below the Coulomb barrier. Literature values are shown as open circles [89], open squares [108], and open stars [109] with the present data represented by solid circles.

The measured excitation function is displayed in Figure 4.2 along with previously published results [89, 108, 109]. As expected, the fusion cross-sections decrease with decreasing $E_{c.m.}$ indicative of a barrier controlled phenomenon. It is noteworthy that even for the lowest energies measured an exponential decrease of the cross-section with decreasing energy is observed. Vertical error bars on the present data include both the

statistical uncertainties as well as a 2% systematic error. Horizontal error bars represent the uncertainty in whether the fusion occurs at the front or back of the target foil. Using the direct measurement of evaporation residues as done in the present experiment, previous measurements only measured the fusion cross-section down to the 25 mb level [89]. In contrast, in the present work the fusion cross-section was measured down to the 2.8 mb level, close to a full order of magnitude lower in cross-section. At energies where the present dataset overlaps with existing data, overall agreement of the cross-sections is good, close to the statistical uncertainties of the prior measurements. This overall agreement not only indicates that our approach in extracting the fusion cross-section is sound but that there are no significant uncertainties in the values of the target thickness or detector efficiency. Closer comparison of the present dataset with the data of Ref. [89] indicates that the presently measured cross-sections are approximately 7% lower for $E_{c.m.} \geq 10$ MeV. This is principally due to an overestimation of the geometric efficiency in this experiment by not correcting for an underprediction of large angle residues by the statistical model code used to determine the efficiency. This can be seen in Figure 4.5 and will be discussed in the following section.

In recent years it has become possible to perform TDHF calculations on a 3D Cartesian grid thus not requiring any artificial symmetry restrictions and with much more accurate numerical methods [78, 111, 112]. In addition, the quality of the effective interactions has been substantially improved [86, 113–116]. Over the past several years, the density constrained TDHF (DC-TDHF) method for calculating heavy-ion potentials [84] has been employed to calculate heavy-ion fusion cross-sections with remarkable success [81, 117]. While most applications have been for systems involving heavy nuclei, recently the theory was used to study above and below barrier fusion cross-sections for lighter systems, specifically for reactions involving various isotopes of O+O and O+C [80, 83] relevant for the reactions that occur in the neutron star crust. One general characteristic of TDHF and DC-TDHF calculations for light systems is that the fusion cross-section at energies

well above the barrier are usually overestimated [118, 119], whereas an excellent agreement is found for sub-barrier cross-sections [83]. This is believed to be due to various breakup channels in higher energy reactions of these lighter systems that are not properly accounted for in TDHF dynamics and contribute to fusion instead. Nevertheless, the agreement is remarkable given the fact that the only input in DC-TDHF is the Skyrme effective N-N interaction, and there are no adjustable parameters.

An unfortunate present limitation of the TDHF approach, however, is the inability to treat pairing during the collision process. This shortcoming in the inclusion of pairing has led to the prediction of deformation of the ground state for some even-even nuclei such as ^{18,20}O in disagreement with self-consistent mean field calculations that include pairing. To overcome this shortcoming, in prior work an average of all orientations of the deformed nucleus with respect to the target nucleus has been performed [80]. It can be qualitatively argued that this averaging nonetheless results in a larger fusion cross-section as compared to the spherical nucleus.

The effect of the inclusion of pairing in the DC-TDHF calculations is presented for the first time in Ref. [90]. This was achieved by performing a BCS pairing calculation for the static solution of ^{18}O resulting in a spherical nucleus with a subsequent density constraint calculation to produce this density as a solution of the ordinary Hartree-Fock equations in the spirit of the density-functional theory. This nucleus with frozen occupations was then used in the TDHF time evolution. Subsequent density-constraint calculations in DC-TDHF method preserves this spherical shape during the entrance channel dynamics. As can be seen in Figure 4.3a, inclusion of pairing in the DC-TDHF calculation for ^{18}O + ^{12}C results in a significant reduction of the fusion cross-section. The standard DC-TDHF calculations are presented as the dashed curve while the calculations that include pairing are depicted as the solid curve. At all energies, pairing acts to reduce the fusion cross-section. At the highest energies shown pairing reduces the cross-section

to $\approx$ 80% of the value calculated without pairing. This difference between the calculations with and without pairing increases dramatically as the incident energy decreases. At the lowest energies shown the introduction of pairing in the calculation reduces the cross-section to $\approx$ 36% of the cross-section calculated without pairing.

Comparison of the experimental fusion excitation function with the DC-TDHF microscopic calculations is presented in Figure 4.3a. The presently measured fusion cross-sections, previously shown in Figure 4.2, are indicated as solid symbols. Overall comparison of the experimental cross-sections with the DC-TDHF calculations indicate that the experimental cross-sections are lower than the theoretical predictions. In order to facilitate a quantitative comparison of the experimental excitation function with the theoretical predictions, the measured cross-sections have been fit with the following functional form:

$$\sigma = \frac{R_c^2}{2E}\hbar\omega \cdot ln\left\{1 + exp\left[\frac{2\pi}{\hbar\omega}(E - V)\right]\right\} \tag{4.1}$$

where E is the incident energy, V_C is the barrier height, R_C is the radius of interaction, and $\hbar\omega$ is the barrier curvature. This functional form, referred to as the Wong formalism, describes the penetration of an inverted parabolic barrier [120]. The fit of the data is shown as the dotted line in Figure 4.3a and has values of R_c = 7.24 $\pm$ 0.16 fm, V = 7.62 $\pm$ 0.14 MeV, and $\hbar\omega$ = 2.78 $\pm$ 0.29 MeV. Shown in Figure 4.3b is the ratio of the fit of the experimentally measured cross-sections to the DC-TDHF calculations with pairing. For energies $E_{c.m.} > 9$ MeV, the ratio $\sigma_{\mathrm{Experiment}}/\sigma_{\mathrm{DC-TDHF}}$ is $\approx$ 0.75 and decreases weakly with decreasing energy. A stronger decrease in the ratio is observed as the energy decreases from $E_{c.m.}$ = 9 MeV to $E_{c.m.}$ = 7 MeV. At this energy, the ratio is minimum with a value of 0.54. As the incident energy decreases further, the ratio increases reaching a value of 1.32 at the lowest energy measured, $E_{c.m.}$ = 6 MeV. The presence of breakup reactions at energies above the barrier could explain the fact that the ratio is less than

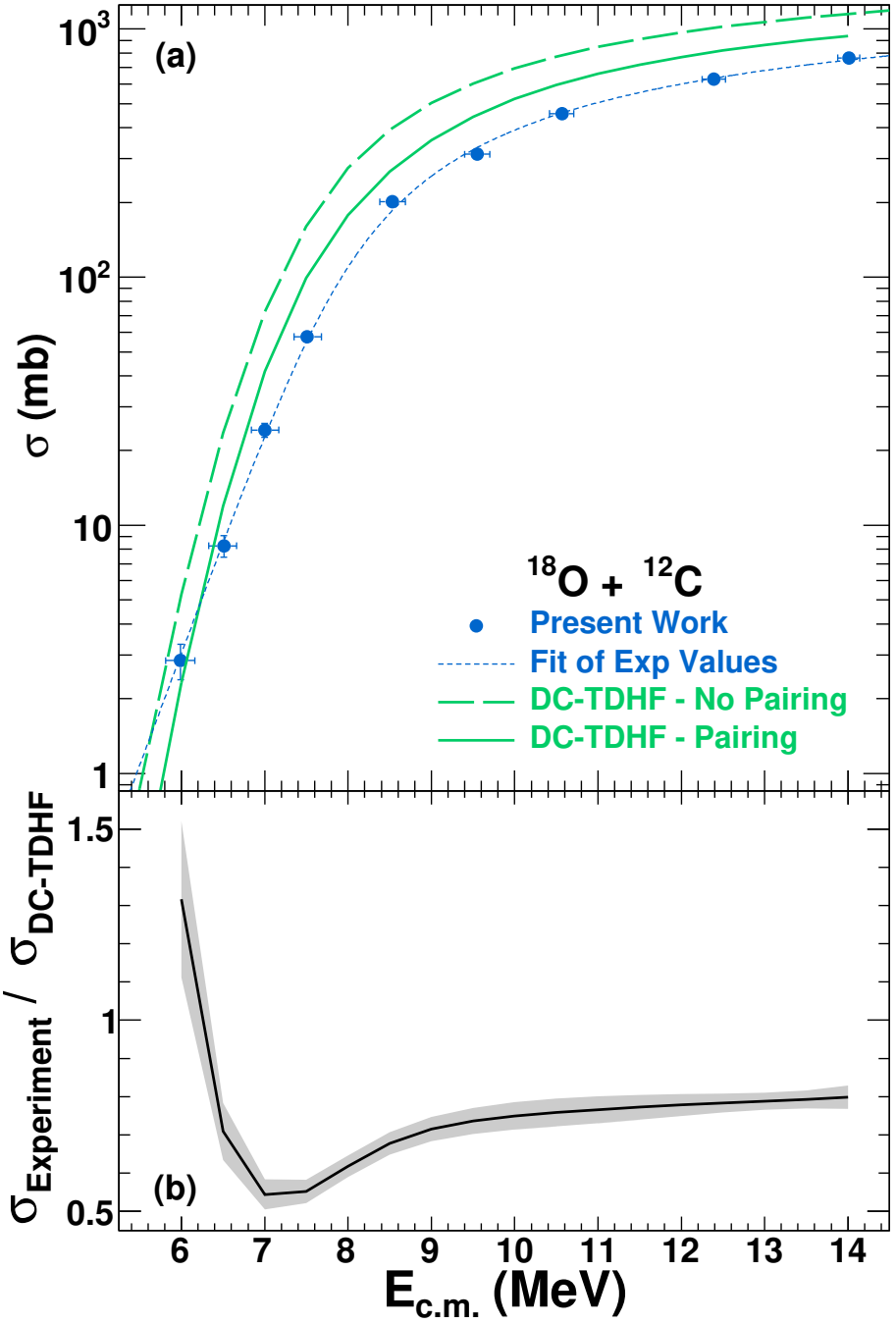

FIGURE 4.3: Top panel: Comparison of the experimentally measured fusion cross-sections (closed symbols) with the results of the DC-TDHF calculations with (solid line) and without (dashed line) pairing. Also shown, as a dotted line, is the result of a fit to the experimental data (see text for details). Bottom panel: Energy dependence of the ratio of the experimentally measured cross-sections to the DC-TDHF predictions which include pairing. The shaded band depicts the uncertainty in the ratio due to the uncertainty in the experimental cross-sections.

unity in this energy range. With decreasing incident energy, the role of breakup reactions diminishes hence the ability of the DC-TDHF method to describe fusion is expected to improve. The sub-barrier region is therefore the area of interest in the comparison of the model with the experiment. The key feature in the ratio is its change with decreasing incident energy in the sub-barrier domain, specifically its increase from a value smaller than unity to a value larger than unity. This trend emphasizes that the experimental and theoretical excitation functions have different shapes with the experimental cross-section falling more slowly with decreasing incident energy than is theoretically predicted by the DC-TDHF method. The impact of the experimental uncertainties on the ratio has been assessed and is presented as a shaded band in Figure 4.3b. It is clearly evident that the trends exhibited by the ratio are significantly larger than the magnitude of the uncertainties.

The fact that the sub-barrier experimental fusion cross-sections decrease more slowly with decreasing energy than the calculated cross-sections can be interpreted as a larger tunneling probability for the experimental data as compared to the theoretical calculations. This enhanced tunneling probability can be associated with a narrower barrier, which deviates from an inverted parabolic shape. The fundamental reason that the barrier determined from the experimental data is weaker than in the theory is presently unclear. It should also be recalled that within the DC-TDHF calculations, inclusion of pairing decreased the predicted cross-sections. It was assumed that the initial occupation numbers calculated with pairing were frozen as the reaction dynamics proceeded. It can be argued that relaxing this stringent condition would result in larger cross-sections. Unfortunately, microscopic calculations which allow the pairing to evolve in response to changes in the shape of the nuclear system as the fusion proceeds are beyond the scope of the present work. Such calculations would provide a more realistic treatment of the impact of pairing on fusion. It is noteworthy that the previous experimental data [89] only extended down to $E_{c.m.} = 7$ MeV. The dramatic increase in cross-section relative to

the DC-TDHF method occurs at energies below $E_{c.m.} = 7$ MeV. This enhancement of the fusion cross-section in the sub-barrier domain demonstrates the importance of measuring the sub-barrier fusion cross-section for light, heavy-ion reactions.

In order to further explore the sub-barrier enhancement demonstrated in Figure 4.3, a follow-up experiment to measure the $^{18}O + ^{12}C$ fusion cross-sections was performed in 2015 at even lower beam energies. This measurement was also carried out at Florida State University with beam energies between $E_{lab} = 13.75$ MeV and $E_{lab} = 32.2$ MeV. Since the motivation of this experiment was to extend the measurement of the fusion excitation functions down to lower energies, reducing the background in the ETOF spectrum at low energies was a crucial goal. As the energy of the beam decreases, the cross-section for fusion dramatically decreases and thus requires more beam on target to measure an appreciable amount of residues, but the cross-section for scattering remains relatively unchanged. Therefore, in the ETOF spectrum for lower energies the residue island becomes less populated but the scatter line becomes more intense, which could potentially obscure the evaporation residues. To reduce the amount of scattering, the 93 $\mu g/cm^2$ thick carbon secondary emission foil in the US MCP detector was replaced with a thinner foil. A 51 $\mu g/cm^2$ carbon foil was used for most of the beam energies, and a 22 $\mu g/cm^2$ carbon foil was used for the lowest beam energy.

The data was analyzed following the same prescription as the previous measurement, and the fusion cross-sections were extracted. The fusion cross-sections from the follow-up experiment are shown in Figure 4.4 as the solid pink triangles, together with the cross-sections from the previous experiment shown as open blue circles [104]. The DC-TDHF calculation that includes pairing is shown as the solid green line. The cross-sections measured in this experiment at energies above $E_{c.m.} = 6$ MeV agree very well with the initial 2014 data set. In the 2015 experiment, the lowest measured cross-section reaches a value of 820 μb, which is $\sim$3.5 times lower than the initial measurement from 2014. The

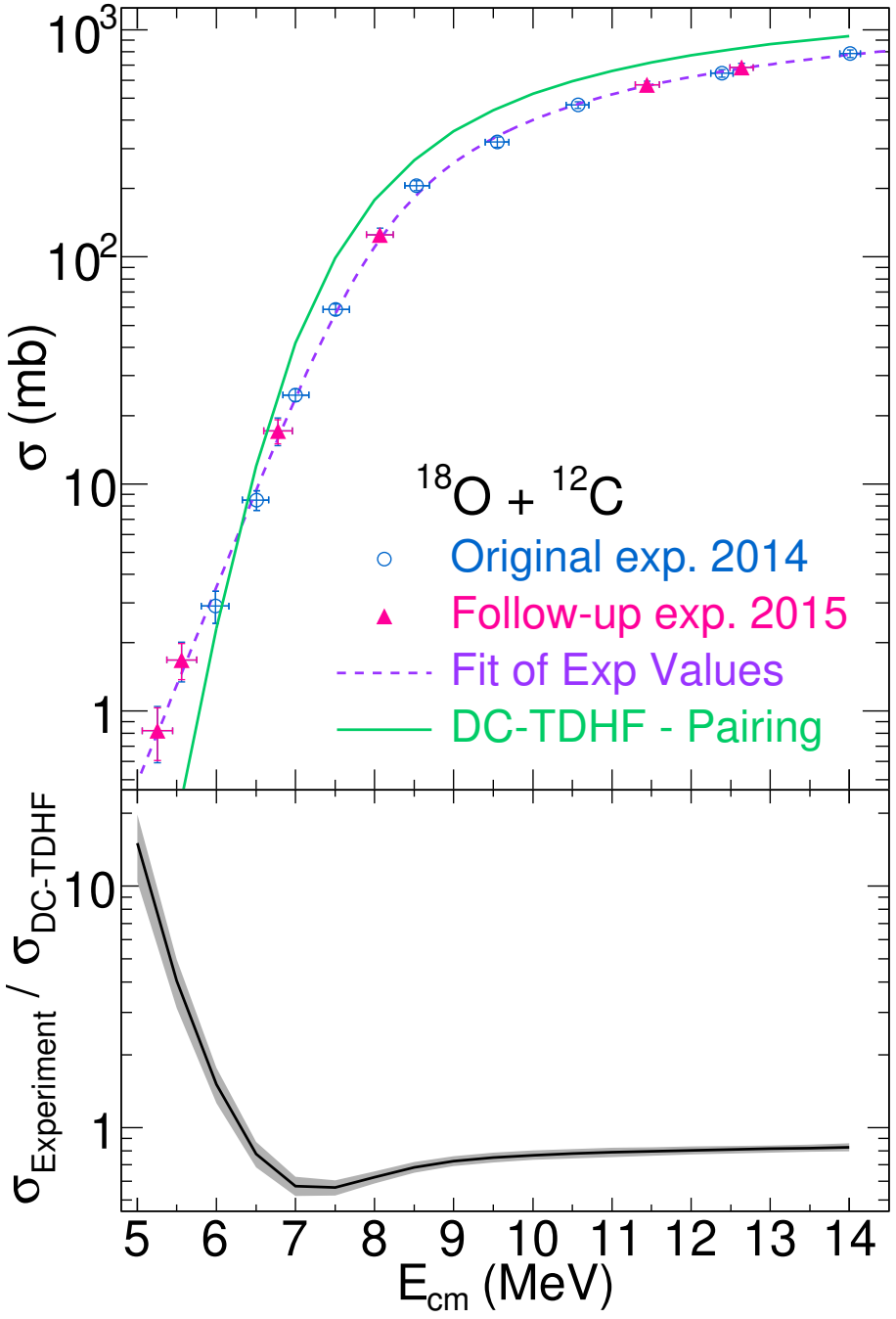

FIGURE 4.4: Top panel: Fusion excitation functions for ^{18}O + ^{12}C. The open blue circles reflect data from the initial measurement from 2014, and the solid pink triangles represent the follow-up measurement from 2015. The purple dashed line corresponds to a fit of the data using the combined data set of both measurements. The result of the DC-TDHF calculations with pairing is shown as the solid green line. Bottom panel: Energy dependence of the ratio of the experimentally measured cross-sections to the DC-TDHF predictions which include pairing. The shaded band depicts the uncertainty in the ratio due to the uncertainty in the experimental cross-sections.

two lowest values at $E_{c.m.} < 6$ MeV continue the trend observed in the initial data set. This is best seen in the bottom panel of Figure 4.4. Just like in Figure 4.3, the bottom panel depicts the ratio between the fit of the measured fusion excitation function (dashed purple line in the top panel) and the DC-TDHF calculations. As expected, the ratio at high $E_{c.m.}$ plateaus at a value of ∼0.8. As $E_{c.m.}$ decreases, the ratio dips down to a minimum value of ∼0.6 at $E_{c.m.} = 7$ MeV before crossing unity and dramatically increasing up to a factor of 10. This demonstrates a clear shape difference between the measured fusion excitation function and that predicted by the DC-TDHF calculations. One potential reason for this sub-barrier deviation could be the overestimation of the number of evaporation residues measured at the lowest energies, where background counts might be contaminating the residue island. In retrospect, it would be a good idea to revisit the data analysis of this experiment and apply the same analysis treatment as in the experiments that will be discussed in Chapters 5 and 6.

4.3 De-excitation of the compound nucleus

In fusion, formation of a compound nucleus involves the amalgamation of two colliding nuclei into a single nucleus which no longer retains a memory of the identity or structure of the colliding nuclei. As the two nuclei fuse, both binding energy and incident kinetic energy are converted into intrinsic excitation and spin. At energies near the Coulomb barrier, the resulting compound nucleus, characterized by its spin and excitation energy, de-excites by emitting neutrons, protons, α particles, and γ rays. To describe this de-excitation of the compound nucleus a statistical framework is typically invoked [121, 122]. The experimental signatures of the de-excitation process are the energy spectra and angular distributions of the emitted particles along with their cross-sections. Although this perspective of fusion reactions, namely the complete equilibration of the

projectile and target nuclei followed by their statistical decay has been largely successful, exceptions have been noted [123]. In these cases, it has been noted that entrance channel effects are observable. To test this survival of entrance channel effects in fusion reactions, the collision of light nuclei with well established α cluster structure was investigated [124, 125]. The extent to which this pre-existing cluster structure survives the fusion process can be probed by examining α particle emission as a function of incident energy.

4.3.1 Characterization of the evaporation residues

The laboratory angular distribution of evaporation residues for incident energies E_{lab}=16.25 MeV to 36 MeV are presented in Figure 4.5 . The horizontal error bars depict the angular coverage of each detector element, and the vertical error bars represent the statistical uncertainty. Also shown are the evaporation residue angular distributions predicted by the statistical model codes EVAPOR [110] (solid red line) and PACE4 [126] (dashed blue line), which employ a Hauser-Feshbach formalism to describe the de-excitation of the fusion product. The model calculations have been normalized to the residues measured in the angular range subtended by the T2 Si detector. At all energies the yield for evaporation residues decreases with increasing laboratory angle. Examination of the angular distributions reveals that the distributions have a two component nature that can be qualitatively understood as the presence of different de-excitation pathways as the excited compound nucleus relaxed. De-excitation of the compound nucleus via single or few nucleon emission will impart less transverse momentum to the recoiling evaporation residue resulting in an angular distribution that is peaked at smaller angles. In contrast, emission of an α particle results in a larger transverse momentum for the evaporation residue and as a result an angular distribution that is peaked at larger angles.

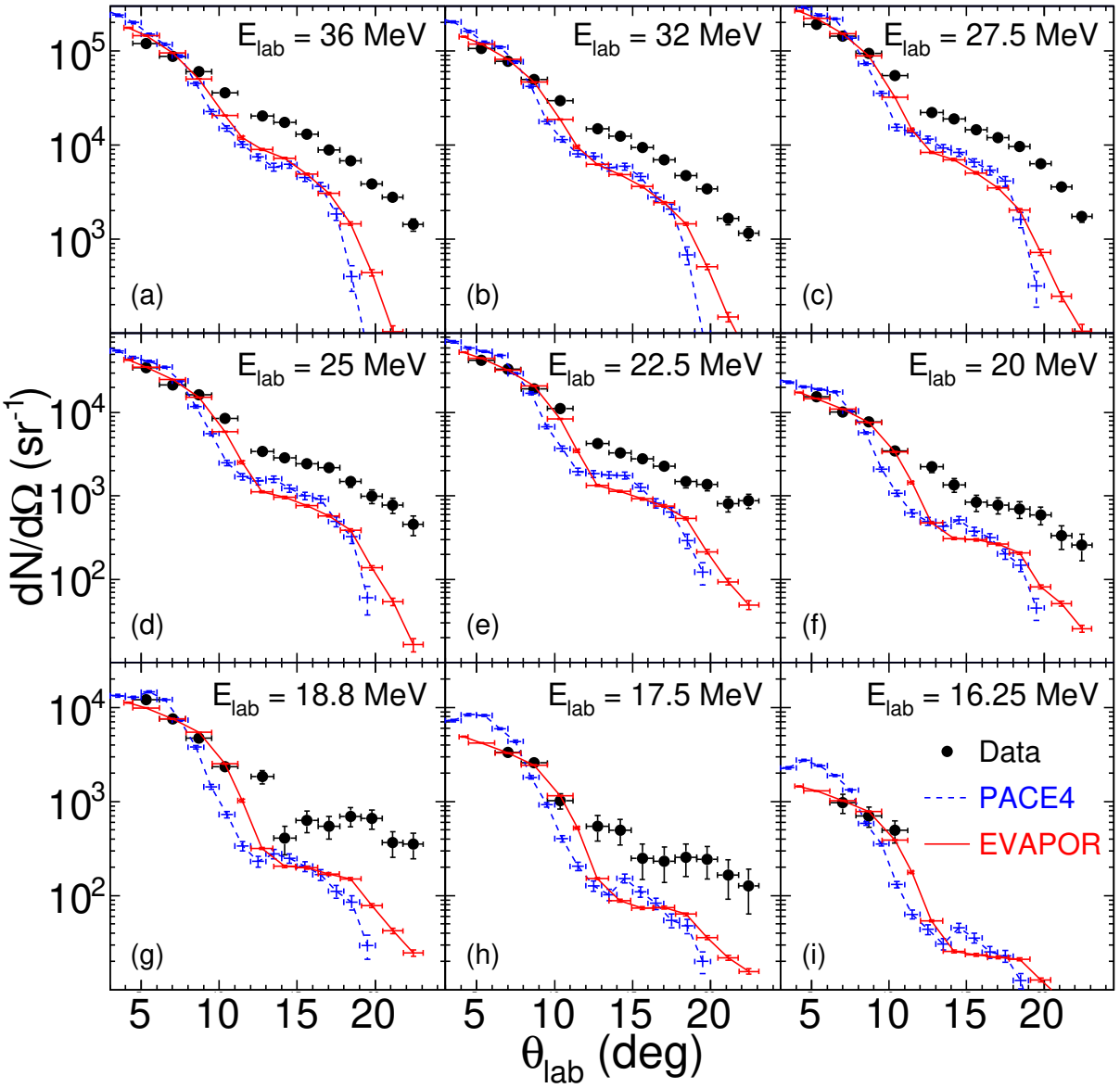

FIGURE 4.5: Angular distribution of evaporation residues in the laboratory frame for different bombarding energies for $^{18}O + ^{12}C$. Solid symbols depict the experimental angular distribution while the solid and dashed curves indicate the angular distributions predicted by the statistical model codes EVAPOR and PACE4 respectively. The model angular distributions have been normalized to the experimental data over the angular range $4.3^\circ \leq \theta_{\rm lab} \leq 11.2^\circ$.

While the small angle component of these distributions is reasonably well described by the statistical model codes, the large angle component is significantly underpredicted.

The energy distributions of evaporation residues are shown in Figure 4.6 for different incident energies. It should be noted that the distributions presented correspond to the energy deposited in the silicon detector. As the atomic number of the residues is not known the energy measured in the silicon detector has not been corrected for the energy loss in the target or the entrance dead layer of the silicon detector. If one assumes, consistent with statistical model calculations, that the evaporation residues are predominantly Si and Al nuclei, then this energy loss correction is typically of the order of 1 to 1.5 MeV. At the five higher energies a clear indication of a bimodal distribution is observed. Qualitative examination of the shape of these energy distributions indicates that the total distribution is dominated by the yield of the high energy component. This observed distribution can be well described by the sum of two Gaussians as shown by the two Gaussian fit indicated by the dashed line. For $E_{lab} \leq 20$ MeV only a single component distribution is observed corresponding to the higher energy component present at higher beam energies.

One possible origin of the two component nature of the energy distributions visible in Figure 4.6 is different de-excitation pathways for the excite ^{30}Si nucleus, namely α emission as compared to nucleon only emission. This conclusion is also consistent with the angular distributions observed in Figure 4.5. To investigate if this hypothesis is correct, the energy distribution of evaporation residues selected on the coincident detection of an α particle in the angular range $4.3^\circ \leq \theta_{lab} \leq 23^\circ$ was constructed. The results are presented as the open symbols in Figure 4.6. All the residue energy distributions coincident with an α particle are single peaked with maxima at E_{Si} = 6-9 MeV. The fact that the α gated residue energy distributions are peaked at essentially the same location as the mean value of the low energy component and have comparable widths, provides strong evidence that

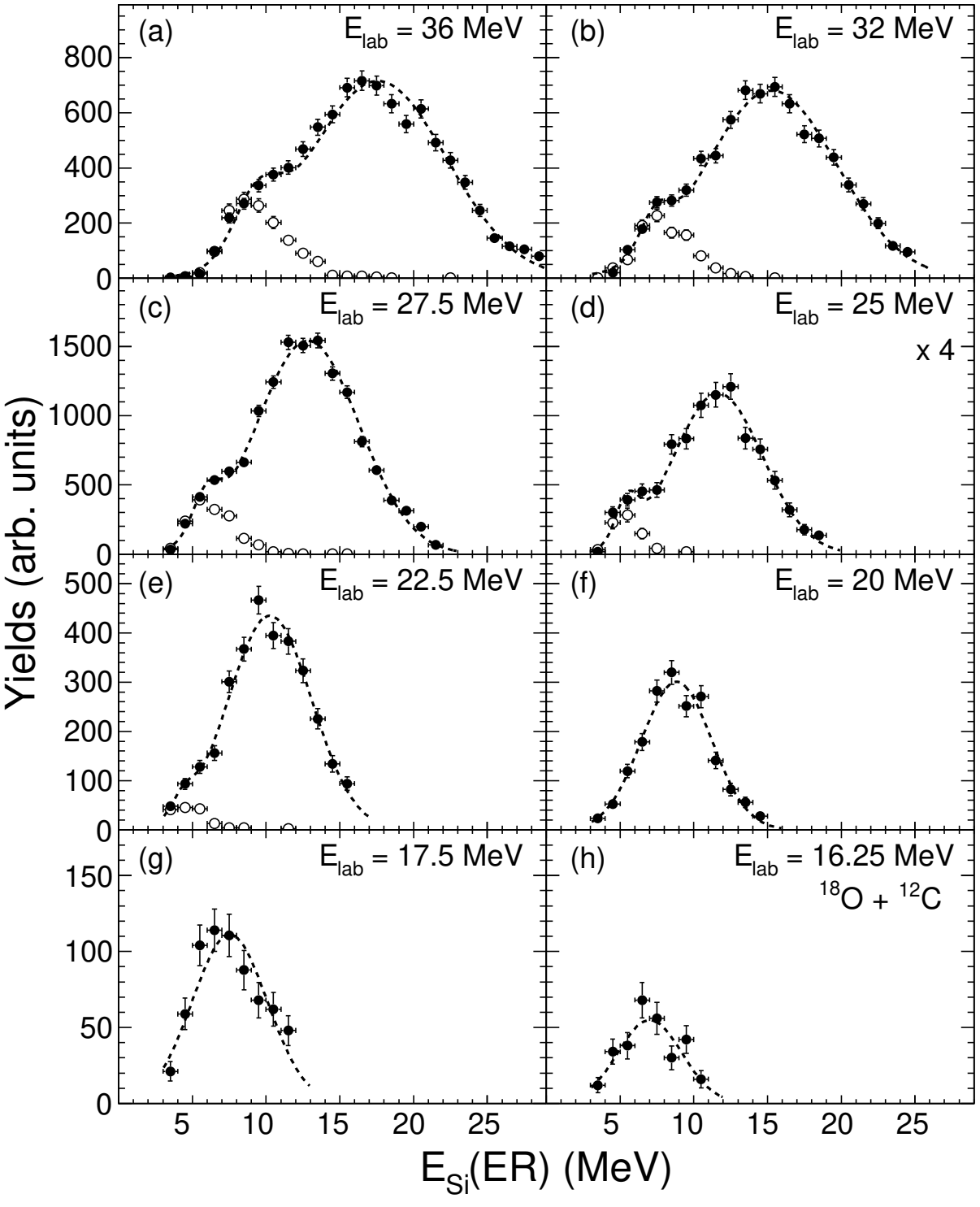

FIGURE 4.6: Solid symbols depict the distribution of deposited energies in the Si detector for evaporation residues at different bombarding energies. Open symbols correspond to the same quantity for which evaporation residues are coincident with α particles. Open symbols have been scaled by a factor of two for clarity. The dashed line corresponds to a two Gaussian fit.

the low energy component in Figure 4.6 is associated with α emission. The reduction of the average energy of the evaporation residue is understandable since the α particle is detected at forward angles hence the recoil imparted to the evaporation residue lowers its energy.

A quantitative perspective of the trends associated with the low and high energy component is examined in Figure 4.7. In the upper panel of the figure one observes that for both the high energy (open triangles) and low energy (open squares) components the average laboratory energy of the residue, $\langle \mathrm{E_{Si}}(ER) \rangle$, increases essentially linearly with the incident energy $\mathrm{E_{c.m.}}$. As expected, the trend for the total distribution (filled circles) follows that of the high energy component since the yield of the high energy component dominates the yield of the total distribution. The trend of the α gated residue energy distributions (solid red squares) unsurprisingly follows that of the low energy component, quantitatively demonstrating that the low energy residues are associated with α emission. At the lowest incident energies measured, the low energy of these evaporation residues emphasizes the need for low detection thresholds. The linear trend observed for the average energies of the residues can be understood as the change of the kinematics of the reaction with increasing incident energy. To quantitatively assess this dependence, the average laboratory energy of the ^{30}Si fusion product as a function of $\mathrm{E_{c.m.}}$ was calculated, and the result is indicated as the solid line in Figure 4.7. To investigate the reason for the difference between the measured values for the evaporation residues (solid circles) and that calculated for the ^{30}Si (solid line), the energy a ^{30}Si nucleus would possess after it passes through the target and front dead layer of the Si detector was calculated. The impact of the target and front dead layer of the Si detector on the detected energy of the ^{30}Si has been calculated using the energy loss program SRIM [127] and the result is depicted as the dotted line. Also shown in Figure 4.7 is the $\langle \mathrm{E_{Si}}(ER) \rangle$ associated with a ^{26}Mg nucleus resulting from the α decay of ^{30}Si. The α emission is assumed to be isotropic with both the α particle and evaporation residue detected in the experimental

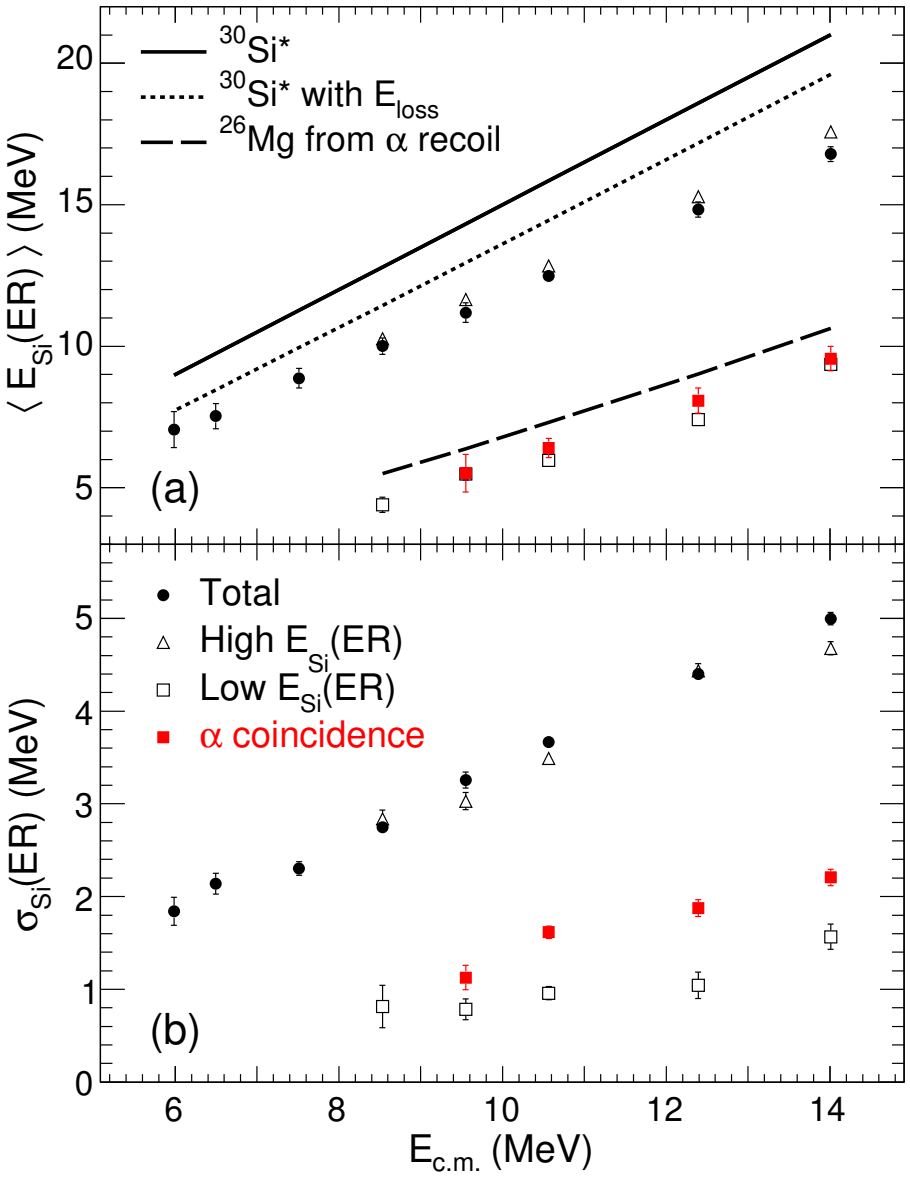

FIGURE 4.7: Top panel: Average energy deposited in the Si detector by fusion residues as a function of the available energy in the center-of-mass (solid circle). The mean energy extracted for the low and high energy components from the fits shown in Figure 4.6 are represented by the open squares and triangles respectively, while the red closed squares correspond to residues in coincidence with α particles. The solid line represents the energy of the excited compound nucleus for complete fusion. The dotted line represents the compound nucleus energy after energy loss in both the target and Si dead layer. The dashed line represents the average energy deposited by a ^{26}Mg nucleus following emission of an α particle. The influence of the target and Si dead layer have been accounted for in the case of the ^{26}Mg. Bottom panel: Widths, σ, associated with the mean values shown in the top panel.

setup. The overall agreement of the dashed line with the low energy component bolsters the conclusion that the low energy component is associated with emission of an α particle.

In the lower panel of Figure 4.7 the trends associated with the widths of the high and low energy components of the total distributions as well as the α gated distributions are shown. The widths of both components of the total distributions increase linearly with $E_{c.m.}$ from 1.8 MeV to 5 MeV in the former case and from 0.8 to 1.6 MeV in the latter case. While the mean values of the α gated distributions are in good agreement with those of the low energy component, the widths of the α gated distributions are systematically slightly larger.

4.3.2 Characterization of the α particles

Having characterized the evaporation residues produced in this reaction, the measured angular distributions of α particles were next examined to ascertain if they exhibit the characteristics of statistical emission from a compound nucleus. The α particles are identified based upon their position in the energy-TOF spectrum. Shown in Figure 4.8 are the α particle angular distributions at two incident energies along with the predictions of the EVAPOR statistical model code normalized to the data. The general trend observed is that the differential yield of α particles, $dN/d\Omega$, decreases slightly with increasing angle. This forward peaking can be understood as being due to the center-of-mass momentum of the compound nucleus. The measured angular distributions are in relatively good agreement with the EVAPOR predictions as evident in the figure.

Having established that the α angular distribution is consistent with statistical decay from the compound nucleus and plays a non-negligible role in the de-excitation of the fusion product, the energy spectra of these emitted particles was directly examined. Shown in Figure 4.9 are the energy distributions of α particles detected in the angular

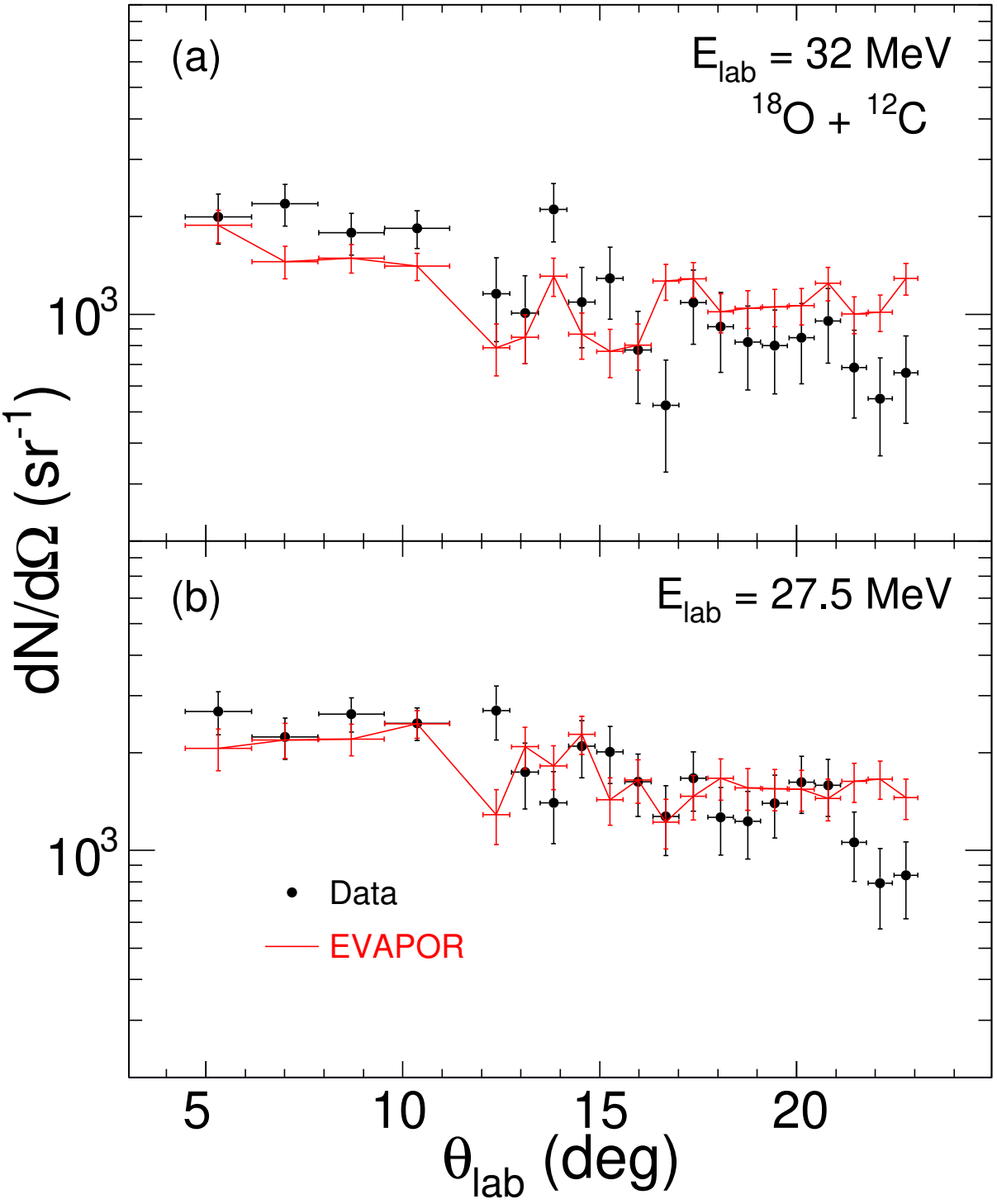

FIGURE 4.8: Angular distributions of α particles in the laboratory frame at E_{lab}=32 MeV and 27.5 MeV. The predictions of the EVAPOR model are indicated as a solid (red) line.

range $4.3^\circ \leq \theta_{\rm lab} \leq 23^\circ$. To facilitate comparison with a statistical model, the energy of the α particle has been transformed into the center-of-mass frame of the system and the resulting distributions are shown in Figure 4.9 along with the EVAPOR predictions. As is evident in the figure, the statistical model provides a reasonably good description of the measured energy distributions of emitted α particles.

In order to make a more quantitative analysis of the measured distributions and provide more detailed comparison with statistical model codes, the first and second moments of the distributions presented in Figure 4.9 were extracted, the dependence of these quantities on $E_{c.m.}$ is examined in Figure 4.10. In the upper panel of Figure 4.10 one observes that $\langle E_{c.m.}(\alpha)\rangle$ increases with increasing incident energy, $E_{c.m.}$, both for the experimental data and the model predictions. For reference, the excitation energy, E^*, of the compound nucleus is displayed on the scale above the top panel. The error bars for the experimental data are defined by the statistics of the measurement. The results of the EVAPOR and PACE4 calculations are presented as the solid and dashed lines respectively. The overall increasing trend of the first moment, $\langle E_{c.m.}(\alpha)\rangle$, observed in the experimental data is reasonably reproduced by both models. EVAPOR is in better agreement with the experimental data than PACE4, which slightly overpredicts $\langle E_{c.m.}(\alpha)\rangle$ at all energies by approximately 0.5 MeV. This deviation between PACE4 and the experimental data increases with increasing $E_{c.m.}$. While for the lower energies the statistical model predictions lie within the statistical uncertainties of the experimental measurement, for the two highest incident energies the statistical uncertainty is less than the deviation between the PACE4 model predictions and the measured values. Presented in the lower panel of Figure 4.10 is the dependence of the second moment of the energy distributions, $\sigma(E_{c.m.}(\alpha))$ on $E_{c.m.}$. The experimental widths increase from 1.2 MeV at the lowest energies to 2.2 MeV at the highest $E_{c.m.}$. In the case of the second moment, good agreement between the PACE4 predictions and the measured widths is observed. In contrast to the PACE4 predictions, EVAPOR predicts slightly lower values for the first moment which

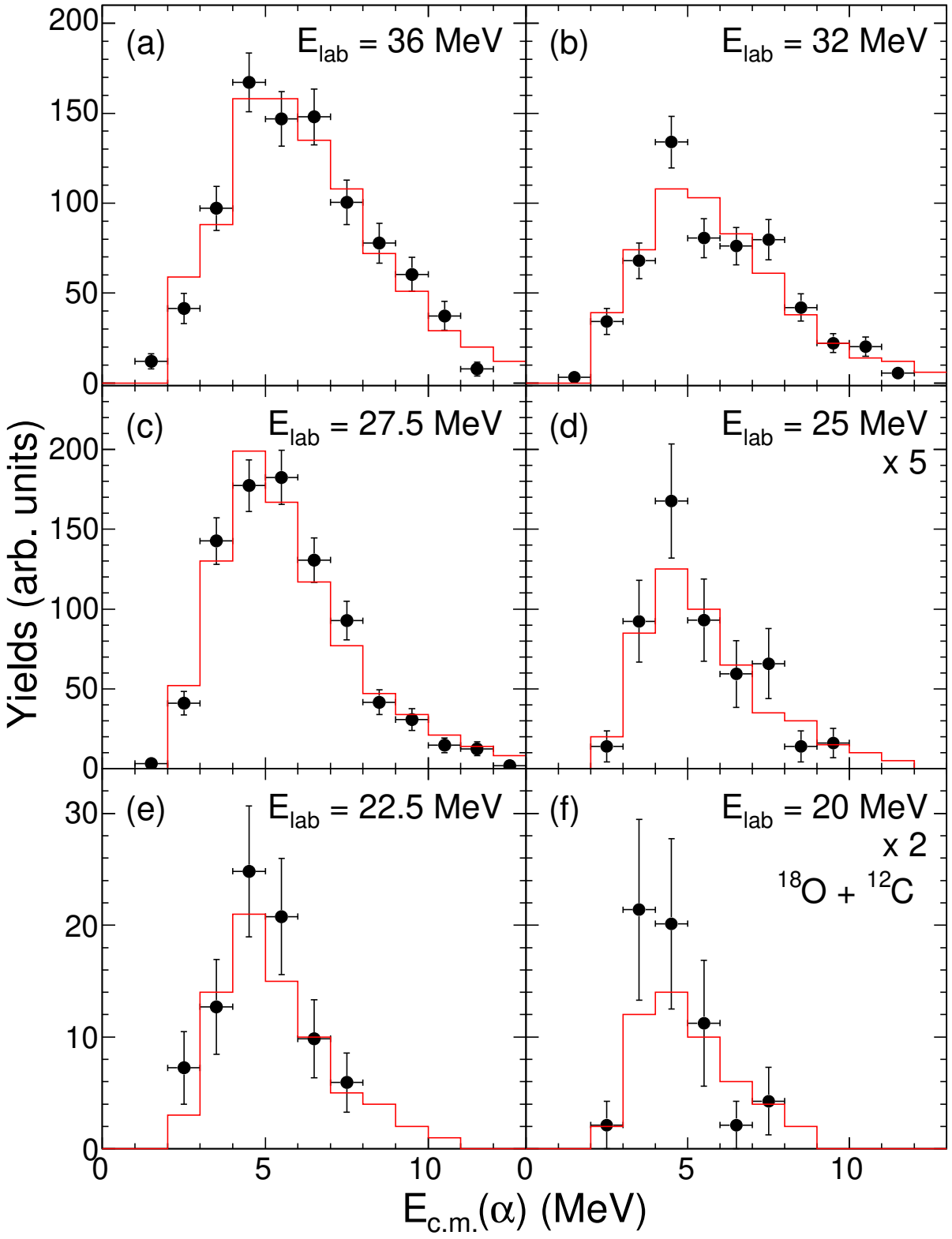

FIGURE 4.9: Energy of α particles in the center-of-mass frame for different bombarding energies. The solid (red) line depicts the prediction of the statistical model code EVAPOR. The predictions have been normalized to the experimental ones in the energy range shown.

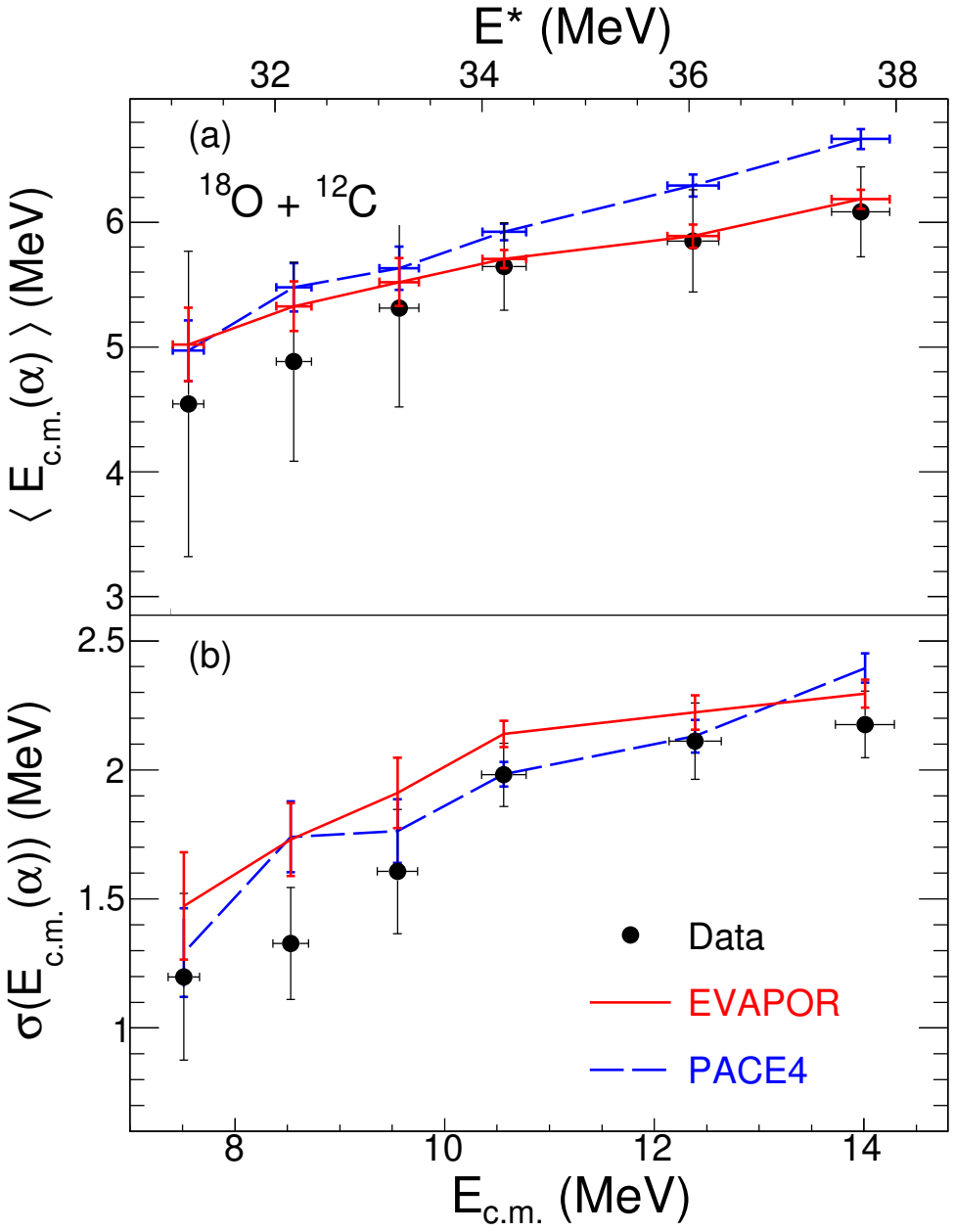

FIGURE 4.10: Top panel: Average energy of α particles in the center-of-mass frame as a function of the available energy in the center-of-mass (solid circle). The solid (red) line represents the average energy predicted by the statistical model code, EVAPOR. The dashed (blue) line represents the average energy predicted by PACE4. Bottom panel: Widths, $\sigma(\mathrm{E_{c.m.}}(\alpha))$, associated with the mean values shown in the top panel.

are in better agreement with the experimental measurement. However, in the case of the second moment EVAPOR slightly overpredicts the experimentally measured values.

In a statistical framework, two factors contribute to the $\langle E_{c.m.}(\alpha)\rangle$ namely the temperature of the emitting nucleus and the Coulomb barrier associated with the α emission. As the second moment is primarily sensitive to the temperature of the emitting system, the larger disagreement of the PACE4 statistical model with the first moment suggests that the Coulomb barrier associated with α emission might be slightly lower than that calculated by the model PACE4. A sensitive probe of the Coulomb barrier is the emission probability of a charged particle. Therefore, the α particle emission cross-section was examined as a function of $E_{c.m.}$, and the results were compared to the predictions of the statistical models.

4.3.3 α particle detection efficiency

In order to extract the α emission cross-section from the measured yields, it is necessary to correct for the efficiency of the experimental setup. To determine the geometric acceptance of the experimental setup the statistical model code EVAPOR was utilized. In the simplest case of isotropic single α particle emission, two factors dominate the geometric efficiency, namely the center-of-mass velocity of the compound nucleus and the energy distribution of the emitted α particle. Emission of additional particles, however, imparts momentum to the evaporation residue which will affect the efficiency. The efficiency determined using the EVAPOR model is shown in Figure 4.11 as a solid (red) line. The efficiency for detection of an α particle in coincidence with an evaporation residue ranges increases from 7.9% at $E_{c.m.}$ = 6.5 MeV to a maximum of 9.8% at $E_{c.m.}$ = 9.5 MeV. A further increase in the incident energy results in a decrease of the efficiency to $\approx$7.8% at $E_{c.m.}$ = 14 MeV. The initial increase can be understood as due to the effect of kinematic focusing.

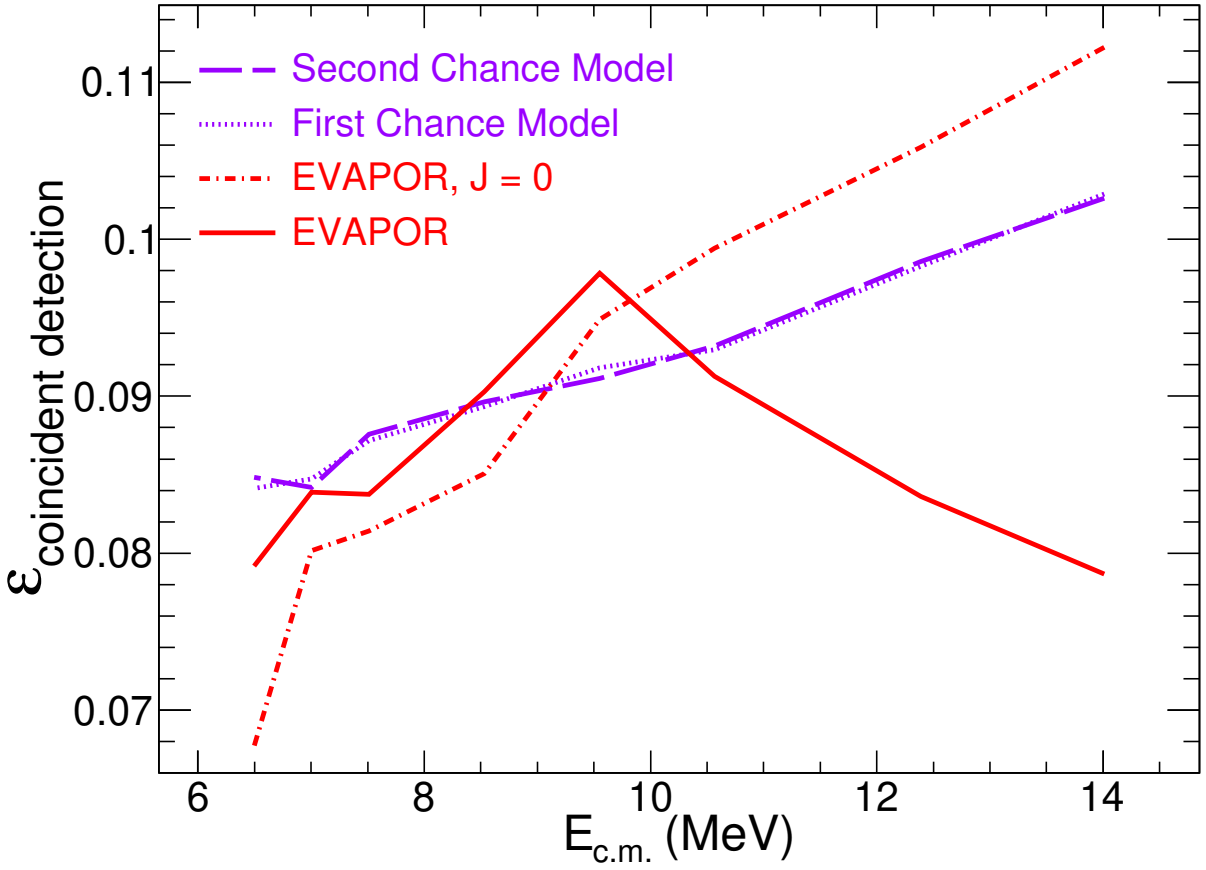

FIGURE 4.11: Efficiency for detection of an α particle in coincidence with an evaporation residue in the experimental setup as determined by the EVAPOR model. Both the α particle and evaporation residue can be detected in either the T2 or T3 silicon detectors. Also shown is the prediction of a zero spin kinematic model described in the text.

To assess the principal factors impacting the efficiency, a simple model was constructed. This model accounted for sequential two-body decays of the compound system, emitting an α particle followed by a neutron (first chance) or a neutron followed by an α particle (second chance). In this model, the compound nucleus, ^{30}Si, travelling with a velocity, v_{CN}, along the beam direction emits the first particle. Isotropic emission is assumed consistent with zero spin. Momentum is conserved between the emitted particle and the resulting evaporation residue. The second particle is then emitted isotropically from the evaporation residue, and momentum is again conserved. The products are then

subjected to the same angular restrictions as the experimental setup. The resulting efficiency is depicted as a dotted line (first chance) and a dashed line (second chance) in Figure 4.11. At the lowest incident energies measured the simple model is in good agreement with the efficiency calculated using EVAPOR. For incident energies $E_{c.m.} > 9.5$ MeV, the simple model and EVAPOR diverge. The divergence of the simple model and EVAPOR may signal the increasing importance of angular momentum which is absent in the simple model. At $E_{c.m.} = 14$ MeV the maximum angular momentum is calculated to be $\approx 10\hbar$. To ascertain if the angular momentum of the compound nucleus was responsible for decrease in efficiency, the efficiency for compound nuclei with zero angular momentum (J=0) was calculated within the EVAPOR model. As can be seen in Figure 4.11 for this case the efficiency increases monotonically with increasing incident energy. As the EVAPOR model includes the competition between different channels as well as the treatment of angular momentum, the efficiency determined using EVAPOR was utilized to extract the α emission cross-section.

4.3.4 Analysis of the α emission cross-sections

Presented in Figure 4.12 is the cross-section for α decay following fusion of the ^{18}O and ^{12}C nuclei. In Figure 4.12 one observes that the cross-section for α decay increases with increasing incident energy with a shape consistent with a barrier emission process. Over the interval measured the α cross-section increases from approximately 2 mb to 700 mb. The total fusion cross-section is also shown for reference. As might be qualitatively expected, at low incident energy, $E_{c.m.}$, only a relatively small fraction of the total fusion cross-section is associated with α decay. As the incident energy increases α decay becomes an increasing fraction of the total fusion cross-section. At the highest energy measured the two cross-sections are almost equal. Also shown for comparison are the predictions

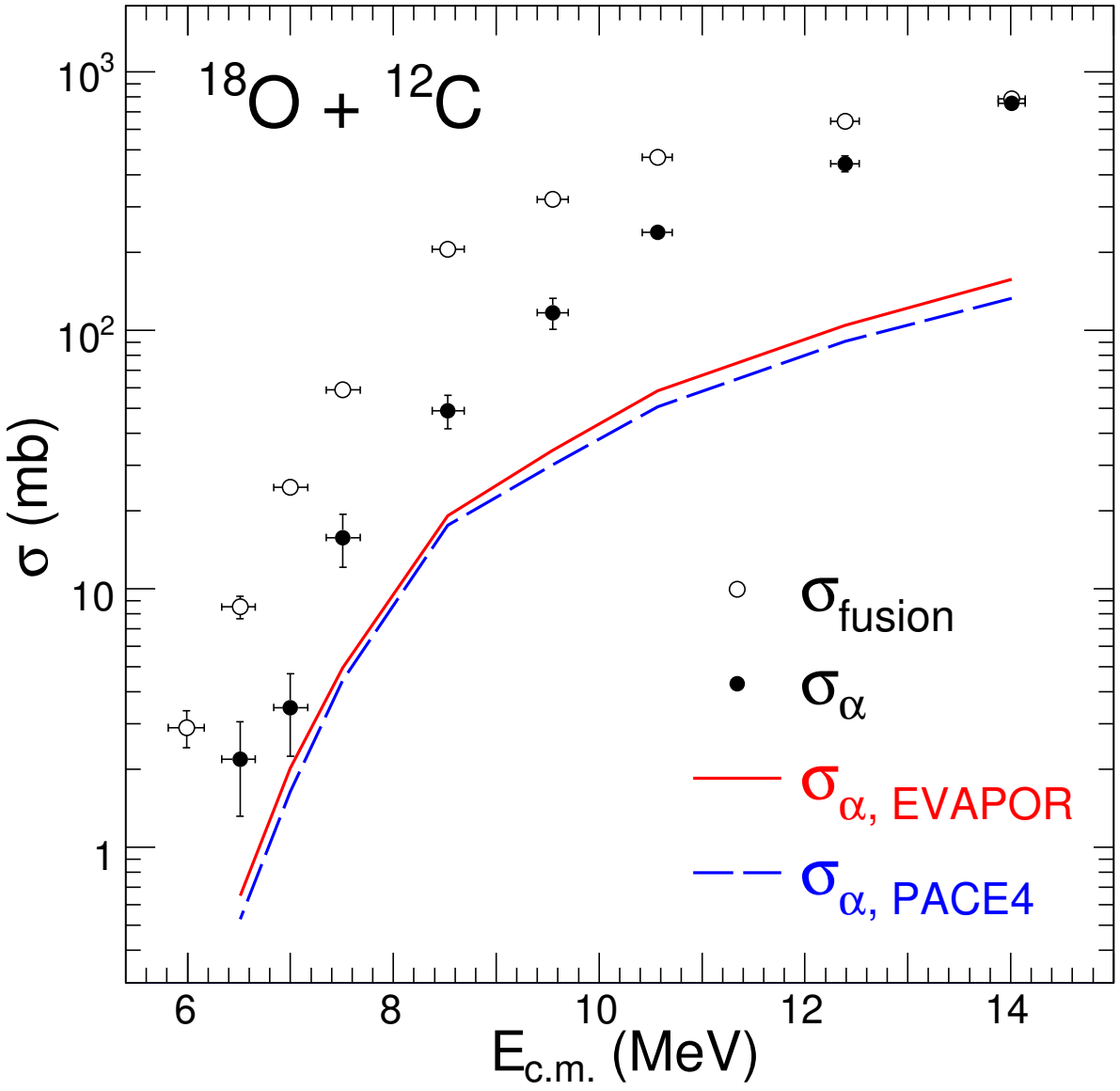

FIGURE 4.12: Comparison of the measured α emission cross-sections (closed symbols) with the statistical model codes EVAPOR (solid red line) and PACE4 (dashed blue line). The total fusion cross-sections are shown as the open symbols.

of the statistical model codes EVAPOR (solid line) and PACE4 (dashed line). The cross-section predicted by the models has been obtained by utilizing the relative probability for all α channels and the experimentally measured total fusion cross-section. While the models exhibit the same qualitative behavior as observed experimentally, both EVAPOR and PACE4 substantially underpredict the experimentally measured cross-sections.

The dramatic increase in the relative cross-section for α emission with excitation energy and the underprediction of the statistical model codes is emphasized in the top panel of Figure 4.13. For the lowest values of $E_{c.m.}$, α emission comprises approximately 25% of the fusion cross-section. This fraction increases rapidly becoming essentially unity by $E_{c.m.} \approx 14$ MeV. Over the same energy interval EVAPOR only predicts an increase in the relative α emission from $\approx 10\%$ to 20%, as shown by the solid line. From Figure 4.12 it is clear that the result for PACE4 would be essentially the same. The discrepancy between the experimental data and the statistical model predictions is twofold. Not only do the statistical model calculations underpredict the magnitude of the relative α particle emission, but they underpredict the rate at which α particle emission increases with $E_{c.m.}$.

While the dramatic increase in the relative α emission cross-section with incident energy and the underprediction of the statistical model codes, evident in Figure 4.13, is remarkable, it should be noted that a hint of this result was already evident in the angular distribution of evaporation residues presented in Figure 4.5. As observation of residues at large laboratory angles is directly related to the emission of an α particle, the failure of the statistical model codes to reproduce the yield of evaporation residues at large angles suggests the underprediction of α emission. Although the energies of the emitted α particles are reasonably reproduced by the statistical model codes and in particular EVAPOR, the models underpredict the measured α cross-section. Moreover, the magnitude of the underprediction increases with increasing incident energy. At the

highest incident energy measured the statistical model code EVAPOR underpredicts the measured α cross-section by a factor of approximately five.

To examine whether this underprediction of α decay by the statistical model is limited to just this reaction or is a more general feature of similar light-ion reactions, the relative α emission fraction for $^{16}O + ^{12}C$ [128, 129] and $^{16}O + ^{13}C$ [130] were examined, and presented in the middle and lower panels of Figure 4.13 respectively. Juxtaposed with the experimental data are the corresponding predictions by the EVAPOR model. In all cases the statistical model clearly underpredicts the experimental data indicating that the underprediction of α decay is a more general feature of light-ion fusion reactions.

In comparing the experimental data in Figure 4.13 with the EVAPOR predictions, two features are evident. The first feature is the observation of an enhanced α emission at the lowest incident energies. This feature is observed for all of the three systems examined. It should be noted that the α fraction for $^{18}O + ^{12}C$ at low $E_{c.m.}$ is approximately 25%, significantly less than the 40% observed for the $^{16}O + ^{12,13}C$ reactions. The second feature is the increase in the α fraction with increasing incident energy. While the experimental data in $^{18}O + ^{12}C$ manifests a stronger dependence as compared to the statistical model code, the dependence in $^{16}O + ^{13}C$ is similar in magnitude to the model predictions. The dependence for the experimental data in $^{16}O + ^{12}C$ appears to be slightly stronger than the model predictions. The comparison for the $^{16}O + ^{12}C$ system is complicated by the fact that two different datasets have been utilized to span the energy range of interest.

One can gain insight into understanding these two features of the offset and slope of the relative α cross-section by examining the EVAPOR predictions for the three systems shown. In all three cases, at low $E_{c.m.}$ EVAPOR predicts α decay to be between 8% and 15%. Initially, this fraction does not exhibit a strong dependence on incident energy. For larger $E_{c.m.}$, a stronger dependence of the relative α emission probability is observed.

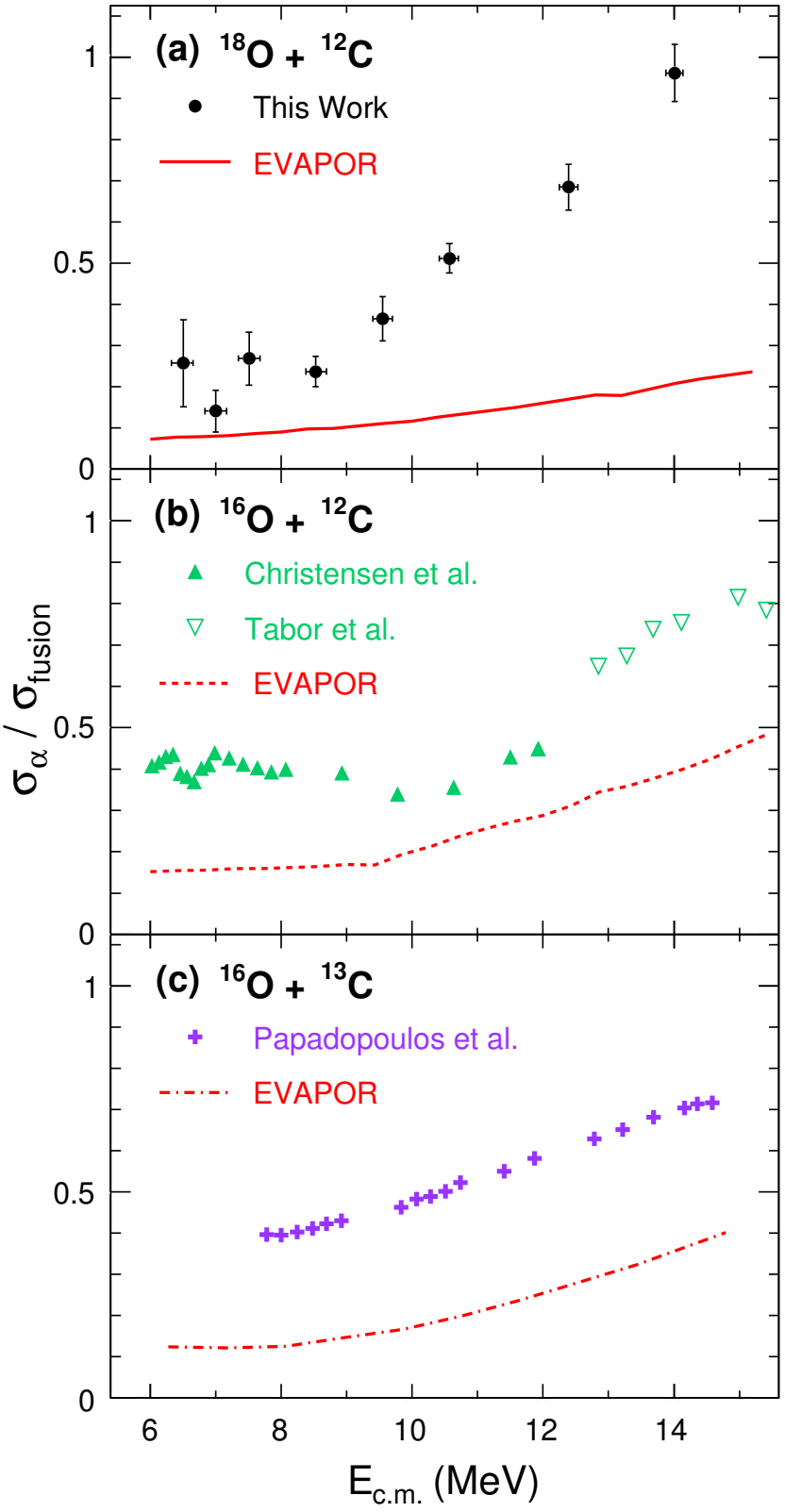

FIGURE 4.13: Dependence of the relative α emission cross-section on $E_{c.m.}$ for several O + C systems (Literature data are taken from Christensen [128], Tabor [129], and Papadopoulos [130]).

Within this context, the underprediction of the α decay for all systems shown at low $E_{c.m.}$ is noteworthy. The α cluster structure of nuclei such as ^{12}C and ^{16}O is well established. Even for the neutron-rich nucleus ^{18}O significant experimental evidence for an α cluster structure exists [124, 125]. Comparison of the measured relative α cross-section at low $E_{c.m.}$ for $^{18}O + ^{12}C$, $^{16}O + ^{12}C$, and $^{16}O + ^{13}C$ indicates that the α cluster structure of the initial projectile and target nuclei influences the α emission following fusion. The lower α emission probability for the ^{18}O induced reaction as compared to the ^{16}O induced reactions at low $E_{c.m.}$ is in agreement with a weaker α cluster nature for ^{18}O relative to ^{16}O. When these data are compared to the statistical model code, EVAPOR, one observes that the data exhibits a marked enhancement in α emission as compared to the model. This enhancement is consistent with the α cluster structure in the entrance channel surviving the fusion process and influencing the decay of the compound nucleus. The larger deviation for relative α emission as compared to the EVAPOR calculations in the case of the ^{18}O induced reaction suggests that neutron emission is overemphasized in the statistical model code as compared to α emission.

Chapter 5

^{19}O,^{17}F + ^{12}C: Initial Radioactive Beam Measurements

5.1 Beam production

When performing an experiment involving a short-lived radioactive isotope, the decay of the isotope presents a challenge. To overcome this challenge, the radioactive isotopes can be created in-flight via a nuclear reaction. This chapter describes the fusion of ^{19}O and ^{17}F ions with ^{12}C target nuclei. The isotopes ^{19}O and ^{17}F have half-lives of 26.9 seconds and 64.5 seconds respectively, and were each produced by a nuclear reaction using a primary beam of stable oxygen ions directly on their production. The experiments were carried out at the John D. Fox Accelerator Facility at Florida State University, using the RESOLUT spectrometer.

To produce ^{19}O, a primary beam of $^{18}O^{7+}$ ions was accelerated first through a 9 MV tandem Van de Graaf accelerator, then through a four cavity linac up to an energy of 80.7 MeV. The fully accelerated beam was incident on the production target, a gas cell filled with D_2 gas at a pressure of 350 torr and cooled to a temperature of 77 K. The ^{19}O ions were produced via the ^{18}O(d,p) reaction, and were separated from both unreacted beam as well as other reaction products by mass/charge selection using the RESOLUT spectrometer [131]. Upon exiting the RESOLUT spectrometer, the $^{19}O^{7+}$ beam was focused into the target chamber with an energy of 59.6 MeV.

For the ^{17}F experiment, a primary beam of $^{16}O^{8+}$ bombarded the D_2 target to produce ^{17}F via the ^{16}O(d,n) reaction. The product ^{17}F was separated from unreacted beam using RESOLUT as previously described, and the resulting ^{17}F beam was focused into the target chamber with an energy of 55.4 MeV. In the following two sections, discussion of the measurement and analysis will focus on the ^{19}O experiment, but a similar analysis has been performed for the ^{17}F experiment.

5.2 Measurement

The setup used to measure fusion of oxygen ions with carbon nuclei in this experiment is depicted in Figure 5.1. After exiting the RESOLUT spectrometer, particles traverse a thin foil (0.5 μm thick aluminized mylar) ejecting electrons in the process. These electrons are accelerated and bent out of the beam path and onto the surface of a microchannel plate detector ($MCP_{RESOLUT}$) where they are amplified to produce a fast timing signal. After traversing the thin foil of $MCP_{RESOLUT}$, the oxygen ions passed through a compact ionization detector (CID) located approximately 3.5 m downstream of $MCP_{RESOLUT}$. In passing through this ionization chamber, ions deposit an energy (ΔE) characterized by their atomic number (Z), mass number (A), and incident energy. After exiting CID the ions are incident on a 105 $\mu g/cm^2$ carbon foil. This carbon foil serves both as a secondary electron emission foil for the target microchannel plate detector (MCP_{TGT}) and as the target for the fusion experiment [99].

The RESOLUT facility has previously produced a beam of ^{19}O with an intensity of 5×10^4 p/s at an energy of 5 MeV/A [131, 132], which is too high for the near-barrier energies explored in the present experiment. However, the cross-section to produce ^{19}O dramatically decreases as the incident energy of the beam decreases. In order to produce a beam with a sufficient rate of ^{19}O ions for this experiment, the energy of the beam was lowered to a minimum value of 3 MeV/A, and thus required the use of a degrader

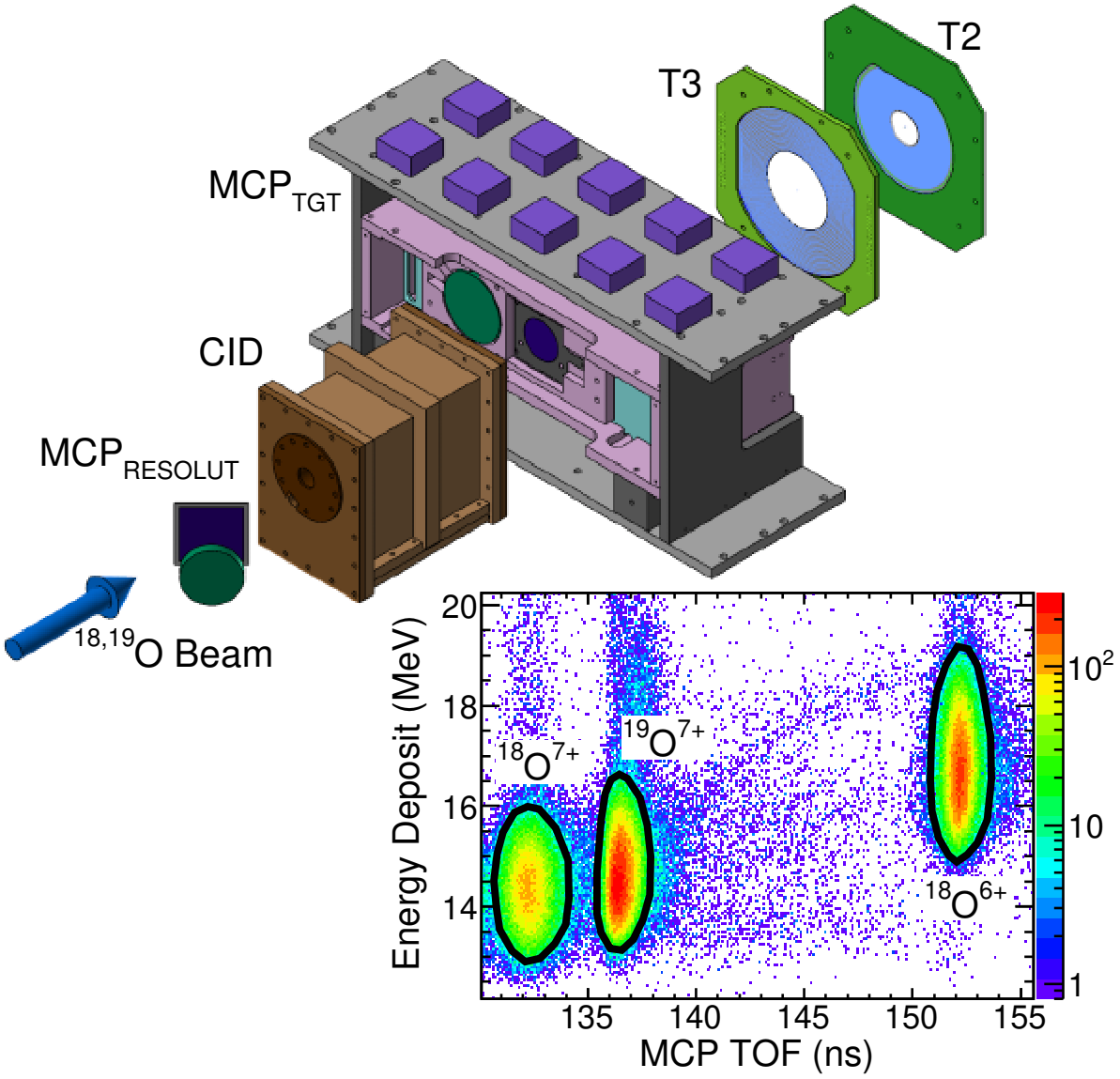

FIGURE 5.1: Schematic illustration of the experimental setup. The $\mathrm{MCP_{RESOLUT}}$ detector is located approximately 3.5 m upstream of the compact ionization chamber (CID) which is situated directly in front of the $\mathrm{MCP_{TGT}}$ detector. Evaporation residues are detected in the annular silicon detectors designated T2 and T3. Inset: Energy deposit versus time-of-flight spectrum for ions exiting RESOLUT that are incident on ^{12}C target at $\mathrm{E_{lab}}$=46.7 MeV. Color is used to represent yield in the two-dimensional spectrum.

to further lower the beam to the desired energies, which was accomplished with CID. In order to adjust the energy of the beam incident on the target the pressure in CID was adjusted. As the gas pressure in CID can be well controlled it provides a much more uniform degrader than a solid foil, which allows for a more precise determination of the beam energy on target. Periodic insertion of a silicon surface barrier detector (SBD) directly into the beam path just prior to the target provided a measurement of the energy distribution of ^{19}O and ^{18}O ions incident on the target. The width, σ, of the energy distribution for ^{19}O ions was between 400-500 keV and was principally determined by straggling in the deuterium gas cell, not CID. All the excitation functions have been corrected for the width of the energy distribution.

By utilizing the timing signals from both of the microchannel plate detectors together with the energy deposit in the ionization chamber, a ΔE-TOF measurement was performed. This measurement allowed for the identification of ions in the beam as indicated in the inset of Figure 5.1. Clearly evident in the figure are three peaks associated with $^{19}O^{7+}$ ions, $^{18}O^{7+}$ ions, and $^{18}O^{6+}$ ions. The cleanly identified ^{19}O ions corresponded to approximately 31 % of the beam intensity with the $^{18}O^{7+}$ and $^{18}O^{6+}$ corresponding to approximately 20 % and 29 % respectively. The simultaneous measurement of ^{18}O provides a benchmark measurement to compare to the high precision measurement from the experiment discussed in the previous chapter, which provides confidence in the ^{19}O measurement. The intensity of the ^{19}O beam incident on the target was 1.5 - 4 x 10^3 ions/s. Fusion of a ^{19}O (or ^{18}O) nucleus in the beam together with a ^{12}C nucleus in the target foil results in the production of an excited ^{31}Si (or correspondingly ^{30}Si) nucleus. For collisions near the Coulomb barrier the excitation of the fusion product is relatively modest, $E^* \approx 35$ MeV. This fusion product de-excites by evaporation of a few neutrons, protons, and α particles resulting in an evaporation residue (ER). Statistical model calculations [110] indicate that for a ^{31}Si compound nucleus, the nuclei ^{30}Si, ^{29}Si, ^{28}Si, ^{29}Al, ^{28}Al, ^{27}Mg, and ^{26}Mg account for the bulk of the ERs. Emission of the light particles

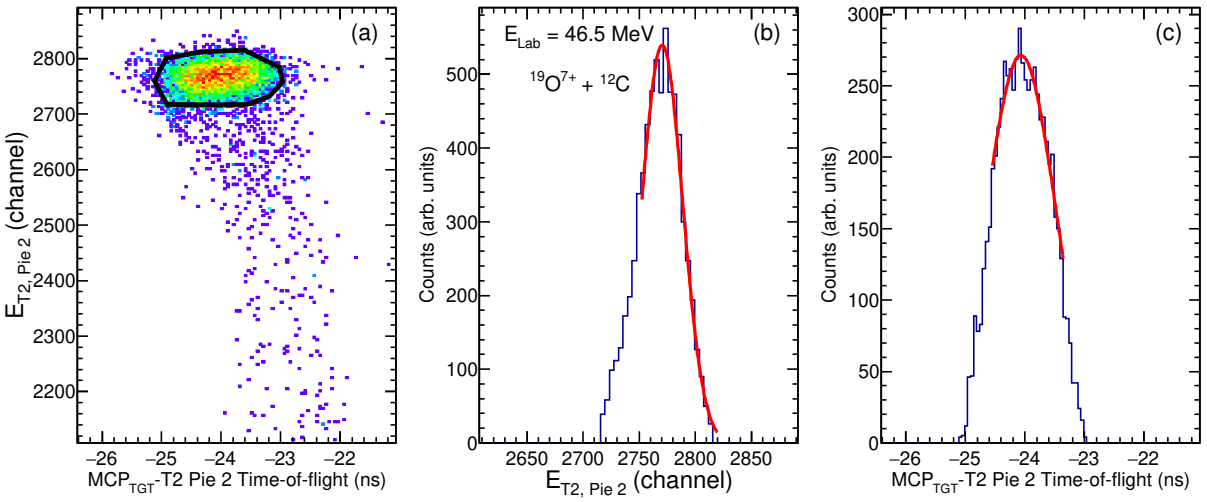

FIGURE 5.2: Panel (a): Raw ETOF spectrum zoomed in on the elastic peak of a representative pie segment in T2. The gate drawn around the peak denotes the boundaries used for the one-dimensional projections. Panel (b): Projection of the elastic peak onto the energy axis. Panel (c): Projection of the elastic peak onto the time axis.

deflects the ER from the beam direction due to momentum conservation allowing its detection and identification using two annular silicon detectors designated T2 and T3 that subtend the angular range $3.5° < \theta_{lab} < 25°$. Evaporation residues are distinguished from scattered beam, as well as emitted light particles, by measuring their time-of-flight between the $\mathrm{MCP_{TGT}}$ detector and the silicon detectors [101] together with the energy deposit in the Si detector. Using the measured energy deposit and the time-of-flight (ETOF), the mass of the ion is calculated allowing ERs to be cleanly distinguished from the incident beam [90, 99].

5.3 Analysis

5.3.1 Silicon detector calibration

In order to identify fusion evaporation residues in the resulting ETOF spectra, each segment of the annular silicon detectors was calibrated in energy and time. The elastic

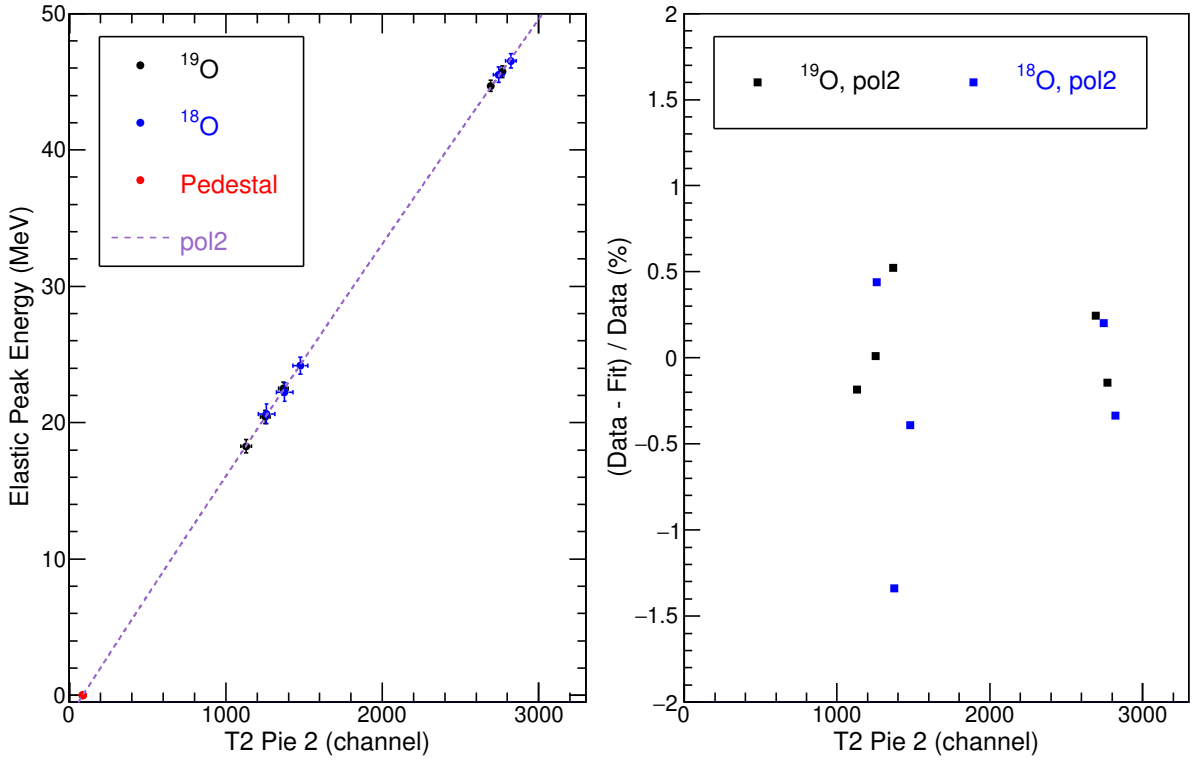

FIGURE 5.3: Panel (a): Calibration curve for a representative pie segment in T2. The blue circles represent the energies of the elastic peaks for $^{18}O^{7+}$, the red circles represent the incident $^{19}O^{7+}$ ions, and the red circle denotes the ADC pedestal. A second-order polynomial fit is shown as the purple dashed line. Panel (b): Deviations of the data points from the calibration fit.

scattering peak for each beam energy was used in the calibration, along with the pedestal (DC offset corresponding to zero energy) of the analog-to-digital converter (ADC). The energy of the elastic peak was determined by directly measuring the energy of the incident beam in the SBD just upstream of the target, and calculating the energy loss of the beam through the target foil and dead layer of the silicon detector using the energy loss program SRIM [127]. The raw elastic peak information was extracted by first gating on the elastic peak of the raw ETOF spectrum, and then projecting the peak onto the energy and time axes as shown in Figure 5.2. The one-dimensional projections were then fit with a Gaussian to extract the mean channel and time, as well as the widths of the distributions. The resultant calibration curve is shown in Figure 5.3a. The data points are well described

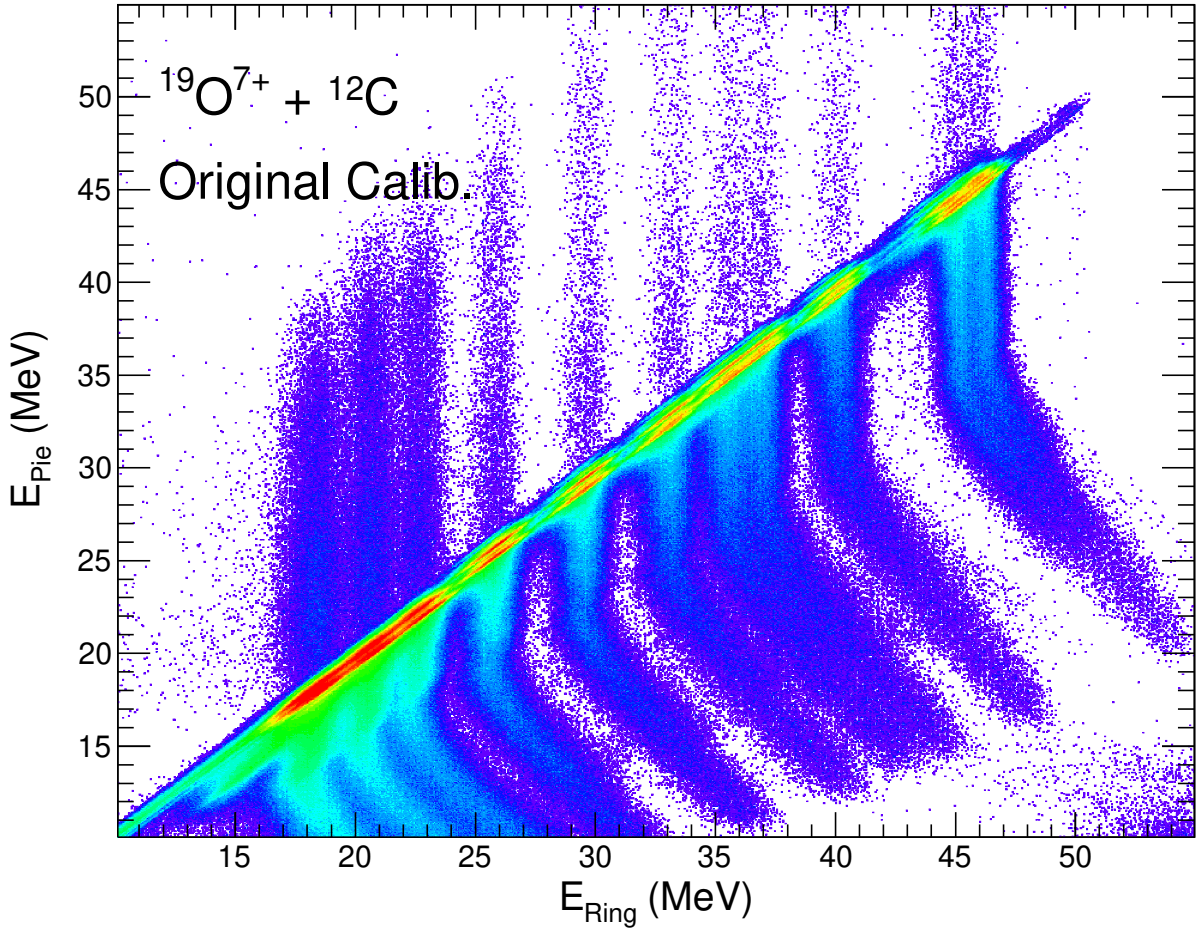

FIGURE 5.4: Calibrated pie energy versus calibrated ring energy for ^{19}O + ^{12}C.

by a second-order polynomial, and all of the points lie within 2% of the fit, which can be seen in Figure 5.3b.

In the initial analysis of the data from this experiment used to produce the published cross-sections [133], the ring segments were calibrated in the same manner: the elastic peak time and channel information was extracted, the beam energy was calculated, and a calibration curve was produced. However, the differential cross-section for elastic scattering drops significantly with increasing angle, so the statistical quality of the elastic peak in the outer ring segments was poor. Since the pie segments and ring segments collect the electrons and holes respectively from an ionization event, and the number of electrons and holes produced are each proportional to the deposited energy, both the pies and the

rings independently measure deposited energy. Consequently, the energy measured by both electrons and holes must be equal. A plot of the calibrated energy measured in the pies versus the calibrated energy measured in the rings should display a 1:1 correlated line. The expected correlation between pie and ring energy is observed in Figure 5.4. Two main features are observed in the plot. Although an overall band is observed along a 45° line, the ±1 MeV band has sub-structure and is seemingly composed of several narrower lines. In addition, one observes bands extending vertically above and below the intense correlated line. The lower bands correspond to incomplete charge collection in the pies or rings. Incomplete charge collection can occur when the charge accumulated on a ring or pie segment is shared with an adjacent ring or pie segment due to imperfect isolation of adjacent pies or rings [134]. The upper bands, in contrast, likely correspond to pileup of signals on a pie. The larger area of a pie, coupled with the fact that they extend to small angles, increases the likelihood that this happens as compared to rings. While the outer rings on the detector are comparable in area to a pie segment, they are not situated at small angles and thus are not subject to as high a rate of elastic scattering. In order to mitigate the influence of pileup and incomplete charge collection, it was required that the energy measured in both the pies and the rings are the same within ±1 MeV, that is, they lie along the correlated band. If the correlated band can be narrowed, a tighter requirement can be applied, reducing these effects even more. Gating on different rings reveals each of the narrow correlated lines belongs to a specific ring, indicating a mismatch in the calibration of the ring segments with the pie segments.

To produce a better calibration of the rings, each ring segment can be calibrated independently using the pie energy calibration. Since the energy measured in the pies should be the same as the energy measured in the rings, plotting the calibrated pie energy for all events as a function of the raw ring channel number provides a calibration to energy for the ring segments, as shown in Figure 5.5. By using this method to calibrate the ring segments, more data than just the elastic peaks can be used. The advantage

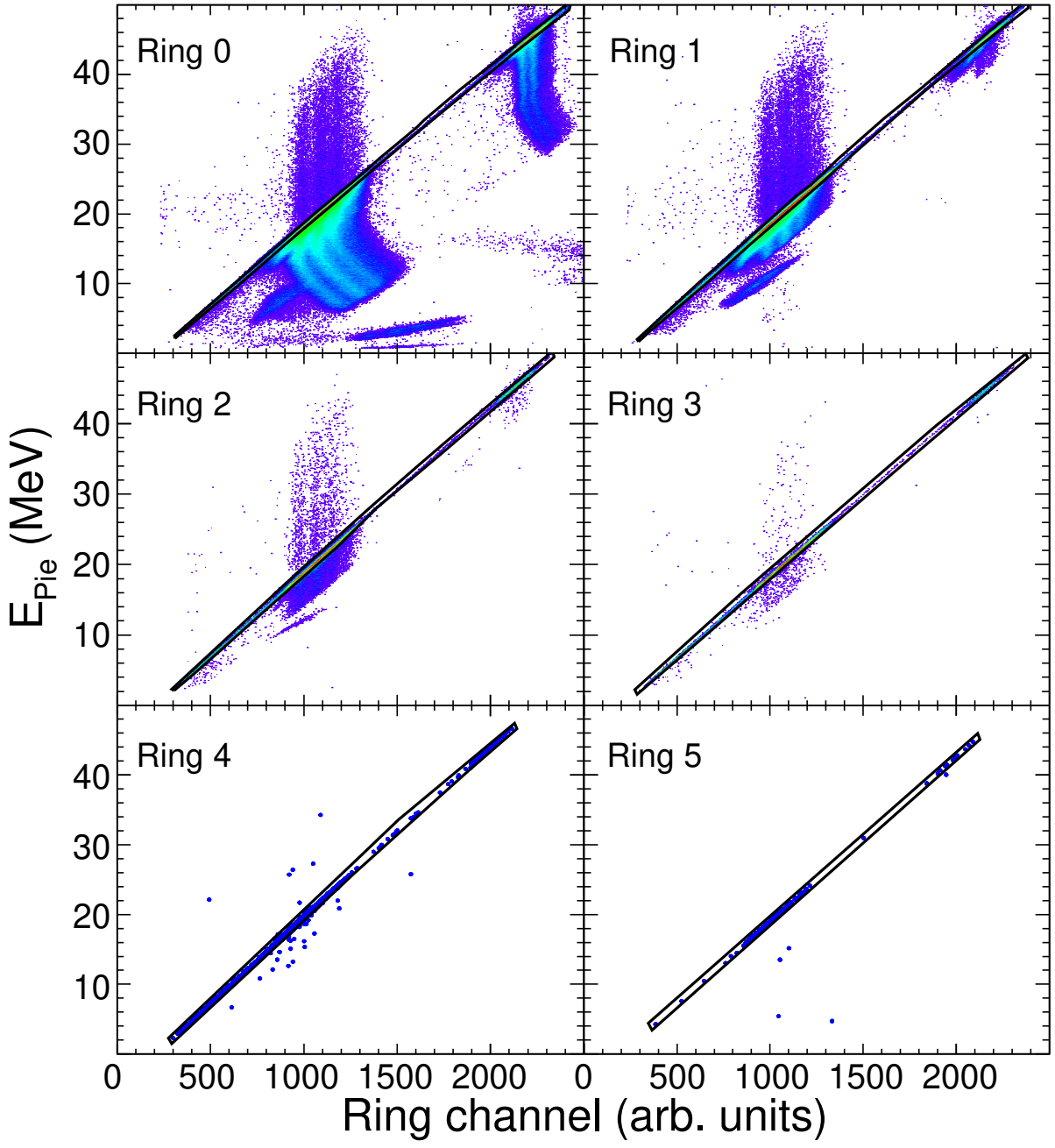

FIGURE 5.5: Calibrated energy measured in the pie segments versus the raw ring channel number for the ring segments in one quadrant of the detector. The correlated band used for the calibration curve is delineated by the area enclosed in black, and the second-order polynomial fit is represented as the solid red line.

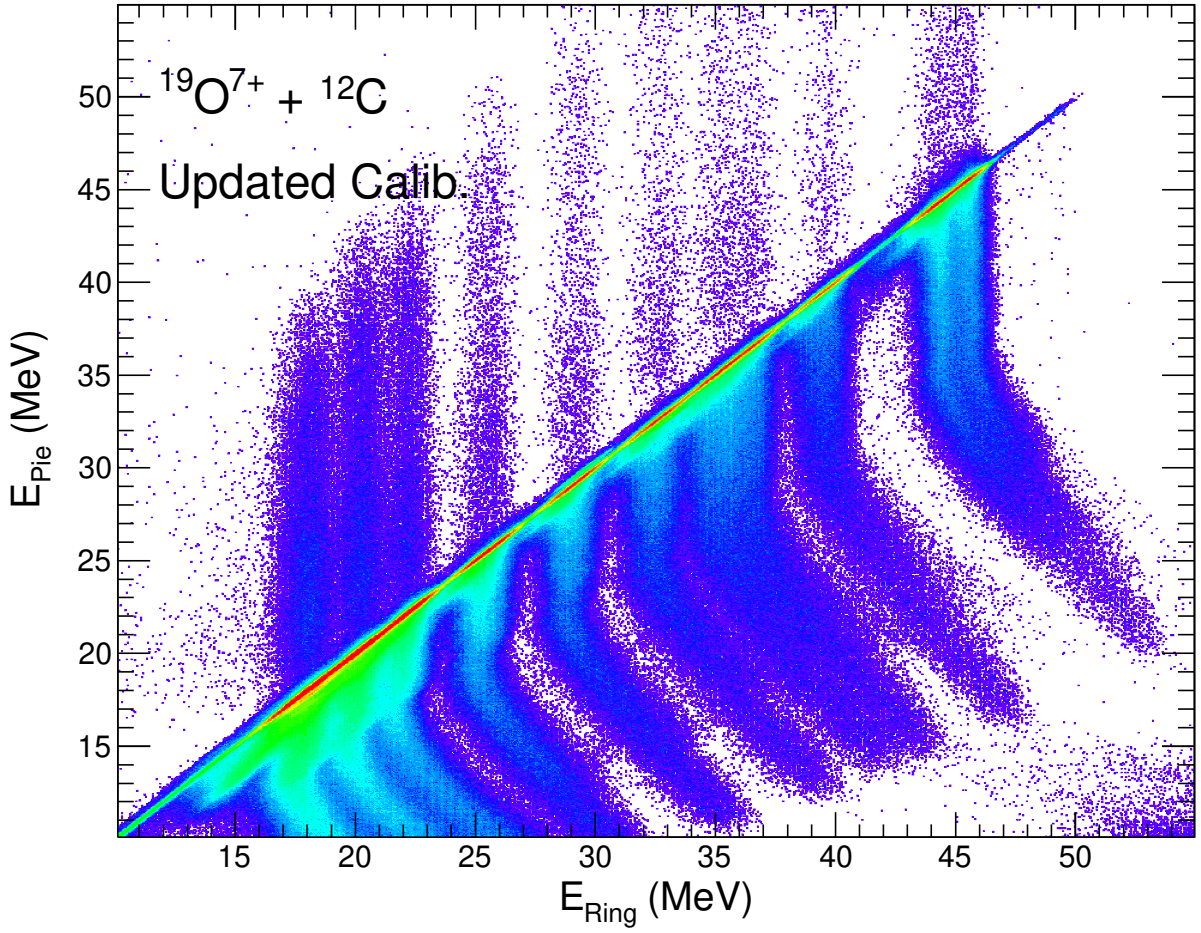

FIGURE 5.6: Calibrated pie energy versus calibrated ring energy for ^{19}O + ^{12}C, with updated calibration of the rings.

of this approach is most evident for Ring 4 and Ring 5, where elastic data is scarce. Figure 5.6 shows the calibrated pie energy versus ring energy using this new calibration. The correlated band is much narrower than the previous calibration, and falls within ±0.25 MeV.

5.3.2 Producing the ETOF spectra

In addition to calibrating the detectors, selection criteria are applied in order to produce useful ETOF spectra. The first criterion is selection on the appropriate isotope incident on the target, as demonstrated in the inset of Figure 5.1. As discussed in the

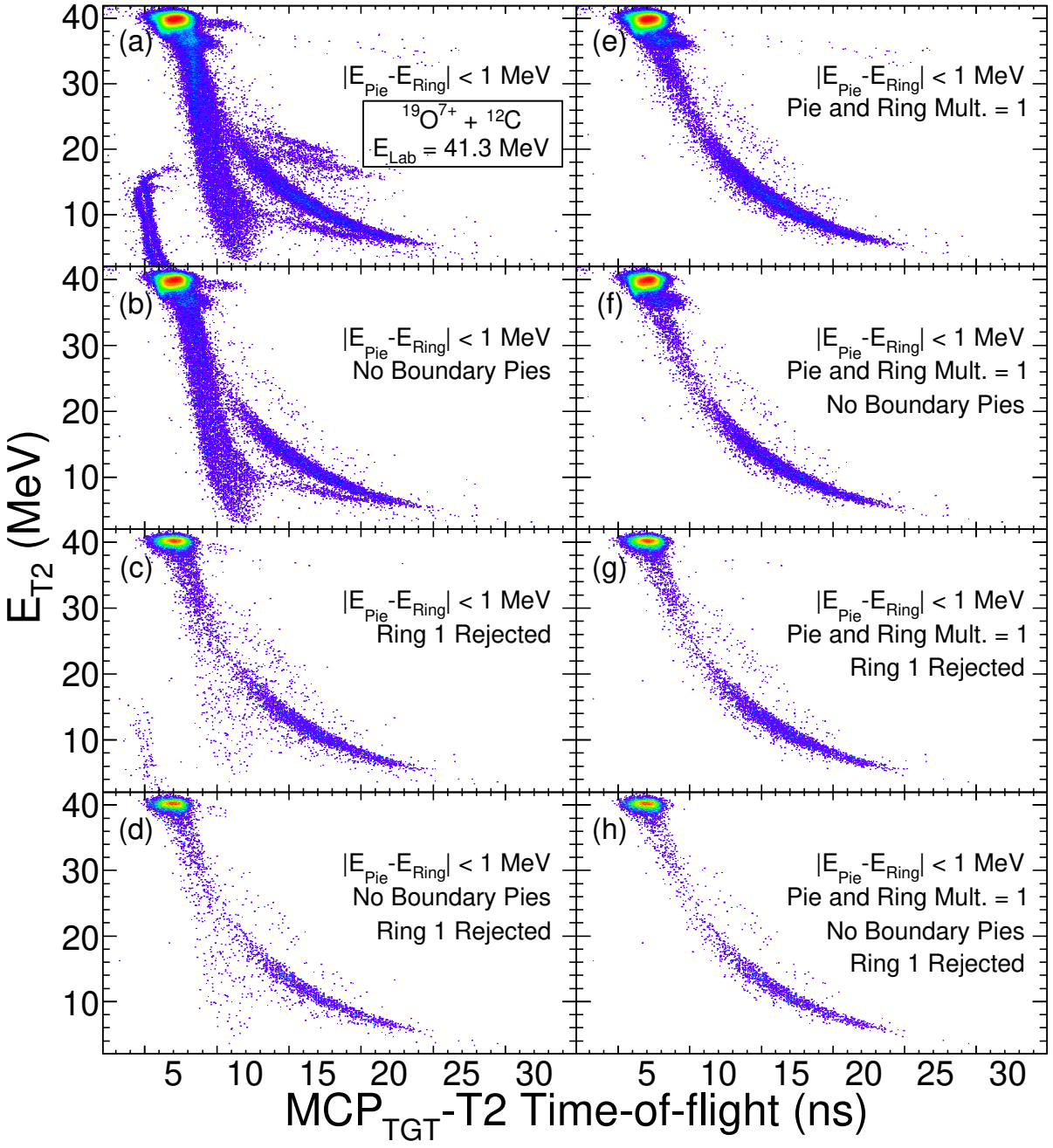

FIGURE 5.7: ETOF spectra for ^{19}O + ^{12}C with different conditional requirements. See text for details.

previous section, following calibration of the pie and ring segments it was required that the energy of a particle measured in both the pie and rings segments be the same within 1 MeV. When the calibration of the rings was improved, this requirement was subsequently tightened to ±0.25 MeV. Events in the innermost ring (Ring 0) were also rejected, since this ring is at the edge of the detector and is consequently subjected to a non-uniform field which results in abberant timing signals.

Figure 5.7(a) depicts the ETOF spectrum with these minimum requirements. There are a number of features in this spectrum, some of which are artifacts that obscure the useable data. The intense crescent band below 22 MeV extending from 10 ns to 25 ns corresponds to scattered beam particles, and represents mass A=19. The heavier evaporation residues should appear to the right of this band; however, the residue island is obscured by two bands at 15 MeV $< E_{T2} \leq$ 22 MeV. The four pairs of pie segments located at the boundary of each ring quadrant are responsible for these bands, as well as the vertical low energy bands at approximately 5 ns and the horizontal haze coming from the elastic peak around 35 MeV. When a particle is incident on a pie segment near the interstrip between segments, the ionization trail can be collected in both the incident pie and the adjacent pie. The field across the detector is also not as well defined at the interstrip between ring quadrants, which affects the timing signals. Rejecting events measured in the eight pie segments at the quadrant boundaries eliminates these artifacts, which is shown in panel (b).

The residue island is visible when the boundary pies are rejected, but there are other artifacts that might artificially contribute yield in the region of interest populated by the ERs, namely the vertical band extending directly down from the elastic peak and the secondary peak just below the elastic. The innermost rings experience the highest count rates due to the angular distribution of the elastic scattering, so Ring 1 was rejected to see if the high count rate and subsequent radiation damage contribute to the noise in the

detector. This condition is shown in panel (c) with all of the pie segments, and panel (d) without the boundary pies. The peak under the elastic is eliminated, and the intensity of other features in the spectra are reduced since Ring 1 contains a large fraction of the events.

The vertical band extending down from the elastic and the haze to the left of the scatter line are primarily due to charge sharing; that is, the total charge of an ionization event is split between two adjacent pie or ring segments. To reduce artifacts introduced by charge sharing, a condition was imposed to require that only one pie and one ring have any significant energy (>0.75 MeV), and that only one timing signal is measured. This condition is shown in the panels on the right of Figure 5.7, which eliminates the charge sharing effect.

5.3.3 Identifying evaporation residues

With the low beam rate of only approximately 2000 ions per second, the number of detected evaporation residues is small. It is therefore extremely important to make as clean a separation between the residue island and the scatter line as possible. Since the separation in energy and time-of-flight is a result of the different masses of the residues and beam particles, a sharp cut can be made at a specific mass. This is best accomplished by transforming the ETOF into a space where the particle mass is a coordinate. Figure 5.8 depicts the transformation of the data presented in Figure 5.7(h) into an energy versus mass space. As expected, the elastic peak and scatter line are centered on mass A=19, with a width of approximately ±3 mass units. The residue island is depicted as the black points to the right of the scatter line, enclosed in a red dotted box. To establish the boundaries in energy for the box, EVAPOR calculations were performed and the highest and lowest energies of an evaporation residue were calculated. No data in Figure 5.8 is observed close to those limits. The mass limits were chosen from a projection of the

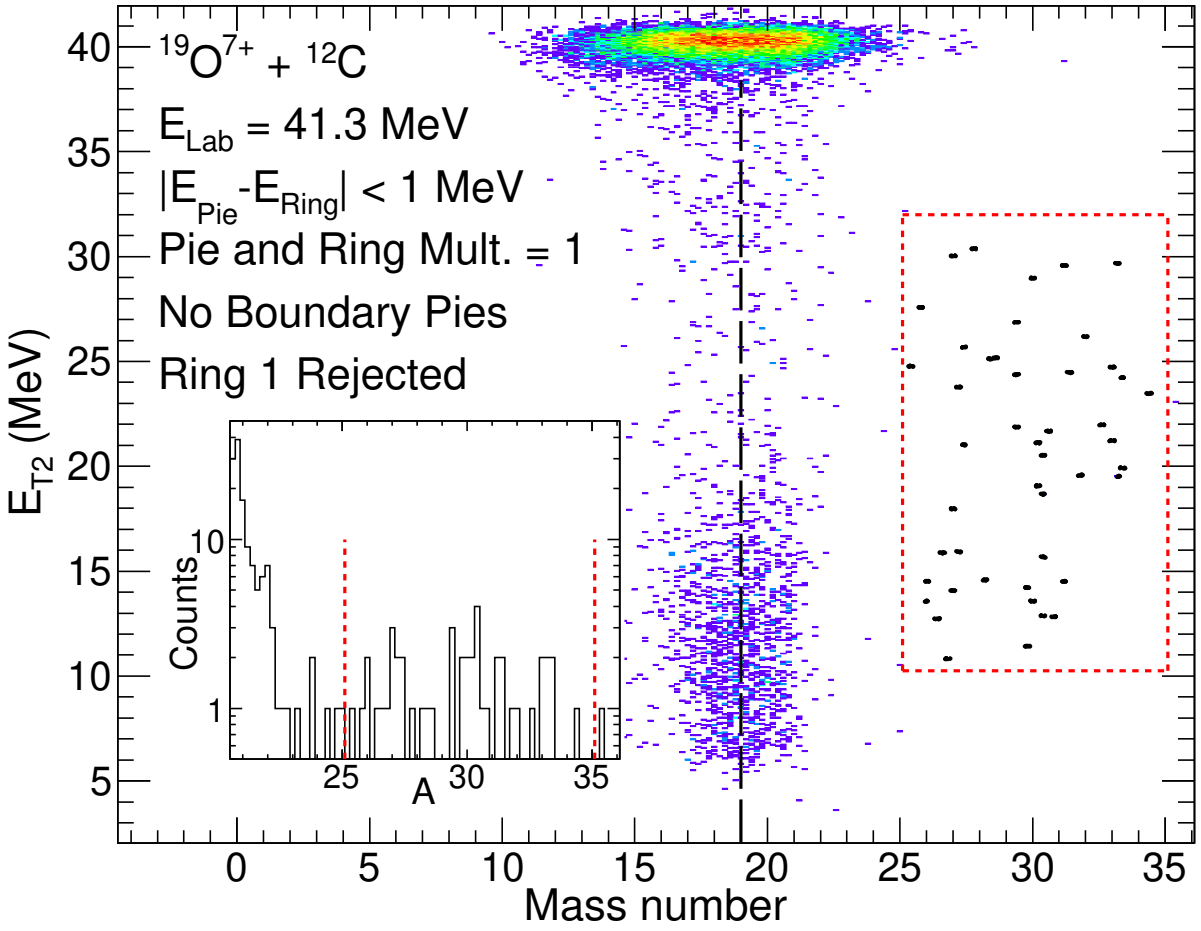

FIGURE 5.8: Energy vs. mass number for ^{19}O + ^{12}C with conditional requirements described in the text. The dashed black line represents the mass of the beam (A=19), the black points enclosed in the red dashed box correspond to evaporation residues, and the inset shows the projection of the spectrum onto the mass axis for energies between the upper and lower energy bounds of the red dashed box.

spectrum onto the mass axis between the upper and lower energy limits, which is shown in the inset of Figure 5.8. There are two distinct peaks belonging to the scatter line at low mass and the residue island at high mass with a clear separation between the two peaks. The mass limits around the residue peak are shown as the red dashed lines in the inset.

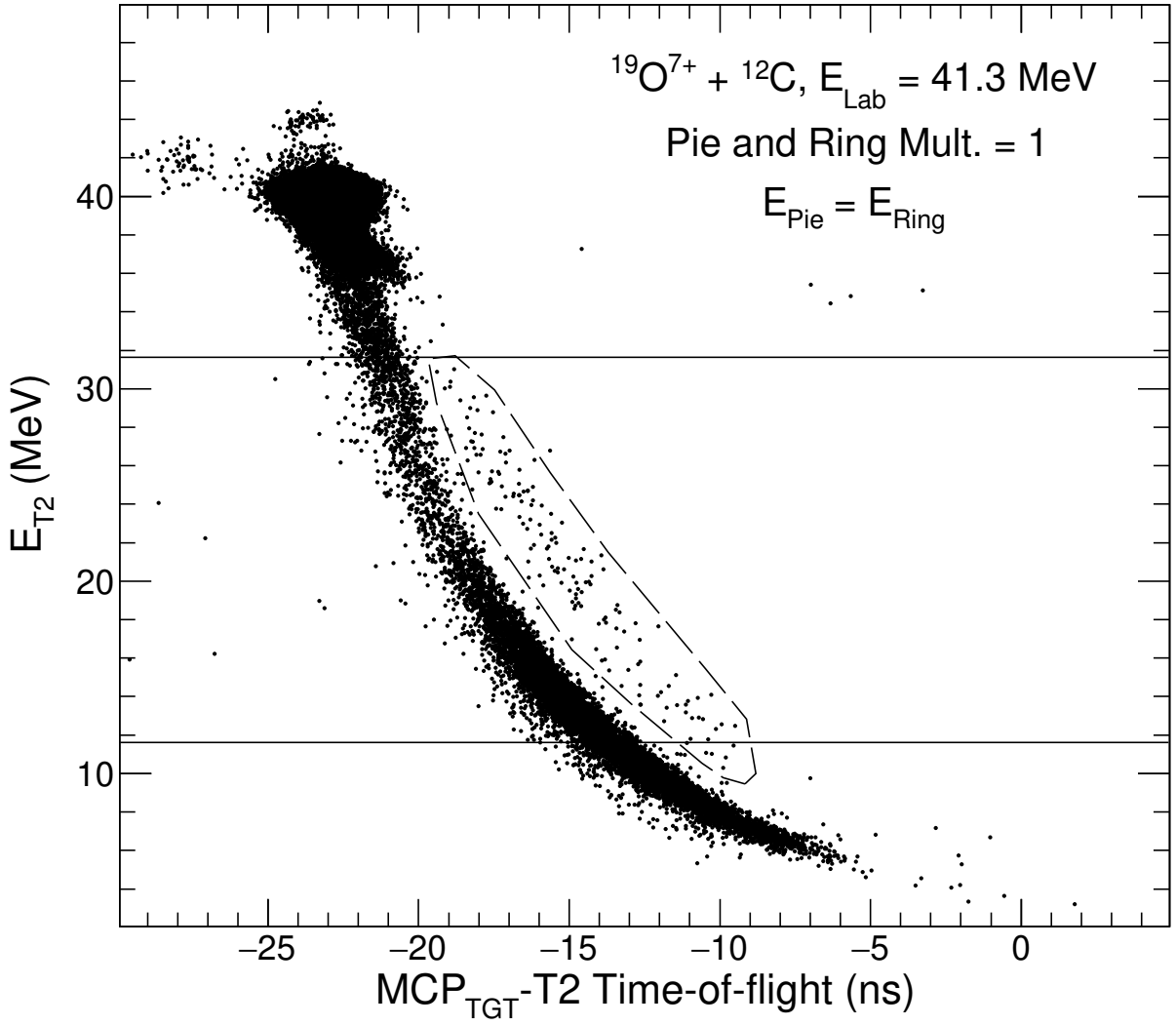

FIGURE 5.9: ETOF spectra for ^{19}O + ^{12}C using the updated narrow ring calibration in Figure 5.6. The solid horizontal lines represent predicted upper and lower energy limits calculated with EVAPOR. The dashed gate encloses the residue island.

5.3.4 Recovering detector segments

Achieving the cleanest spectra for identifying evaporation residues required rejecting data in half of the pie segments as well as Ring 0 and Ring 1. Under the selection criteria presented, the number of ERs at a given energy is typically 100 or less. This resulted in a cross-section measurement with a statistical uncertainty of approximately 10%. Using the updated calibration in Figure 5.6, the restrictions to produce a clean

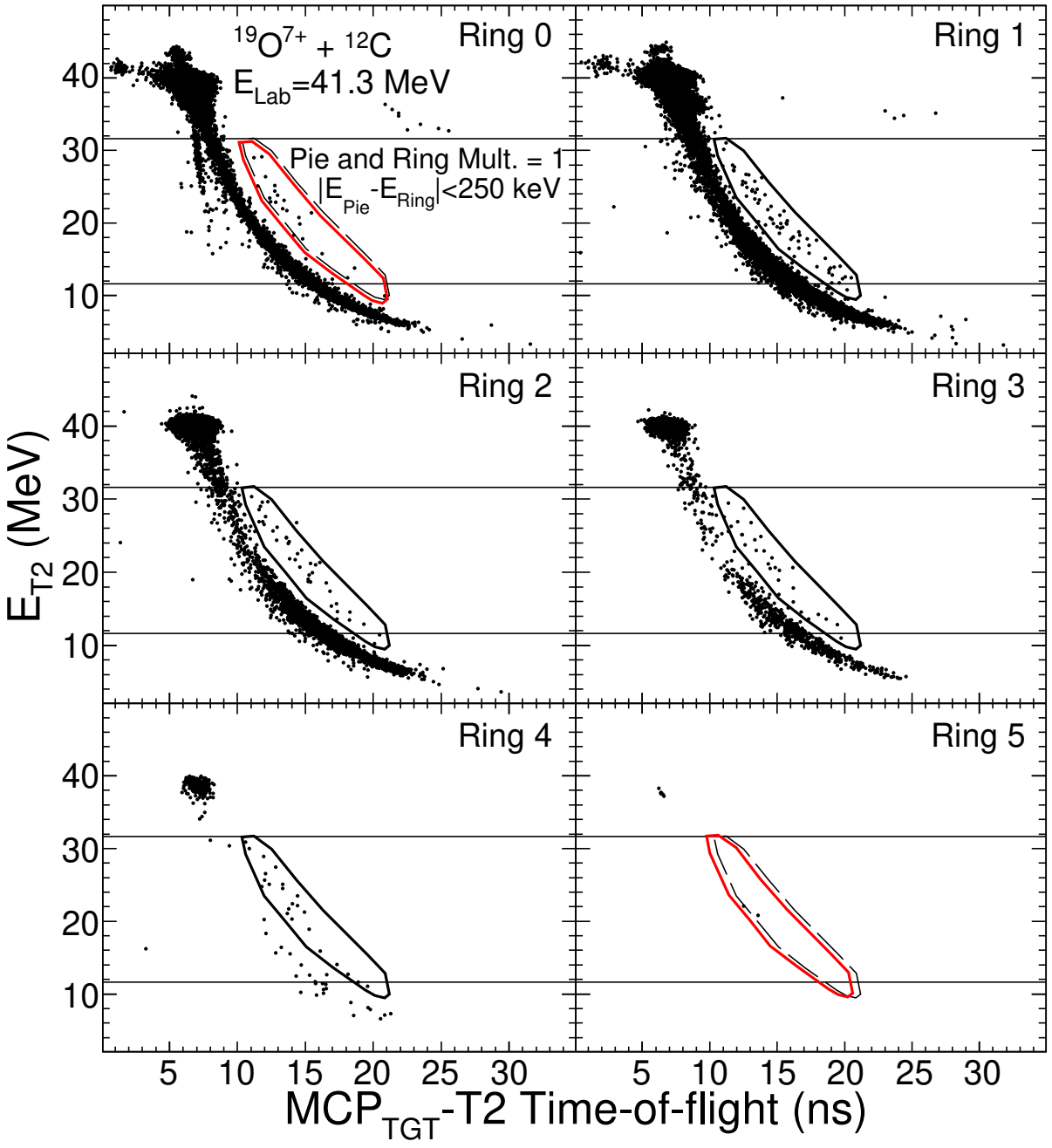

FIGURE 5.10: ETOF spectra for ^{19}O + ^{12}C for each ring in T2.

ETOF spectrum could be relaxed. Requiring that only one pie and one ring have measureable time and energy, and that the energy measured in the pie is within ±0.25 MeV of the energy measured in the rings, a clean ETOF spectrum can be produced without rejecting whole segments of the detector. This spectrum is shown in Figure 5.9. Horizontal lines representing the upper and lower residue energy limits calculated by EVAPOR are shown as a guide. With these conditions, the residue island shown enclosed by the dashed gate is clearly separated from the scatter line.

TABLE 5.1: Number of evaporation residues for $^{19}O + ^{12}C$ determined with the updated analysis compared with that used for the published cross-sections.

$E_{c.m.}$ (MeV)	Original analysis [133]	Updated analysis
18.086	94	358
18.055	43	196
17.672	91	380
15.999	53	238
14.755	61	277
14.210	63	240
13.298	49	201
11.902	29	118
10.386	39	182
9.053	40	116
8.245	43	130
7.413	35	65

To draw a better separation between the residue island and the scatter line, each ring of the detector was treated separately. Figure 5.10 shows the ETOF for each ring. The gate that was used on the summed spectrum in Figure 5.9 is represented as the dashed enclosure, and the gate for each given ring is shown as the solid enclosure. Since Ring 0 and Ring 5 are the edge rings and have a non-uniform field across them, the timing response is faster, so the gate is shifted to lower time-of-flight values as represented by the red contours. By using the updated cleaning conditions and treating each ring separately, the number of residues measured increased by almost a factor of four for each energy. The number of measured residues is tabulated in Table 5.1. The number of residues

originally determined for the published cross-sections [133] is compared with the number of residues determined with the current method of analysis for each incident beam energy. The number of residues in the updated analysis also includes those residues measured in the T3 detector, which is described in the next section.

5.3.5 T3 detector

It has been demonstrated that alpha emission can be much more probable than predicted by statistical model calculations [93] possibly due to dynamic alpha cluster formation [135], indicating the need for a measurement of the residues resulting from alpha-emission of the compound nucleus. These decays preferentially populate larger angles. The T3 detector is situated to cover large angles, complementing the low angle coverage of T2 and accounting for the rest of the residue angular distribution. T3 was calibrated in the same way as T2. Figure 5.11 shows the pie versus ring energy correlation for T3, which has a width of ± 0.5 MeV. The same conditions used for T2 were applied for T3: only one pie with measureable energy and time, only one ring with measureable energy, and the pie energy must be within ± 0.5 MeV of the ring energy. The resulting ETOF is shown in Figure 5.12. The elastic peak and scatter line are enclosed by the solid red gate, which was drawn on the ETOF spectrum of every beam energy added together. As for T2, the upper and lower energy limits used to guide the residue gate are shown as the horizontal lines, and the residues are enclosed by the dashed gate. The points within the residue contour but outside the specified energy limits are included, as the energy limits do not factor in detector resolution and are simply used to guide the eye.

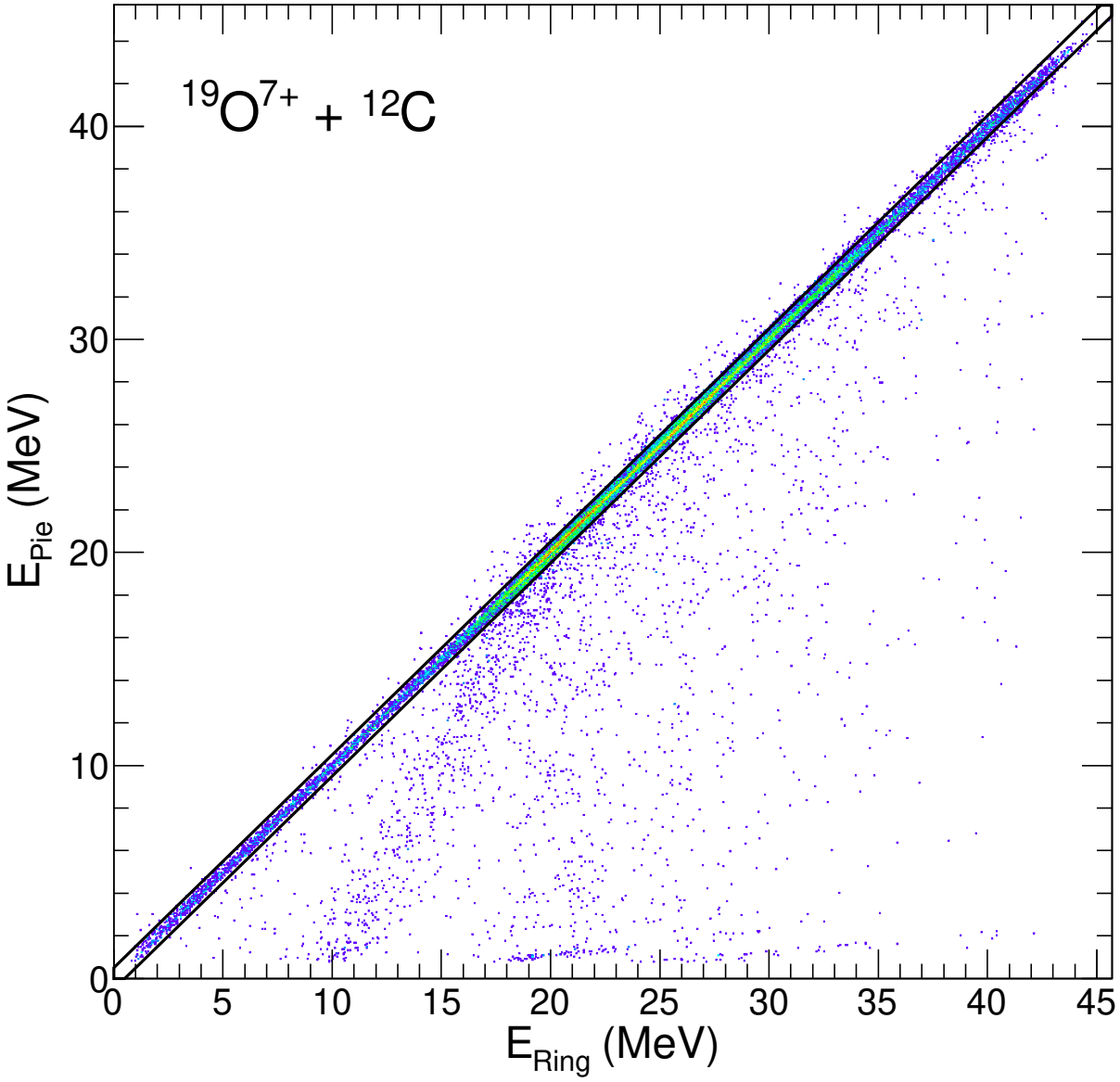

FIGURE 5.11: Calibrated T3 pie energy versus calibrated ring energy for ^{19}O + ^{12}C. The black lines represent the same energy in the pies and the rings within ± 0.5 MeV.

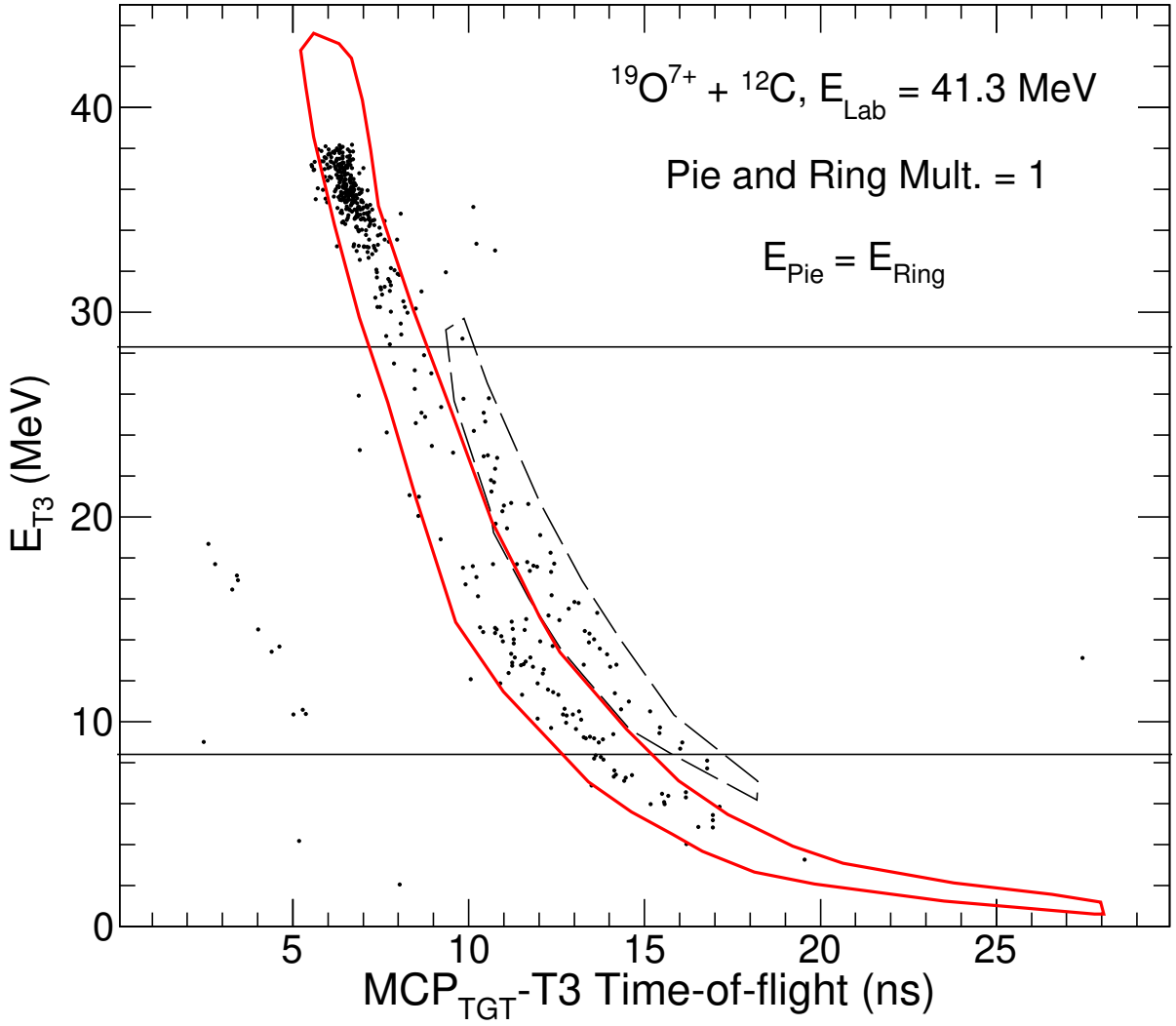

FIGURE 5.12: ETOF spectra from T3 for ^{19}O + ^{12}C. The solid red gate represents the elastic peak and scatter line. The solid horizontal lines represent predicted upper and lower energy limits calculated with EVAPOR. The dashed gate encloses the residue island.

5.3.6 Residue angular distributions

Since T2 and T3 do not cover 4π steradians, the geometric efficiency of the detector setup needs to be assessed. Historically, this has been done by using the predicted residue angular distributions from a statistical model calculation; however, as mentioned previously, the predictions of the statistical model code are not necessarily accurate. Between T2 and T3, and with the ring segmentation of both detectors, the angular distribution

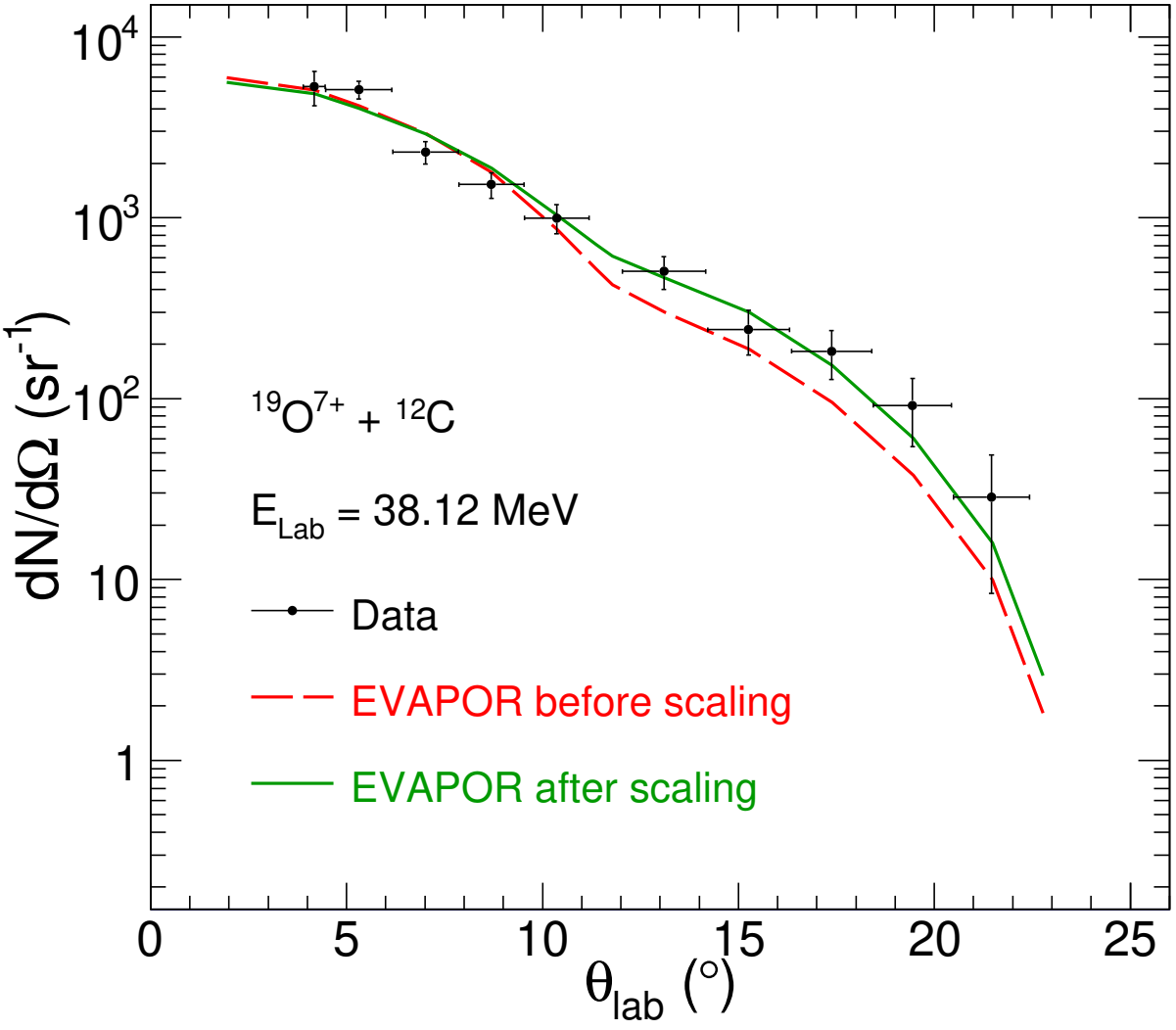

FIGURE 5.13: Angular distribution of the evaporation residues for ^{19}O + ^{12}C. The horizontal error bars represent the angular coverage of each detector segment, and the vertical error bars represent the statistical uncertainty. The prediction calculated by EVAPOR is shown as the red dashed line. The EVAPOR calculation after scaling the α-channels to the data is shown as the green solid line.

of the residues can be measured. An example of the measured angular distribution for ^{19}O + ^{12}C is depicted in Figure 5.13. The data is represented as the closed circles, where the horizontal error bars denote the angular coverage of each detector segment and the veritcal error bars represent the statistical uncertainty. The measured angular distribution of residues exhibits a two peak structure. The peak at lower angles is associated principally with nucleon only de-excitation of the compound nucleus, while the larger

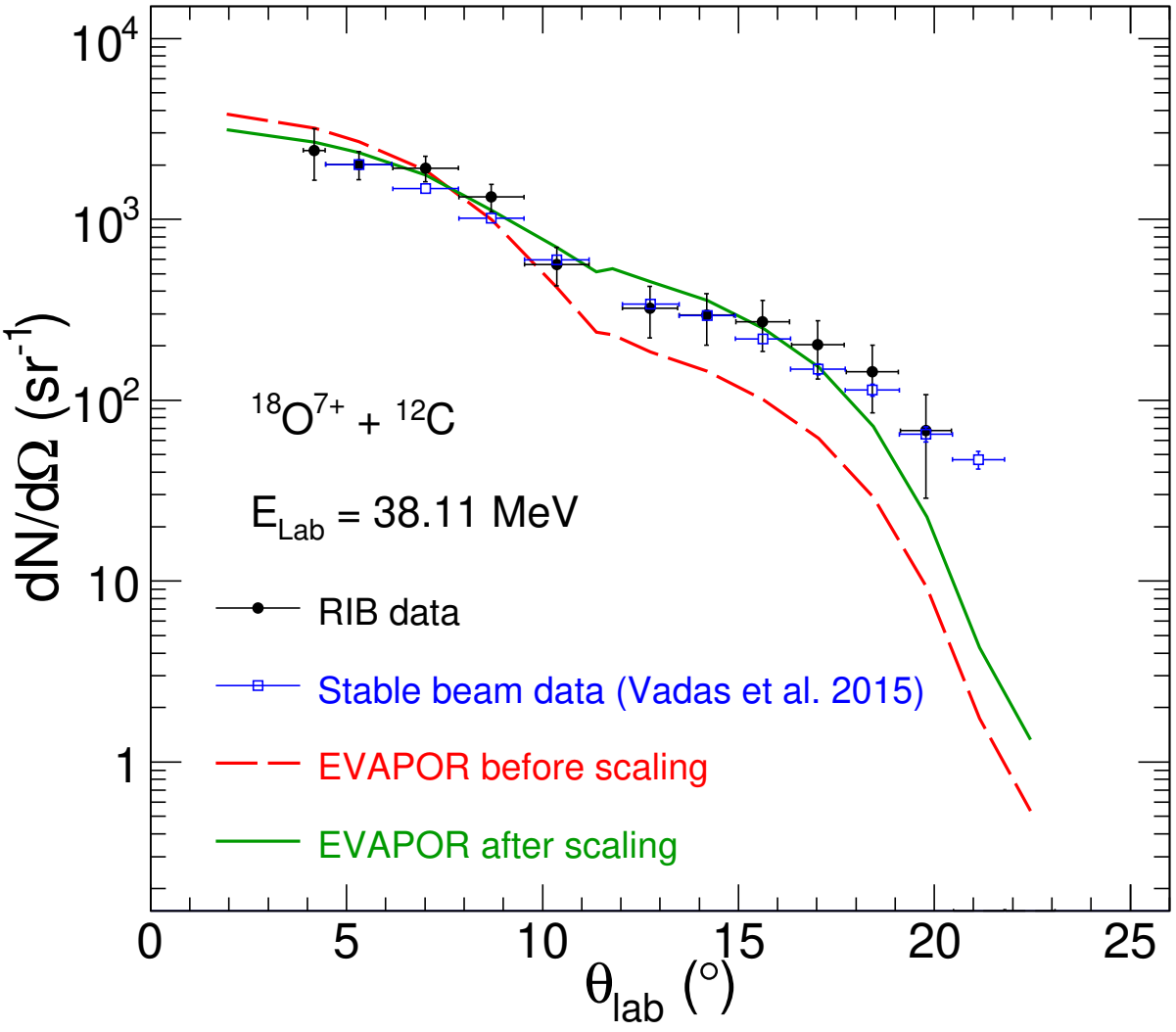

FIGURE 5.14: Angular distribution of the evaporation residues for ^{18}O + ^{12}C. The data from the present measurement of $^{18}O^{7+}$ acquired simultaneously with the ^{19}O radioactive ion beam (RIB) is presented as the closed black circles. For comparison, the high precision residue angular distribution from Figure 4.5(a) at E_{lab} = 36 MeV measured with the ^{18}O stable beam is shown as the open blue squares [93]. The high precision measurement has been renormalized to the RIB data.

angle peak is associated with α emission. This connection of the de-excitation with the angular distribution of the residues is simply due to the larger momentum recoil associated with the α particles and has been previously demonstrated in $^{18}O + ^{12}C$ [93]. For comparison, the residue angular distributions for the ^{18}O reaction measured simultaneously with ^{19}O is shown in Figure 5.14 as the solid black circles together with the ^{18}O data from the high precision measurement discussed in Chapter 4, shown here as open blue squares. As expected, there is remarkable agreement between the two measurements after renormalizing the data. In juxtaposition with the data, the prediction calculated by EVAPOR is shown as the red dashed line. As expected, there is reasonable agreement with the data at angles below 11°, but for larger angles the model underpredicts the measured values. To produce better agreement with the data, the EVAPOR calculation was separated into two parts: exit channels involving the emission of only nucleons and exit channels involving the emission of at least one α particle. Both parts of the distribution were scaled to minimize the χ^2 with the data, and the result is shown as the solid green line. The α channel part had to be scaled by a factor of $\sim$1.5 - 2.5 times higher than the nucleon channel part for ^{19}O, and for ^{18}O the α channels had to be scaled up by a factor of $\sim$2 - 3.5 times the nucleon channels. Better agreement could be achieved by further subdividing the EVAPOR calculations into individual exit channels, but the data is not sensitive enough to the different exit channels to provide reasonable constraints. The geometric efficiency is then determined by taking the ratio of the measured distribution to the scaled EVAPOR calculation. At all energies, for both ^{18}O and ^{19}O, the total efficiency is approximately 75% - 80% with the scaled EVAPOR distributions, and 70% - 75% for the unscaled distributions. The relative weighting of the individual T2 and T3 efficiencies drastically changed, where T2 saw a $\sim$10% reduction in its scaled efficiency compared to the unscaled efficiency, and the scaled efficiency of T3 doubled from its unscaled value. The scaled total efficiency is used in determining the fusion cross-sections.

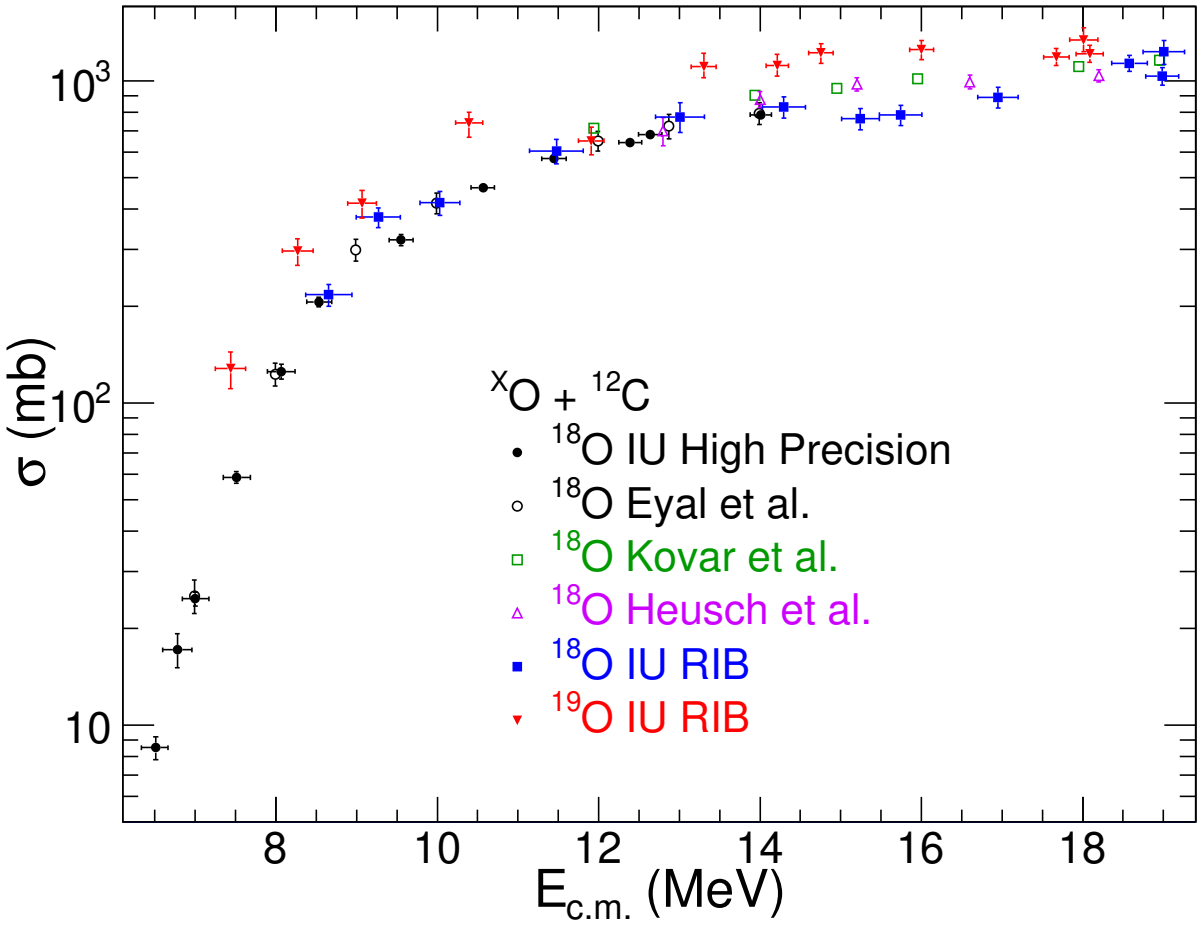

FIGURE 5.15: Fusion excitation functions for ^{18,19}O ions incident on ^{12}C target nuclei. The cross-sections for the ^{19}O induced reaction are represented as solid red inverted triangles, and those for the ^{18}O induced reaction measured simultaneously in this experiment are shown as the solid blue squares. For comparison, the high resolution measurement of ^{18}O + ^{12}C with this same technique is shown as the solid black circles, and other cross-sections for ^{18}O + ^{12}C reported in literature are represented as open symbols.

5.4 Fusion excitation functions

5.4.1 ^{18,19}O + ^{12}C experiment

The fusion cross-section is extracted from the measured yield of evaporation residues through the relation σ_{fusion} = N$_{ER}$/(ϵ_{ER} x t x N$_I$) where N$_I$ is the number of beam particles of a given type incident on the target, t is the target thickness, ϵ_{ER} is the

detection efficiency, and N_{ER} is the number of evaporation residues detected. The number N_I is determined by counting the particles with the appropriate time-of-flight between the two microchannel plates that additionally have the correct identification in the ΔE-TOF map depicted in the inset of Figure 5.1. The target thickness, t, of 105 $\mu g/cm^2$ was optically measured by the manufacturer with an uncertainty of ± 0.5 $\mu g/cm^2$ [136]. The number of detected residues, N_{ER}, is determined by summing the number of detected residues clearly identified by the ETOF technique [99]. As described in the previous section, the detection efficiency ϵ_{ER} was obtained by utilizing a statistical model with the measured angular distribution of the evaporation residues.

Presented in Figure 5.15 is the dependence of the fusion cross-section on incident energy for $^{19}O + ^{12}C$ (red inverted triangles) and $^{18}O + ^{12}C$ (blue squares) measured in this experiment. The high resolution measurement of $^{18}O + ^{12}C$ [99] discussed in the previous chapter is also shown for comparison, along with cross-section measurements reported in the literature for $^{18}O + ^{12}C$ [89, 108, 109]. The cross-sections for the ^{18}O induced reaction measured in this experiment are in good agreement with the other measurements, providing confidence in the ^{19}O radioactive beam cross-sections simultaneously measured in the present experiment.

For clarity, the excitation functions for $^{18,19}O$ measured with this experimental technique have been reproduced in Figure 5.16(a). All of the excitation functions depicted in Figure 5.16(a) manifest the same general trend. With decreasing incident energy the cross-section decreases as expected for a barrier controlled process. At essentially all energies measured the ^{19}O data exhibits a larger fusion cross-section as compared to the ^{18}O data. To examine the differences in the fusion excitation functions in more detail and quantify them, the measured cross-sections have been fit with the Wong formula from Equation 4.1, which describes the penetration of an inverted parabolic barrier [120].

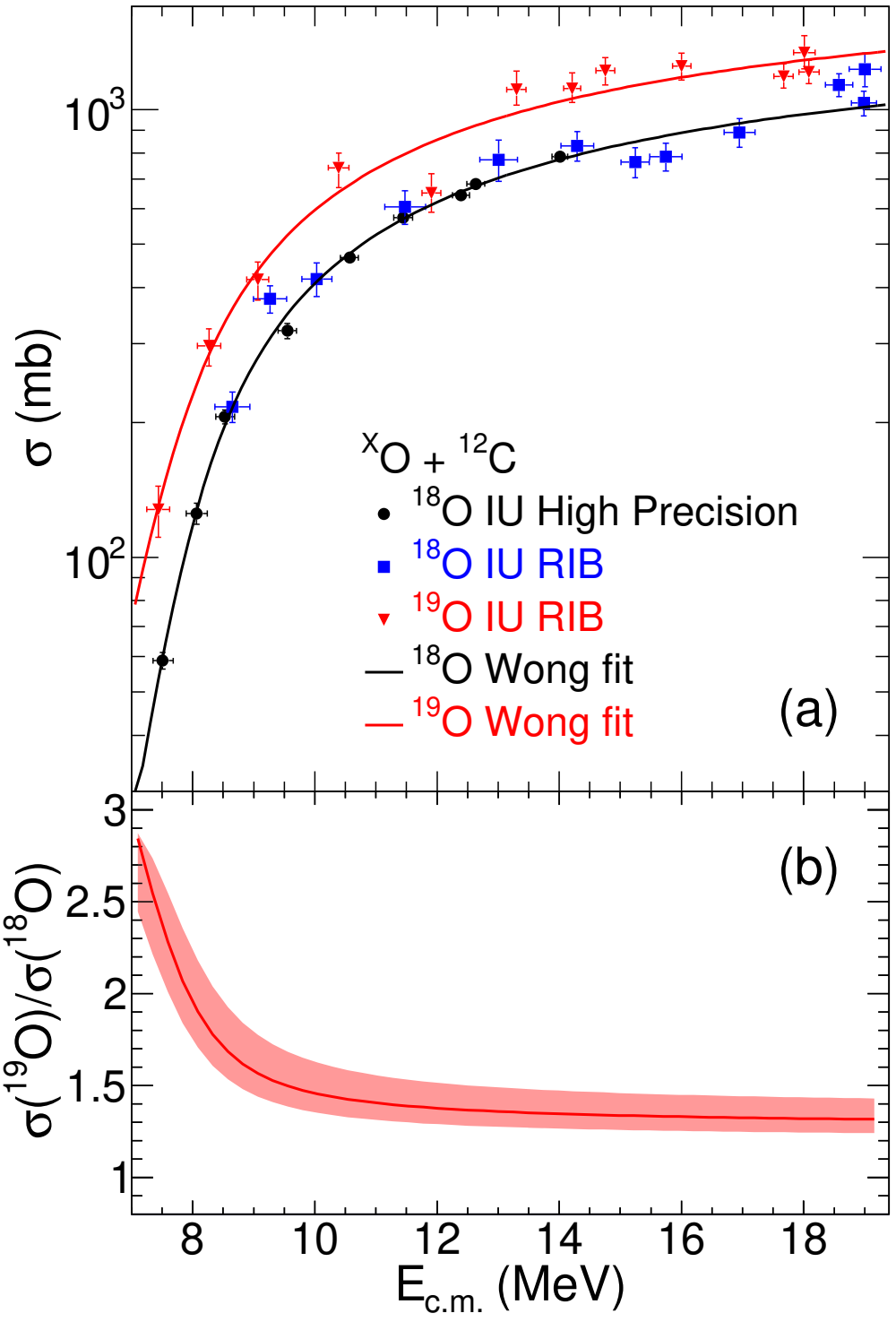

FIGURE 5.16: Top panel: Fusion excitation functions for ^{18,19}O + ^{12}C, fit with a functional form describing a one-dimensional parabolic barrier (Wong formula [120]). Bottom panel: The relative cross-section, $\sigma(^{19}\mathrm{O})/\sigma(^{18}\mathrm{O})$, is depicted as a solid line. The shaded region represents the uncertainties in the cross-section ratio. See text for details.

The fit of the high resolution ^{18}O data combined with the ^{18}O data from the RESOLUT beam is indicated as the solid black line in Figure 5.16(a). The solid red curve in Figure 5.16(a) depicts the fit of the ^{19}O data. With the exception of the cross-section measured at $E_{c.m.} \approx 12$ MeV, the measured ^{19}O cross-sections are reasonably described by this parametrization. The extracted parameters for the ^{18}O and ^{19}O reactions are summarized in Table 5.2. It is not surprising that the barrier height, V_C, remains essentially the same for both of the reactions examined as the charge density distribution is essentially unchanged. The barrier height of ^{19}O is slightly lower than that of ^{18}O, which reflects how the extended neutron density distribution of ^{19}O acts to increase the range of the attractive nuclear potential. With increasing neutron number an increase in R_C is observed as one might expect. However, the increase observed for the addition of a single neutron is larger than expected. If the interaction radius is described as $R_C = r_0({A_p}^{1/3} + {A_t}^{1/3})$ where A_p and A_t are the mass numbers of the projectile and target respectively and r_0 is the radius parameter, then r_0 for the ^{19}O induced reaction is 1.67, as opposed to the value of 1.49 for the ^{18}O data.

TABLE 5.2: Fit parameters for the indicated fusion excitation functions. See text for details.

	V_C (MeV)	R_C (fm)	$\hbar\omega$ (MeV)
^{18}O + ^{12}C	7.58 ± 0.04	7.32 ± 0.06	2.70 ± 0.09
^{19}O + ^{12}C	7.24 ± 0.23	8.28 ± 0.18	3.05 ± 1.75

Depicted in Figure 5.16b as the solid red line is the dependence of the measured ratio of $\sigma(^{19}\text{O})/\sigma(^{18}\text{O})$ on $E_{c.m.}$. At energies well above the barrier $\sigma(^{19}\text{O})/\sigma(^{18}\text{O})$ is essentially flat at a value of ≈ 1.35. As one approaches the barrier it increases to a value of approximately 2.5. As the ratio removes the average behavior of the Coulomb-dominated barrier, it allows one to examine more closely the change in the attractive nuclear potential due to additional neutrons. At high energies above the barrier where the cross-section is largely geometric, the addition of a single neutron results in an increase in the cross-section of 35%. The rapid increase in the ratio with decreasing energy suggests

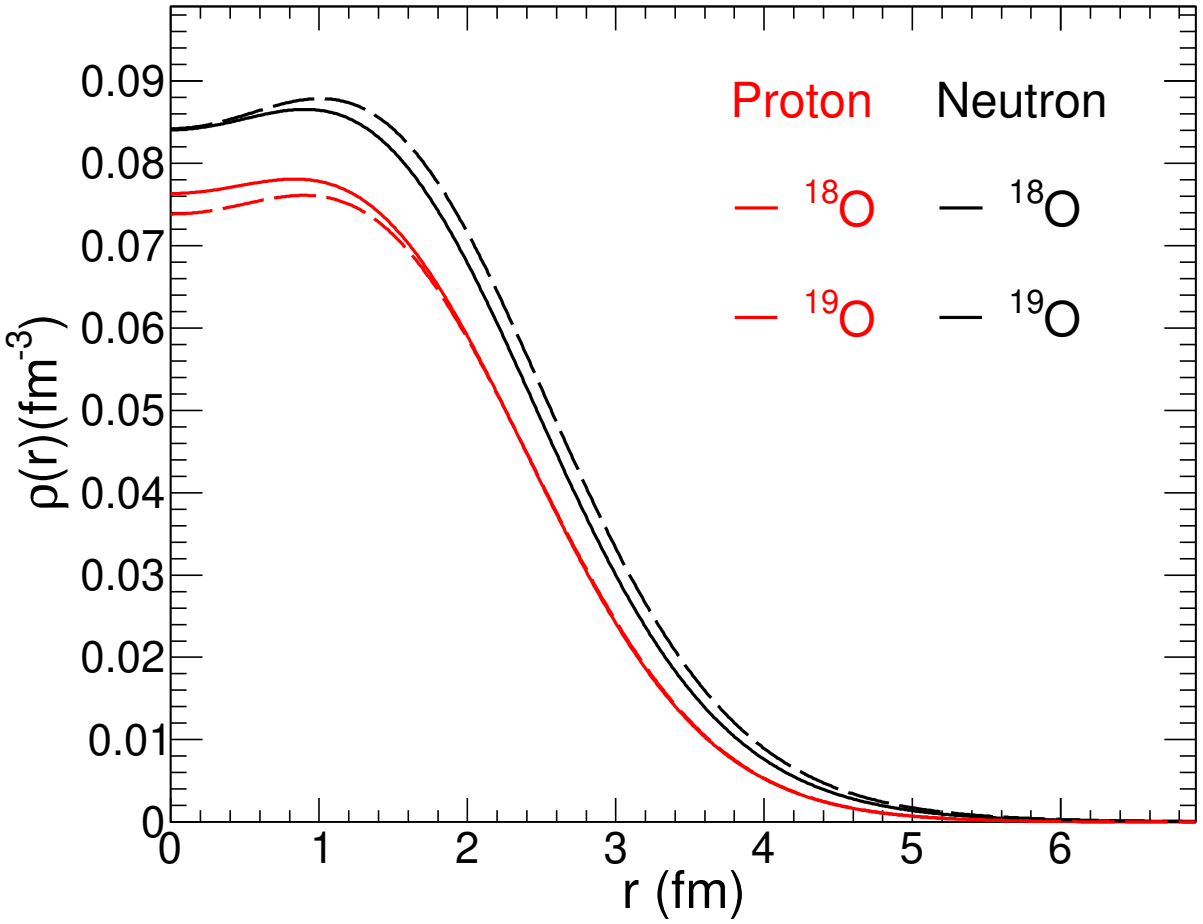

FIGURE 5.17: Proton and neutron density distributions for ^{18}O and ^{19}O calculated with a relativistic mean field approach.

that the barrier for ^{19}O is smaller than that of ^{18}O due to the increased range of the nuclear potential.

In order to better understand whether the fusion enhancement observed for ^{19}O is associated with changes in the nuclear structure or an increased role of dynamics as the neutron number is increased, different models were used to calculate the fusion of oxygen isotopes with ^{12}C nuclei. To disentangle the role of structure from dynamics, fusion of the two nuclei has been calculated both with a static model and with a model which includes dynamics. The static model chosen, the Sao Paulo model [64], allows one to assess the changes in the fusion cross-section due solely to the changes in the density distributions

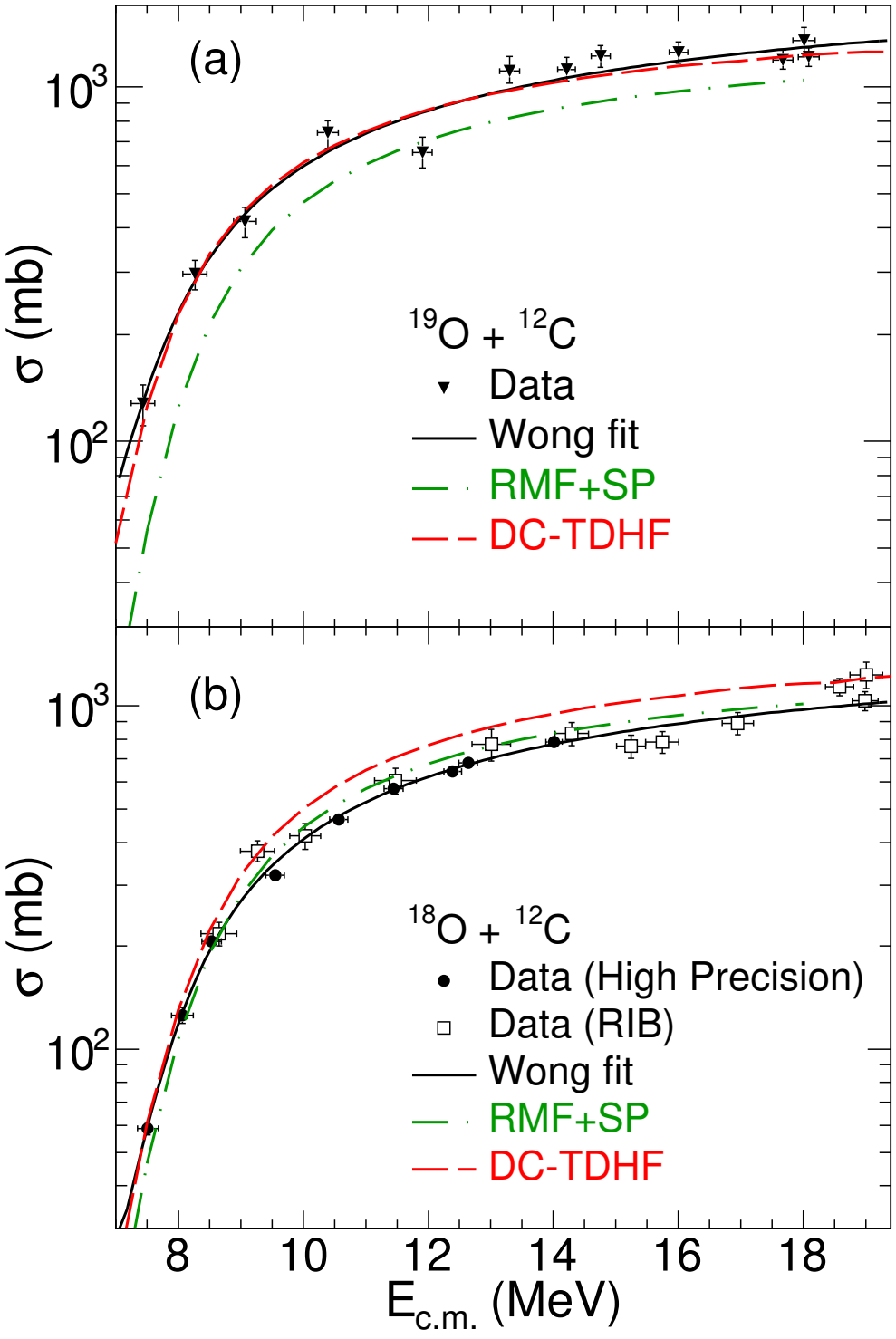

FIGURE 5.18: Top panel: Comparison of the fusion excitation function for ^{19}O + ^{12}C with model calculations. See text for details. Bottom panel: Same as above, but for ^{18}O + ^{12}C.

of the nuclei. These density distributions have been calculated with a relativistic mean field method [67, 137], and are shown in Figure 5.17. As expected, within the RMF calculation, with increasing neutron number the tail of the neutron density distribution increases slightly while the proton density distribution is largely unchanged. The cross-sections predicted from the RMF+Sao Paulo model is depicted in Figure 5.18. While the RMF+SP calculation provides a reasonable description of the ^{18}O induced reaction, the model significantly underpredicts the ^{19}O + ^{12}C cross-sections.

To see if the inclusion of dynamics better explains the observed fusion enhancement, the experimental results were compared with predictions of a microscopic model. In recent years it has become possible to perform time-dependent Hartree-Fock (TDHF) calculations on a 3D Cartesian grid thus not requiring any artificial symmetry restrictions and with much more accurate numerical methods [78, 112]. Over the past several years, the density constrained TDHF (DC-TDHF) method for calculating heavy-ion potentials [84] has been employed to calculate heavy-ion fusion cross-sections with considerable success [81]. While most applications have been for systems involving heavy nuclei, recently the theory was used to study above and below barrier fusion cross-sections for lighter systems, specifically for reactions involving various isotopes of O+O and O+C [80, 83, 99] relevant for the reactions that occur in the neutron star crust. One general characteristic of TDHF and DC-TDHF calculations for light systems is that the fusion cross-section at energies well above the barrier are usually overestimated [118, 119], whereas an excellent agreement is found for sub-barrier cross-sections [83]. This overestimation is believed to be due to various breakup channels in higher energy reactions of these lighter systems that are not properly accounted for in TDHF dynamics and contribute to fusion instead. Nevertheless, the agreement is remarkable given the fact that the only input in DC-TDHF is the Skyrme effective nucleon-nucleon interaction, and there are no adjustable parameters. The DC-TDHF calculations involving the ^{18}O nucleus requires the use of pairing to obtain a correct spherical initial Hartree-Fock state. The density dependent pairing

with the SV-bas Skyrme parametrization [115] was used to achieve this. This nucleus with frozen occupations was then used in the TDHF time evolution. The initial state for the ^{19}O nucleus requires, in addition to pairing, the use of all the time-odd interaction terms in the Skyrme interaction due to the odd neutron number, which are present in the TDHF program.

Presented in Figure 5.18 is a comparison of the measured fusion cross-sections with those predicted by the DC-TDHF model. While the model provides a reasonable description of the fusion excitation function for ^{19}O in the energy regime measured, its description of the fusion excitation function for ^{18}O is notably poorer. Closer examination of the ^{18}O excitation function reveals that the model overpredicts the cross-section at above barrier energies but provides a good description in the interval 7.5 MeV $< E_{c.m.} <$ 8.5 MeV. For even lower energies than those depicted here it has been demonstrated that the DC-TDHF calculations underpredict the experimental cross-sections [99]. As the treatment of pairing within the initial nuclei is known to have a significant influence on the fusion excitation function [99], it is reasonable to hypothesize that the better prediction for ^{19}O is due to the lack of pairing in the last valence neutron of ^{19}O. By extending the measurement of the ^{19}O excitation function to lower energies as well as performing a high quality measurement of ^{20,21}O + ^{12}C this hypothesis could be tested. The availabity of these neutron-rich oxygen beams at the GANIL/SPIRAL1 facility in Caen, France makes this measurement feasible. With an approved experiment to measure ^{20,21}O + ^{12}C at the GANIL facility, execution of this experiment in the next couple years is anticipated.

5.4.2 ^{16}O,^{17}F + ^{12}C experiment

The fusion cross-sections for the experiment with the ^{17}F beam were extracted in the same way as with the ^{19}O beam. Shown in Figure 5.19(a) represented as the solid blue squares is the fusion excitation function for ^{16}O + ^{12}C measured in the present

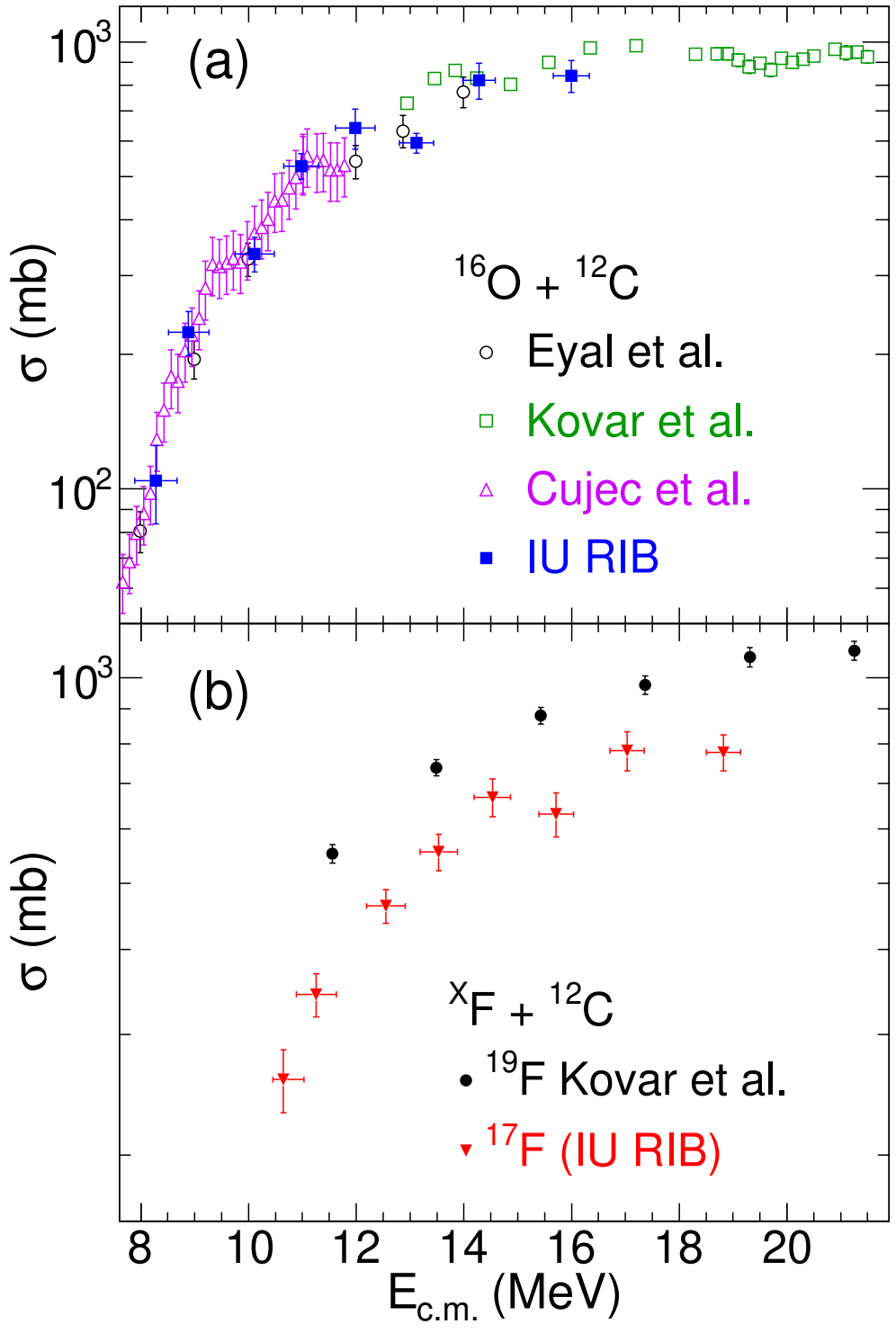

FIGURE 5.19: Fusion excitation functions for oxygen and fluorine ions incident on ^{12}C target nuclei. Top panel: Comparison of the ^{16}O + ^{12}C fusion cross-sections measured in this experiment with values reported in the literature. Bottom panel: Comparison of the ^{17}F + ^{12}C fusion cross-sections with those reported in the literature for a ^{19}F induced reaction.

experiment and compared with prior measurements reported in the literature [89, 109, 138], represented as the open symbols. Just as in the case of the ^{18}O measurement from the previous experiment described in the previous sections, the ^{16}O measurement in the present experiment is in good agreement with the previously reported values, once again providing confidence in the radioisotope beam measurement. The ^{17}F + ^{12}C fusion cross-sections measured in this experiment are presented in Figure 5.19(b) as red inverted triangles, along with the fusion excitation function of the stable analog system ^{19}F + ^{12}C [109]. The cross-sections of the ^{17}F induced reactions are lower than those of the ^{19}F system at all energies.

To more quantitatively compare the two fluorine induced reactions, the excitation functions were parameterized with the Wong formula, which is shown in Figure 5.20(a). The fit parameters are summarized in Table 5.3. Since ^{17}F is smaller than ^{19}F, the interaction radius is smaller, and correspondingly the barrier height is much larger due to the shorter range of the attractive nuclear potential. For these systems, the barrier curvature is about the same, although there is no data below the barrier to constrain the curvature parameter, particularly in the case of ^{19}F. The relative cross-section $\sigma(^{19}\mathrm{F})/\sigma(^{17}\mathrm{F})$ is shown in Figure 5.20(b) and shows an increase in the ^{19}F cross-sections of 25% above the ^{17}F cross-sections at high energies, before the onset of a rapid increase towards lower energies as one approaches the barrier.

TABLE 5.3: Fit parameters for the indicated fusion excitation functions. See text for details.

	V_C (MeV)	R_C (fm)	$\hbar\omega$ (MeV)
^{17}F + ^{12}C	8.73 ± 0.30	6.97 ± 0.21	0.27 ± 0.03
^{19}F + ^{12}C	7.99 ± 0.18	7.58 ± 0.11	0.28 ± 0.01

As with the previous experiment, model calculations were used to better understand the extent to which the observed fusion cross-sections are due to structure or dynamics.

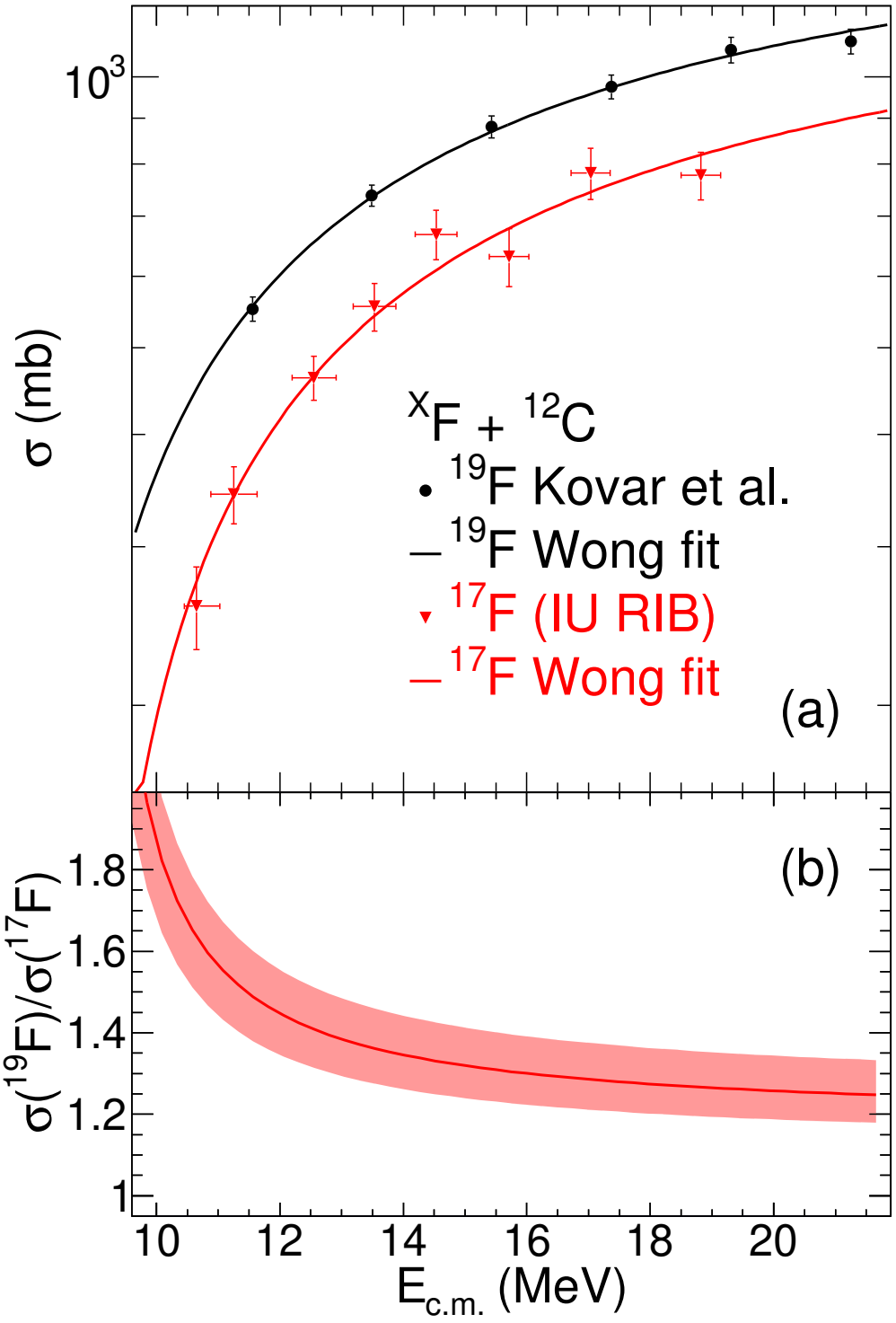

FIGURE 5.20: Top panel: Fusion excitation functions for ^{17,19}F + ^{12}C, fit with a functional form describing a one-dimensional parabolic barrier (Wong formula [120]). Bottom panel: The relative cross-section, $\sigma(^{19}\mathrm{F})/\sigma(^{17}\mathrm{F})$, is depicted as a solid line. The shaded region represents the uncertainties in the cross-section ratio.

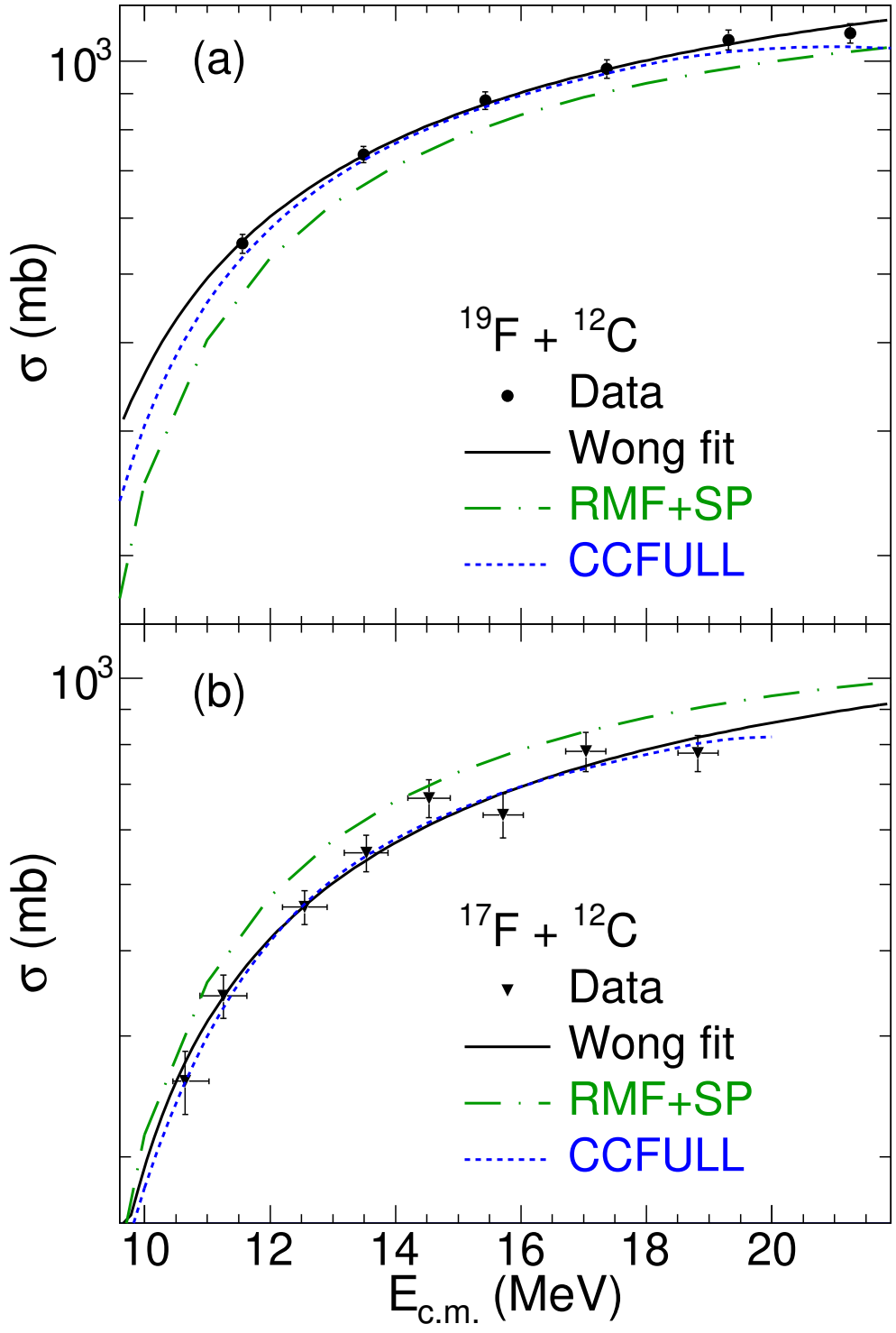

FIGURE 5.21: Top panel: Comparison of the fusion excitation function for ^{19}F + ^{12}C with model calculations. See text for details. Bottom panel: Same as above, but for ^{17}F + ^{12}C.

Presented in Figure 5.21 are the fusion excitation functions for the fluorine induced reactions along with predictions from model calculations. The static Sao Paulo model with RMF densities both underpredict the ^{19}F induced cross-sections and overpredict the ^{17}F induced cross-sections.

TABLE 5.4: Woods-Saxon potential parameters for the measured systems. See text for details.

	V_0 (MeV)	r_0 (fm)	a (fm)
^{17}F + ^{12}C	-280	0.77	0.725
^{19}F + ^{12}C	-380	0.72	0.74

TABLE 5.5: Excited states and deformation parameters used in the coupled channels calculations for the projectiles.

	J^π	Level (MeV)	β_2	β_4
^{17}F	7/2+	8.416	0.061	0.152
^{19}F	3/2+	1.554	0.262	0.18
^{19}F	5/2+	4.550	0.262	0.18

While a microscopic description of the fusion process with a model such as DC-TDHF is desirable, calculation of fusion for the odd-A nuclei in these systems is particularly challenging. As pairing significantly impacts the fusion cross-section [99], a correct treatment of the unpaired proton is essential and presently beyond the scope of the model. The role of dynamics for these systems was therefore explored using coupled channels calculations [69] with the code CCFULL [139]. The Coulomb part of the potential is given by Coulomb's law, modified at small internuclear separation to account for overlap. The nuclear part of the potential utilized a Woods-Saxon form, with the depth V_0, radius parameter r_0, and diffuseness parameter a. The values of these parameters were chosen to reflect the same effective potential as that of the RMF+SP calculations, and are presented in Table 5.4. Coupling to the 4.44 MeV 2+ state of the ^{12}C target with $\beta_2 = 0.57$ was included with coupling to the 3/2+ and 5/2+ states of the ^{19}F rotational band built on the 1/2+ ground state. Coupling with ^{17}F included the 7/2+ rotational level built on the 5/2+ ground state. The parameters used for the couplings are displayed in Table 5.5.

In the case of ^{17}F, the Q-value for proton transfer from the projectile to the target is $Q_p = 1.343$ MeV, so the effect of charge transfer was included with a strength of $F_{tr} = 0.7$. As the Q-value for charge transfer in the ^{19}F + ^{12}C system is negative, the effect of transfer was not included. Inclusion of dynamics within this framework provides better agreement with the measured ^{19}F + ^{12}C cross-sections just above the barrier, but starts to deviate at higher energies. At lower energies as one approaches the barrier, there is a hint that the CCFULL calculations begin to deviate from the data and follow the same slope as the RMF+SP calculations. The inclusion of dynamics via coupled channels has a more profound impact on the ^{17}F + ^{12}C system. Since the valence proton in ^{17}F is weakly bound with a separation energy of only 600 keV, and the Q-value for proton transfer to the target is positive, inclusion of proton transfer effects on the fusion cross section at above-barrier energies is associated with transfer that does not lead to fusion.

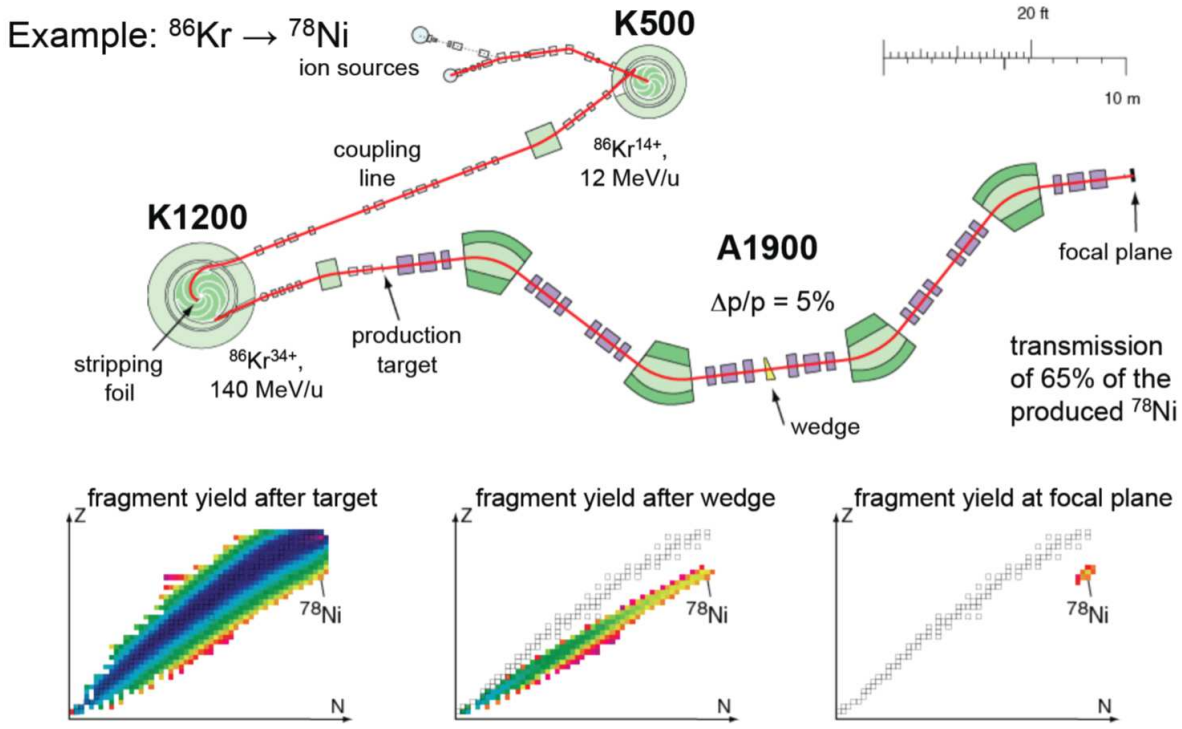

FIGURE 6.1: Schematic of the Coupled Cyclotron Facility at the National Superconducting Cyclotron Laboratory [140].

Chapter 6

^{39,47}K + ^{28}Si: Far from Stability with a Reaccelerated Radioactive Beam

6.1 ReA3 at NSCL

6.1.1 Beam production

Radioactive beams at the National Superconducting Cyclotron Laboratory (NSCL) are produced in the Coupled Cyclotron Facility (CCF), which consists of a K500 cyclotron coupled to a K1200 cyclotron. A schematic of the CCF is shown in Figure 6.1. In the case of the ^{47}K beam utilized in this experiment, a primary beam of ^{48}Ca was accelerated through the coupled cyclotrons to an energy of 140 MeV/u and bombarded a thick ^{9}Be production target. The reaction products following bombardment result from fragmentation of the projectile into a spectrum of lighter nuclei, requiring the ^{47}K particle of interest, which has a half-life of 17.5 s, to be filtered out from the rest of the products. This is accomplished with the A1900 fragment separator immediately downstream of the production target. The graphs at the bottom of Figure 6.1 show the initial and final yields of reaction products from the given example reaction as they pass through the A1900 separator. The resulting rare isotope beam can then be utilized in experiments. These experiments are categorized in three groups: those that utilize fast beams, those that require the beam to be stopped, and those that require the beam to be stopped and then reaccelerated.

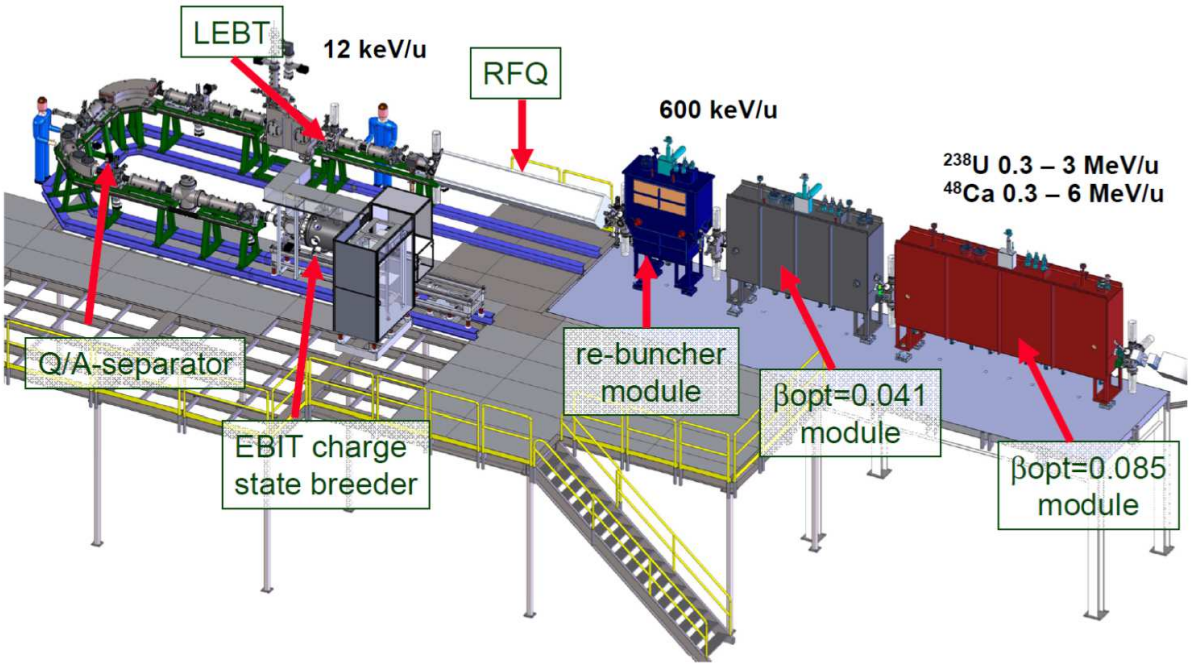

FIGURE 6.2: Schematic of the ReA3 reaccelerator at the National Superconducting Cyclotron Laboratory [140].

6.1.2 Reacceleration

In order to utilize the rare isotope beam produced by the CCF (E/A > 100 MeV/u) in experiments at astrophysically relevant energies (2-3 MeV/u), the beam is first stopped and then reaccelerated [50]. After the A1900, the fast radioactive beam is thermalized in a linear gas stopper. The 60 keV singly charged ions are extracted from the gas stopper and transported to the ReA3 facility, shown in Figure 6.2. The extracted ions are first sent to an initial buncher in order to bunch the beam into ion pulses. The beam pulses are then injected into the electron beam ion trap (EBIT), which acts as a charge state breeder to ionize the beam to a high charge state. Pulsing the beam allows all the ions in each pulse to enter the EBIT at essentially the same time, improving the capture and breeding efficiency [141]. The n^+ ions are then extracted from EBIT and sent through a charge state (Q/A) separator, which selects on the desired charge state and suppresses background ions before acceleration. The beam is then transported to the first stage

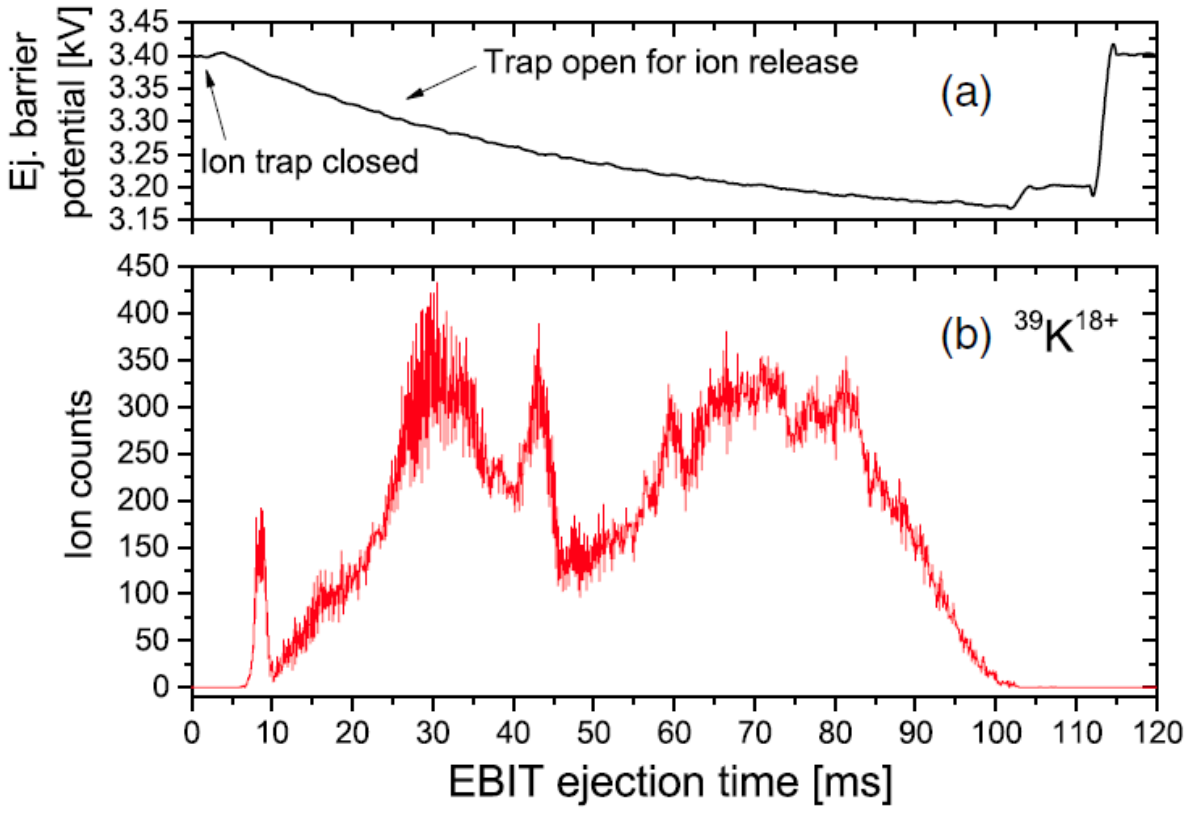

FIGURE 6.3: Panel (a): Exponential voltage ramp function used to eject the beam from EBIT. Panel (b): Time distribution of $^{39}K^{18+}$ ions ejected from EBIT using the ramp function in panel (a).

of the reaccelerator, a room temperature 4-rod radiofrequency quadrupole (RFQ) which will accelerate the beam from 12 keV/u to 600 keV/u. The beam is then injected into the three-stage superconducting linac to provide the rest of the acceleration up to 6 MeV/u. Following acceleration the beam is then guided to the experimental area by the ion transport system. Utilization of the CCF for beam production is not necessary in the case of stable beams, as a stable ion source can be mounted directly in the beam buncher preceding EBIT [141].

6.1.3 Beam characteristics

The maximum single charge state efficiency in the EBIT for ^{39}K and ^{47}K occurs for the charge states 15+ and 17+ respectively [141]. Achieving these high charge states requires the ion pulses to be charge bred for hundreds of milliseconds, but ejection from EBIT occurs within microseconds if a simple step function is used to lower the ejection barrier potential. This ejection time can be stretched to approximately 100 ms if logarithmic or exponential functions are used to lower the ejection barrier potential, such as the exponential voltage ramp function shown in Figure 6.3(a). The corresponding stretched intensity profile of the beam pulse is shown in Figure 6.3(b). Since the beam is ejected from EBIT within 100 ms with a breeding time of approximately 400 ms, the ions experience a time compression which increases the instantaneous beam rate experienced by any detector in the beam path to a factor of five times higher than the average rate. While particle identification required to eliminate beam contamination in a radioactive beam is a relatively routine process, in the present experiment the timing structure of the ReA3 beam and high instantaneous rate necessitated the development of an ionization chamber capable of handling high beam rates $>10^5$ particles per second. The following section details the development and performance of a simple high-rate axial field ionization chamber, designated the Rare Ion Purity Detector (RIPD), which inserts a minimal amount of material into the beam path.

6.2 RIPD

6.2.1 Design and construction

Due to the low-energy beams utilized in these experiments, particular attention was given to the total thickness of the detector in order to minimize the beam divergence and

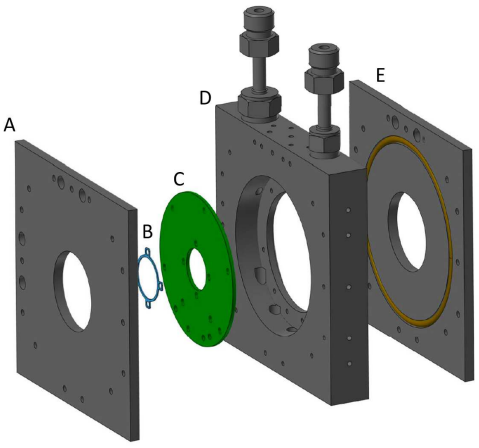

FIGURE 6.4: CAD drawing of the Rare Ion Purity Detector in an exploded view. A: window frame. B: anode ring. C: PCB. D: RIPD. body E: window frame. The mylar windows and central anode foil are omitted for clarity.

energy straggling incurred by inserting the detector into the beam path. Prior experience established that minimizing scattering of the beam was essential. This requirement meant eliminating any wire planes in the beam path. To implement the simplest axial field geometry while minimizing the electron collection time, a central anode is used with the metallized windows serving as cathodes.

A CAD drawing of RIPD is shown in Figure 6.4. The detector is comprised of an aluminum body, two stainless steel window plates, and a thin central anode foil. The anode is coupled to a charge sensitive amplifier (CSA) housed inside the aluminum body. The body measures approximately 11 cm x 11 cm transverse to the beam direction and 2.0 cm thick along the beam axis. The window plates are 5 mm thick and have a 38 mm diameter opening for the beam to pass through, over which 0.5 μm aluminized mylar is epoxied. These mylar foils serve to contain the gas within the active volume and act as cathodes. The window plates are sealed to the body of the detector using O-rings. No support wires are used with these windows to minimize scattering of the incident beam. Using this geometry, it is possible to operate the detector at a pressure of 30 torr of CF_4 for several days without any noticeable degradation in the window performance.

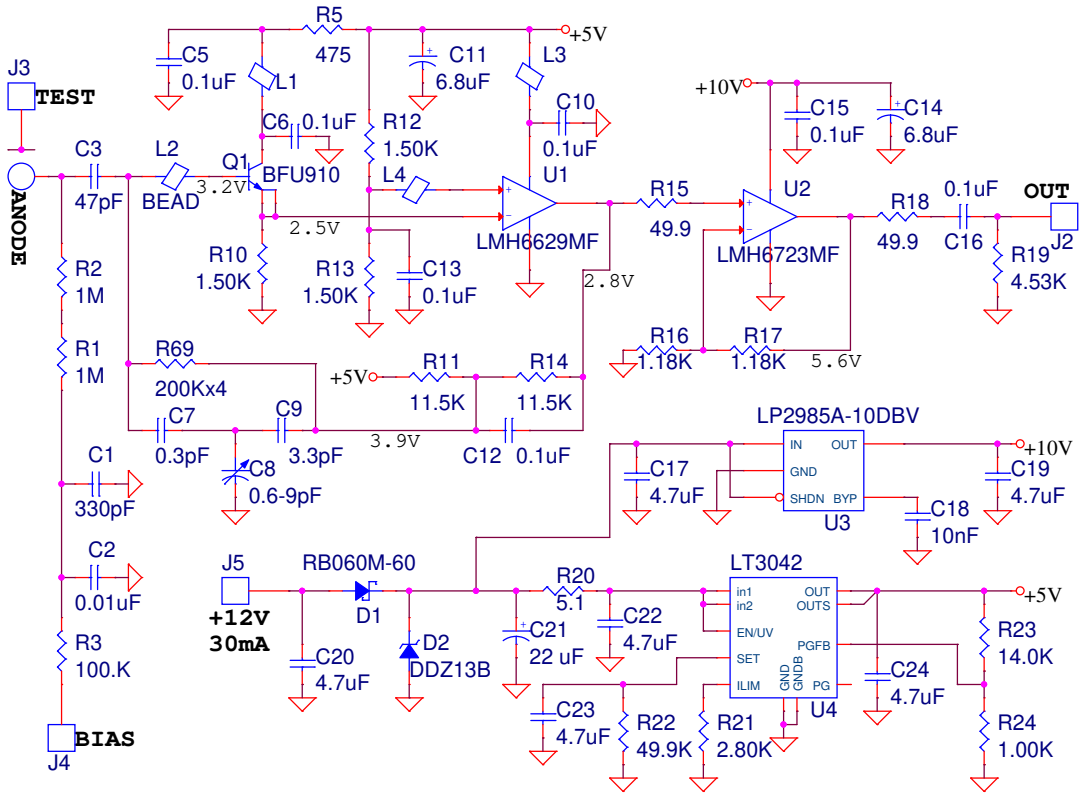

FIGURE 6.5: Schematic of the charge sensitive amplifier for RIPD.

Repeatedly filling the detector with gas also did not cause a noticeable deterioration in the mylar window. The 0.5 μm mylar anode foil, which is doubly aluminized, is mounted on a 2.0 cm diameter stainless steel ring. This ring is attached to an annular printed circuit board (PCB) with an inner diameter of 2.0 cm and an outer diameter of 7.4 cm. The position of the PCB is chosen so that the distance between the anode foil and each cathode foil is 1 cm. Holes in the PCB allow gas to flow between the two halves of the detector. This arrangement of the anode and CSA in close proximity minimizes any additional capacitance at the input of the CSA.

6.2.2 Charge sensitive amplifier

As a key goal in the design of this axial field ionization chamber is its ability to maintain good energy resolution while sustaining a high rate with minimimum pileup of

signals, it was necessary to develop a fast, low-noise charge sensitive amplifier. Ionization of the detector gas induced by a beam particle traversing RIPD quasi-instantaneously produces an ionization track in the detector. Electrons in this track migrate under the influence of the applied electric field and are collected at the central anode. It should be noted that in contrast to the tilted foil design [142, 143] the electric field in RIPD does not move the electrons away from the path of the ionizing beam. Thus, in comparison to the tilted foil geometry the effects of recombination and screening are expected to be larger. This disadvantage is offset by the simplicity of the present design. Carbon tetrafluoride (CF_4) was chosen as the detector gas due to its high electron drift velocity [105]. Based upon the electron drift velocity for a reduced field of 1 kV cm^{-1} atm^{-1}, a rise time of 100 ns is anticipated. This charge collection time defined one of the necessary characteristics of the CSA. To minimize the impact of stray capacitance, the CSA was situated on the PCB as close as practically possible to the central anode. The input capacitance of the detector was calculated to be 2.25 pF, which was confirmed by measurement.

The CSA is a new design that is intended to enable high count rates for low capacitance detectors. The schematic of the CSA is shown in Figure 6.5. The first operational amplifier (U1) provides most of the gain with only a small contribution to the overall noise. However, its bias current, input current noise, and input capacitance are too high for direct connection to the anode, so a SiGe microwave transistor (Q1) is added to serve as an input buffer. This particular transistor offers very high current gain (about 2000) and extremely low input capacitance, and is also very quiet. The signal response of this composite amplifier is defined by the feedback network of R69 and C7, 8, and 9. R69 is actually 4 chip resistors totaling 800 kohms, which were stacked end to end to minimize stray capacitance. The capacitors form a network with an equivalent capacitance adjustable from 0.1 to 0.3 pF. The anode board also comprises an output buffer with a gain of 2, two voltage regulators (U4 is remarkably low noise), level shift, and anode bias

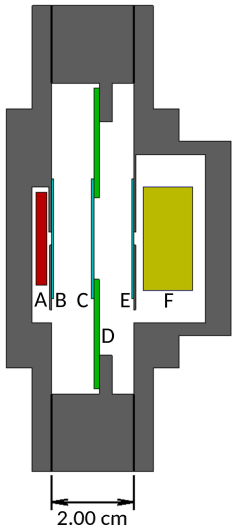

FIGURE 6.6: Cross-sectional view of the experimental setup to measure the energy loss of α particles. An ^{241}Am α source was placed just upstream of the entrance foil in a cap that was made common with the active volume. Alpha particles that pass through the full length of the detector were then measured in a silicon surface barrier detector (SBD) placed just downstream of the exit window in a cap that was also made common with the active volume. A: ^{241}Am α source. B: Entrance cathode foil. C: Anode foil. D: CSA. E: Exit cathode foil. F: SBD.

circuits. This circuit was realized on the annular FR4 printed circuit board on which the RIPD anode was mounted.

6.2.3 Source testing

To characterize the performance of RIPD, the energy resolution for α particles from an ^{241}Am source was measured. To test RIPD with α particles, which have a low ionization density, it is necessary to operate RIPD at gas pressures that exceed the maximum pressure sustainable with the thin windows. For these tests, the entrance and exit window plates were replaced with flanges, as shown in Figure 6.6. The entrance flange allowed an ^{241}Am source to be situated prior to an entrance cathode foil but within the gas volume. Correspondingly, the exit flange allowed a silicon surface barrier detector (SBD) to be placed after an exit cathode foil within the gas volume. Both the ^{241}Am

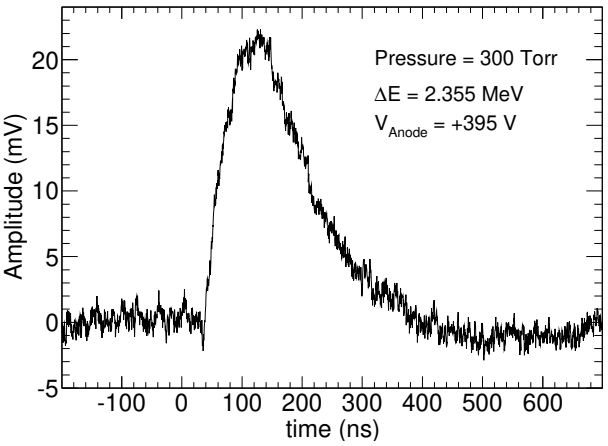

FIGURE 6.7: Typical signal from the CSA corresponding to the energy loss of an ^{241}Am α particle with 300 torr of CF_4 gas in the detector.

source and SBD had a collimation of 3 mm. Triggering on the SBD signal associated with arrival of α particles selected particles that had traversed the entire thickness of RIPD. Using this configuration, signals in RIPD could be examined for pressures between 100 and 400 torr. At a pressure of 100 torr the 5.48 MeV α particles deposit just 680 keV in the gas. This energy deposit increases to ~3.5 MeV at 400 torr.

A typical signal from the CSA at a pressure of 300 torr is shown in Figure 6.7. The anode was biased to a potential of +395 V to produce a reduced field of 1 kV cm^{-1} atm^{-1}. The signal time from baseline to peak is approximately 100 ns with a rise time of 60 ns. Although the observed signal rise time corresponds to the convolution of the electron collection time and the CSA response, as the CSA response is fast (<10 ns), the observed signal principally reflects the electron collection time, consistent with the reported literature value for the electron drift velocity at the reduced field utilized. The CSA signal returns to baseline after approximately 300 ns. Thus the whole signal duration is under 500 ns, which corresponds to a maximum calculated rate of ~2×10^6 ions/second without pileup. The gain of the CSA is approximately 9.5 mV/MeV. With a signal amplitude of ~23 mV and peak-to-peak noise of 4 mV, the signal-to-noise ratio is 5.7.

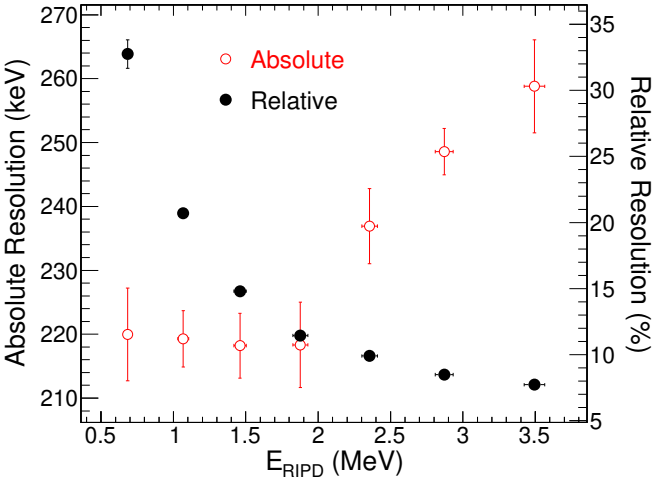

FIGURE 6.8: Resolution as a function of energy deposit in the gas volume of RIPD for α particles from a ^{241}Am source.

To handle these fast signals, the development of a fast shaping amplifier was required. This requirement was realized by modifying an in-house octal shaper module which handles input signals of both polarities. With the modified fast shaper module shaping times between 100 ns and 800 ns in increments of 100 ns can be selected. The coarse gain is controlled by two 4-bit stages, while a fine gain adjustment is provided using a 12-bit multiplying ADC. Another 12-bit multiplying ADC allows adjustment of the pole-zero. All of these parameters can be adjusted under computer control through a USB 2.0 interface. With a shaping time of 200 ns the fast shaping amplifier transforms the typical input CSA signal depicted in Figure 6.7 into a Gaussian-like pulse shown with an amplitude of ∼950 mV and a peak-to-peak high frequency noise of ∼30 mV. Thus the shaping amplifier improves the signal-to-noise ratio to a value of approximately 31.

To determine the energy resolution of RIPD, the signal from the shaping amplifier was digitized by a CAEN V785 peak-sensing ADC. The energies of particles measured in RIPD was first calibrated using the measured energies in the SBD detector after accounting for the energy lost in the mylar foils [127]. The calibrated RIPD energy spectrum was used to determine the energy resolution by comparing the FWHM of the energy distribution to its centroid. The dependence of the energy resolution on the energy deposited in

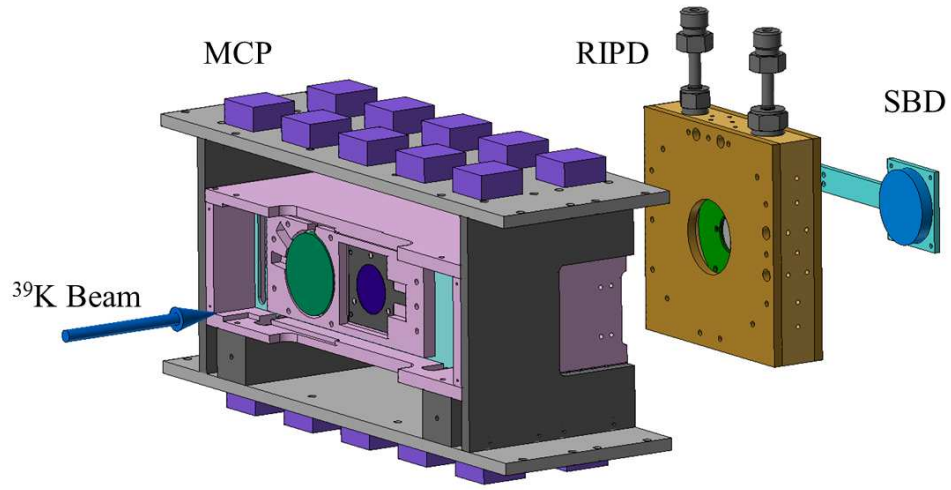

FIGURE 6.9: CAD representation of the experimental setup used to characterize RIPD with beam.

the gas volume is shown in Figure 6.8. For energies up to ∼2 MeV, the absolute resolution is constant at a value of approximately 220 keV, suggesting that for these energy deposits the electronic noise dominates the total noise. Above 2 MeV the absolute resolution deteriorates reaching a value of ∼260 keV at 3.5 MeV of energy deposit. In the energy deposit interval measured the relative resolution decreases smoothly from 32% to ∼7.5%. This 7.5% resolution can be understood as a combination of the signal-to-noise after the fast shaper as well as the variations in the path length of the measured α particles through the gas volume.

6.2.4 Beam testing

In order to characterize the performance of RIPD with beams of different intensity a test was conducted at the ReA3 facility at Michigan State University's National Superconducting Cyclotron Laboratory (NSCL). The ReA3 80 MHz linac, which can be used to accelerate either stable beams or radioactive ions produced by the NSCL's coupled

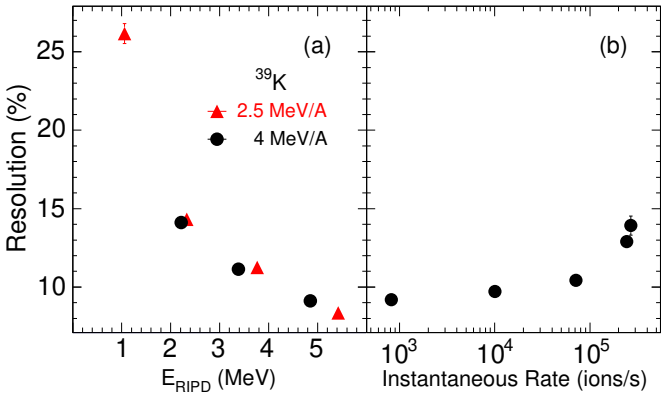

FIGURE 6.10: Panel a: Dependence of the energy resolution on the deposited energy in RIPD. Panel b: Impact on energy resolution of increased instantaneous beam rate.

cyclotron facility, was used to accelerate ^{39}K to energies of 2.5 MeV/A and 4 MeV/A. The beam was extracted from the charge breeding ion trap EBIT within 100 milliseconds at a repetition rate of 2 Hz. This time structure results in the instantaneous rate experienced by any detector in the beam path being effectively a factor of five higher than the average rate. The experimental setup used is depicted in Figure 6.9. The first element of the setup was a microchannel plate detector [99]. In this detector, passage of a beam particle through a 100 μg/cm^2 carbon foil ejects electrons that are transported by crossed electric and magnetic fields to the surface of a chevron microchannel plate (MCP). The fast response of the MCP results in each beam ion incident on the carbon foil being individually recorded. The rate at which the MCP triggers was recorded by a 250 MHz VME scaler providing a measure of the beam rate. Approximately 44 cm downstream of the MCP, RIPD was mounted on a retractable arm. For low-intensity beams a SBD situated immediately after RIPD was used to measure the residual energy of ions traversing RIPD. The SBD was retracted from the beam path when a high-intensity beam was used.

Shown in Figure 6.10a as the closed triangles is the energy resolution of the energy deposited in RIPD by 2.5 MeV/A ^{39}K ions traversing RIPD at nominal gas pressures of 5, 10, 15, and 20 torr. The gas pressure and flow through the detector were maintained by a

high quality gas handling system with a stability of 0.2 torr. With increasing gas pressure the energy deposit in the gas increases from approximately 1 MeV to approximately 5 MeV. As the energy deposit in the gas increases the relative resolution of RIPD improves from 25% at the lowest energy deposit to approximately 9% at the highest energy deposit in reasonable agreement with the source testing results presented in Figure 6.8. The electronic noise as well as the stability of the electronics were monitored during the measurement by injecting a calibration pulse into the charge sensitive amplifier at a low rate. The electronic noise was measured to be approximately 1 %, significantly less than the measured energy resolution of the detector. To determine the response of the energy resolution of RIPD to a change in the beam intensity, the beam intensity of a 4 MeV/A ^{39}K beam was increased from 800 ions/s to 3 x 10^5 ions/s. The impact of the beam intensity on the energy resolution of RIPD is shown in Figure 6.10b. With increasing beam intensity the measured energy resolution degrades from approximately 9% to ∼14% at the highest intensity measured.

Aside from the degradation in the energy resolution the increased beam intensity can also impact the total charge collection due to increased recombination in the detector at high beam intensities. This effect is manifested in the upper panel of Figure 6.11. A decrease in the centroid of the energy deposited in RIPD by 4 MeV/A ^{39}K ions is evident. With increasing beam intensity the location of the energy centroid shifts to lower values consistent with recombination of electrons and cations in the detector gas. At an instantaneous rate of 3 x 10^5 ions/s a peak shift of ∼12% is observed as compared to a low intensity beam of 800 ions/s. As recombination impacts both the ions of interest as well as any contaminants, identifying the nuclide of primary interest from other contaminants is still achieveable. However, correcting for any significant changes in the beam intensity becomes important.

The impact of beam intensity on the pileup observed is indicated in the lower panel

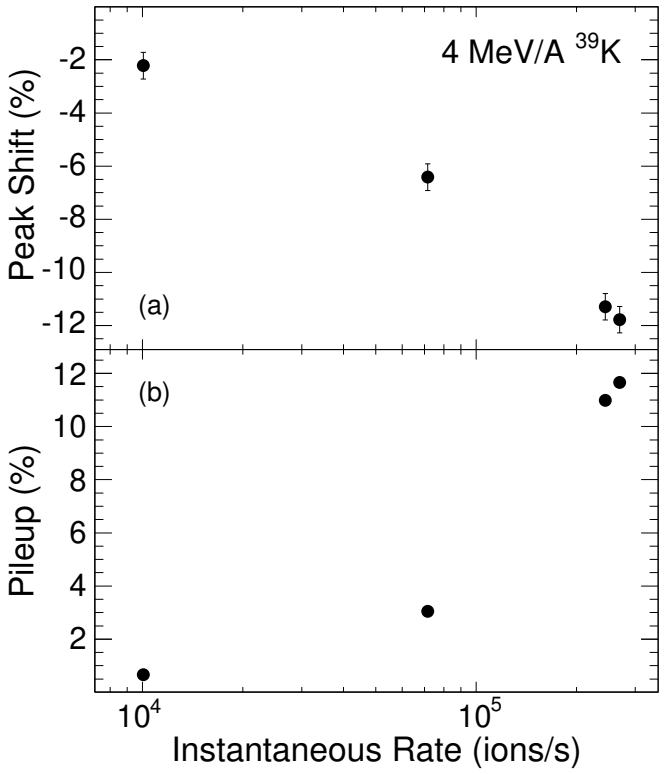

FIGURE 6.11: Impact of the beam intensity on the charge collection (panel a) and pileup (panel b) in RIPD.

of Figure 6.11. Pileup is clearly distinguished as observation of pulses with energies exceeding that of the full beam energy. As expected the pileup increases with increasing instantaneous rate from <1% at 1 x 10^4 ions/s to just under 12% at 3 x 10^5 ions/s. As anticipated the fast response of RIPD enables the use of the detector at high rates without significant pileup.

6.3 Fusion experiment

The experimental setup used to measure fusion of potassium ions with silicon nuclei is depicted in Figure 6.12. The beam first passed through an upstream E×B microchannel plate (MCP) detector, designated MCP_{US}, followed by another MCP detector in the target position (MCP_{TGT}) approximately 1.3 m downstream of the MCP_{US}. These detectors

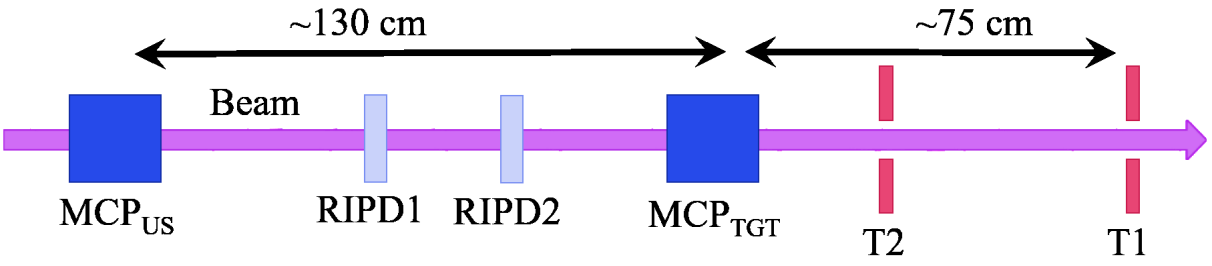

FIGURE 6.12: Schematic of the experimental setup.

[99] provided a time-of-flight (TOF) measurement of the beam particles. The 327 μg/cm^2 thick ^{28}Si secondary emission foil of the MCP$_{TGT}$ served as the target for the experiment. The silicon target foil was enriched to 99% in ^{28}Si, since the natural abundance of ^{28}Si is only 92%. The time-of-flight measurement between the MCP detectors allowed rejection of beam particles scattered or degraded prior to the target and provided a direct measure of the number of beam particles incident on the target. The intensity of the ^{39}K beam on the target was 3 - 4.5 $\times$ 10^4 ions/s, and that of the ^{47}K beam was 1 - 2.5 $\times$ 10^4 ions/s.

In order to identify contaminants in the ^{47}K beam, two compact axial field ionization chambers [106] designated RIPD1 and RIPD2 were inserted in the beam path between the two MCP detectors. Particle identification was achieved by ΔE-TOF, where the time-of-flight for each particle was measured between the MCP detectors. The energy distribution of incident ^{39}K and ^{47}K ions was measured by periodically inserting a silicon surface barrier detector just upstream of the target. The width, σ, of the energy distribution was $\sim$300 keV for ^{39}K and $\sim$600 keV for ^{47}K.

Fusion of a ^{39}K (or ^{47}K) projectile nucleus with a ^{28}Si target nucleus produces an excited ^{67}As (^{75}As) compound nucleus (CN). Near the fusion barrier, the excitation energy of the CN is $\sim$40 MeV ($\sim$55 MeV). De-excitation of the CN via evaporation of light particles imparts transverse momentum to the evaporation residue (ER), allowing its detection in the annular silicon detectors designated T1 and T2 which subtend the angles $1.0^\circ \leq \theta_{lab} \leq 7.3^\circ$. This experimental approach provides an efficient means of measuring

the fusion cross-section with beam intensities as low as 10^3 ions/s. While active target approaches have been successfully utilized to measure the fusion cross-section with low-intensity beams [144], with the present approach beam intensities as high as 10^6 ions/s can also be used providing efficient measurement with beams closer to β-stability.

6.4 Analysis

To distinguish ERs from scattered beam, reaction products detected in the silicon detectors are identified by their mass using the energy vs. time-of-flight (E-TOF) technique [90, 99, 133], with the time-of-flight measured between the $\mathrm{MCP_{TGT}}$ and the silicon detectors [101]. The measured yield of evaporation residues ($\mathrm{N_{ER}}$) is then used to calculate the fusion cross-section σ_{fusion} using $\sigma_{\mathrm{fusion}} = \mathrm{N_{ER}} \ / \ (\epsilon_{\mathrm{ER}} \times \mathrm{N_{Beam}} \times \mathrm{t})$, where ϵ_{ER} is the detection efficiency, $\mathrm{N_{Beam}}$ is the number of beam particles incident on the target and t is the target thickness. $\mathrm{N_{Beam}}$ was determined using the time-of-flight between the MCP detectors and particle identification in the ΔE-TOF spectrum. The thickness of the target was gauged using α particles from sources [127] after accounting for an oxide layer present on the foil. The detection efficiency ϵ_{ER} was calculated by using EVAPOR [110] and the geometric acceptance of the silicon detectors. For both systems, the combined geometric efficiency of T1 and T2, for all incident energies measured, was $\sim$80%.

6.4.1 Particle identification

To measure the fusion cross-section accurately, it is necessary to make sure the reaction products measured in each event result from fusion of potassium ions at the appropriate energy with the silicon target nuclei. Imposing a requirement on the time-of-flight between the US and TGT MCPs thus ensures that beam particles degraded in energy and all product nuclei from reactions occurring upstream of the target are

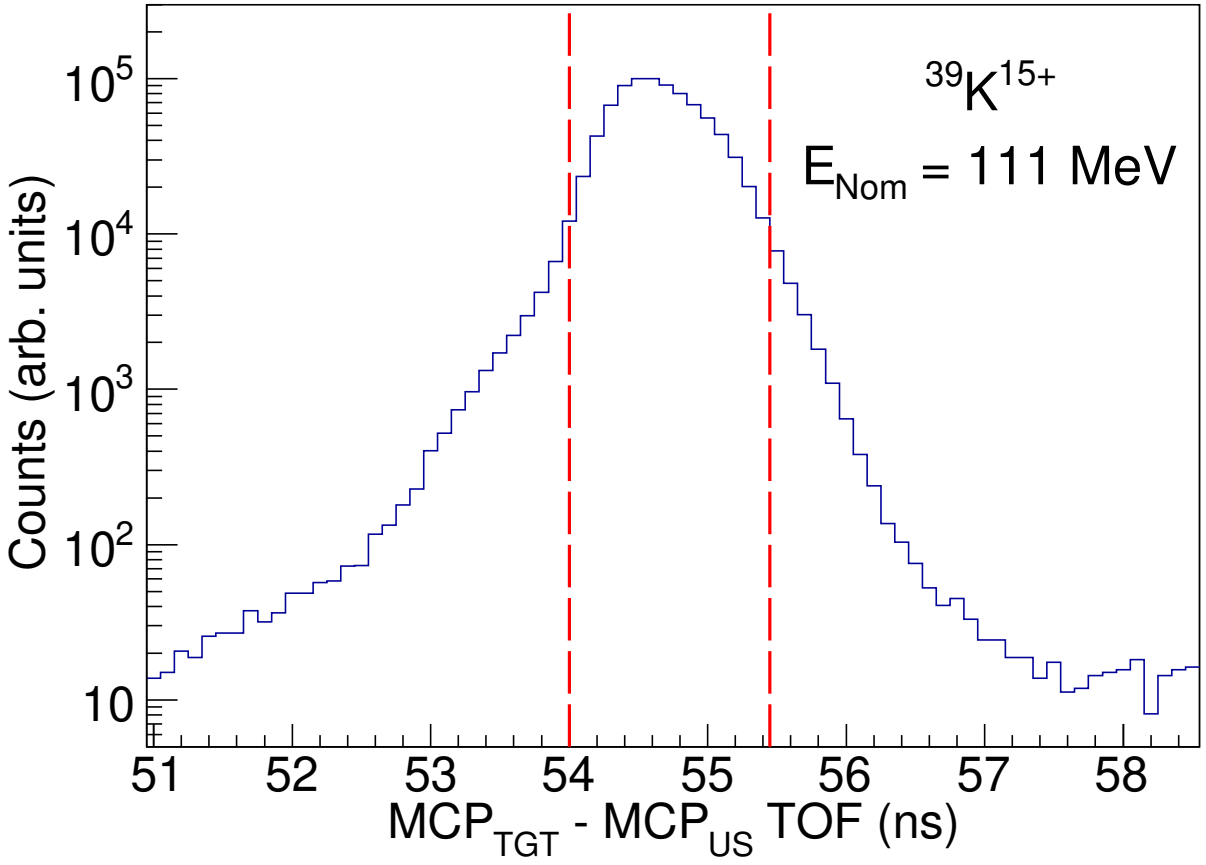

FIGURE 6.13: Time of flight of $^{39}K^{15+}$ ions between the MCP_{US} and MCP_{TGT}. Beam particles with the appropriate time of flight are enclosed by the two dashed vertical lines.

gated out. The MCP_{TGT} - MCP_{US} time-of-flight for ^{39}K at one beam energy is shown in Figure 6.13. The narrow 1.45 ns wide acceptance window is represented as the dashed red lines on either side of the main peak. This time-of-flight is also used to count the number of incident beam particles, N_{Beam}.

For ^{47}K, RIPD was inserted between the two MCP detectors to help eliminate contamination of the beam with ions of the same charge to mass ratio. As the contaminant species have the same E/A and thus the same TOF, the energy loss of each ion through RIPD provided an additional dimension with which to identify the incident beam particles. Figure 6.14 shows the energy loss measured in RIPD versus the MCP-MCP TOF for each incident beam particle. $^{47}K^{17+}$, circled in black, makes up a majority of the

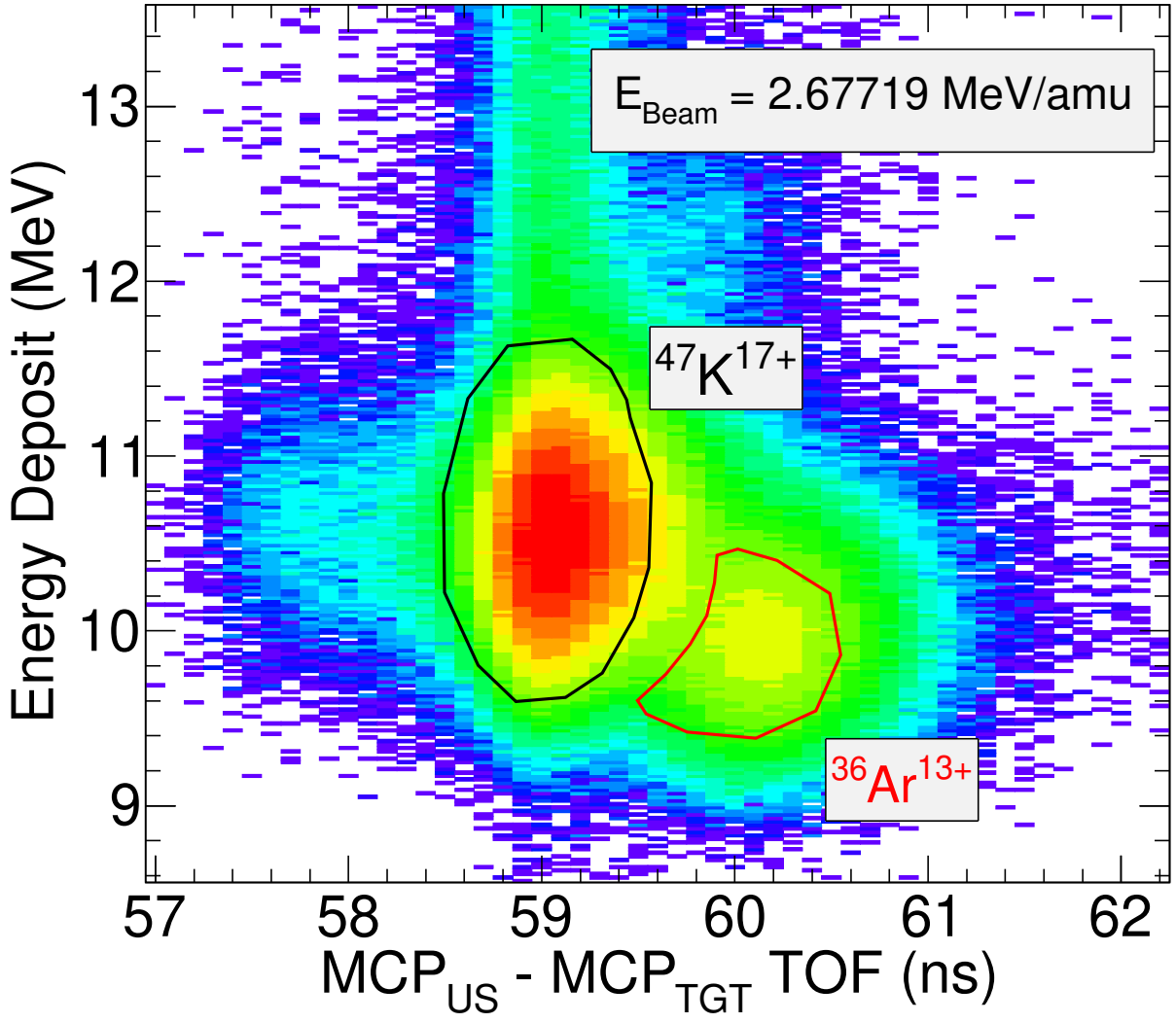

FIGURE 6.14: Energy deposit measured in RIPD1 + RIPD2 versus MCP_{TGT} - MCP_{US} time of flight. $^{47}K^{17+}$ ions are enclosed within the black gate, and $^{36}Ar^{13+}$ ions are denoted by the red gate.

beam, and the $^{36}Ar^{13+}$ contamination shown in the red gate is cleanly separated out. The contribution of the ^{36}Ar in the beam ranges from approximately 5% to 10% of the incident beam. The intense line extending vertically from the ^{47}K peak results from pileup in RIPD, and the tail to the left of the ^{47}K peak corresponds to events in which the MCP_{TGT} signal is saturated and produced an artificially short TOF.

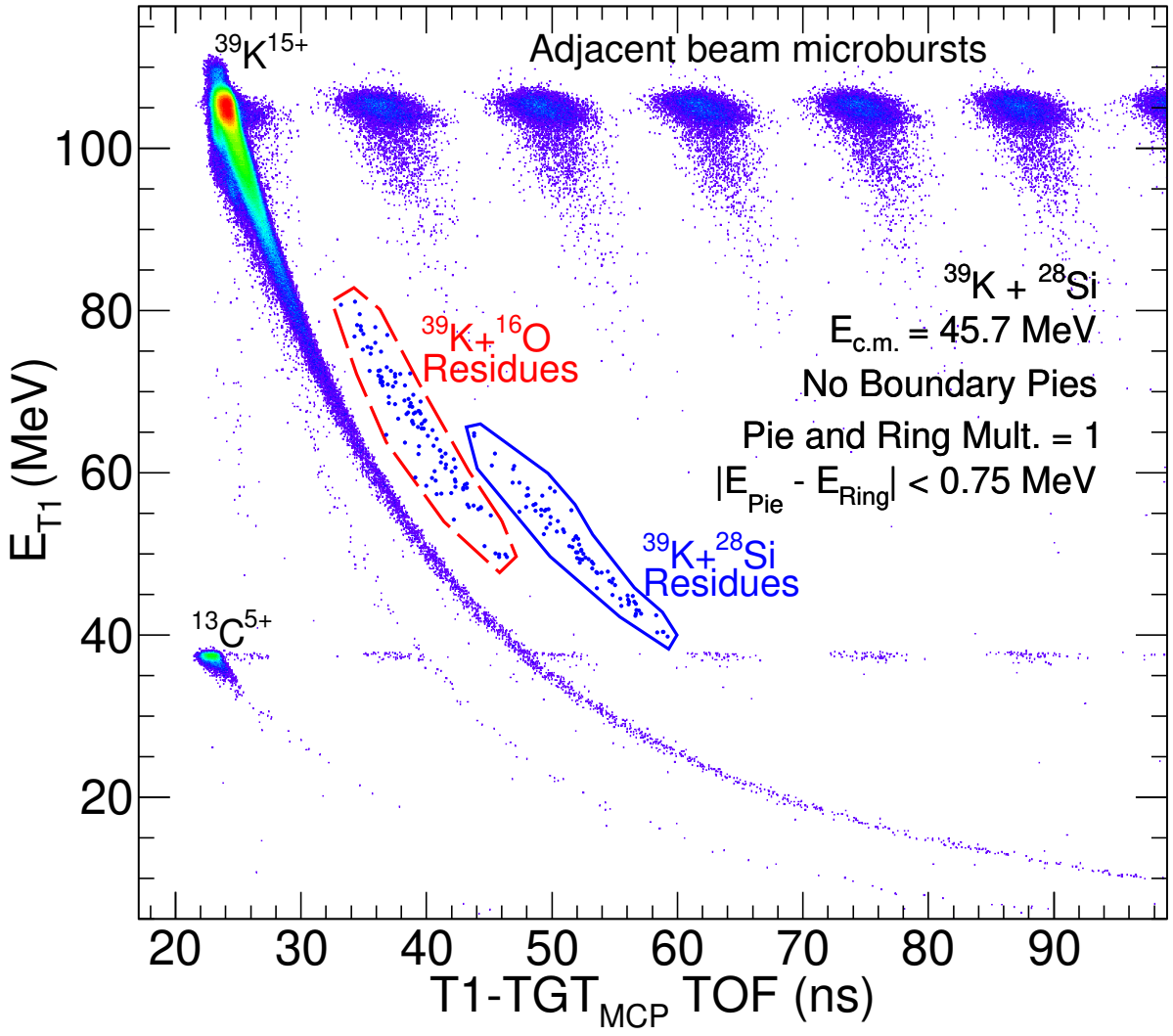

FIGURE 6.15: Energy versus time-of-flight spectrum for ^{39}K + ^{28}Si with the T1 detector.

6.4.2 E-TOF

Guided by the analysis of the ^{19}O + ^{12}C experiment, a clean ETOF spectrum was produced by applying three selection criteria in addition to the MCP-MCP time-of-flight requirement. The three criteria imposed were: a) exactly one pie and one ring are required to have a significant energy, b) the energy measured in the pies and rings should be the same within 750 keV, and c) the quadrant boundary pie segments were rejected. Figure 6.15 shows the resulting ETOF spectrum after all conditions have been

met. In addition to the elastic peak and scatter band of the ^{39}K beam, there are other prominent features in the spectrum that require explanation. The most visible anomaly is the regularly repeating locus of points at the same energy as the elastic peak. Each peak is spaced by approximately 12.5 ns, or 80 MHz, which matches the frequency of the ReA3 LINAC, and can be understood in the following way. When a beam particle passes through the emission foil of the MCP$_{TGT}$ detector and triggers the MCP, the logic signal produced by the MCP signal is held true for ∼100 ns which renders the detector dead for that time period. That beam particle can pass through the rest of the setup unimpeded if it does not react with the target nuclei, but the MCP$_{TGT}$ is still triggered. If another beam particle in one of the following few beam microbursts within that ∼100 ns window reacts with the target and is scattered into T1 or T2, then the time-of-flight will be artificially long by a time equal to the time between the two incident beam particles, which is quantized by the frequency of the LINAC. The start time will have been triggered by the first particle but the stop time will have been triggered by the second. This can also be seen in the repetition of the elastic peak of some ^{13}C contamination from the source shown in the figure at E$_{T1}$ = 37 MeV. Despite this complication, the evaporation residues can still be clearly distinguished.

A more challenging complication than the high frequency of the linac is the presence of residue islands corresponding to two different fusion-evaporation reactions. These two islands correspond to the fusion reaction of the beam with oxygen and silicon nuclei present in the target. The mass of oxygen is sufficiently smaller than silicon such that the evaporation residue islands resulting from reactions with both target nuclei are clearly separated. In Figure 6.15, the residues resulting from fusion with ^{16}O are encircled within the dashed red gate, and those resulting from the reaction with ^{28}Si are circled in blue.

The two residue islands are even better distinguished in the ETOF spectrum for

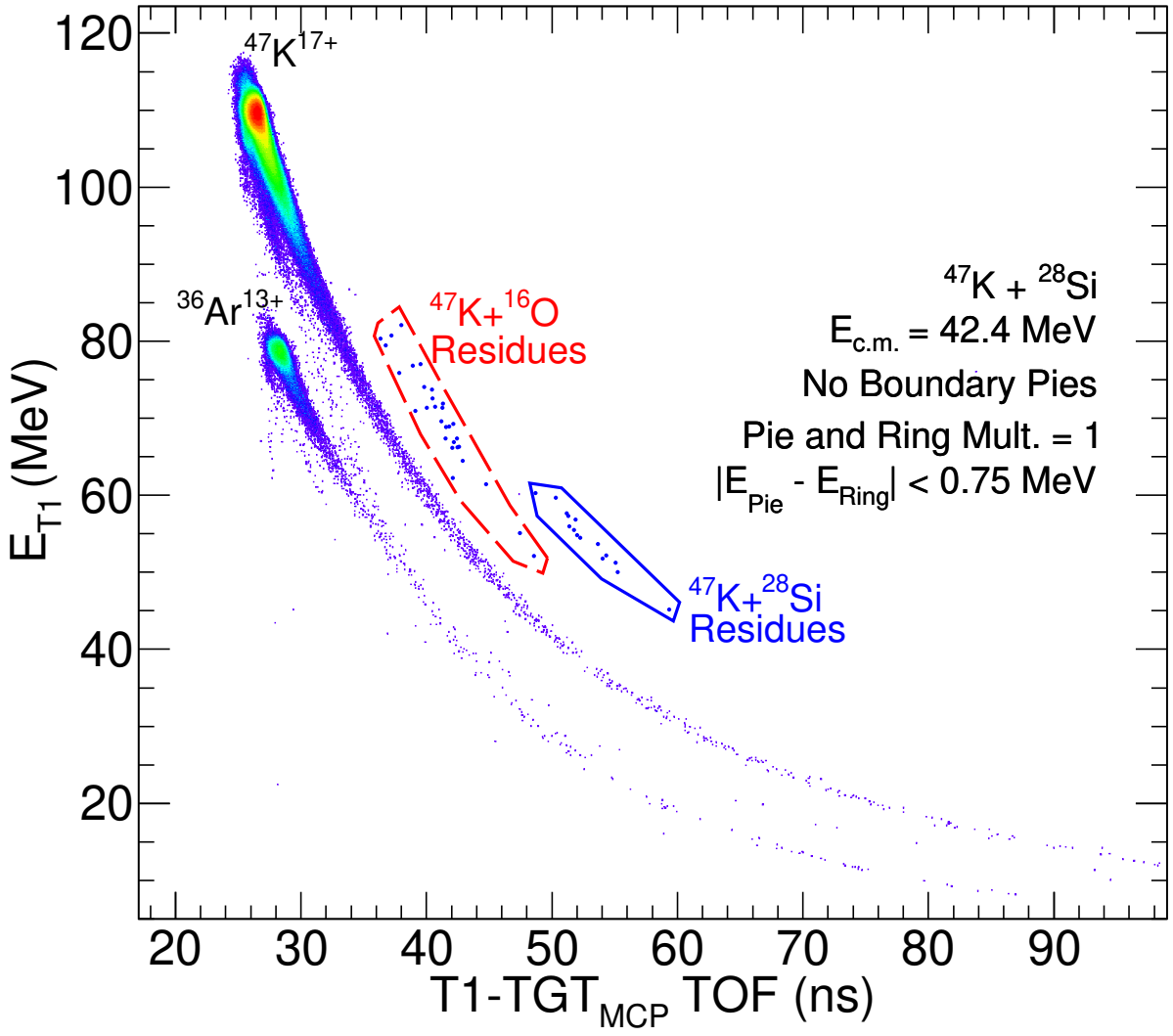

FIGURE 6.16: Energy versus time-of-flight spectrum for ^{47}K + ^{28}Si with the T1 detector.

the ^{47}K induced reaction shown in Figure 6.16. Insertion of RIPD and gating on the ΔE-TOF rejected pileup events, eliminating events where successive beam particles were too closely spaced. Since the electron drift time in RIPD is approximately 100 ns, successive beam particles that enter RIPD within that time period will all ionize the detector gas, and the event will be recorded as the sum of the energy deposit of the two particles. The particle identification requirement of the ΔE-TOF spectrum has an energy component, so events with ΔE greater than a single beam particle will be rejected. The result is an ETOF spectrum like the one in Figure 6.16 where there is no repetitive artifact. The

two residue islands are better distinguished, and the elastic peak and scatter line of some ^{36}Ar beam contamination are visible to the left of the ^{47}K band.

The two residue islands are not as well resolved in the T2 detector, however. Since it is three times closer to the target foil than T1, the time-of-flight from the target foil to T2 is shorter than to T1, so separation in time-of-flight is notably worse. Figure 6.17 depicts the ETOF spectrum from T2 for ^{47}K+28Si. In this best case scenario, the two residue islands are just barely separated and share a somewhat ambiguous boundary. To more accurately distinguish between the two residue islands, the ETOF spectrum can be transformed into an Energy versus Mass Number space, linearized with the relationship $A \propto Et^2$.

6.4.3 Mass calibration

The scatter line for each projectile defines the energy versus time-of-flight relationship for the mass of the projectile, with reasonable statistical quality at all energies. The time-of-flight to mass number conversion was calibrated with the scatter lines for both ^{39}K and ^{47}K. The calibration and conversion are done for each energy to eliminate detector effects such as the "walk" associated with longer times-of-flight for low energy events due to the leading edge discriminator used. To perform the calibration as a function of energy, the scatter line for each projectile was summed across all incident beam energies and projected onto a profile histogram, which plots the average time-of-flight associated with each energy bin as a function of energy. The profile histograms were then fit with a 9th order polynomial, shown in Figure 6.18, which provided the best description of the time-of-flight as a function of energy. Figure 6.19 depicts the summed ETOF spectra for the ^{39}K induced reaction (left) and ^{47}K induced reaction (right). The dashed red lines outlining the scatter lines represent the boundaries used to produce the profile histograms, and the solid black line represents the fit of the profile histograms.

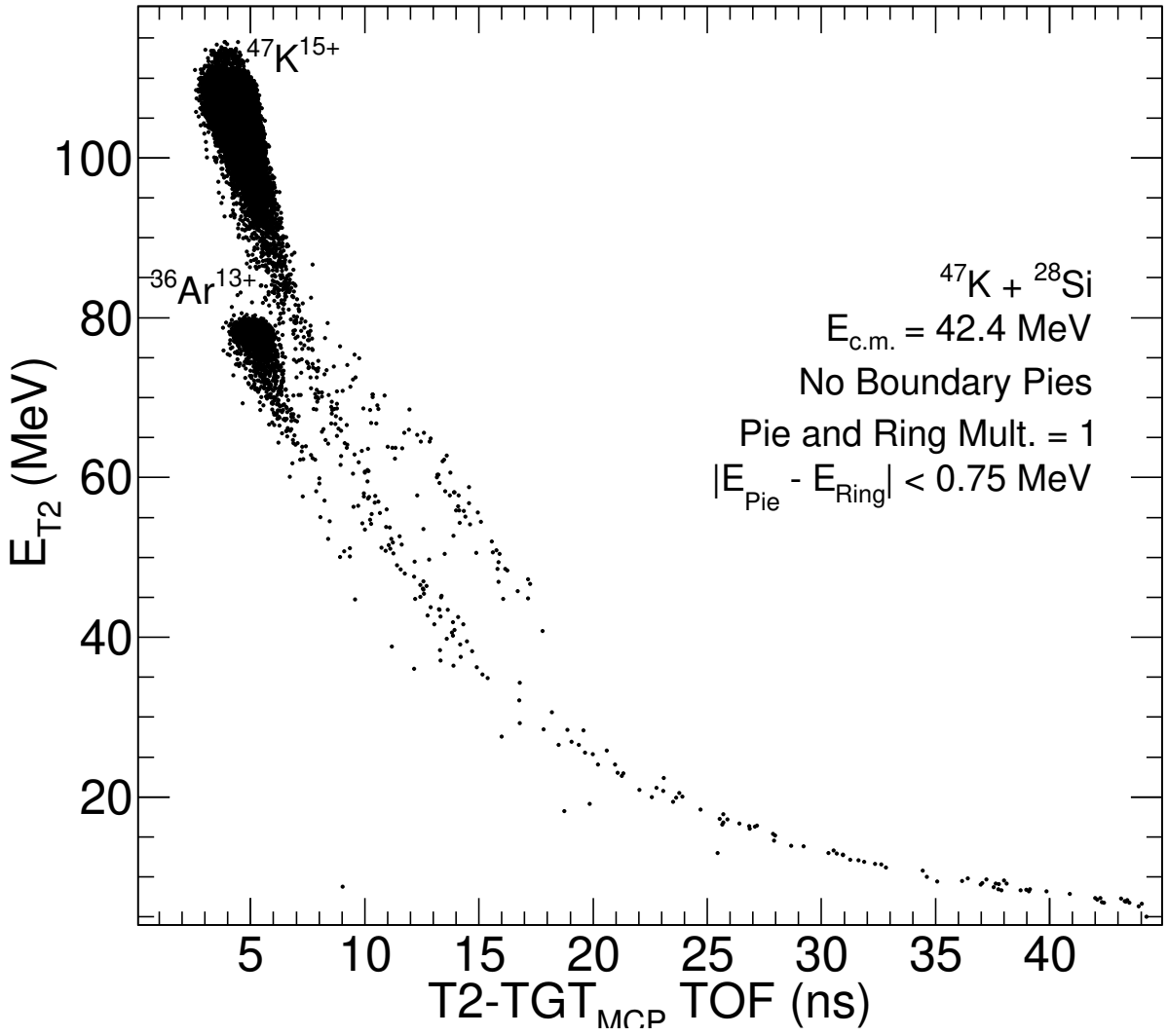

FIGURE 6.17: Energy versus time-of-flight spectrum for ^{47}K + ^{28}Si with the T2 detector.

6.4.4 E vs. A

To convert the time-of-flight to a mass number for a given energy event, the mass curve fits were evaluated at that energy to extract the time-of-flight of the mass curves. A two-point calibration curve was then constructed by plotting the square root of the mass numbers versus time-of-flight. The mass number of the event was then determined by linearly extrapolating the calibration curve out to the measured time-of-flight. Figure 6.20 shows the resulting energy versus mass spectra for T1 and T2. Based on the width of the

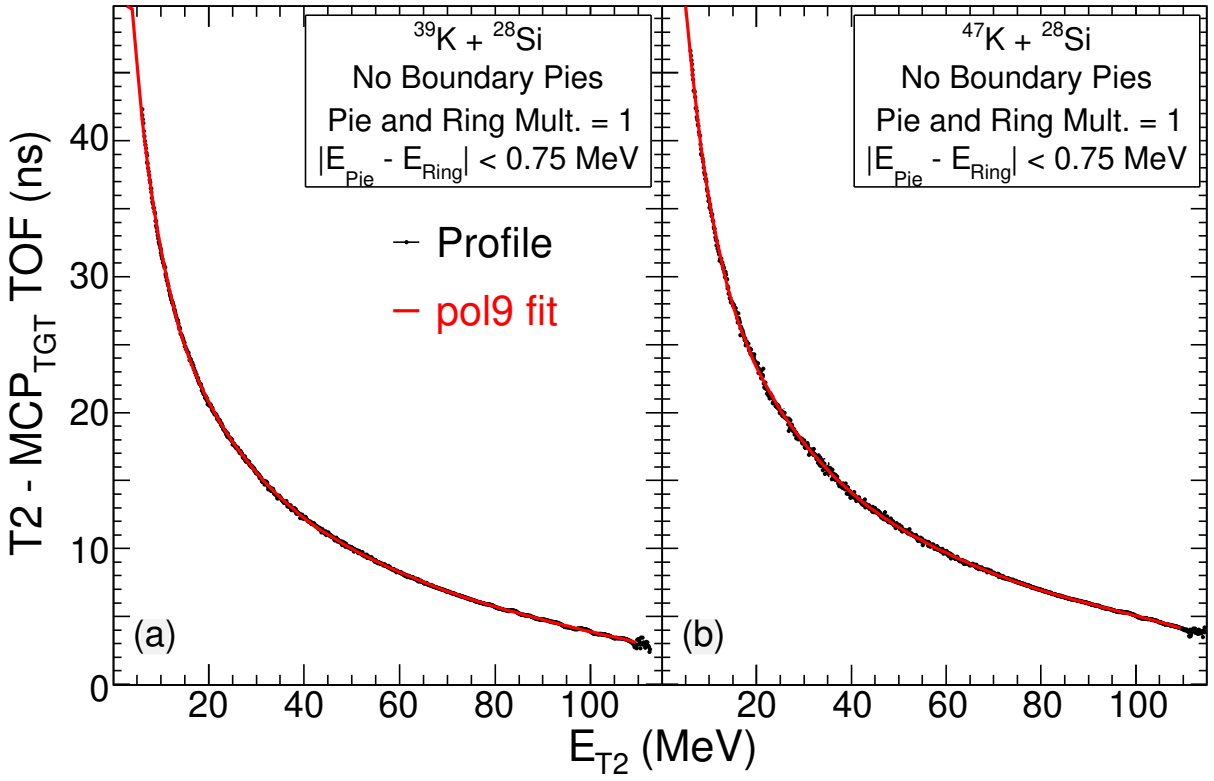

FIGURE 6.18: Profile histograms of the beam scatter lines fit with a 9th order polynomial.

scatter line in this reference frame, the mass resolution of the detectors is ∼0.9 mass units for T1 and ∼2.4 mass units for T2. In this frame of reference, the separation between the oxygen and silicon residue islands is notably improved. Two distinct islands cleanly separated from the scattered beam particles are apparent at high mass (shown in bold). The inset shows the mass distribution of these islands, where a clear separation between the two islands is observed. Although a separation is observed in the projection, a better separation can be observed in the 2D spectrum, especially for T2.

6.4.5 Target thickness

The thickness of the ^{28}Si target foil is the last quantity required to determine the fusion cross-section. The thickness of a pure foil can usually be determined by measuring

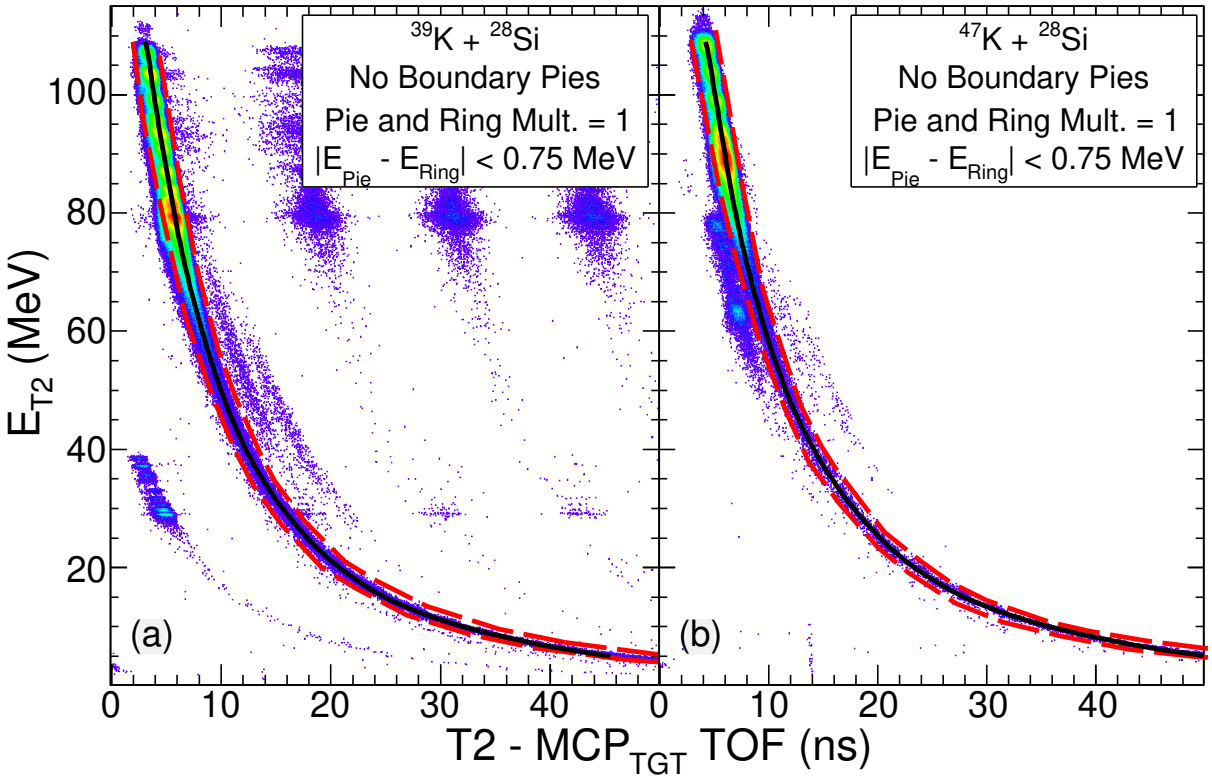

FIGURE 6.19: ETOF spectra for T2 summed over all incident beam energies.

the energy loss of an α particle from a radioactive source as it passes through the foil. Isotopically enriched (>99%) foils were produced by collaborators at INFN - Legnaro in Legnaro, Italy. The foils were produced via electron beam evaporation of silicon metal. Upon deposition of ^{28}Si vapor onto a substrate, the hot silicon atoms are highly sensitive to residual oxygen in the evaporation chamber. Pressures of $<10^{-7}$ torr are desirable. However, for the production of the present target foils, pressures of only 10^{-5} - 10^{-6} torr were achieved. At a temperature of ~1400 °C, the hot silicon foil more rapidly oxidizes, reacting with air that either leaks into the vacuum chamber during the deposition, or air that exposes the foil after deposition and during removal of the foil from the evaporator. Figure 6.21 depicts a typical silicon target foil, with its iridescent sheen owing to the presence of an oxide layer. To ascertain how much of the foil is comprised of silicon nuclei, the amount of oxygen must be determined. The oxygen content can be assessed by using the measured evaporation residues resulting from fusion of potassium ions with

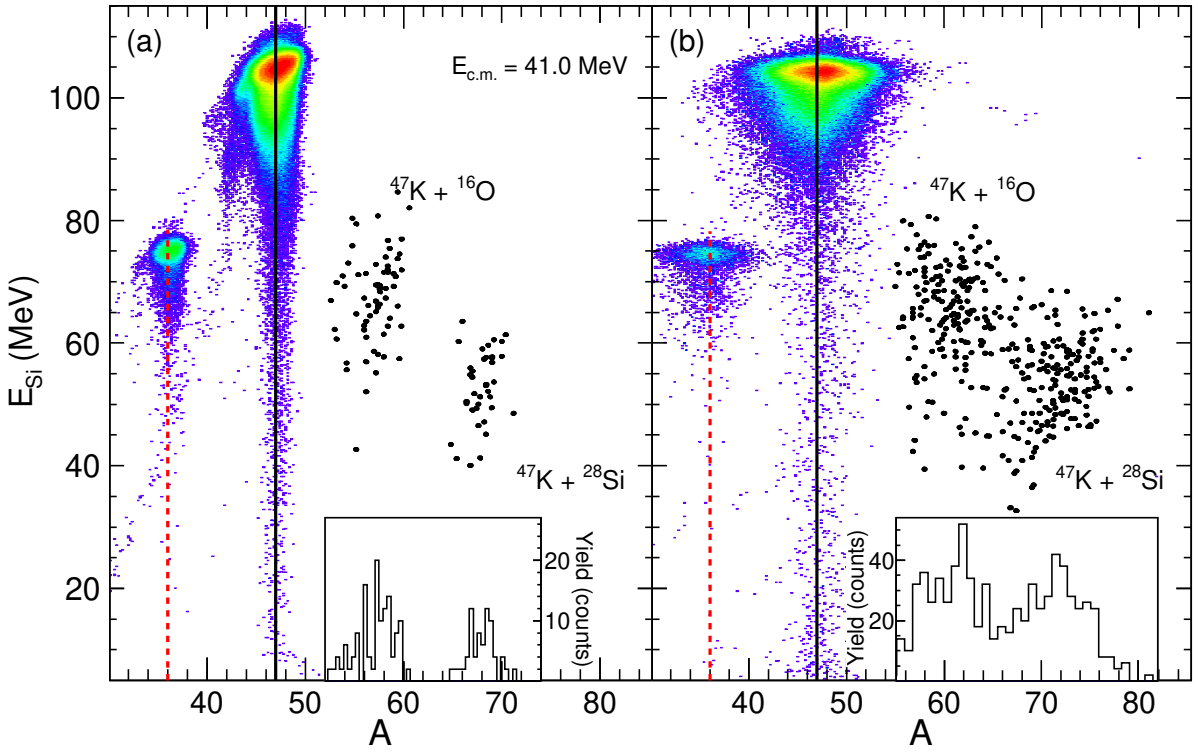

FIGURE 6.20: Energy versus mass number for reaction products measured in T1 (a) and T2 (b). For reference, a solid (black) line and dashed (red) line are shown at A=47 and A=36, respectively. Evaporation residues are shown in bold. Inset: Mass distribution of evaporation residues.

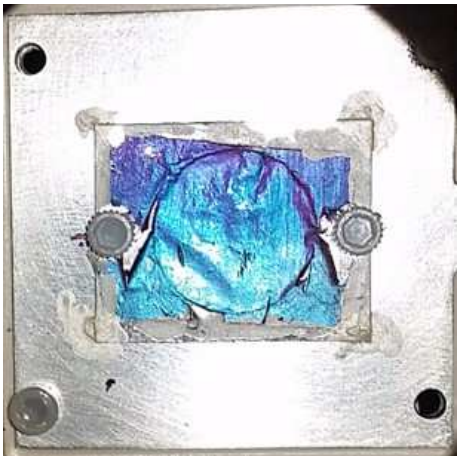

FIGURE 6.21: Photograph of ^{28}Si target foil mounted to a frame.

the oxygen nuclei present in the target foil.

Since the atomic number of oxygen is much lower than that of silicon, the center-of-mass energy for the K+O reactions will be much higher than that of K+Si, and well above the fusion barrier. In this region, the fusion cross-section is less sensitive to the shape of the barrier, so a model can be used to calculate the cross-section with reasonable accuracy. By comparing the calculated cross-section with the measured evaporation residues, the number of oxygen nuclei in the target can be determined.

The fusion excitation functions for ^{39,47}K + ^{16}O, shown in Figure 6.22 as the thick solid lines, were calculated using the coupled channels code CCFULL [139]. The quantity σ_{fusion}/t was determined for each incident energy, where t is the thickness of oxygen. An optimization was then performed to find the value of t that would minimize the χ^2 comparison between the measured σ_{fusion} and the CCFULL calculations for all of the incident beam energies. The value of t was found to be 104.2 $\pm$ 6.7 μg/cm^2 for the ^{39}K data set, and 102.5 $\pm$ 11 μg/cm^2 for the ^{47}K data set. Since the target foil used for both experiments was the same, the oxygen thickness used to determine the silicon content was then taken to be the average of the two data sets, 103.3 $\pm$ 13 μg/cm^2, which corresponds to a SiO_2 linear thickness of 880 nm, using a density of 2.2 g/cm^3 for amorphous SiO_2. This value was also used to calculate the measured fusion cross-sections depicted in Figure 6.22 as the open and closed symbols. Each data set was also fit with the Wong formula, where the fits are represented by the thin dashed lines in the figure. For reference, an arrow marking the height of the fusion barrier is also shown.

To ascertain the remaining amount of silicon nuclei in the target, the energy loss of α particles from a ^{148}Gd source and a ^{241}Am source was measured. Both sources are monoenergetic, with the α particle energy emitted by ^{148}Gd is 3.183 MeV, while the α particle from ^{241}Am has 5.486 MeV. The foil was placed between the source and an SBD, which measured the α particle's residual energy. The energy loss of the ^{148}Gd α was 365

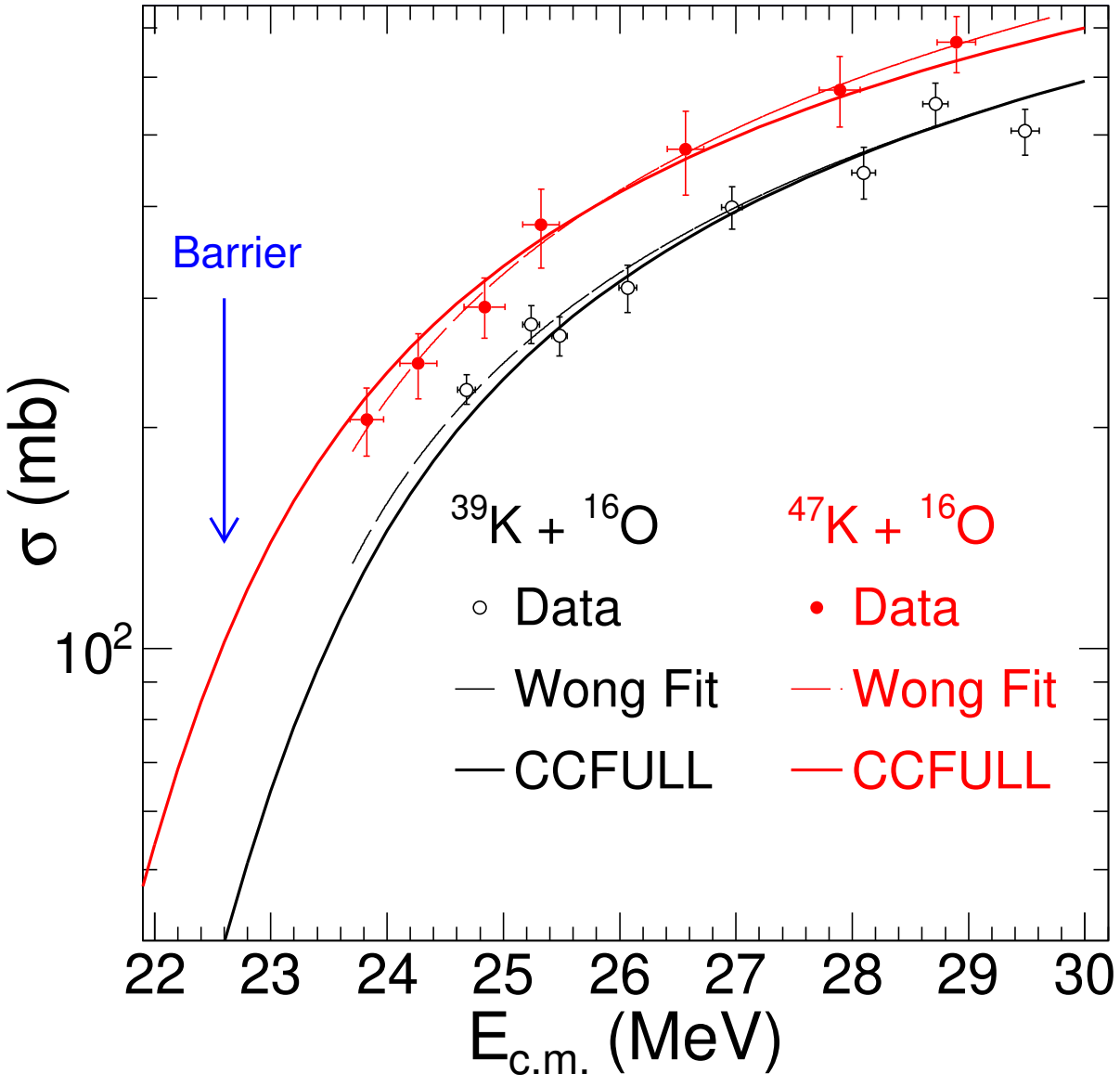

FIGURE 6.22: Fusion excitation functions for ^{39,47}K + ^{16}O. Open and closed symbols depict the results for the ^{39}K and ^{47}K beams respectively. Dashed lines correspond to a fit of the experimental data with the Wong parameterization. Solid lines correspond to model calculations using the code CCFULL.

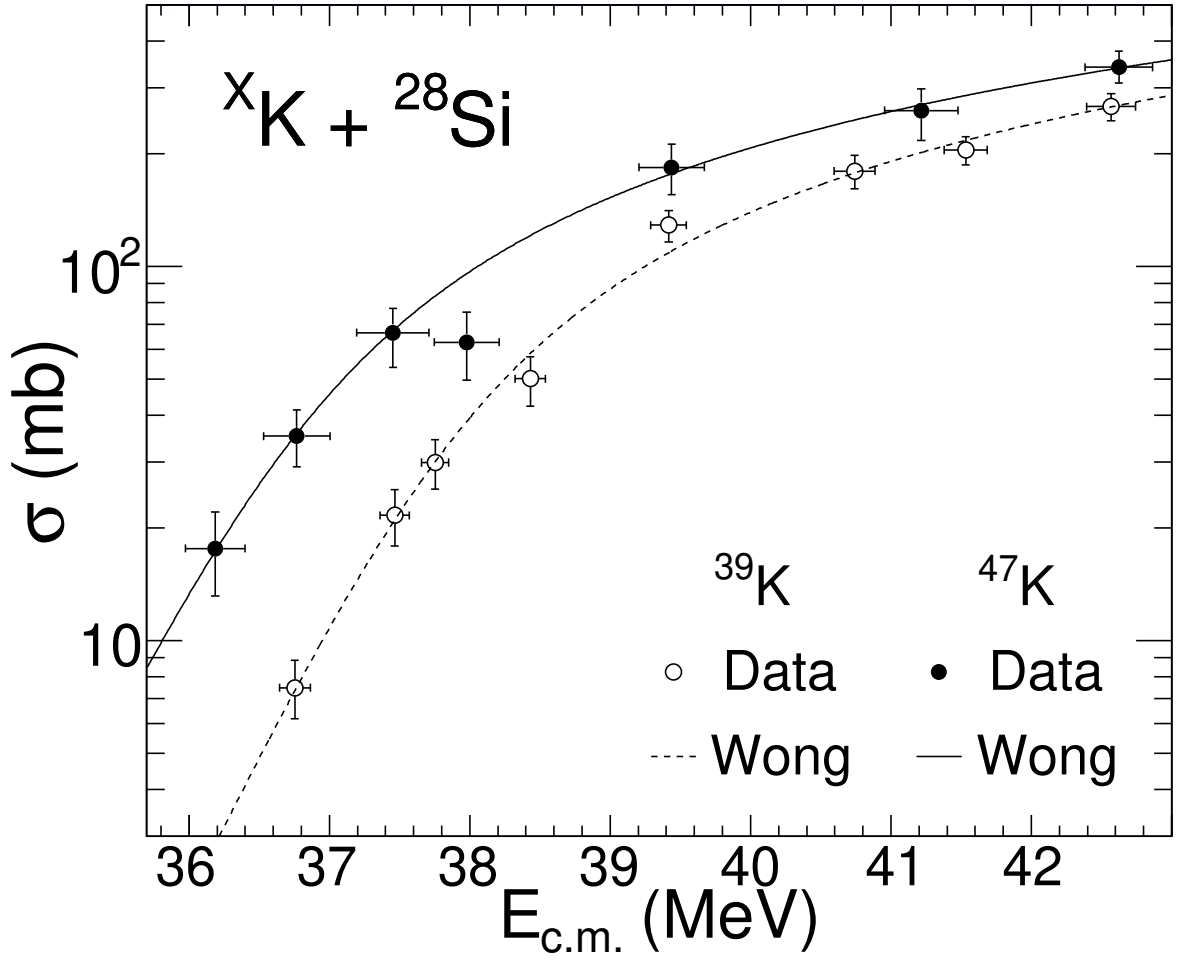

FIGURE 6.23: Experimental fusion excitation functions for ^{39,47}K + ^{28}Si. Open and closed symbols depict the results for the ^{39}K and ^{47}K beams respectively. Dashed and solid lines correspond to a fit of the experimental data with the Wong parameterization.

keV, and that of the ^{241}Am α was 258 keV. Using the program SRIM to calculate charged particle energy loss through media [127], in addition to the 880 nm of SiO_2, the linear thickness of pure silicon required to match the measured energy loss was 970 nm. Using a silicon density of 2.33 g/cm^3, combined with the amount of silicon from the SiO_2, the corresponding total silicon thickness is 316.4 $\pm$ 10 μg/cm^2.

6.5 Excitation functions

The fusion cross-sections as a function of incident energy for ^{39}K + ^{28}Si (open circles) and ^{47}K + ^{28}Si (closed circles) are shown in Figure 6.23. The uncertainty in $E_{c.m.}$ reflects the spread in the beam energy measured just upstream of the target, while the uncertainty in the fusion cross-sections includes both measurement statistics and systematic errors. Both fusion excitation functions exhibit the general trend expected for a barrier-driven process. With decreasing incident energy, the fusion cross-section decreases slowly for energies above the barrier then drops dramatically at and below the barrier. To facilitate comparison of the two systems, the measured fusion excitation functions were parameterized using a functional form that describes the penetration of an inverted parabolic barrier (Wong formula) [120]. The fits of the ^{39}K and ^{47}K data are shown in Figure 6.23 as the dashed and solid lines respectively. With the exception of the ^{47}K cross-section measured at $E_{c.m.}\sim$38 MeV the excitation functions for both systems are reasonably well described by this parameterization.

6.6 Models

In order to better understand the extent to which the observed fusion cross-sections are due to the nuclear size, structure, or dynamics, the fusion of potassium isotopes with ^{28}Si nuclei was calculated with different models. The simplest model utilized is a Sao Paulo (SP) model [64], which allows one to assess the changes in the fusion cross-section due solely to the changes in the density distributions of the nuclei. These density distributions have been calculated within a relativistic mean field (RMF) model [67, 137], and were utilized in a folding potential to predict the fusion cross-sections. As the density distributions are spherically symmetric, initial deformation of the projectile and target nuclei are ignored in this approach. The cross-section predicted from the RMF+SP

model is depicted in Figure 6.24 as the dash-dot (green) line. While this static model provides reasonable agreement at above-barrier energies, it significantly underpredicts the measured cross-sections at energies near and below the barrier for both reactions, indicating that the size of the colliding nuclei alone is insufficient to explain the observed fusion cross-sections.

TABLE 6.1: Woods-Saxon potential parameters for the measured systems.

	V_0 (MeV)	r_0 (fm)	a (fm)
^{39}K + ^{28}Si	-55.03	1.16	0.612
^{47}K + ^{28}Si	-55.97	1.16	0.622

For mid-mass stable nuclei, the role of dynamics (collective modes) in describing the fusion cross-section in the near-barrier regime is well established [62]. Coupled channels calculations [69] were performed, which have been successful at describing the fusion of stable and near β-stable nuclei [62].

The coupled channels calculations performed to describe the fusion of potassium and silicon nuclei utilized the code CCFULL [139], with the potential parameters shown in Table 6.1. For these calculations, coupling to the 1/2+ ground state and the 3/2+ and 5/2+ excited states of ^{47}K were included, and considered to be members of a rotational band. For ^{39}K, the 3/2+ ground state and excited 5/2+ and 7/2+ levels were included. Coupling in the ^{28}Si target nucleus included the 2+ and 4+ levels of the rotational band built on the 0+ ground state. The results of these calculations are shown in Figure 6.24 as the short-dashed (blue) line. While in the case of ^{39}K + ^{28}Si (panel b) the CCFULL calculations provide a good description of the experimental cross-sections, for the ^{47}K induced reaction (panel a) the model slightly overpredicts the data. Although neutron transfer plays no role in the case of ^{39}K due to the associated negative Q-value, in the case of ^{47}K, $Q_{2n} = 3.844$ MeV, suggesting that neutron transfer may play a role. Neutron transfer channels were therefore included in the CCFULL calculations of the ^{47}K induced

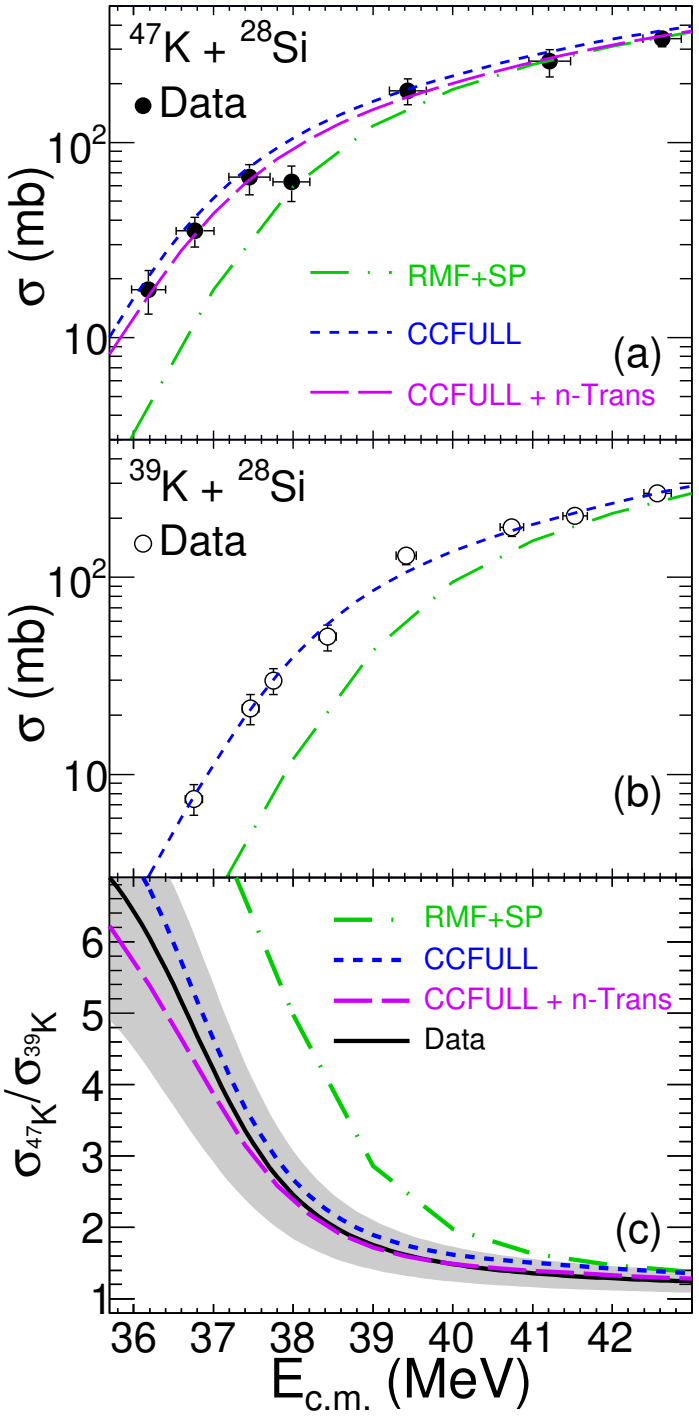

FIGURE 6.24: Panel (a): Experimental data for ^{47}K + ^{28}Si are represented by symbols. Dashed (colored) lines correspond to different models described in the text. Panel (b): Same as above for ^{39}K projectile ions. Panel (c): The relative cross-section, $\sigma(^{47}\mathrm{K})/\sigma(^{39}\mathrm{K})$ is depicted as a solid (black) line, corresponding to the ratio of the Wong fits of the experimental data. The shaded band represents the measurement uncertainty. The dashed (colored) lines correspond to model calculations described in the text.

reaction as a pair-transfer coupling between the ground states, using the macroscopic coupling form factor given by

$$F_{trans}(r) = F_t \frac{dV_N^0}{dr} \tag{6.1}$$

where F_t is the coupling strength and has a value ranging between zero and unity [139]. Inclusion of a coupling with $F_t = 0.25$ provides the best description of the experimental data, as shown by the dashed (purple) line in Figure 6.24(a). Increasing the coupling strength for neutron transfer above $F_t = 0.35$ significantly underpredicts the measured cross-sections in the energy range shown. The reduction in the fusion cross-section with the inclusion of neutron transfer above the barrier is likely associated with transfer that does not lead to fusion. At energies below the barrier, outside the presented energy regime, inclusion of neutron transfer results in an enhancement in the fusion cross-section as expected.

In addition to examining the fusion excitation functions, it is also instructive to construct the relative cross-section, $\sigma(^{47}\mathrm{K})/\sigma(^{39}\mathrm{K})$, as presented in Figure 6.24(c). For an isotopic chain, examining the relative cross-section is valuable as it removes the average behavior of the Coulomb-dominated, barrier-driven process emphasizing the change in the nuclear potential with increasing neutron number. This ratio also results in cancellation of systematic errors common to the measurement of both excitation functions. For energies above the barrier, the ratio for the experimental data is essentially flat with a value of $\sim$1.2, but as $E_{c.m.}$ decreases to and below the barrier, the ratio rapidly increases to a factor of $\sim$6 at the lowest measured energy.

All the model calculations shown in Figure 6.24(c) exhibit the same qualitative trend exhibited by the data. At the highest energies measured, all of the model calculations converge and are in good agreement with the experimental data. This result is

unsurprising, as the cross-section at above-barrier energies are dictated by the geometric cross-section. For energies below the barrier, all the models shown exhibit the trend of increasing relative cross-section with decreasing $E_{c.m.}$. The increase in the relative cross-section with decreasing energy reflects both the larger size of the neutron-rich nucleus, specifically the increased extent of its neutron density distribution, and the dynamics associated with the additional neutrons. The RMF+SP model, with static density distributions, manifests the onset of this rapid increase in the relative cross-section energy at a higher energy than the data. As expected from their agreement with the excitation functions, the CCFULL calculations both excluding and including neutron transfer provide a reasonably good description of the measured relative cross-section within the measurement uncertainties (shaded region). These uncertainties are dominated by the statistical quality of the data. Improvements made after the experiment will enable future experiments to acquire data of better statistical quality, hopefully allowing one to more quantitatively assess the impact of neutron transfer on fusion for neutron-rich nuclei.

Chapter 7

Conclusions

An efficient method for measuring fusion cross-sections of both neutron-rich light and mid-mass nuclei has been established. This method is well suited for measurements of both low-intensity radioactive beams as well as stable beams, making it ideal for systematic comparisons across an isotopic chain of nuclei. The technique is designed to directly detect evaporation residues following fusion between two nuclei and determine the fusion cross-section from the measured evaporation residue cross-section. The direct measurement is accomplished by an energy and time-of-flight technique, where microchannel plate detectors provide timing information and annular silicon detectors situated around the beam axis provide both timing and energy information.

The initial demonstration of this technique was first realized by measuring the fusion cross-sections of ^{18}O + ^{12}C [90], which established a high-precision baseline for a systematic measurement of neutron-rich oxygen isotopes. The measurement was performed using the FN tandem accelerator at the John D. Fox accelerator facility at Florida State University. The beam was pulsed at a rate of 12.125 MHz with an intensity of $\sim 4 \times 10^5$ p/s. The beam was accelerated to energies between 16.25 MeV and 36 MeV. The lowest energy measured corresponds to a cross-section of 2.8 mb, a full order of magnitude lower

than previous measurements. There is good agreement of the cross-section at higher energies where this measurement overlaps with previous measurements, providing a high quality measurement of the fusion excitation function for this system.

This experimentally determined fusion excitation function was then compared with DC-TDHF calculations, which is a fully microscopic many-body theory. This comparison reveals a shape difference in the fusion excitation functions, where the calculations overpredicted the cross-sections at energies above $E_{c.m.} = 7$ MeV and underpredict the cross-sections at energies below 7 MeV. The overprediction at higher energies is not surprising, since DC-TDHF does not account for breakup channels that compete with complete fusion. The fact that the experimental cross-sections decrease more slowly with decreasing energy than the calculated cross-sections can be interpreted as a larger tunneling probability for the experimental data as compared to the DC-TDHF calculations. This enhanced tunneling probability can be associated with a narrower barrier, which deviates from an inverted parabolic shape. The fundamental reason that the barrier determined from the experimental data is weaker than in the theory is presently unclear.

This sub-barrier enhancement prompted another measurement of the $^{18}O + ^{12}C$ fusion cross-sections at Florida State University at even lower beam energies, pushing the measured cross-section down to the 820 μb level. At these lower energies, the deviation between the measurement and the DC-TDHF calculations increases to a factor of 10 at the lowest energy, up from a deviation of a factor of 1.3 from the previous lowest energy point. This significant shape difference in the sub-barrier regime highlights the importance of measuring the fusion cross-section at sub-barrier energies.

The de-excitation of the $^{30}Si^*$ compound nucleus formed in the $^{18}O + ^{12}C$ reaction was also characterized with a simultaneous measurement of the light charged particles emitted following fusion. Angular distributions and energy spectra of the evaporation

residues and α particles were measured, and correlations between the two were constructed. These distributions were then compared with statistical model calculations using the code EVAPOR. The angular distribution of the residues revealed that EVAPOR significantly underpredicts the yield of large angle residues associated with α emission exit channels. The energy spectra and angular distributions of the α particles indicate that the α particles were emitted via statistical decay, but the total yield of α particles was significantly underpredicted by EVAPOR. The α emission cross-sections of other ^{X}O + ^{X}C reactions were constructed from previous measurements found in the literature, and also found to be significantly higher than the predictions from EVAPOR. These results provide confidence that the larger α emission cross-sections compared to statistical model calculations is a more general feature of light heavy-ion reactions, and not simply restricted to the ^{18}O + ^{12}C system or the result of systematic uncertainties in the measurement. The increase in α emission following fusion suggests a preference for α emission over other exit channels. Since oxygen and carbon isotopes are known to exhibit α cluster structure [124, 125], one interpretation of this increase could be that the initial α cluster structure in the entrance channel persists through the fusion process, making α emission following fusion more likely. Recent theoretical developments have suggested another interpretation, that there is dynamic α cluster formation in precompound states formed during fusion between light nuclei [135].

Continuing the campaign to measure the fusion cross-sections for increasingly neutron-rich isotopes of oxygen, the fusion excitation function for ^{19}O + ^{12}C was measured for the first time [133]. This also represents the first measurement of a low-intensity radioactive beam made with the present experimental setup. The experiment was also performed at Florida State University, where a primary beam of ^{18}O ions was accelerated with the tandem accelerator before impinging on a deuterium gas cell. ^{19}O ions were produced via a (d,p) reaction and separated from other reaction products using the RESOLUT spectrometer. A gas ionization chamber was added to the experimental setup to modify

the incident beam energy and provide a way to reject beam contaminants. Since ^{18}O was one of the beam contaminants, a simultaneous measurement of the fusion cross-sections for ^{18}O + ^{12}C was made. There is good agreement between the ^{18}O measurement from the radioactive beam and the previous high-precision ^{18}O measurement made with the stable beam, providing confidence in the measured fusion cross-sections in the ^{19}O + ^{12}C system.

The measured fusion excitation function for ^{19}O + ^{12}C was compared with the ^{18}O + ^{12}C high-precision measurement. At all incident energies, the fusion cross-sections for the ^{19}O induced reaction are higher than those for the ^{18}O induced reaction. The enhancement of the ^{19}O cross-sections is approximately constant at a factor of 1.3 higher than the ^{18}O cross-sections for energies above the barrier. Below the barrier, the cross-sections for the ^{19}O induced reaction decrease more gradually than the ^{18}O induced reaction, increasing the enhancement to a factor of $\sim$3 at the lowest energy measured. This represents the first experimental evidence for fusion enhancement in radioactive oxygen isotopes.

Comparisons with different model calculations were made in order to better understand whether the fusion enhancement observed for ^{19}O is associated with changes in the nuclear structure or an increased role of dynamics as the neutron number increases. To see if these changes were primarily due to structure, a static barrier penetration model was used to calculate the fusion cross-sections using the Sao Paulo method with nucleon density distributions calculated from an RMF model. The RMF+SP calculations provide a reasonably good description of the ^{18}O + ^{12}C system, but they significantly underpredict the ^{19}O + ^{12}C fusion cross-sections. DC-TDHF calculations were used to see if the inclusion of dynamics better explains the observed fusion enhancement. The DC-TDHF calculations agree quite well with the ^{19}O + ^{12}C fusion excitation function, but overpredict the fusion cross-sections for ^{18}O + ^{12}C at energies above the barrier. It has been previously demonstrated that the treatment of nucleon pairing in the DC-TDHF

significantly affects the above-barrier fusion cross-sections [90], so the good agreement with ^{19}O + ^{12}C could be attributed to the lack of pairing in the last valence neutron of ^{19}O. This hypothesis will be tested in an upcoming experiment to measure the fusion cross-sections of ^{20,21}O + ^{12}C, anticipated to be performed in the next few years at the GANIL/SPIRAL1 facility in Caen, France.

In an effort to explore the degree of fusion enhancement for neutron-rich mid-mass nuclei, the fusion cross-sections for ^{39,47}K + ^{28}Si were measured [145]. This system allows exploration of the influence of a large change in the number of neutrons - a span of 8 neutrons from stability. This experiment was performed at the National Superconducting Cyclotron Laboratory at Michigan State University using the ReA3 reaccelerator facility, which provided beams of ^{39}K and ^{47}K at energies of 2-3 MeV/u with intensities of 1-4.5$\times10^4$ p/s.

The fusion excitation function for ^{47}K + ^{28}Si was compared with that for the ^{39}K + ^{28}Si system. At all energies, the ^{47}K induced cross-sections are higher than those for ^{39}K, where an increase of a factor of 1.2 is seen at energies above the barrier. Below the barrier, the fusion cross-sections for ^{47}K + ^{28}Si decrease more gradually than ^{39}K + ^{28}Si, increasing the enhancement to a factor of $\sim$6 at the lowest measured energy. A series of model calculations were performed to better understand the extent to which the observed fusion cross-sections are due to nuclear size, structure, or dynamics. The RMF+SP model was used to assess changes in the fusion cross-sections due solely to changes in the density distributions of the nuclei. At energies above the barrier, the RMF+SP calculations agree with the experimental data for both systems, but as the energy decreases below the barrier, the RMF+SP calculations increasingly underpredict the experimental data. This indicates that size alone is insufficient to explain the observed fusion cross-sections at sub-barrier energies. The role of dynamics was probed by performing coupled-channels calculations with the CCFULL code. By utilizing previously measured energy levels in the

projectile and target nuclei, the effects of coupling to vibrational and rotational collective modes from mutual excitations as the nuclei approach each other could be included in the cross-section calculation. The CCFULL calculations provide a good description of the ^{39}K induced reaction. When coupling to neutron transfer channels is included, the coupled channels calculations are also able to describe the ^{47}K induced reaction. This description of both the ^{39}K and ^{47}K induced reactions by CCFULL indicates that the coupled channels approach is capable of describing the change in the dynamics as the projectile becomes more neutron-rich.

The successful description of the fusion excitation functions by the CCFULL calculations requires further investigation. Whether this agreement is due to the fact that both projectile nuclei have a closed neutron shell of N=20 and N=28 will be determined in an upcoming experiment to measure the fusion cross-sections for ^{41,45}K + ^{28}Si. It is anticipated that this experiment will be performed at NSCL within the next year. To explore the effect of the unpaired proton, another experiment will measure the fusion cross-sections for ^{36,44}Ar + ^{28}Si at NSCL. Both of these experiments will provide more insight into the role of nuclear structure on the fusion process for neutron-rich nuclei.

Appendix A

Electronics

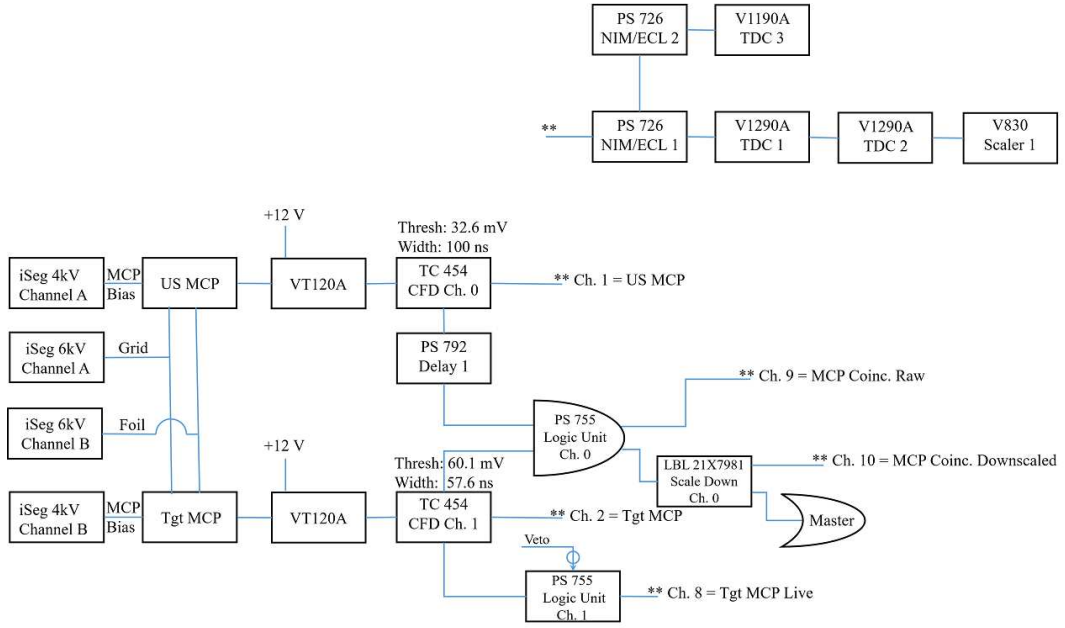

FIGURE A.1: Electronics diagram for the MCP detectors used in the ^{39,47}K + ^{28}Si experiment.

The electronics diagrams for the ^{39,47}K + ^{28}Si experiment are described in this section. The diagrams for ^{18}O + ^{12}C can be found in the thesis of T. K. Steinbach [104]. Figure A.1 shows the electronics diagram for the upstream (US) and target (TGT) microchannel plate (MCP) detectors. Each MCP, as well as the emission foils and accelerating plates in both detectors, were biased using computer controlled iSeg high voltage power supplies (HVPS). The microchannel plate in each detector produces a fast timing

signal for an incident charged particle on the secondary emission foil. Each MCP detector utilizes an ORTEC VT120A fast timing pre-amplifier to amplify the anode signal by a factor of 200. The VT120A pre-amplifiers were located immediately outside of the vacuum chamber to minimize noise pick-up prior to the amplification. The signals were then sent to a Tennelec TC 454 constant fraction discriminator (CFD). One output of each CFD was sent to a Phillips Scientific (PS) level translator to convert the logic signal from NIM standard to ECL. The ECL signal was then sent two CAEN V1290A time-to-digital converters (TDCs), a CAEN V1190A TDC, and a CAEN V830 scaler. A second output of the CFD for both the US and TGT MCPs was sent to a PS 755 logic unit operating in AND mode. The US MCP signal was first sent through a PS 792 cable delay module to match the timing of the TGT MCP signal. This produced a coincidence logic signal when both the US and TGT MCP detectors were fired. This coincidence was sent to the three TDCs and the scaler. One branch of the MCP-MCP coincidence was sent to a downscaler which reduced the rate of the signal by a factor of ***. This downscaled signal was also sent to the the TDCs and scaler as well as to the master trigger, which triggers the data acquisition (DAQ) to record all of the detector signals. The importance of downscaling the coincidence used in the master trigger is to prevent the full electronics from triggering every time a beam particle passes through the MCP detectors and will instead just sample the beam at a reduced rate. A third output of the CFD for the TGT MCP goes to a logic unit that is vetoed by the computer/hardware busy to report how often the DAQ is busy. This is useful during the experiment to monitor the DAQ system.

Figures A.2 and A.3 show the electronics diagrams for the T1 and T2 silicon detectors respectively. Each detector was biased using an Ortec Quad HVPS. The analog signals from the Si detectors provides information on the energy deposited into the detector as well as timing information. The ring segments of each detector produced an energy signal while the pie segments of each detector produced both an energy signal as well as a timing signal. The 24 ring signals were amplified by charge sensitive amplifiers (CSAs)

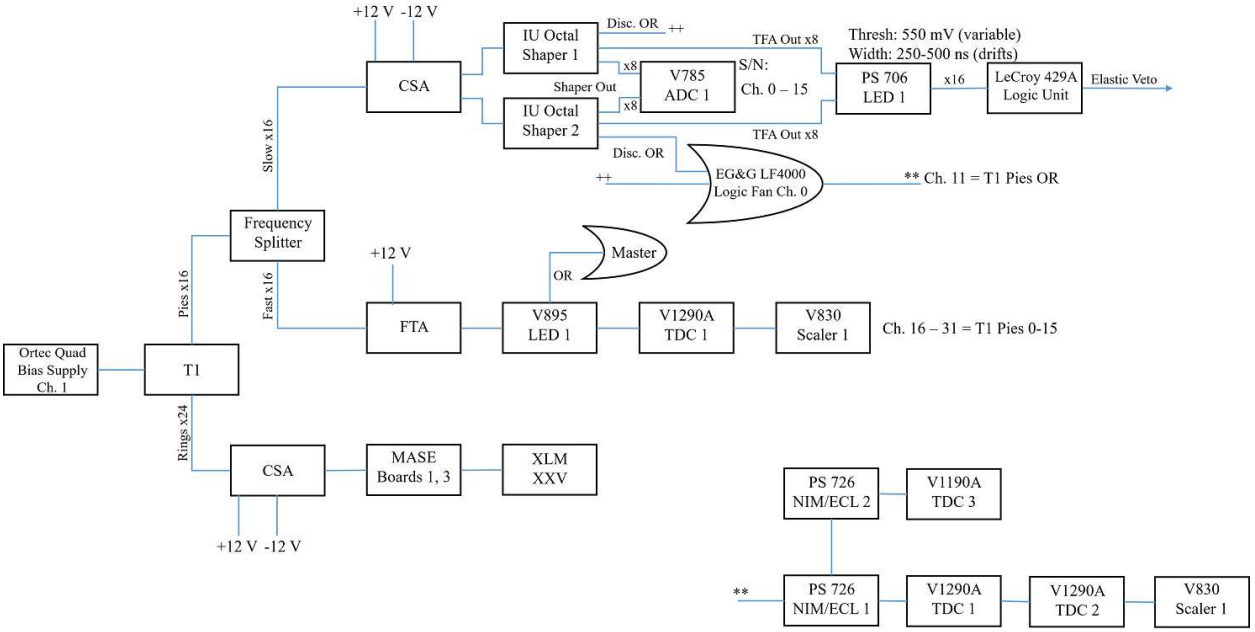

FIGURE A.2: Electronics diagram for the T1 silicon detector used in the ^{39,47}K + ^{28}Si experiment.

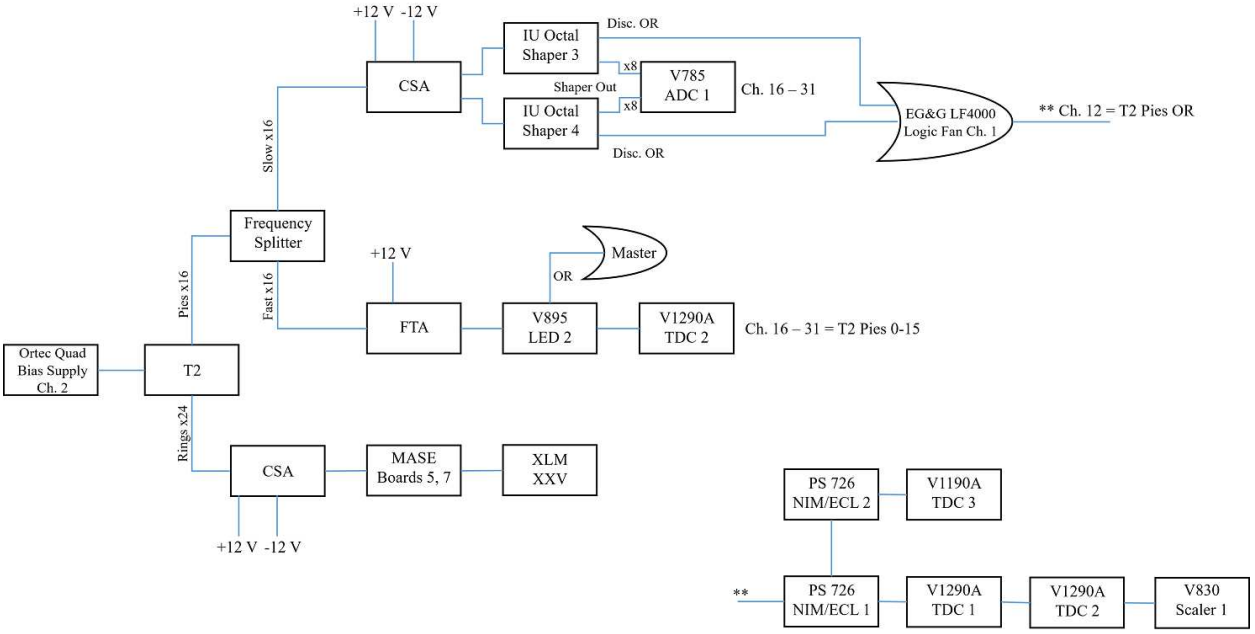

FIGURE A.3: Electronics diagram for the T2 silicon detector used in the ^{39,47}K + ^{28}Si experiment.

with a gain of 15 mV/MeV and then sent to MASE shaping amplifiers [146] followed by a JTEC XLM XXV module. The 16 pie signals are split into fast and slow signals using a frequency splitter. The fast signals were sent to fast timing amplifiers (FTAs) [101], while the slow signals were sent to CSAs. After the FTAs the fast timing signals were sent to a CAEN V895 leading edge discriminator (LED) and then individually sent to a CAEN V1290A TDC and scaler. The OR logic output of the LED was sent to the master trigger. After the CSAs, the slow signals were sent to 8-channel shaper/discriminator/timing-filter-amplifier (TFA) modules (IU Octal Shaper) [106]. The shaper and discriminator settings are computer controlled. The analog outputs of the shaper were then sent to a CAEN V785 peak sensing analog-to-digital converter (ADC). The OR logic output of the discriminators were then combined as an OR with an EG&G LF4000 logic unit, and this output was sent to the three TDCs and the scaler. Since the angles covered by T1 are much smaller than T2, the rate of triggering this detector on elastically scattered beam particles is much higher than T2. Therefore, an attempt to build in a rejection of the elastic trigger was incorporated. The analog TFA outputs of the IU Octal Shaper units were sent to a PS 706 LED unit, where the threshold was set to just below the signal height corresponding to the elastic beam energy. An OR of the logic output of this LED was then sent into the trigger veto.

In the design of this experiment, it was anticipated that the protons and α particles emitted following the decay of the compound nucleus would be measured in a silicon detector telescope designated T3. However, the yield of these particles was far too low to adequately analyze, so the data from the T3 detectors was not used in the analysis of the experiment. For the sake of accuracy, the electronics for the T3 telescope is described here. The diagram for the T3 telescope electronics is shown in Figure A.4. The telescope is comprised of a 300 μm-thick S1-type silicon detector (T3a) backed by a 500 μm-thick S1-type silicon detector (T3b). The rings of each detector utilize the same electronic path as the rings of T1 and T2. However, some of the ring segments for the T3b detector were

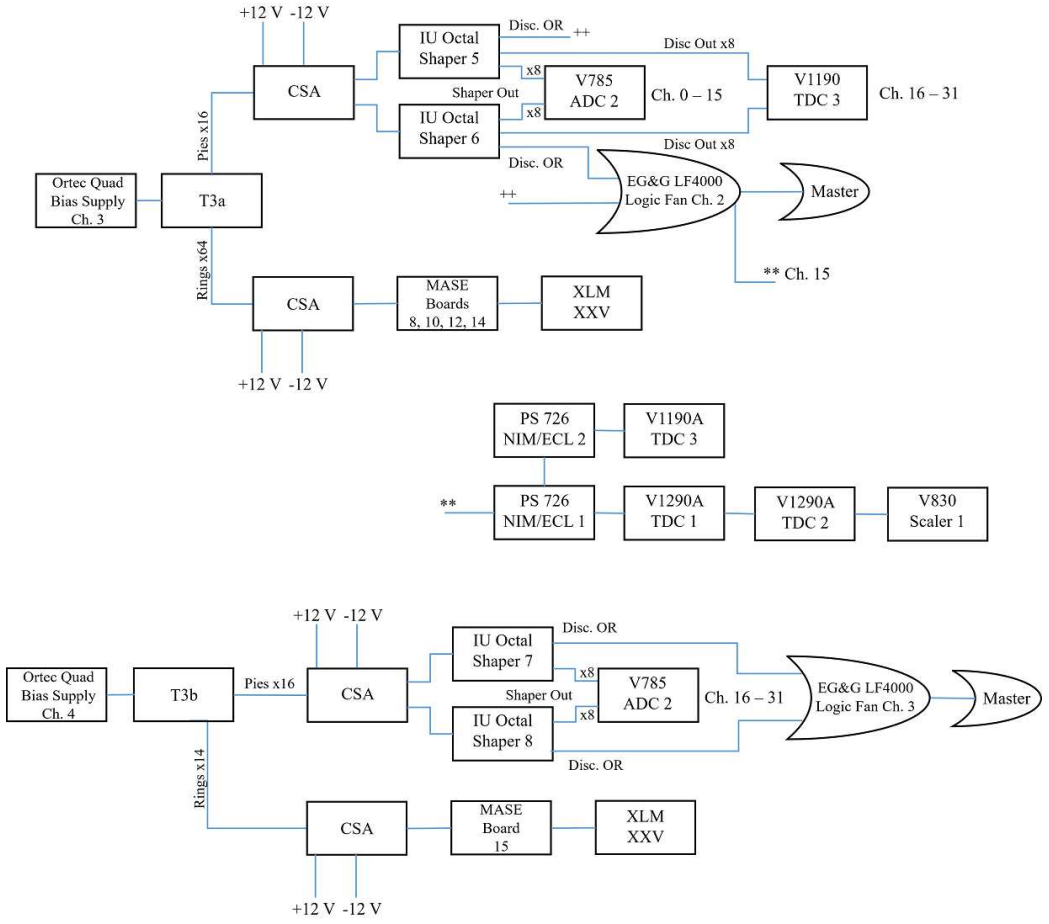

FIGURE A.4: Electronics diagram for the T3 silicon detector telescope designed for the ^{39,47}K + ^{28}Si experiment.

shorted together to reduce the number of channels from 64 down to 14. Unlike T1 and T2, the pie signals from the T3 detectors went directly to CSAs without splitting into two frequency components. The amplified signals were then sent to IU octal shaper modules, and the shaped output signals were sent to a V785 ADC. The timing signals for T3a were recorded by sending the individual discriminator outputs from the IU octal shaper module to the V1190 TDC. The OR outputs of the discriminators for both T3a and T3b were sent to the master trigger, and the OR of T3a was also sent to the TDC/scaler branch.

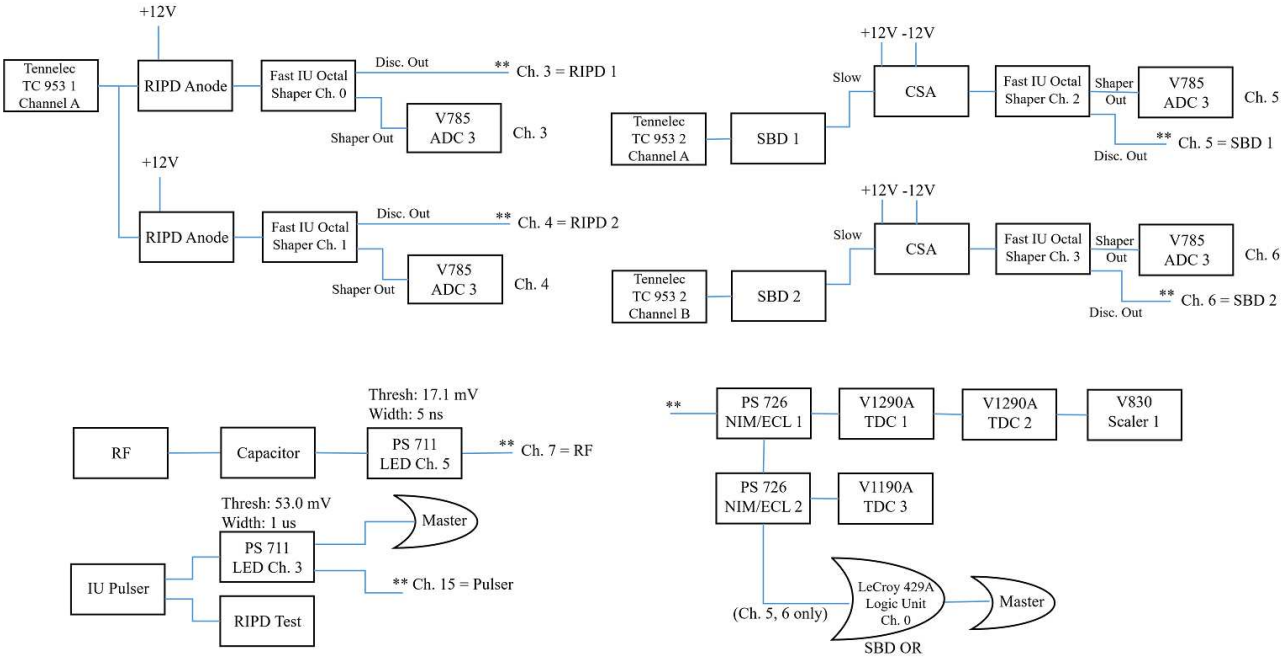

FIGURE A.5: Electronics diagram for the SBDs, RIPDs, RF signal, and pulser used in the ^{39,47}K + ^{28}Si experiment.

The diagram for the RIPD high-rate ionization chambers and surface barrier detectors (SBDs) are shown in Figure A.5. The anodes of RIPD and the SBDs were biased by two Tennelec TC 953 HVPS. The RIPD anode signals from the integrated fast CSAs, as well as the CSA signals from the SBDs, were sent to a fast IU Octal Shaper module [106]. The outputs of the shaper were then sent to an ADC. The discriminator outputs were sent to the three TDCs and scaler. The 80 MHz RF signal of the accelerator was sent to the TDCs and scaler, as well as a 0.5 Hz signal from a test pulser that was also sent to the test input of RIPD.

The master trigger electronics shown in Figure A.6 are used to produce a "master" logic signal which determines when events will be recorded by the computer. The master trigger is created by making an OR of the T1 fast OR, the T2 fast OR, and the downscaled Tgt/US MCP-MCP coincidence. There is also a veto to this trigger that is created from the OR of the computer busy and hardware busy signals, and occasionally a logic signal

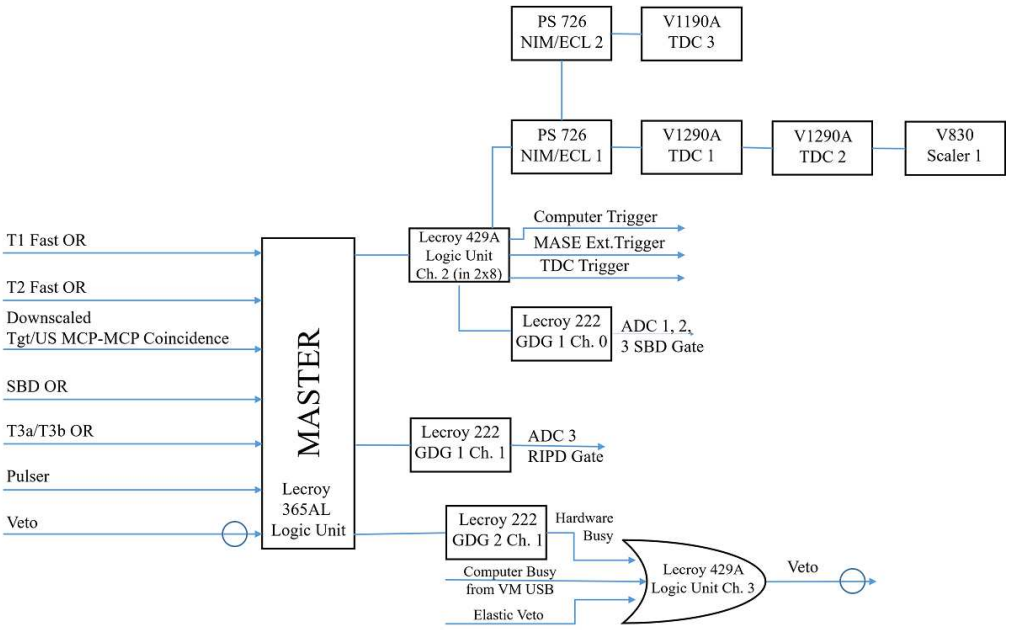

FIGURE A.6: Electronics diagram for the master trigger used in the ^{39,47}K + ^{28}Si experiment.

from the elastic beam signals in T1. The computer busy signal is provided by the O1 output of the Wiener VM-USB controller. The hardware busy was created using a Lecroy 222 gate and delay generator (GDG) triggered off of the master trigger to produce a logic signal 42 μs long. The 42 μs duration is long enough to allow the DAQ to receive all of the data from each individual module. The master trigger was then sent to the three TDCs as the reference and also to the scaler. In addition, the master trigger was used to trigger the TDCs, MASE, and the computer. The master trigger was also sent to a Lecroy 222 GDG to create the ADC gates.

Appendix B

Foil thickness determination

B.1 Setup

B.1.1 Foils

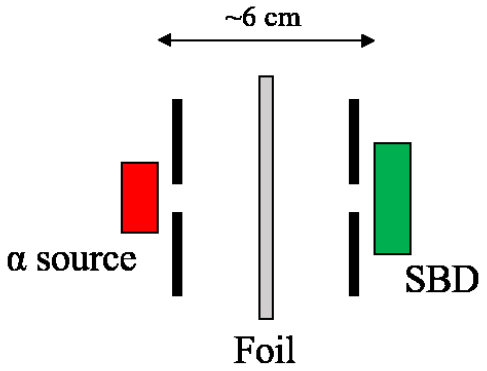

FIGURE B.1: Experimental setup used to determine foil thicknesses. The α particles emitted by a radioactive source traverse the foil and are detected by a silicon surface barrier detector (SBD). 5 mm diameter collimators (shown in black) are placed in front of the α source (red) and SBD (green). The foil (grey) is inserted between the source and the SBD, which are separated by ~6 cm.

Aluminum foils were prepared by vapor deposition using an electron beam evaporator. Glass microscope slides were used as substrates, and detergent was used as a parting agent. Carbon foils were provided by Arizona Carbon Foil Company (ACF), and ^{28}Si foils were provided by Legnaro National Laboratory (LNL). The aluminum and carbon foils

were floated off of the glass substrates onto the surface of a bowl of DI water. The foils were then picked up onto stainless steel frames each with a 13 mm diameter opening. The ^{28}Si foils provided by LNL were already mounted on 15 mm diameter aluminum frames, where half of the frames held two foil layers. Each foil was given an identification number in the following manner. The aluminum foils were labeled with their slide number and position on the slide (e.g. foil 4A is the first foil from slide 4). The carbon foils were labeled with their nominal thickness given by ACF and the number of foil layers measured (e.g. foil 2x50 is a measurement of 2 layers of nominally 50 μg/cm^2 C). Mylar foils were labeled based on their nominal thickness in μm, and the ^{28}Si foils were labeled by their number of layers; foils starting with *A* correspond to the single layer ^{28}Si foils, and those starting with *B* correspond to the double layer ^{28}Si foils.

B.1.2 Thickness Measurement

The experimental setup is shown in Figure B.1. Alpha particles emitted by a radioactive source with a 5 mm diameter collimation were measured by a silicon surface barrier detector (SBD) with a 5 mm diameter aperture, situated 6 cm away from the source. Thin self-supporting foils were inserted between the source and the SBD. The sources used were ^{148}Gd and ^{241}Am. A ^{226}Ra source was also used in the SBD calibration. The signal from the SBD was first amplified by a charge-sensitive amplifier, and then by a custom shaping amplifier (IU Octal Shaper). The shaped signal was then sent to a V795 peak sensing analog-to-digital converter (ADC).

B.2 Calibration

The SBD was calibrated by measuring the α particles from ^{148}Gd, ^{241}Am, and ^{226}Ra with the foils retracted out of the flight path. The energy of α particles emitted by

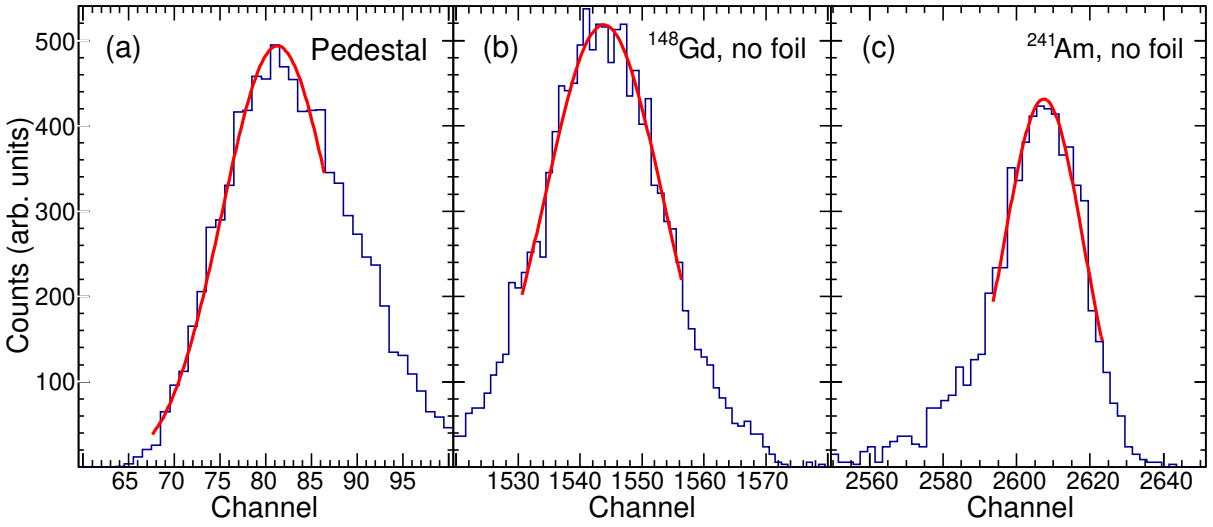

FIGURE B.2: Measured spectra of α particles from ^{148}Gd (b) and ^{241}Am (c). The pedestal is shown in panel (a).

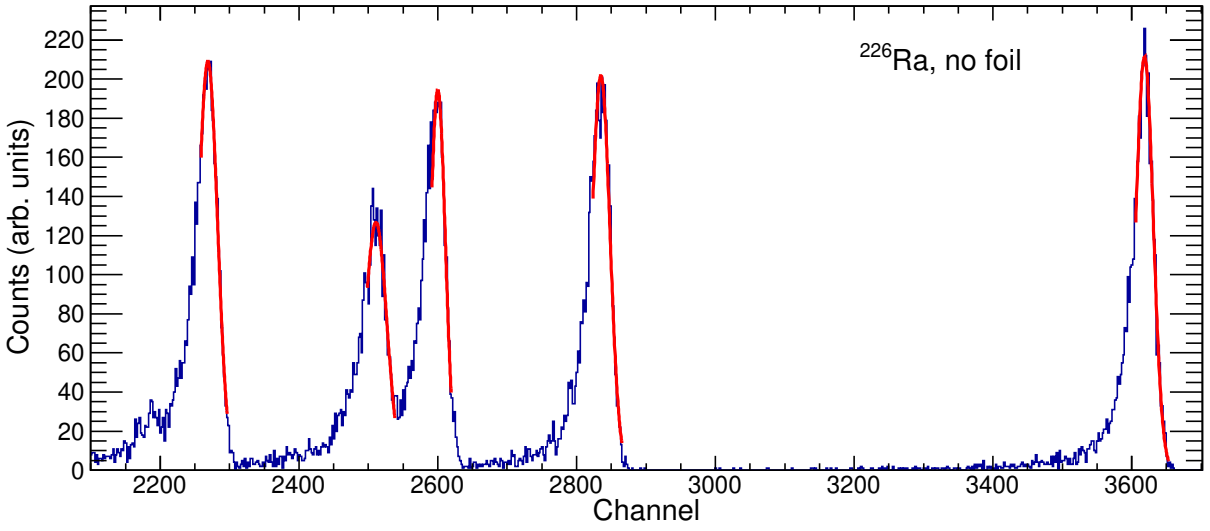

FIGURE B.3: Measured spectrum of α particles from ^{226}Ra.

these sources are well known (3.183 MeV for ^{148}Gd, 5.486 MeV for ^{241}Am, 4.784, 5.304, 5.489, 6.002, and 7.686 MeV for ^{226}Ra). Figures B.2 and B.3 depict the uncalibrated energy spectra of these different sources, where the peaks corresponding to the energies of the different α particles are shown parameterized by Gaussian distributions. Figure B.2 also depicts the peak of the "pedestal", which is the background level of the ADC corresponding to zero energy (no signals from the detector). The centroids of the Gaussian fits and their associated errors were used to produce a calibration curve, shown in Figure

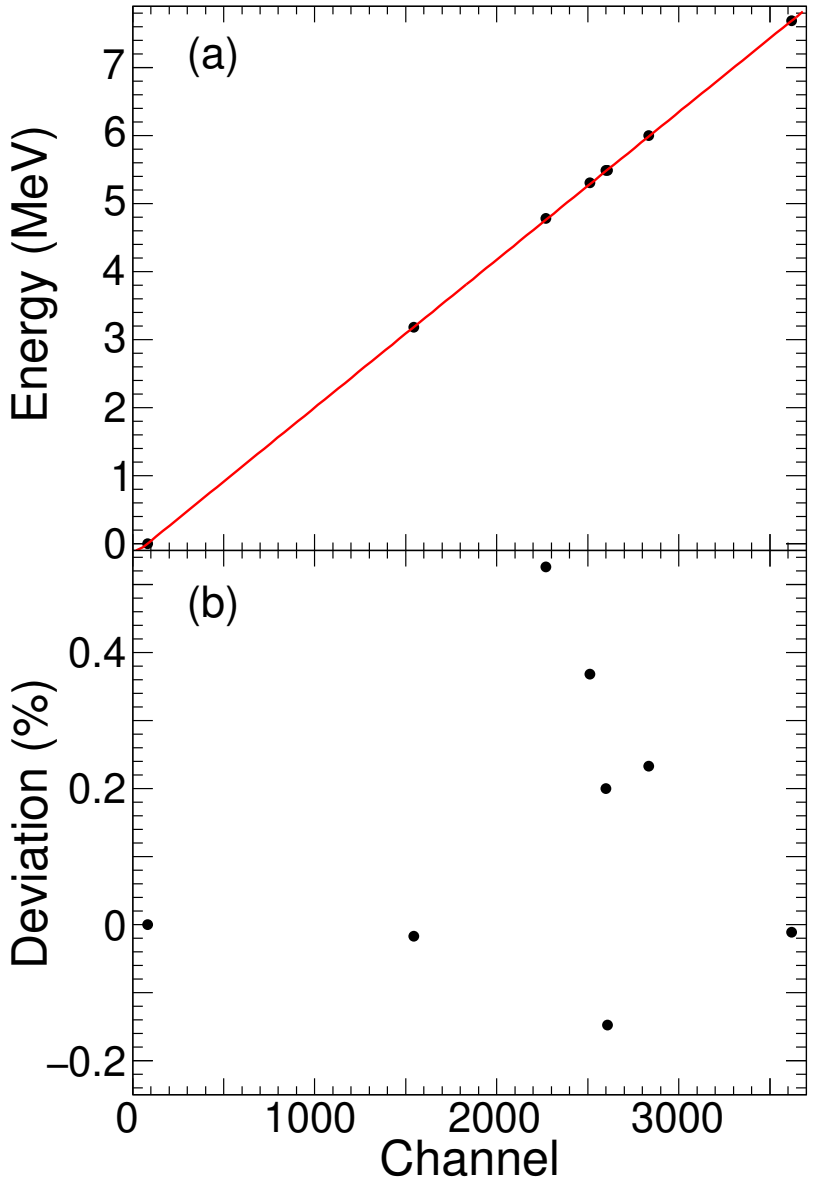

FIGURE B.4: Top panel: Calibration curve for the SBD with a second degree polynomial. Bottom panel: Deviation of the data from the fit.

B.4. The calibration curve is a second order polynomial fit to the data, with deviations from the data less than ∼0.5%.

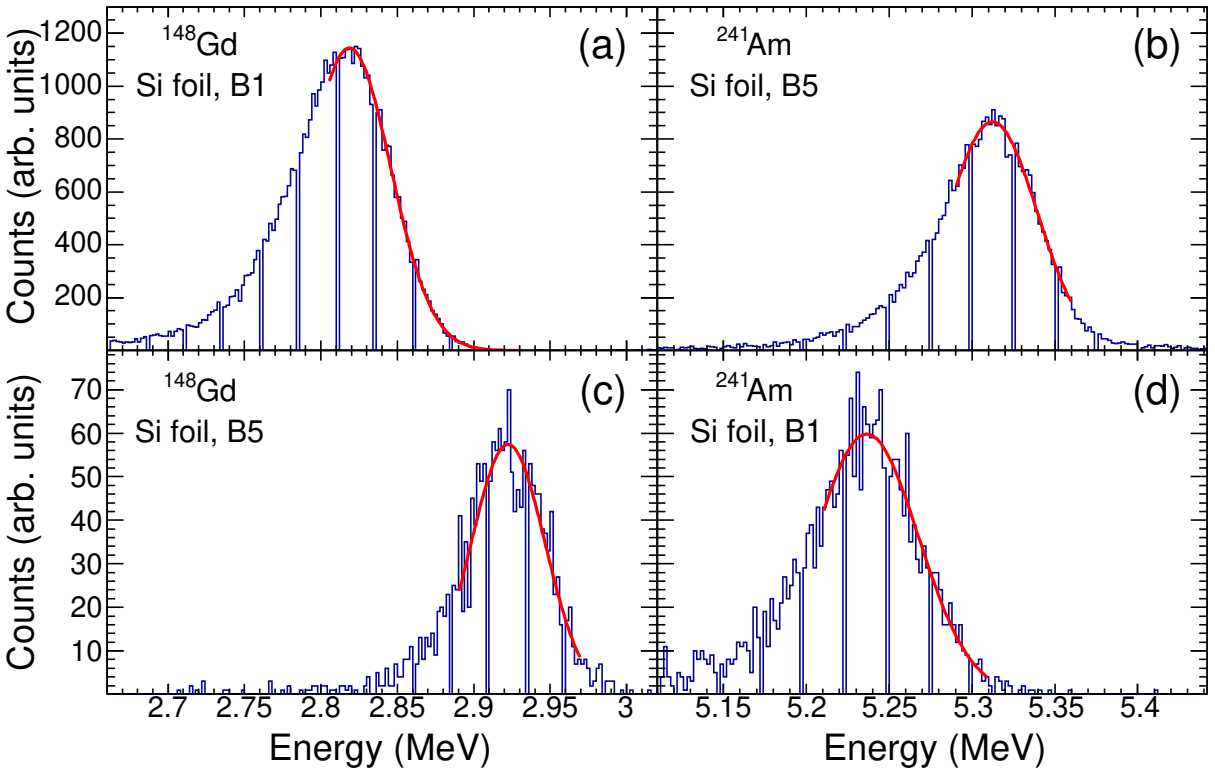

FIGURE B.5: Energy spectra of α particles after passing through two different ^{28}Si foils.

B.3 Results

The thickness of each foil was determined by measuring the energy loss of the α particles and integrating the reciprocal stopping power $(dE/dx)^{-1}$ of each foil over the range of energy lost. The function $(dE/dx)^{-1}(E)$ was obtained by using values of dE/dx calculated with the program TRIM [127] for α energies ranging from 2.783-3.183 MeV and 5.086-5.486 MeV in increments of 20 keV. Figure B.5 shows a few representative spectra of α particles after passing through a foil. The measured energy loss values for each foil are shown in Table B.1, and the resulting foil thickness values are summarized in Table B.2. In all cases, the measurements from both ^{148}Gd and ^{241}Am were within a few percent of each other. The error for each individual measurement is associated with the error in the centroid of the measured energy distributions. The average value

adds the errors in quadrature, along with the relative deviation of each measurement from the mean. In addition to the α particle measurements, the aluminum foils were also measured by a quartz crystal monitor (QCM) during the vapor deposition process, and by weight after the deposition. The results of these different measurements are shown in Table B.3. The measurements by weight are within $\sim$20% of the values obtained from the α measurements, but the QCM measurements are much lower. The carbon and mylar foils were measured to be within $\sim$10% of their nominal values. The ^{28}Si foils were nominally 100 μg/cm^2 (A foils) and 200 μg/cm^2 (B foils) as measured by a QCM during evaporation, but the α particle measurements range from approximately 1.5 to 2.5 times greater than their nominal values. The crystal monitor values for the aluminum foils as well as the ^{28}Si foils are likely lower than the measured values due to the geometry of the crystal monitor and substrates relative to the source during evaporation.

TABLE B.1: Amount of energy lost by the α particles passing through the foils. All energy loss measurements are in units of keV.

Foil	ID	^{148}Gd energy loss (keV)	^{241}Am energy loss (keV)
^{nat}Al	1A	196.5 ± 0.9	134.7 ± 1.5
^{nat}Al	4A	229.5 ± 1.2	159.6 ± 1.2
^{nat}Al	4B	236.7 ± 1.2	166.2 ± 1.5
^{nat}Al	6A		119.0 ± 1.5
^{nat}Al	6B		104.3 ± 1.5
^{nat}C	2x50	122.2 ± 1.1	83.6 ± 1.2
^{nat}C	2x100	247.9 ± 1.0	167.4 ± 1.7
^{nat}C	2x110	227.3 ± 1.2	154.2 ± 1.4
Mylar	0.5μm	88.9 ± 1.1	59.6 ± 2.1
Mylar	1.5μm	246.6 ± 1.5	165.4 ± 1.2
^{28}Si	A1	155.7 ± 0.8	107.4 ± 1.9
^{28}Si	A2	131.4 ± 1.2	87.9 ± 2.4
^{28}Si	A3	131.6 ± 1.2	97.2 ± 2.3
^{28}Si	A4	176.0 ± 0.8	126.3 ± 1.5
^{28}Si	A5	165.5 ± 1.2	118.1 ± 1.8
^{28}Si	A6	109.4 ± 0.9	81.7 ± 1.7
^{28}Si	A7	153.3 ± 1.7	109.5 ± 1.9
^{28}Si	B1	365.1 ± 0.9	257.6 ± 1.9
^{28}Si	B2	340.6 ± 1.5	239.5 ± 1.5
^{28}Si	B3	229.5 ± 0.9	161.5 ± 2.4
^{28}Si	B4	228.7 ± 1.4	158.7 ± 2.5
^{28}Si	B5	261.3 ± 1.2	181.8 ± 1.2
^{28}Si	B6	273.5 ± 1.2	190.0 ± 1.7
^{28}Si	B7	320.0 ± 1.6	219.9 ± 1.9

TABLE B.2: Foil thicknesses determined by α particle energy loss measurements. All measurements are in units of $\mu g/cm^2$, except the mylar foils which are in units of μm.

Foil	ID	^{148}Gd measurement	^{241}Am measurement	Average
^{nat}Al	1A	247.1 ± 1.1	234.8 ± 2.6	241.0 ± 9.1
^{nat}Al	4A	287.8 ± 1.5	277.7 ± 2.1	282.7 ± 7.6
^{nat}Al	4B	296.6 ± 1.5	289.2 ± 2.6	292.9 ± 6.0
^{nat}Al	6A		207.6 ± 2.6	207.6 ± 2.6
^{nat}Al	6B		182.1 ± 2.6	182.1 ± 2.6
^{nat}C	2x50	110.8 ± 1.0	110.0 ± 1.5	110.4 ± 1.9
^{nat}C	2x100	222.1 ± 0.8	218.8 ± 2.2	220.4 ± 3.3
^{nat}C	2x110	204.0 ± 1.1	201.7 ± 1.8	202.8 ± 2.7
Mylar	0.5μm	0.551 ± 0.007	0.536 ± 0.019	0.544 ± 0.023
Mylar	1.5μm	1.505 ± 0.009	1.476 ± 0.010	1.491 ± 0.025
^{28}Si	A1	193.3 ± 1.0	184.8 ± 3.3	189.1 ± 6.9
^{28}Si	A2	163.5 ± 1.5	151.5 ± 4.1	157.5 ± 9.5
^{28}Si	A3	163.8 ± 1.5	167.4 ± 3.9	165.6 ± 4.9
^{28}Si	A4	218.2 ± 1.0	217.2 ± 2.6	217.7 ± 2.9
^{28}Si	A5	205.3 ± 1.5	203.2 ± 3.1	204.3 ± 3.7
^{28}Si	A6	136.4 ± 1.1	140.9 ± 3.0	138.6 ± 4.5
^{28}Si	A7	190.4 ± 2.1	188.5 ± 3.3	189.5 ± 4.1
^{28}Si	B1	445.0 ± 1.1	439.6 ± 3.3	442.3 ± 5.1
^{28}Si	B2	416.0 ± 1.8	409.2 ± 2.6	412.6 ± 5.8
^{28}Si	B3	283.2 ± 1.1	277.0 ± 4.1	280.1 ± 6.1
^{28}Si	B4	282.2 ± 1.7	272.4 ± 4.3	277.3 ± 8.4
^{28}Si	B5	321.4 ± 1.4	311.6 ± 2.0	316.5 ± 7.4
^{28}Si	B6	336.1 ± 1.5	325.5 ± 3.0	330.8 ± 8.2
^{28}Si	B7	391.6 ± 2.0	376.0 ± 3.3	383.8 ± 11.6

TABLE B.3: Aluminum foil thicknesses measured by quartz crystal monitor (QCM) during vapor deposition, by weight after deposition, and by α particle energy loss measurements. All measurements are in units of $\mu g/cm^2$.

Foil ID	QCM	Weight	α measurement
1A	189	194	241
4A	189	264	283
4B	189	264	293
6A	162	165	208
6B	162	165	182

Appendix C

Cross-section details

The details of the cross-section calculations for each system described in the previous chapters are displayed in the tables below. For each system, the number of residues measured in each detector at each beam energy is integrated. Each detector residue count is then corrected for analysis conditions by dividing by the correction factors ϵ_{TX}. The corrected residue counts were then added, and the geometric efficiency was applied by dividing the summed residues by ϵ_{geo}. The geometric efficiency is determined by calculating the residue angular distributions with the EVAPOR statistical model code [110] and determining the fraction of the angular distribution subtended by the detectors. For the light systems (^{16,18,19}O,^{17}F + ^{12}C), the calculated angular distributions were subdivided into nucleon-only decay channels and α particle decay channels. These two distributions were then weighted differently to match the measured residue angular distributions and then added together before determining the fraction covered by the detectors. The calculated distributions for the ^{39,47}K + ^{28}Si,^{16}O systems were not weighted differently because the measured angular distributions were too coarse for such analysis. The rejection of ring segments not used in the analysis of some beam energies is taken into account in the determination of the geometric efficiency. The target thickness is reported in μg/cm^2, and then converted to atoms/mb using the atomic weight of the target isotope along with Avogadro's number. The cross-section is then calculated using Equation 3.1 by dividing

the total corrected number of residues by the beam count and target thickness in atoms/mb. The errors in the cross-section values reflect statistical uncertainties, systematic uncertainties, and residue identification uncertainties.

The energy of the reaction is determined by calculating the energy of the beam at the center of the target foil using the energy loss program SRIM [127]. Since the beam loses energy through the foil, and the cross-section for fusion decreases rapidly with decreasing energy below the barrier, the assumption that reactions occur in the center of the foil becomes less accurate for low beam energies and thicker targets. Therefore, the reaction energy $E_{c.m.}$ assigned to each incident beam energy should be adjusted to be weighted closer to the entrance of the foil. This weighting was accomplished in the following way. The reaction energies at both the entrance and exit of the target foil were calculated. The fusion excitation function was constructed using the center foil values for $E_{c.m.}$. The excitation function was then parameterized with the Wong formula. For each point, the range of energies between the foil entrance energy and foil exit energy was divided into 20 bins, and a weighted average was calculated based on the product of the bin energy with the cross-section value of the Wong parameterization evaluated at the bin energy. The new weighted-average value of $E_{c.m.}$ was then used to reconstruct the fusion excitation function, which was once again parameterized by the Wong formula. Another weighted average was determined, and the process was repeated until the $E_{c.m.}$ values converged.

TABLE C.1: Cross-section information for ^{19}O + ^{12}C. The first column designates the ID number used in the analysis to denote each point. The energy is listed in the second column, and the cross-section is listed in the third column. The quantities used in the cross-section determination are given in the remaining columns: the total number of measured evaporation residues in T2 ($N_{ER,T2}$) and T3 ($N_{ER,T3}$), the number of beam particles incident on the target (N_{beam}), the combined geometric efficiency (ϵ_{geo}) of both T2 and T3, and the correction factor (ϵ_{T2}) applied to the residues in T2 from the analysis conditions. A correction factor of $\epsilon_{T3} = 15/16$ was applied to the residues in T3 to make up for one faulty pie segment that was missing in the experiment. The target thickness (t) used in this experiment was 105 μg/cm^2 of ^{12}C.

ID	$E_{c.m.}$ (MeV)	σ (mb)	$N_{ER,T2}$	$N_{ER,T3}$	N_{beam}	ϵ_{geo}	ϵ_{T2}
36	18.010 ± 0.175	$1340.5\ ^{+120.7}_{-107.6}$	160	36	39288417	0.7617	0.9249
37	18.086 ± 0.166	$1211.9\ ^{+76.4}_{-70.6}$	290	68	79925670	0.7599	0.9197
42	17.672 ± 0.159	$1186.3\ ^{+76.9}_{-68.9}$	304	76	85263872	0.7707	0.9220
62	16.002 ± 0.150	$1251.1\ ^{+84.9}_{-86.3}$	184	54	50154849	0.7735	0.9286
76	14.755 ± 0.152	$1221.4\ ^{+85.0}_{-86.9}$	221	56	60026939	0.7710	0.9280
81	14.212 ± 0.140	$1115.0\ ^{+93.7}_{-78.8}$	190	50	56821695	0.7730	0.9281
91	13.301 ± 0.157	$1107.8\ ^{+112.0}_{-84.2}$	168	33	49197757	0.7626	0.9140
104	11.908 ± 0.157	$651.3\ ^{+67.3}_{-61.6}$	94	24	47652912	0.7795	0.9227
118	10.392 ± 0.168	$741.6\ ^{+58.2}_{-72.5}$	147	35	64426442	0.7774	0.9282
130	9.067 ± 0.180	$417.2\ ^{+39.6}_{-42.2}$	83	33	94001436	0.6068	0.9203
137	8.267 ± 0.191	$296.5\ ^{+27.1}_{-29.0}$	93	37	163740887	0.5567	0.9033
144	7.438 ± 0.189	$127.9\ ^{+16.2}_{-17.1}$	55	10	220960668	0.5038	0.8544

TABLE C.2: Cross-section information for ^{18}O + ^{12}C measured simultaneously with ^{19}O + ^{12}C. The first column designates the ID number used in the analysis to denote each point. The energy is listed in the second column, and the cross-section is listed in the third column. The quantities used in the cross-section determination are given in the remaining columns: the total number of measured evaporation residues in T2 ($N_{ER,T2}$) and T3 ($N_{ER,T3}$), the number of beam particles incident on the target (N_{beam}), the combined geometric efficiency (ϵ_{geo}) of both T2 and T3, and the correction factor (ϵ_{T2}) applied to the residues in T2 from the analysis conditions. A correction factor of $\epsilon_{T3} = 15/16$ was applied to the residues in T3 to make up for one faulty pie segment that was missing in the experiment, except 14/16 was used for the lowest energy point due to analysis. The target thickness (t) used in this experiment was 105 μg/cm^2 of ^{12}C.

ID	$E_{c.m.}$ (MeV)	σ (mb)	$N_{ER,T2}$	$N_{ER,T3}$	N_{beam}	ϵ_{geo}	ϵ_{T2}
36	19.005 ± 0.259	1230.8 ± 106.5	100	41	29513308	0.8008	0.9128
37	18.985 ± 0.206	1033.8 ± 65.3	212	67	69987028	0.7933	0.9178
42	18.579 ± 0.222	1135.6 ± 66.4	239	92	74583597	0.8011	0.9214
62	16.950 ± 0.252	889.5 ± 65.8	152	45	58224248	0.7781	0.9250
76	15.743 ± 0.264	784.4 ± 56.4	145	65	67476257	0.8093	0.9273
81	15.243 ± 0.233	762.8 ± 58.9	133	47	59968048	0.8020	0.9288
91	14.294 ± 0.268	829.9 ± 63.9	132	49	55776667	0.8005	0.9232
104	13.008 ± 0.306	772.8 ± 82.0	69	23	31023403	0.7810	0.9307
118	11.477 ± 0.334	606.1 ± 52.5	101	40	58932692	0.7990	0.9377
130	10.031 ± 0.246	418.2 ± 36.2	80	61	95879858	0.7129	0.9352
137	9.268 ± 0.273	377.5 ± 26.4	135	87	204556290	0.5892	0.9187
144	8.653 ± 0.286	216.8 ± 17.0	108	67	290424937	0.5964	0.8545

TABLE C.3: Cross-section information for ^{17}F + ^{12}C. The first column designates the ID number used in the analysis to denote each point. The energy is listed in the second column, and the cross-section is listed in the third column. The quantities used in the cross-section determination are given in the remaining columns: the total number of measured evaporation residues in T2 ($N_{ER,T2}$) and T3 ($N_{ER,T3}$), the number of beam particles incident on the target (N_{beam}), the combined geometric efficiency (ϵ_{geo}) of both T2 and T3, and the correction factor (ϵ_{T2}) applied to the residues in T2 from the analysis conditions. A correction factor of $\epsilon_{T3} = 15/16$ was applied to the residues in T3 to make up for one faulty pie segment that was missing in the experiment. The target thickness (t) used in this experiment was 105 μg/cm^2 of ^{12}C.

ID	$E_{c.m.}$ (MeV)	σ (mb)	$N_{ER,T2}$	$N_{ER,T3}$	N_{beam}	ϵ_{geo}	ϵ_{T2}
20	$18.820\ ^{+0.319}_{-0.320}$	777.3 ± 47.4	212	84	95529655	0.8127	0.9282
38	$17.034\ ^{+0.320}_{-0.318}$	781.6 ± 51.2	167	84	78576875	0.8294	0.9339
49	$15.713\ ^{+0.318}_{-0.322}$	630.9 ± 46.6	143	51	76202133	0.8193	0.9337
60	$14.532\ ^{+0.339}_{-0.337}$	668.1 ± 42.3	182	89	98114733	0.8398	0.9327
68	$13.532\ ^{+0.347}_{-0.348}$	555.5 ± 33.8	205	91	129546738	0.8321	0.9384
76	$12.551\ ^{+0.356}_{-0.358}$	462.9 ± 26.2	233	117	183115201	0.8394	0.9317
86	$11.256\ ^{+0.372}_{-0.374}$	343.5 ± 25.1	138	61	140891027	0.8362	0.9314
91	$10.648\ ^{+0.198}_{-0.378}$	257.7 ± 27.2	57	34	84026821	0.8531	0.9332

TABLE C.4: Cross-section information for ^{16}O + ^{12}C measured simultaneously with ^{17}F + ^{12}C. The first column designates the ID number used in the analysis to denote each point. The energy is listed in the second column, and the cross-section is listed in the third column. The quantities used in the cross-section determination are given in the remaining columns: the total number of measured evaporation residues in T2 ($N_{ER,T2}$) and T3 ($N_{ER,T3}$), the number of beam particles incident on the target (N_{beam}), the combined geometric efficiency (ϵ_{geo}) of both T2 and T3, and the correction factor (ϵ_{T2}) applied to the residues in T2 from the analysis conditions. A correction factor of $\epsilon_{T3} = 15/16$ was applied to the residues in T3 to make up for one faulty pie segment that was missing in the experiment. The target thickness (t) used in this experiment was 105 μg/cm^2 of ^{12}C.

ID	$E_{c.m.}$ (MeV)	σ (mb)	$N_{ER,T2}$	$N_{ER,T3}$	N_{beam}	ϵ_{geo}	ϵ_{T2}
20	$15.994\ ^{+0.336}_{-0.336}$	839.2 ± 69.1	113	41	45412671	0.8099	0.9503
38	$14.281\ ^{+0.299}_{-0.301}$	820.7 ± 75.7	102	20	37498690	0.7987	0.9428
49	$13.119\ ^{+0.317}_{-0.319}$	593.9 ± 30.2	303	146	184561155	0.8274	0.9405
60	$11.981\ ^{+0.367}_{-0.367}$	641.7 ± 65.9	73	24	37532793	0.8150	0.9379
68	$10.980\ ^{+0.330}_{-0.329}$	527.3 ± 34.4	208	48	122587083	0.7988	0.9416
76	$10.114\ ^{+0.362}_{-0.362}$	335.5 ± 29.6	100	33	97998810	0.8178	0.9391
86	$8.885\ ^{+0.375}_{-0.377}$	223.9 ± 25.2	60	20	87932363	0.8220	0.9384
91	$8.280\ ^{+0.392}_{-0.394}$	104.4 ± 20.8	17	8	59186094	0.8189	0.9383

TABLE C.5: Cross-section information for ^{39}K + ^{28}Si. The first column designates the ID number used in the analysis to denote each point. The energy is listed in the second column, and the cross-section is listed in the third column. The quantities used in the cross-section determination are given in the remaining columns: the total number of measured evaporation residues in T1 ($N_{ER,T1}$) and T2 ($N_{ER,T2}$), the number of beam particles incident on the target (N_{beam}), and the combined geometric efficiency (ϵ_{geo}) of both T1 and T2. All rings were used in T2, but only rings 2 and 3 were used in T1 (except for #94, where only ring 3 was used in T1). T1 was not used for #105, #93, and #91. A correction factor of $\sim$0.99 was applied to the residues in T1 and T2 from the analysis conditions. The target thickness (t) used in this experiment was 316 μg/cm^2 of ^{28}Si.

ID	$E_{c.m.}$ (MeV)	σ (mb)	$N_{ER,T1}$	$N_{ER,T2}$	N_{beam}	ϵ_{geo}
108	42.568 ± 0.173	$267.4\ ^{+22.5}_{-22.6}$	22	156	143768070	0.6860
105	41.533 ± 0.153	$204.7\ ^{+17.8}_{-17.8}$	0	163	190579834	0.6186
103	40.741 ± 0.146	$179.9\ ^{+18.4}_{-18.4}$	10	100	127703005	0.7100
99	39.417 ± 0.127	$128.9\ ^{+12.3}_{-12.6}$	19	111	206881455	0.7234
96	38.431 ± 0.108	$50.1\ ^{+7.3}_{-7.8}$	10	41	207595511	0.7281
94	37.753 ± 0.096	$29.9\ ^{+4.5}_{-4.5}$	8	43	371914347	0.6807
93	37.465 ± 0.105	$21.6\ ^{+3.7}_{-3.7}$	0	36	393928065	0.6279
91	36.754 ± 0.109	$7.5\ ^{+1.4}_{-1.3}$	0	35	1102774888	0.6290

TABLE C.6: Cross-section information for ^{47}K + ^{28}Si. The first column designates the ID number used in the analysis to denote each point. The energy is listed in the second column, and the cross-section is listed in the third column. The quantities used in the cross-section determination are given in the remaining columns: the total number of measured evaporation residues in T1 ($N_{ER,T1}$) and T2 ($N_{ER,T2}$), the number of beam particles incident on the target (N_{beam}), and the combined geometric efficiency (ϵ_{geo}) of both T1 and T2. All rings were used in T2, but only rings 1,2, and 3 were used in T1 (except for #126, where only rings 2 and 3 were used in T1). A correction factor of ∼0.99 was applied to the residues in T1 and T2 from the analysis conditions. The target thickness (t) used in this experiment was 316 μg/cm^2 of ^{28}Si.

ID	$E_{c.m.}$ (MeV)	σ (mb)	$N_{ER,T1}$	$N_{ER,T2}$	N_{beam}	ϵ_{geo}
144	42.624 ± 0.241	$340.7\ ^{+34.7}_{-32.1}$	40	108	80298629	0.8001
139	41.216 ± 0.260	$261.0\ ^{+37.3}_{-43.8}$	18	53	50181633	0.8027
134	39.437 ± 0.233	$183.9\ ^{+28.3}_{-28.3}$	16	30	46091846	0.8051
12514	37.978 ± 0.230	$62.8\ ^{+12.8}_{-13.0}$	9	16	73571791	0.8049
128	37.452 ± 0.259	$66.6\ ^{+10.6}_{-12.8}$	15	39	149683340	0.8060
126	36.768 ± 0.237	$35.2\ ^{+6.1}_{-6.1}$	16	20	207193381	0.7322
125	36.187 ± 0.212	$17.6\ ^{+4.5}_{-4.5}$	2	14	168087532	0.8037

TABLE C.7: Cross-section information for ^{39}K + ^{16}O. The first column designates the ID number used in the analysis to denote each point. The energy is listed in the second column, and the cross-section is listed in the third column. The quantities used in the cross-section determination are given in the remaining columns: the total number of measured evaporation residues in T1 ($N_{ER,T1}$) and T2 ($N_{ER,T2}$), the number of beam particles incident on the target (N_{beam}), and the combined geometric efficiency (ϵ_{geo}) of both T1 and T2. All rings were used in T2, but only rings 1, 2, and 3 were used in T1. T1 was not used for #105. A correction factor of ∼0.99 was applied to the residues in T1 and T2 from the analysis conditions. The beam count for #91 is different for the residues in T1 (365397329), as the T1 detector was removed halfway through data collection during that energy. The target thickness (t) was determined to be 103.3 μg/cm^2 of ^{16}O.

ID	$E_{c.m.}$ (MeV)	σ (mb)	$N_{ER,T1}$	$N_{ER,T2}$	N_{beam}	ϵ_{geo}
108	29.485 ± 0.131	$507.0\ ^{+37.6}_{-35.1}$	46	181	143768070	0.8086
105	28.715 ± 0.130	$551.3\ ^{+37.4}_{-37.1}$	0	242	190579834	0.5972
103	28.099 ± 0.130	$444.3\ ^{+35.4}_{-36.8}$	43	134	127703005	0.8112
99	26.966 ± 0.130	$398.9\ ^{+26.2}_{-26.4}$	62	197	206881455	0.8168
96	26.070 ± 0.130	$310.0\ ^{+23.1}_{-22.7}$	30	172	207595511	0.8178
94	25.483 ± 0.130	$266.4\ ^{+16.2}_{-16.4}$	61	250	371914347	0.8181
93	25.239 ± 0.131	$276.1\ ^{+16.0}_{-16.7}$	76	265	393928065	0.8166
91	24.683 ± 0.132	$225.1\ ^{+10.1}_{-11.0}$	66	580	1102774888	0.8171

TABLE C.8: Cross-section information for ^{47}K + ^{16}O. The first column designates the ID number used in the analysis to denote each point. The energy is listed in the second column, and the cross-section is listed in the third column. The quantities used in the cross-section determination are given in the remaining columns: the total number of measured evaporation residues in T1 ($N_{ER,T1}$) and T2 ($N_{ER,T2}$), the number of beam particles incident on the target (N_{beam}), and the combined geometric efficiency (ϵ_{geo}) of both T1 and T2. All rings were used in T2, but only rings 1,2, and 3 were used in T1 (except for #126, where only rings 2 and 3 were used in T1). A correction factor of ∼0.99 was applied to the residues in T1 and T2 from the analysis conditions. The target thickness (t) was determined to be 103.3 μg/cm^2 of ^{16}O.

ID	$E_{c.m.}$ (MeV)	σ (mb)	$N_{ER,T1}$	$N_{ER,T2}$	N_{beam}	ϵ_{geo}
144	28.895 ± 0.123	$669.0\ ^{+60.5}_{-56.3}$	62	96	80298629	0.7624
139	27.893 ± 0.125	$576.1\ ^{+63.5}_{-63.9}$	33	52	50181633	0.7627
134	26.567 ± 0.124	$478.5\ ^{+64.0}_{-60.1}$	24	41	46091846	0.7657
12514	25.324 ± 0.127	$377.6\ ^{+48.2}_{-44.6}$	27	55	73571791	0.7695
128	24.839 ± 0.125	$291.7\ ^{+27.2}_{-27.8}$	46	83	149683340	0.7675
126	24.269 ± 0.125	$244.4\ ^{+25.7}_{-24.0}$	38	91	207193381	0.6629
125	23.825 ± 0.124	$205.1\ ^{+22.2}_{-21.1}$	42	60	168087532	0.7692

Bibliography

[1] E. M. Burbidge, G. R. Burbidge, W. A. Fowler, and F. Hoyle. Synthesis of the elements in stars. *Reviews of Modern Physics*, 29:547, 1957.

[2] W. D. Loveland, D. J. Morrissey, and G. .T Seaborg. *Modern Nuclear Chemistry*. John Wiley & Sons, Inc., 2006.

[3] National Nuclear Data Center Chart of the Nuclides, 2017. URL http://www.nndc.bnl.gov/chart/.

[4] K. A. Olive, G. Steigman, and T. P. Walker. Primordial nucleosynthesis: theory and observations. *Physics Reports*, 333:389, 2000.

[5] S. Burles, K. M. Nollett, and M. S. Turner. Big bang nucleosynthesis predictions for precision cosmology. *The Astrophysical Journal Letters*, 552:L1, 2001.

[6] J. Lippuner. *r-Process nucleosynthesis in neutron star mergers with the new nuclear reaction network SkyNet*. PhD thesis, California Institute of Technology, 2018.

[7] T. Kodama and K. Takahashi. R-process nucleosynthesis and nuclei far from the region of β-stability. *Nuclear Physics A*, 239:489, 1975.

[8] W. Hillebrandt, K. Takahashi, and T. Kodama. R-process nucleosynthesis - a dynamic model. *Astronomy & Astrophysics*, 52:63, 1976.

[9] B. S. Meyer, G. J. Mathews, W. M. Howard, S. E. Woosley, and R. D. Hoffman. R-process nucleosynthesis in the high-entropy supernova bubble. *The Astrophysical Journal*, 399:656, 1992.

[10] S. Goriely, N. Chamel, H. -T. Janka, and J. M. Pearson. The decompression of the outer neutron star crust and r-process nucleosynthesis. *Astronomy & Astrophysics*, 531:A78, 2011.

[11] S. Goriely, P. Demetriou, H. -Th. Janka, J. M. Pearson, and M. Samyn. The r-process nucleosynthesis: a continued challenge for nuclear physics and astrophysics. *Nuclear Physics A*, 758:587, 2005.

[12] K. Hotokezaka, P. Beniamini, and T. Piran. Neutron star mergers as sites of r-process nucleosynthesis and short gamma-ray bursts. *International Journal of Modern Physics D*, 27:1842005, 2018.

[13] S. E. Woosley, J. R. Wilson, G. J. Mathews, R. D. Hoffman, and B. S. Meyer. The r-process and neutrino-heated supernova ejecta. *The Astrophysical Journal*, 433: 229, 1994.

[14] S. Wanajo. The r-process in proto-neutron star winds with anisotropic neutrino emission. *The Astrophysical Journal Letters*, 650:L79, 2006.

[15] Y. Z. Qian and S. E. Woosley. Nucleosynthesis in neutrino-driven winds. I. The physical conditions. *The Astrophysical Journal*, 471:331, 1996.

[16] S. Wanajo. The r-process in proto-neutron-star wind revisited. *The Astrophysical Journal Letters*, 770:L22, 2013.

[17] N. Nishimura, T. Takiwaki, and F. -K. Thielemann. The r-process nucleosynthesis in the various jet-like explosions of magnetorotational core-collapse supernovae. *The Astrophysical Journal*, 810:109, 2015.

[18] A. Gomboc. Unveiling the secrets of gamma ray bursts. *Contemporary Physics*, 53: 339, 2012.

[19] J. M. Lattimer and M. Prakash. Ultimate energy density of observable cold baryonic matter. *Physical Review Letters*, 94:111101, 2005.

[20] D. J. Price and S. Rosswog. Producing ultrastrong magnetic fields in neutron star mergers. *Science*, 312:719, 2006.

[21] A. Bauswein, S. Goriely, and H. -T. Janka. Systematics of dynamical mass ejection, nucleosynthesis, and radioactively powered electromagnetic signals from neutron-star mergers. *The Astrophysical Journal*, 773:78, 2013.

[22] S. Wanajo, Y. Sekiguchi, N. Nishimura, K. Kiuchi, K. Kyutoku, and M. Shibata. Production of all the r-process nuclides in the dynamical ejecta of neutron star mergers. *The Astrophysical Journal Letters*, 789:L39, 2014.

[23] C. Freiburghaus, S. Rosswog, and F. -K. Thielemann. R-process in neutron star mergers. *The Astrophysical Journal*, 525:L121, 1999.

[24] A. Abramovici, W. E. Althouse, R. W. P. Drever, Y. Gürsel, S. Kawamura, F. J. Raab, D. Shoemaker, L. Sievers, R. E. Spero, K. S. Thorne, R. E. Vogt, R. Weiss, S. E. Whitcomb, and M. E. Zucker. LIGO: The Laser Interferometer Gravitational-Wave Observatory. *Science*, 256:325, 1992.

[25] LIGO Facts, 2018. URL https://www.ligo.caltech.edu/page/facts.

[26] Virgo Collaboration. The Virgo interferometer. *Classical and Quantum Gravity*, 14:1461, 1997.

[27] LIGO Scientific Collaboration and Virgo Collaboration. Upper limits on the rates of binary neutron star and neutron star-black hole mergers from Advanced LIGO's first observing run. *The Astrophysical Journal Letters*, 832:L21, 2016.

[28] B. Paczyński. Gamma-ray bursters at cosmological distances. *The Astrophysical Journal*, 308:L43, 1986.

[29] E. Berger, W. Fong, and R. Chornock. An r-process kilonova associated with the short-hard GRB 130603B. *The Astrophysical Journal Letters*, 774:L23, 2013.

[30] L. -X. Li and B. Paczyński. Transient events from neutron-star mergers. *The Astrophysical Journal Letters*, 507:L59, 1998.

[31] B. D. Metzger and E. Berger. What is the most promising electromagnetic counterpart of a neutron star binary merger? *The Astrophysical Journal*, 746:48, 2012.

[32] LIGO Scientific Collaboration and Virgo Collaboration. GW170817: Observation of gravitational waves from a binary neutron star inspiral. *Physical Review Letters*, 119:161101, 2017.

[33] LIGO Scientific Collaboration and Virgo Collaboration. LIGO/Virgo identification of a possible gravitational-wave counterpart. *GCN*, page 21505, 2017.

[34] LIGO Scientific Collaboration and Virgo Collaboration. Gravitational waves and gamma-rays from a binary neutron star merger: GW170817 and GRB 170817A. *The Astrophysical Journal Letters*, 848:L13, 2017.

[35] A. Goldstein, P. Veres, E. Burns, M. S. Briggs, R. Hamburg, D. Kocevski, C. A. Wilson-Hodge, R. D. Preece, S. Poolakkil, O. J. Robers, C. M. Hui, V. Connaughton, J. Racusin, A. von Kienlin, T. Dal Canton, N. Christensen, T. Littenberg, K. Siellez, L. Blackburn, J. Broida, E. Bissaldi, W. H. Cleveland, M. H. Gibby, M. M. Giles, R. M. Kippen, S. McBreen, J. McEnery, C. A. Meegan, W. S. Paciesas, and M. Stanbro. An ordinary short gamma-ray burst with extraordinary implications: Fermi-GBM detection of GRB 170817A. *Astro. Phys. Jour. Lett.*, 848:L14, 2017.

[36] D. A. Coulter, C. D. Kilpatrick, M. R. Siebert, R. J. Foley, B. J. Shappee, M. R. Drout, J. S. Simon, A. L. Piro, and A. Rest. Potential optical counterpart discovered by Swope telescope. *GCN*, page 21529, 2017.

[37] M. Nicholl, E. berger, D. Kasen, B. D. Metzger, J. Elias, C. Briceño, K. D. Alexander, P. K. Blanchard, R. Chornock, P. S. Cowperthwaite, T. Eftekhari, W. Fong, R. Margutti, V. A. Villar, P. K. G. Williams, W. Brown, J. Annis, A. Bahramian, D. Brout, D. A. Brown, H. -Y. Chen, J. C. Clemens, E. Dennihy, B. Dunlap, D. E. Holz, E. Marchesini, F. Massaro, N. Moskowitz, I. Pelisoli, A. Rest, F. Ricci, M. Sako, M. Soares-Santos, and J. Strader. The electromagnetic counterpart of the binary neutron star merger LIGO/Virgo GW170817. III. Optical and UV spectra of a blue kilonova from fast polar ejecta. *The Astrophysical Journal Letters*, 848: L18, 2017.

[38] LIGO Scientific Collaboration and Virgo Collaboration. Estimating the contribution of dynamical ejecta in the kilonova associated with GW170817. *The Astrophysical Journal Letters*, 850:L39, 2017.

[39] T. Strohmayer and L. Bildsten. *Compact Stellar X-ray Sources*. Cambridge University, 2006.

[40] W. Baade and F. Zwicky. Remarks on super-novae and cosmic rays. *Physical Review*, 43:76, 1934.

[41] G. Baym. Neutron stars: observing the properties of high-density nuclear matter. *Nuclear Physics A*, 590:233, 1995.

[42] J. Grindlay, H. Gursky, H. Schnopper, D. R. Parsignault, J. Heise, A. C. Brinkman, and J. Schrijver. Discovery of intense X-ray bursts from the globular cluster NGC 6624. *The Astrophysical Journal*, 205:L127, 1976.

[43] G. Kopp and J. L. Lean. A new, lower value of total solar irradiance: evidence and climate significance. *Geophysical Research Letters*, 38:L01706, 2011.

[44] H. Schatz, A. Aprahamian, V. Barnard, L. Bildsten, A. Cumming, M. Ouellette, T. Rauscher, F. -K Thielemann, and M. Wiescher. End point of the rp process on accreting neutron stars. *Physical Review Letters*, 86:3471, 2001.

[45] S. E. Woosley, A. Heger, A. Cumming, R. D. Hoffman, J. Pruet, T. Rauscher, J. L. Fisker, H. Schatz, B. A. Brown, and M. Wiescher. Models for Type I X-ray bursts with improved nuclear physics. *The Astrophysical Journal Supplement Series*, 151: 75, 2004.

[46] S. Gupta, E. F. Brown, H. Schatz, P. Möller, and K. -L. Kratz. Heating in the accreted neutron star ocean: implications for superburst ignition. *The Astrophysical Journal*, 662:1188, 2007.

[47] C. J. Horowitz, H. Dussan, and D. K. Berry. Fusion of neutron-rich oxygen isotopes in the crust of accreting neutron stars. *Physical Review C*, 77:045807, 2008.

[48] M. J. G. Borge. Highlights of the ISOLDE facility and the HIE-ISOLDE project. *Acta Physica Polonica B*, 47:591, 2016.

[49] S. Gales. GANIL-SPIRAL2: a new era. *Journal of Physics: Conference Series*, 267:012009, 2011.

[50] O. Kester, D. Bazin, C. Benatti, J. Bierwagen, G. Bollen, S. Bricker, A. C. Crawford, S. Chouhan, C. Compton, K. Davidson, J. DeLauter, M. Doleans, L. Dubbs, K. Elliott, A. Lapierre, W. Hartung, M. Johnson, S. Krause, F. Marti, J. Ottarson, G. Perdikakis, L. Popielarski, J. Popielarski, M. Portillo, R. Rencsok, D. Sanderson, S. Schwarz, N. Verhanovitz, J. Vincent, J. Wlodarczak, X. Wu, J. Yurkon, A. Zeller, Q. Zhao, A. Schempp, and J. Schmidt. ReA3 - the Rare Isotope Reaccelerator at MSU. *Proceedings, 25th International Linear Accelerator Conference,*

LINAC2010: Tsukuba, Japan, September 12-17, 2010, page MO203, 2011. URL http://accelconf.web.cern.ch/AccelConf/LINAC2010/papers/mo203.pdf.

[51] G. Bollen. FRIB - Facility for Rare Isotope Beams. *AIP Conference Proceedings*, 1224:432, 2010.

[52] N. Rowley, G. R. Satchler, and P. H. Stelson. On the "distribution of barriers" interpretation of heavy-ion fusion. *Physics Letters B*, 254:25, 1991.

[53] V. I. Zagrebaev et al. Fusion codes of the NRV. URL http://nrv.jinr.ru/nrv/.

[54] T. D. Thomas. Cross section for compound-nucleus formation in heavy-ion-induced reactions. *Physical Review*, 116:703, 1959.

[55] J. Lilley. *Nuclear Physics: Principles and Applications*. John Wiley & Sons, Inc., 2003.

[56] J M. Blatt and V. F. Weisskopf. *Theoretical Nuclear Physics*. John Wiley and Sons, Inc., 1952.

[57] J. R. Huizenga and G. Igo. Theoretical reaction cross sections for alpha particles with an optical model. *Nuclear Physics*, 29:462–473, 1962.

[58] D. L. Hill and J. A. Wheeler. Nuclear constitution and the interpretation of fission phenomena. *Physical Review*, 89:1102, 1953.

[59] Ö. Akyüz and A. Winther. Nuclear structure and heavy ion reactions. In R. A. Broglia et al., editors, *Proceedings of the Enrico Fermi International School of Physics, 1979*, 1981.

[60] J. O. Newton, R. D. Butt, M. Dasgupta, D. J. Hinde, I. I. Gontchar, C. R. Morton, and K. Hagino. Systematic failure of the Woods-Saxon nuclear potential to describe both fusion and elastic scattering: possible need for a new dynamical approach to fusion. *Physical Review C*, 70:024605, 2004.

[61] A. M. Stefanini, G. Montagnoli, R. Silvestri, S. Beghini, L. Corradi, S. Courtin, E. Fioretto, B. Guiot, F. Haas, D. Lebhertz, N. Mărginean, P. Mason, F. Scarlassara, R. N. Sagaidak, and S. Szilner. Fusion of the positive Q-value system ^{36}S + ^{48}Ca well below the Coulomb barrier. *Physical Review C*, 78:044607, 2008.

[62] G. Montagnoli, A. M. Stefanini, H. Esbensen, C. L. Jiang, L. Corradi, S. Courtin, E. Fioretto, A. Goasduff, J. Grebosz, F. Haas, M. Mazzocco, C. Michelagnoli, T. Mijatovic, D. Montanari, C. Parascandolo, K. E. Rehm, F. Scarlassara, S. Szilner, X. D. Tang, and C. A. Ur. Effects of transfer channels on near- and sub-barrier fusion of ^{32}S + ^{48}Ca. *Physical Review C*, 87:014611, 2013.

[63] L. C. Vaz, J. M. Alexander, and G. R. Satchler. Fusion barriers, empirical and theoretical: evidence for dunamic deformation in subbarrier fusion. *Physics Reports*, 69:373–399, 1981.

[64] L. R. Gasques, L. C. Chamon, D. Pereira, M. A. G. Alvarez, and E. S. Rossi, Jr. and C. P. Silva and B. V. Carlson. Global and consistent analysis of the heavy-ion elastic scattering and fusion processes. *Physical Review C*, 69:034603, 2004.

[65] L. C. Chamon, D. Pereira, M. S. Hussein, M. A. Cândido Ribeiro, and D. Galetti. Nonlocal description of the nucleus-nucleus interaction. *Physical Review Letters*, 79:5218, 1997.

[66] L. C. Chamon, B. V. Carlson, L. R. Gasques, D. Pereira, C. De Conti, M. A. G. Alvarez, M. S. Hussein, M. A. Cândido Ribeiro, E. S. Rossi, Jr., and C. P. Silva. Toward a global description of the nucleus-nucleus interaction. *Physical Review C*, 66:014610, 2002.

[67] P. Ring. Relativistic mean field theory in finite nuclei. *Progress in Particle and Nuclear Physics*, 37:193, 1996.

[68] K. Hagino and N. Takigawa. Subbarrier fusion reactions and many-particle quantum tunneling. *Progress of Theoretical Physics*, 128:1001, 2012.

[69] C. H. Dasso, S. Landowne, and A. Winther. Channel-coupling effects in heavy-ion fusion reactions. *Nuclear Physics A*, 405:381, 1983.

[70] M. Beckerman, M. Salomaa, A. Sperduto, J. D. Molitoris, and A. DiRienzo. Sub-barrier fusion of ^{58,64}Ni with ^{64}Ni and ^{74}Ge. *Physical Review C*, 25:837, 1982.

[71] M. Dasgupta, D. J. Hinde, A. Diaz-Torres, B. Bouriquet, C. I. Low, G. J. Milburn, and J. O. Newton. Beyond the coherent coupled channels description of nuclear fusion. *Physical Review Letters*, 99:192701, 2007.

[72] T. Ichikawa, K. Hagino, and A. Iwamoto. Signature of smooth transition from sudden to adiabatic states in heavy-ion fusion reactions at deep sub-barrier energies. *Physical Review Letters*, 103:202701, 2009.

[73] K. Hagino and J. M. Yao. Present status of coupled-channels calculations for heavy-ion subbarrier fusion reactions. *EPJ Web of Conferences*, 117:08003, 2016.

[74] M. Beckerman, J. Ball, H. Enge, M. Salomaa, A. Sperduto, S. Gazes, A. DiRienzo, and J. D. Molitoris. Near- and sub-barrier fusion of ^{58}Ni with ^{58}Ni. *Physical Review C*, 23:1581, 1981.

[75] J. R. Leigh, M. Dasgupta, D. J. Hinde, J. C. Mein, C. R. Morton, R. C. Lemmon, J. P. Lestone, J. O. Newton, H. Timmers, J. X. Wei, and N. Rowley. Barrier distributions from the fusion of oxygen ions with ^{144,148,154}Sm and ^{186}W. *Physical Review C*, 52:3151, 1995.

[76] Ş. Mişicu and H. Esbensen. Hindrance of heavy-ion fusion due to nuclear incompressibility. *Physical Review Letters*, 96:112701, 2006.

[77] J. W. Negele. The mean-field theory of nuclear structure and dynamics. *Reviews of Modern Physics*, 54:913, 1982.

[78] A. S. Umar and V. E. Oberacker. Three-dimensional unrestricted time-dependent Hartree-Fock fusion calculations using the full Skyrme interaction. *Physical Review C*, 73:054607, 2006.

[79] V. E. Oberacker and A. S. Umar. Microscopic analysis of sub-barrier fusion enhancement in ^{132}Sn + ^{40}Ca versus ^{132}Sn + ^{48}Ca. *Physical Review C.*, 87:034611, 2013.

[80] R. T. deSouza, S. Hudan, V. E. Oberacker, and A. S. Umar. Confronting measured near- and sub-barrier fusion cross sections for ^{20}O+^{12}C with a microscopic method. *Physical Review C*, 88:014602, 2013.

[81] B. B. Back, H. Esbensen, C. L. Jiang, and K. E. Rehm. Recent developments in heavy-ion fusion reactions. *Reviews of Modern Physics*, 86:317, 2014.

[82] A. S. Umar and V. E. Oberacker. Time-dependent response calculations of nuclear resonances. *Physical Review C*, 71:034314, 2005.

[83] A. S. Umar, V. E. Oberacker, and C. J. Horowitz. Microscopic sub-barrier fusion calculations for the neutron star crust. *Physical Review C*, 85:055801, 2012.

[84] A. S. Umar and V. E. Oberacker. Heavy-ion interaction potential deduced from density-constrained time-dependent Hartree-Fock calculation. *Physical Review C*, 74:021601(R), 2006.

[85] A. S. Umar and V. E. Oberacker. *Private Communications*, 2013.

[86] E. Chabanat, P. Bonche, P. Haensel, J. Meyer, and R. Schaeffer. A Skyrme parametrization from subnuclear to neutron star densities Part II. Nuclei far from stabilities. *Nuclear Physics A*, 635:231, 1998.

[87] E. Chabanat, P. Bonche, P. Haensel, J. Meyer, and R. Schaeffer. Erratum to "A Skyrme parametrization from subnuclear to neutron star densities. (II): Nuclei far from stability". *Nuclear Physics A*, 643:441, 1998.

[88] A. S. Umar and V. E. Oberacker. Density-constrained time-dependent Hartree-Fock calculation of ^{16}O + ^{208}Pb fusion cross-sections. *The European Physical Journal A*, 39:243, 2009.

[89] Y. Eyal, M. Beckerman, R. Checkhik, Z. Fraenkel, and H. Stocker. Nuclear size and boundary effects on the fusion barrier of oxygen with carbon. *Physical Review C*, 13:1527, 1976.

[90] T. K. Steinbach, J. Vadas, J. Schmidt, C. Haycraft, S. Hudan, R. T. deSouza, L. T. Baby, S. A. Kuvin, I. Wiedenhöver, A. S. Umar, and V. E. Oberacker. Sub-barrier enhancement of fusion as compared to a microscopic method in ^{18}O + ^{12}C. *Physical Review C*, 90:041603(R), 2014.

[91] D. Bazin. *RIA Summer School*, July 17-21 2006.

[92] A. Mukherjee, U. Datta Pramanik, M. Saha Sarkar, A. Goswami, P. Basu, S. Bhattacharya, S. Sen, M. L. Chatterjee, and B. Dasmahapatra. ^{7}Li+^{12}C and ^{7}Li+^{13}C fusion reactions at subbarrier energies. *Nuclear Physics A*, 596:299, 1996.

[93] J. Vadas, T. K. Steinbach, J. Schmidt, V. Singh, C. Haycraft, S. Hudan, R. T. deSouza, L. T. Baby, S. A. Kuvin, and I. Wiedenhöver. Evidence for survival of the α cluster structure in light nuclei through the fusion process. *Physical Review C*, 92:064610, 2015.

[94] P. F. F. Carnelli, S. Almaraz-Calderon, K. E. Rehm, M. Albers, M. Alcorta, P. F. Bertone, B. Digiovine, H. Esbensen, J. Fernández Niello, D. Henderson, C. L. Jiang, J. Lai, S. T. Marley, O. Nusair, T. Palchan-Hazan, R. C. Pardo, M. Paul, and

C. Ugalde. Multi-Sampling Ionization Chamber (MUSIC) for measurements of fusion reactions with radioactive beams. *Nuclear Instruments and Methods in Physics Research A*, 799:197–201, 2015.

[95] N. T. Sullivan, D. Beaulieu, A. Treason, P. D. Rouffignac, and M. D. Potter. Method of fabricating micro channel plate device with multiple emissive layers. *US Patent*, 08052284, 2011.

[96] J. L. Wiza. Microchannel plate detectors. *Nuclear Instruments and Methods in Physics Research*, 162:587–601, 1979.

[97] Del Mar Photonics, Inc., 2017. URL http://www.dmphotonics.com/MCP_MCPImageIntensifiers/microchannel_plates.htm.

[98] J. D. Bowman and R. H. Heffner. A novel zero time detector for heavy ion spectroscopy. *Nuclear Instruments and Methods in Physics Research*, 148:503–509, 1978.

[99] T. K. Steinbach, M. J. Rudolph, Z. Q. Gosser, K. Brown, B. Floyd, S. Hudan, R. T. deSouza, J. F. Liang, D. Shapira, and M. Famiano. Measuring the fusion cross-section of light nuclei with low-intensity beams. *Nuclear Instruments and Methods in Physics Research A*, 743:5–13, 2014.

[100] W. R. Leo. *Techniques for Nuclear and Particle Physics Experiments*. Springer-Verlag, 1987.

[101] R. T. deSouza, A. Alexander, K. Brown, B. Floyd, Z. Q. Gosser, S. Hudan, J. Poehlman, and M. J. Rudolph. Sub-nanosecond time-of-flight for segmented silicon detectors. *Nuclear Instruments and Methods in Physics Research A*, 632: 133–136, 2011.

[102] Micron Semiconductor Ltd. URL www.micronsemiconductor.com.

[103] M. J. Rudolph. Measuring fusion cross-sections for the ^{20}O + ^{12}C system at near barrier energies. Master's thesis, Indiana University, 2011.

[104] T. K. Steinbach. *Near and sub-barrier fusion of neutron-rich oxygen and carbon nuclei using low-intensity beams.* PhD thesis, Indiana University, 2016.

[105] J. Va'Vra, P. A. Coyle, J. A. Kadyk, and J. Wise. Measurement of electron drift parameters for helium and CF-4 based gases. *Nuclear Instruments and Methods in Physics Research A*, 324:113–126, 1993.

[106] J. Vadas, V. Singh, G. Visser, A. Alexander, S. Hudan, J. Huston, B. B. Wiggins, A. Chbihi, M. Famiano, M. M. Bischak, and R. T. deSouza. High-rate axial-field ionization chamber for particle identification of radioactive beams. *Nuclear Instruments and Methods in Physics Research A*, 837:28, 2016.

[107] R. Brun and F. Rademakers. ROOT – an object oriented data analysis framework. *Nuclear Instruments and Methods in Physics Research A*, 389:81–86, 1997.

[108] B. Heusch, C. Beck, J.P. Coffin, P. Engelstein, R. M. Freeman, G. Guillaume, F. Haas, and P. Wagner. Entrance channel effect for complete fusion of O + C isotopes. *Physical Review C*, 26:542, 1982.

[109] D. Kovar, D.F. Geesaman, T.H. Braid, Y. Eisen, W. Henning, T.R. Ophel, M. Paul, K.E. Rehm, S.J. Sanders, P. Sperr, J.P. Schiffer, S.L. Tabor, S. Vigdor, B. Zeidman, and F.W. Prosser Jr. Systematics of carbon- and oxygen-induced fusion on nuclei with $12 \leq A \leq 19$. *Physical Review C*, 20:1305, 1979.

[110] N. G. Nicolis and J. R. Beene. evapOR: a multi-particle monte-carlo evaporation code intended to extend statistical-model calculations to the high-energy regime. *unpublished*, 1993.

[111] A. S. Umar, M. R. Strayer, J. S. Wu, D. J. Dean, and M. C. Güçlü. Nuclear Hartree-Fock calculations with splines. *Physical Review C*, 44:2512–2521, 1991.

[112] J. A. Maruhn, P.-G. Reinhard, P. D. Stevenson, and A. S. Umar. The TDHF code Sky3D. *Computer Physics Communications*, 185:2195–2216, 2014.

[113] P.-G. Reinhard, A. S. Umar, K. T. R. Davies, M. R. Strayer, and S. J. Lee. Dissipation and forces in time-dependent Hartree-Fock calculations. *Physical Review C*, 37:1026–1035, 1988.

[114] A. S. Umar, M. R. Strayer, P.-G. Reinhard, K. T. R. Davies, and S.-J. Lee. Spin-orbit force in time-dependent Hartree-Fock calculations of heavy-ion collisions. *Physical Review C*, 40:706–714, 1989.

[115] P. Klupfel, P.-G. Reinhard, T. J. Burvenich, and J. A. Maruhn. Variations on a theme by Skyrme: a systematic study of adjustments of model parameters. *Physical Review C*, 79:034310, 2009.

[116] M. Kortelainen, T. Lesinski, J. More, W. Nazarewicz, J. Sarich, N. Schunck, M. V. Stoitsov, and S. Wild. Nuclear energy density optimization. *Physical Review C*, 82: 024213, 2010.

[117] R. Keser, A. S. Umar, and V. E. Oberacker. Microscopic study of Ca + Ca fusion. *Physical Review C*, 85:044606, 2012.

[118] C. Simenel, R. Keser, A. S. Umar, and V. E. Oberacker. Microscopic study of ^{16}O+^{16}O fusion. *Physical Review C*, 88:024617, 2013.

[119] A. S. Umar, C. Simenel, and V. E. Oberacker. Energy dependence of potential barriers and its effect on fusion cross sections. *Physical Review C*, 89:034611, 2014.

[120] C. Y. Wong. Interaction barrier in charged-particle nuclear reactions. *Physical Review Letters*, 31:766, 1973.

[121] V. Weisskopf. Statistics and nuclear reactions. *Physical Review*, 52:295, 1937.

[122] W. Hauser and H. Feshbach. The inelastic scattering of neutrons. *Physical Review*, 87:366, 1952.

[123] Y. Nagashima, J. Schimizu, T. Nakagawa, Y. Fukuchi, W. Yokota, K. Furuno, M. Yamanouchi, S. M. Lee, N. X. Dai, T. Mikumo, and T. Motobayashi. Effects of entrance channel and compound nucleus in the fusion cross sections for ^{28}Si+^{28}Si, ^{16}O+^{40}Ca, and ^{12}C+^{50}Cr. *Physical Review C*, 33:176, 1986.

[124] E. D. Johnson. *The cluster structure of oxygen isotopes*. PhD thesis, Florida State University, 2008.

[125] W. von Oertzen, M. Milin, T. Dorsch, H.G. Bohlen, R. Krücken, T. Faestermann, R. Hertenberger, Tz. Kokalova, M. Mahgoub, C. Wheldon, and H. -F. Wirth. Shell model and band structures in ^{19}O. *The European Physical Journal A*, 43:17, 2010.

[126] A. Gavron. Statistical model calculations in heavy ion reactions. *Physical Review C*, 21:230, 1980.

[127] J. F. Ziegler, M. D.Ziegler, and J. P. Biersack. SRIM: the stopping and range of ions in matter. *Nuclear Instruments and Methods in Physics Research B*, 268:1818, 2010.

[128] P. R. Christensen, Z. E. Switkowski, and R. A. Dayras. Sub-barrier fusion measurements for ^{12}C+^{16}O. *Nuclear Physics A*, 280:189–204, 1977.

[129] S. L. Tabor, Y. Eisen, D. G. Kovar, and Z. Vager. Comparison of light- and heavy-ion emission from the ^{12}C+^{16}O system. *Physical Review C.*, 16:673, 1977.

[130] C. T. Papadopoulos, R. Vlastou, E. N. Gazis, P. A. Assimakopoulos, C. A. Kalfas, S. Kossionides, and A. C. Xenoulis. Fusioin cross section of the ^{16}O+^{13}C reaction. *Physical Review C*, 34:196, 1986.

[131] I. Wiedenhöver et al. Studies of exotic nuclei at the resolut facility of florida state university. In J.H. Hamilton and A.V. Ramayya, editors, *Fifth International Conference on Fission and Properties of Neutron-rich Nuclei*. World Scientific, 2012. ISBN 978-981-4525-42-8.

[132] D. Santiago-Gonzalez. *Experimental investigations on the nuclear structure of the neutron-rich nuclides ^{44}S and ^{20}O*. PhD thesis, Florida State University, 2013.

[133] Varinderjit Singh, J. Vadas, T. K. Steinbach, B. B. Wiggins, S. Hudan, R. T. deSouza, Zidu Lin, C. J. Horowitz, L. T. Baby, S. A. Kuvin, Vandana Tripathi, and I. Wiedenhöver. Fusion enhancement at near and sub-barrier energies in ^{19}O + ^{12}C. *Physics Letters B*, 765:99–103, 2017.

[134] T. Paduszynski, P. Sprunger, R. T. deSouza, S. Hudan, A. Alexander, B. Davin, G. Fleener, A. Mcintosh, C. Metelko, R. Moore, N. Peters, J. Poehlman, J. Gauthier, F. Grenier, R. Roy, D. Thériault, E. Bell, J. Garey, J. Iglio, A. L. Keksis, S. Parketon, C. Richers, D. V. Shetty, S. N. Soisson, G. A. Soulioutis, B. Stein, and S. J. Yennello. Resolving multiple particles in a highly segmented silicon array. *Nucl. Instr.and Meth. A*, 547:464, 2005.

[135] B. Schuetrumpf and W. Nazarewicz. Cluster formation in precompound nuclei in the time-dependent framework. *Physical Review C*, 96:064608, 2017.

[136] ACF-Metals, The Arizona Carbon Foil Co., Inc., 2018. URL https://www.acf-metals.com/product-information.

[137] B. D. Serot and J. D. Walecka. The relativistic nuclear many-body problem. *Advances in Nuclear Physics*, 16:1, 1986.

[138] B. Cujec and C. A. Barnes. Total reaction cross-section for ^{12}C+^{16}O below the Coulomb barrier. *Nuclear Physics A*, 266:461–493, 1976.

[139] K. Hagino, N. Rowley, and A. T. Kruppa. A program for coupled-channel calculations with all order couplings for heavy-ion fusion reactions. *Computer Physics Communications*, 123:143–152, 1999.

[140] B. M. Sherrill. Overview of the Facility for Rare Isotope Beams. *Presented at: 240th American Chemical Society National Meeting; Boston, MA*, 2010.

[141] A. Lapierre, G. Bollen, D. Crisp, S. W. Krause, L. E. Linhardt, K. Lund, S. Nash, R. Rencsok, R. Ringle, S. Schwarz, M. Steiner, C. Sumithrarachchi, T. Summers, A. C. C. Villari, S. J. Williams, and Q. Zhao. First two operational years of the electron-beam ion trap charge breeder at the National Superconducting Cyclotron Laboratory. *Physical Review Accelerators and Beams*, 21:053401, 2018.

[142] K. Kimura, T. Izumikawa, R. Koyama, T. Ohnishi, T. Ohtsubo, A. Ozawa, W. Shinozaki, T. Suzuki, M. Takahashi, I. Tanihata, T. Yamaguchi, and Y. Yamaguchi. High-rate particle identification of high-energy heavy ions using a tilted electrode gas ionization chamber. *Nuclear Instruments and Methods in Physics Research A*, 538:608, 2005.

[143] K. Y. Chae, S. Ahn, D. W. Bardayan, K. A. Chipps, B. Manning, S. D. Pain, W. A. Peters, K. T. Schmitt, M. S. Smith, and S. Y. Strauss. Construction of a fast ionization chamber for high-rate particle identification. *Nuclear Instruments and Methods in Physics Research A*, 751:6, 2014.

[144] P. F. F. Carnelli, S. Almaraz-Calderon, K. E. Rehm, M. Albers, M. Alcorta, P. F. Bertone, B. Digiovine, H. Esbensen, J. O. Fernández Niello, D. Henderson, C. L. Jiang, J. Lai, S. T. Marley, O. Nusair, T. Palchan-Hazan, R. C. Pardo, M. Paul, and C. Ugalde. Measurements of fusion reactions of low-intensity radioactive carbon beams on ^{12}C and their implications for the understanding of X-ray bursts. *Physical Review Letters*, 112:192701, 2014.

[145] J. Vadas, V. Singh, B. B. Wiggins, J. Huston, S. Hudan, R. T. deSouza, Z. Lin, C. J. Horowitz, A. Chbihi, D. Ackermann, M. Famiano, and K. W. Brown. Probing the fusion of neutron-rich nuclei with re-accelerated radioactive beams. *Physical Review C*, 97:031601(R), 2018.

[146] C. Metelko, A. Alexander, S. Hudan, J. Poehlman, and R. T. deSouza. MASE: a novel approach to readout of a highly segmented silicon detector array. *Nuclear Instruments and Methods in Physics Research A*, 569:815, 2006.

Jessica Elizabeth Vadas

Departments of Chemistry and Physics
Center for Exploration of Energy and Matter
Indiana University, Bloomington, IN 47408
jvadas@iu.edu

Education

Postdoctoral Certificate, Medical Physics, *Indiana University, Bloomington, IN* — Jan. 2018 – Dec. 2018
Advisor: Susan Klein

Ph.D., Chemical Physics, *Indiana University, Bloomington, IN* — Aug. 2013 – Dec. 2018
Advisor: Romualdo de Souza

B.A., Chemistry, Physics, *Earlham College, Richmond, IN* — Aug. 2009 – May 2013
Advisor: Lori Watson

Select Awards & Honors

Indiana University, Bloomington:

Carroll Family Fellowship	2018
IUB Provost's Travel Award for Women in Science	2018
US Nomination to the 67th Lindau Nobel Laureate Meeting	2017
Division of Nuclear Physics Travel Grant - 2015 APS April Meeting	2015
National Science Foundation Graduate Research Fellowship	2015

Earlham College:

George Van Dyke Distinguished Student in Physics Award	2013
Nuclear Chemistry Summer School Outstanding Student Award	2012
Russell M. Lawall Physics Research Award	2012
Verne F. Swaim Memorial Scholarship	2012
Gertrude Pardieck Hubbard Distinguished Student Award	2011

Research Experience

Department of Chemistry, Indiana University, Bloomington, IN — 2013 – 2018
Graduate Research Associate, advisor: Romualdo de Souza
Probing the fusion of neutron-rich nuclei with reaccelerated radioactive beams

- Investigated the role of additional neutrons in the fusion process as nuclei become increasingly neutron-rich by designing and executing radioactive beam experiments at leading accelerator facilities.

Department of Physics, Earlham College, Richmond, IN — 2011 – 2012
Undergraduate Research Assistant, advisor: Maria-Teresa Herd
Ultrasonic attenuation in cell pellets using through transmission

- Measured ultrasonic attenuation coefficients of malignant and benign cell lines with a through transmission approach.

Peer-reviewed Publications

1. Probing the fusion of neutron-rich nuclei with re-accelerated radioactive beams, **J. Vadas**, et al., *Phys. Rev. C* 97, 031601(R) (2018).

2. An efficient and cost-effective microchannel plate detector for slow neutron radiography, B. B. Wiggins, **J. Vadas**, et al., *Nucl. Instr. Meth. In Phys. Res. A* 891, 53 (2018).

3. Achieving high spatial resolution using a microchannel plate detector with an economic and scalable approach, B. B. Wiggins, Z. O. deSouza, **J. Vadas**, et al., *Nucl. Instr. Meth. In Phys. Res. A* 872, 144 (2017).

4. Development of a compact ExB microchannel plate detector for beam imaging, B. B. Wiggins, V. Singh, **J. Vadas**, et al., *Nucl. Instr. Meth. In Phys. Res. A* 866, 202 (2017).

5. Fusion enhancement at near and sub-barrier energies in $^{19}O + ^{12}C$, Varinderjit Singh, **J. Vadas**, et al., *Phys. Lett. B* 765, 99 (2017).

6. High-rate axial-field ionization chamber for particle identification of radioactive beams, **J. Vadas**, et al., *Nucl. Instr. Meth. In Phys. Res. A* 837, 28 (2016).

7. Evidence for survival of the α cluster structure in light nuclei through the fusion process, **J. Vadas**, et al., *Phys. Rev. C* 92, 064610 (2015).

8. Sub-barrier enhancement of fusion as compared to a microscopic method in $^{18}O + ^{12}C$, T.K. Steinbach, **J. Vadas**, et al., *Phys. Rev. C* 90, 041603(R) (2014).

Research Presentations

1. Probing the fusion of neutron-rich nuclei with re-accelerated radioactive beams, *American Physical Society April Meeting, Columbus, OH.* Oral presentation. 2018

2. Exploring the stars with radioactive beams, *Nuclear Chemistry Seminar, Department of Chemistry, Indiana University, Bloomington, IN.* Oral presentation. 2017

3. Measuring the fusion cross-section of $^{39,47}K + ^{28}Si$ at near barrier energies, *Exotic Beam Summer School, Argonne National Lab, Lemont, IL.* Oral presentation. 2017

4. Measuring the fusion cross-section of $^{39,47}K + ^{28}Si$ at near barrier energies, *Exotic Beam Summer School, Argonne National Lab, Lemont, IL.* Poster presentation. 2017

5. Exploring the stars with radioactive beams, *Nuclear Chemistry Summer School, Brookhaven National Lab, Brookhaven, NY.* Oral presentation. 2017

6. Measuring the fusion cross-section of $^{39,47}K + ^{28}Si$ at near barrier energies, *Gordon Research Conference, New London, NH.* Poster presentation. 2017

7. Measuring the fusion cross-section of ^{39,47}K + ^{28}Si at near barrier energies, *Gordon Research Seminar, New London, NH.* Oral presentation. 2017

8. Measuring the fusion cross-section of ^{39,47}K + ^{28}Si at near barrier energies, *American Physical Society April Meeting, Washington, DC.* Oral presentation. 2017

9. Enhancement of fusion at near-barrier energies for neutron-rich light nuclei: ^{19}O + ^{12}C, *American Physical Society April Meeting, Washington, DC.* Oral presentation. 2017

10. Does the alpha cluster structure in light nuclei persist through the fusion process?, *American Physical Society April Meeting, Salt Lake City, UT.* Oral presentation. 2016

11. Exploring fusion of neutron-rich light nuclei using radioactive beams, *Physical Chemistry Seminar, Department of Chemistry, Indiana University, Bloomington, IN.* Oral presentation. 2015

12. Does the alpha cluster structure in light nuclei survive the fusion process?, *Physics Seminar, Department of Physics, Florida State University, Tallahassee, FL.* Oral presentation. 2015

13. Alpha emission in the de-excitation of ^{30}Si at E* = 30 to 38 MeV, *American Physical Society April Meeting, Baltimore, MD.* Oral presentation. 2015

14. Light charged particle emission following the fusion of ^{18}O ions with ^{12}C nuclei at energies near and below the Coulomb barrier, *American Chemical Society Fall Meeting, San Francisco, CA.* Oral presentation. 2014

15. Ultrasonic Attenuation Measurements of Cell Pellets Using Through Transmission, *American Physical Society Fall Meeting, APS Ohio-Region Section, Muncie, IN.* Poster presentation. 2011

Teaching Experience

Associate Instructor, *Indiana University* 2017

- I taught the discussion section of the Nuclear Chemistry class, developed and administered quizzes, proctored and graded exams, and held office hours.

Academic Tutor, *Earlham College* 2010 - 2013

- I tutored student both individually and in group settings in both General Physics II (Electricity and Magnetism) and Analytical Chemistry.

Laboratory Teaching Assistant, *Earlham College* 2010 - 2013

- I supervised the laboratory sections for Environmental Chemistry, Inorganic Chemistry, Analytical Chemistry, and General Chemistry.